Light Weakly Interacting Particles: Constraints and Connection to Dark Matter

Dissertation
zur Erlangung des Doktorgrades
des Departments Physik
der Universität Hamburg

vorgelegt von

Sarah Andreas
aus Pirmasens, Deutschland

Hamburg
2013

Gutachter der Dissertation:	Dr. Andreas Ringwald
	Prof. Dr. Günter Sigl
Gutachter der Disputation:	Dr. Andreas Ringwald
	Dr. Torsten Bringmann
Datum der Disputation:	21.06.2013
Vorsitzender des Prüfungsausschusses:	Dr. Georg Steinbrück
Vorsitzender des Promotionsausschusses:	Prof. Dr. Peter Hauschildt
Dekan der Fakultät MIN:	Prof. Dr. Heinrich Graener

Abstract

The so far unknown particle nature of dark matter is a main motivation for extending the Standard Model of particle physics. A recently promoted approach to solving this puzzle is the concept of hidden sectors. Since the interactions of such sectors with the visible sector are very weak, so are the current experimental bounds. Hidden sectors might even contain sub-GeV scale particles that have so far escaped detection.

In this thesis, we study the phenomenology of Weakly Interacting Slim Particles (WISPs) as well as their connection to dark matter in different Standard Model extensions. In the Next-to-Minimal Supersymmetric Standard Model (NMSSM), a light CP-odd Higgs, arising from spontaneous breaking of approximate symmetries, represents an example of a WISP. Light gauge bosons of an extra U(1) symmetry in a hidden sector are other well motivated candidates for WISPs and called hidden photons. Such light hidden photons appear naturally in supersymmetry or string theory and might resolve the observed deviation in the muon anomalous magnetic moment from predictions. Moreover, scenarios in which hidden sector dark matter interacts via a light hidden photon with the visible sector exhibit appealing features in view of recent astrophysical anomalies.

We study how the coupling of the CP-odd Higgs A^0 to fermions can be constrained by current measurements for the case where the A^0 is lighter than two muons. Analysing measurements of different rare and radiative meson decays, the muon anomalous magnetic moment as well as results from beam dump and reactor experiments, we severely constrain the CP-odd Higgs to be heavier than 210 MeV or to couple to fermions four orders of magnitude weaker than the Standard Model Higgs. These results apply more generally to the coupling of an axion-like particle to matter.

Hidden photons can be constrained by experiments since they couple to charged Standard Model particles via kinetic mixing with the ordinary photon. We derive several constraints on the kinetic mixing for MeV-scale hidden photons from their production in past electron beam dump experiments. Including previously unconsidered experiments and taking into account the experimental acceptances, we exclude parts of the parameter space which had not been constrained by any similar study before.

Additionally, we analyse different extensions of the Standard Model in which the hidden sector contains a light dark matter particle besides the hidden photon. For a minimal toy model and string-inspired supersymmetric hidden sector models with gravity mediation, we perform a parameter scan and compute the dark matter relic abundance and the scattering cross sections in direct detection experiments. We then compare the results of these computations to current experimental measurements. In this way, for the different models, we find viable dark matter candidates with potentially interesting signals in direct detection experiments.

In summary, this work shows that WISPs, even though they only interact weakly with the Standard Model, can be probed by experiments. Moreover, hidden photons especially in connection to dark matter are found to exhibit interesting phenomenological features.

Zusammenfassung

Die noch immer unbekannte Natur der Dunklen Materie ist einer der Hauptgründe, das Standardmodell der Teilchenphysik zu erweitern. Versteckte Sektoren bieten einen interessanten Ansatz zur Lösung dieses Rätsels. Da diese Sektoren sehr schwach mit dem Standardmodell wechselwirken, sind sie kaum durch Experimente beschränkt. Selbst sehr leichte Teilchen könnten darin enthalten und bisher unbeobachtet geblieben sein.

Diese Arbeit beschäftigt sich mit der Phänomenologie solcher leichter, schwach wechselwirkender Teilchen, genannt WISPs (Weakly Interacting Slim Particles), sowie deren Verbindung zur Dunklen Materie in verschiedenen Erweiterungen des Standardmodells. Im Nicht-Minimalen Supersymmetrischen StandardModell (NMSSM), ist das leichte CP-ungerade Higgs, welches durch spontane Brechung approximativer Symmetrien entstehen kann, ein mögliches WISP. Ein weiteres Beispiel ist das leichte, versteckte Photon, das Eichboson einer zusätzlichen U(1) Symmetrie im versteckten Sektor. Leichte versteckte Photonen können in Supersymmetrie oder in der Stringtheorie vorkommen und beispielsweise die Abweichung im anomalen magnetischen Moment des Myons erklären. Außerdem haben versteckte Sektoren mit Dunkler Materie, welche über versteckte Photonen wechselwirkt, besondere Merkmale im Hinblick auf astrophysikalische Anomalien.

Wir untersuchen, wie die Kopplung des CP-ungeraden Higgs A^0 an Fermionen durch aktuelle Messungen beschränkt werden kann, wenn das A^0 leichter ist als zwei Myonen. Durch die Analyse verschiedener Mesonzerfälle, des anomalen magnetischen Moments des Myons sowie Ergebnissen aus Experimenten an Reaktoren und mit festem Target (beam dump) finden wir, dass das A^0 schwerer als 210 MeV sein muss oder um vier Größenordnungen schwächer an Fermionen koppelt als das Higgs. Diese Ergebnisse gelten allgemein für die Kopplung axion-ähnlicher Teilchen an Materie.

Das versteckte Photon kann experimentell untersucht werden, da es aufgrund der kinetischen Mischung mit dem Photon an geladene Standardmodell-Teilchen koppelt. Wir bestimmen Grenzen für diese Mischung aus der Produktion von versteckten Photonen mit Massen im MeV-Bereich in Experimenten, die Elektronen auf feste Targets schießen. Dank bisher unberücksichtigter Experimente und unter Verwendung der experimentellen Akzeptanzen, schließen wir einen neuen Parameterbereich aus.

Desweiteren analysieren wir Erweiterungen des Standardmodells, die außer versteckten Photonen auch Dunkle Materie im versteckten Sektor enthalten. Für ein Toy-Modell und supersymmetrische versteckte Sektoren überprüfen wir, ob die Dunkle Materie in der richtigen Menge produziert werden kann und ihre Streuung an Kernen mit experimentellen Grenzen verträglich ist. In den verschiedenen Modellen finden wir mögliche Dunkle Materie Kandidaten mit interessanten experimentellen Signaturen.

Insgesamt zeigt diese Arbeit, dass WISPs trotz ihrer schwachen Wechselwirkungen experimentell überprüfbar sind. Außerdem können sie insbesondere in Verbindung mit Dunkler Materie eine interessante Phänomenologie aufweisen.

Contents

Introduction

The existence of a large amount of non-luminous, non-baryonic dark matter is nowadays well established by numerous observations made on galactic up to cosmological length-scales [1–4]. Dark matter is known to account for more than 80% of the matter density in the Universe and thought to be abundantly present in form of large massive halos in galaxies, including the Milky Way. Its particle nature, however, is still unidentified and poses one of the most important open questions in both particle physics and cosmology. Much effort is being made, both on the theoretical and the experimental side, to find clues and provide approaches that allow us to improve our understanding and, hopefully, finally solve this puzzle.

The Standard Model of particle physics is remarkably successful in being consistent with many experimental tests. However, different shortcomings and open questions point towards the existence of new physics. For example, the Standard Model does not include neutrino masses and requires fine-tuning in order for the Higgs mass to remain small despite large quantum corrections (hierarchy problem). Furthermore, it is generally accepted that the Standard Model does not provide an appropriate dark matter candidate. A vast number of models extending the Standard Model exist. They range from minimal models addressing one specific phenomenon to sophisticated frameworks that aim at solving all the known fundamental problems. Many of these models also provide candidates for dark matter [1–7]. The most prominent candidates are the so-called Weakly Interacting Massive Particles (WIMPs), since these are naturally produced in the correct amount and further hopefully observable through weak-scale interactions. Among the various Standard Model extensions, supersymmetry (SUSY) is a widely-used framework. Specific well-studied examples include the Minimal and the Next-to-Minimal Supersymmetric Standard Model, abbreviated as MSSM and NMSSM, respectively. Recently, there has also been much interest in the concept of so-called hidden sectors, which are the main focus of this thesis. These are characterised as lacking a direct connection to the Standard Model and interact only very weakly through some messenger particle with the visible sector. In general, the commonly considered models of physics beyond the Standard Model frequently postulate new particles at the TeV scale. On the other hand, there are also models predicting light particles with masses in the sub-GeV range which, for example, reside in a hidden sector and could have connections to dark matter.

Until now, dark matter has only been observed through gravitational interactions. To solve the mystery of its particle nature and identify it as being a candidate of a particular model, it is essential to also observe it via other interactions. Although, in principle, such interactions may be absent, in this work, dark matter is assumed to undergo some weak-scale interactions. Various experiments seeking to discover a signal of such interactions have already been carried out and are currently in operation. One usually distinguishes three different detection methods allowing complementary searches. Direct detection experiments try to observe the recoil caused by the scattering of dark matter on a nucleus [8–11]. Additionally, indirect detection experiments search for signs of dark matter annihilation products, like neutrinos, gamma rays or positrons in cosmic rays [12, 13]. Furthermore, dark matter might be produced in interactions of Standard Model particles at a collider like the Large Hadron Collider (LHC) and would appear as missing energy.

Much experimental work is dedicated to revealing the nature of dark matter and finding concrete signs of physics beyond the Standard Model, especially to discovering new particles at the TeV scale. However, no such particles have been detected yet. Negative results in searches at the LHC progressively increase the mass scales at which new particles might exist. Simultaneously, null results from indirect and direct detection experiments continuously decrease the bounds on the strength with which dark matter is allowed to self-annihilate or scatter on nuclei.

However, new *light* particles with masses in the sub-GeV to GeV range might still be allowed and could have escaped detection because of very weak couplings to the Standard Model. In analogy to their heavy counterparts, the WIMPs, such particles are called WISPs, for Weakly Interacting Slim Particles. In general, an entirely new sector with unobserved particles might exist where the gauge interactions are not directly linked to the Standard Model sector. Then, the only interaction with the visible sector might be very weakly through a messenger particle. Such scenarios with hidden sectors are well motivated both from a theoretical and a phenomenological perspective. They call for new physics searches at the high-intensity frontier and present a complementary approach to high-energy experiments like the LHC. This thesis deals with two examples of WISPs — the CP-odd Higgs of the NMSSM and the gauge boson, named hidden photon, of an extra U(1) symmetry — and their phenomenological implications as well as their connection to dark matter.

Hidden sectors are a generic feature of various Standard Model extensions, e.g. supersymmetric models, where these can be the source of SUSY breaking [4, 14, 15]. In the case of a hidden sector with an extra U(1) gauge symmetry, the corresponding gauge boson, the hidden photon, acts as messenger to the Standard Model. Such scenarios with a hidden U(1), which may remain unbroken down to low energies, arise frequently in supersymmetric extensions [16–19] or string theories [20, 21]. The dominant interaction of the hidden photon with the Standard Model occurs in the low-energy effective

Lagrangian at the dimension four level through kinetic mixing with the ordinary photon [22–25] and is therefore not suppressed by some higher scale. This kinetic mixing can be generated at high energies by loops of heavy particles charged under both the hidden and the visible U(1) so that a typical estimate for the kinetic mixing is of the order of a loop factor $\sim 10^{-3}$. A mass $m_{\gamma'}$ for the hidden photon arises if the extra U(1) symmetry is broken by a Higgs or Stückelberg mechanism. Masses for the hidden photon in the MeV to GeV range can be obtained naturally for certain string compactifications and additionally provide phenomenologically interesting features. The contribution of an MeV-scale hidden photon to the anomalous magnetic moment of the muon can solve the long-standing discrepancy between the measured value and the theoretical prediction [26]. In connection with dark matter in the hidden sector, an MeV to GeV scale hidden photon can enhance the present-day dark matter annihilation cross section by the so-called Sommerfeld effect [27]. Additionally, the annihilation proceeding through the hidden photon is naturally leptophilic if the hidden photon is so light that it can only decay into leptons. These two special characteristics are advantageous when trying to fit the anomalous excess in the positron fraction in cosmic rays observed by PAMELA [28], FERMI [29, 30] and, recently, AMS [31] with positrons from dark matter annihilations. Moreover, the signals reported by the direct detection experiments DAMA [32–34], CoGeNT [35, 36] and CRESST [37, 38], as well as the very recent claim by CDMS [39], can be explained with an $\mathcal{O}(10\ \text{GeV})$ dark matter particle that undergoes spin-independent scattering on nuclei mediated by a hidden photon.

In this thesis, we study how the parameter space of WISPs can be constrained by experiments despite their very weak interactions. In particular, we explore different aspects of hidden sectors with a light hidden photon and the connection to dark matter. The kinetic mixing with the photon produces an effective coupling of the hidden photon to the electromagnetic current of the Standard Model which is suppressed by the kinetic mixing parameter χ. This interaction allows the hidden photon to be probed and constrained by experiments. Like a normal photon, it can, for example, be produced off an initial electron beam in a process similar to ordinary bremsstrahlung. Furthermore, due to kinetic mixing, hidden photons can decay into charged Standard Model particles, notably into an electron-positron pair in the mass range of interest in this work. Experiments try to produce hidden photons by colliding an electron beam onto a fixed target and to observe their decay products in a detector behind a thick beam dump. Since the hidden photon only interacts very weakly, it traverses this dump while the Standard Model background is absorbed. From the number of events expected in such an experiment from the decay of the hidden photon we derive constraints on its mass $m_{\gamma'}$ in the MeV range and on the size of the kinetic mixing χ. Besides a theoretical calculation, we also take the actual experimental acceptance into account. For this purpose, we simulate events with a Monte Carlo generator and construct trajectories for the hidden photon and its decay products. We then compute the acceptances by comparing these trajectories with the set-up of different experiments while applying possible energy cuts.

The resulting constraints of these searches for very weakly coupled light particles profit from high intensities and are therefore complementary to the aforementioned efforts at the energy frontier.

With the same kind of experiments it is also possible to probe other WISPs with masses in the MeV range like the NMSSM CP-odd Higgs or axion-like particles in general. Similar to hidden photons, these particles can be emitted off the initial electron beam either in bremsstrahlung or by Primakoff production, see, e.g. [40]. They can subsequently be searched for via their decay into a pair of photons or an electron-positron pair. By analysing results obtained from the above-mentioned beam dump experiments in terms of the CP-odd Higgs, we deduce constraints on its mass and its coupling to Standard Model fermions. Moreover, we derive various other limits from different meson decays, the muon anomalous magnetic moment and reactor experiments. Even though this analysis was performed for the CP-odd Higgs, it does not rely on specific details of the NMSSM and the resulting bounds can therefore be applied to the coupling of any light pseudoscalar (axion-like) particle to Standard Model fermions.

Hidden sector models containing a dark matter particle in addition to a hidden photon exhibit further interesting features. In view of the aforementioned direct detection signals, we focus on scenarios with an $\mathcal{O}(10\text{ GeV})$ dark matter particle. First, we consider a toy model, which is appealing because of its minimal particle content and few parameters allowing for definite phenomenological predictions. Second, we study a more sophisticated model of a dark sector embedded in a supersymmetric framework. In this case, we examine two mechanisms by which the hidden gauge symmetry can be broken, as these have different phenomenological implications. For all these models, we analyse whether the dark matter particle can be produced in the right amount to yield the observed dark matter relic abundance. Furthermore, we compute the scattering cross sections of the dark matter particle and compare these to the aforementioned signal claims as well as limits from direct detection experiments. In doing so, it is necessary to distinguish whether the dark matter particle is a Dirac fermion or a Majorana fermion. While the former scatters on nuclei in a predominantly spin-independent manner, which could potentially explain the signal claims, the latter essentially only exhibits spin-dependent scattering. This different behaviour leads to distinct signatures in direct detection searches. Such experiments are thus able to probe complementary regions of the parameter space.

In the following, we describe how the remainder of this thesis is organised.

Chapter 1 gives the theoretical background and ingredients for the analyses reported in the subsequent chapters. We recapitulate the observational evidence for dark matter and the properties demanded of a viable dark matter candidate. We also discuss the three detection methods that are used to search for dark matter and comment on the challenges they face. Furthermore, we introduce and motivate the different concepts of the Standard

Model extensions that are relevant for this work. The basics of hidden sectors with a hidden photon and kinetic mixing are established. Additionally, we introduce the different models with a dark matter particle, besides the hidden photon, in the hidden sector. We set the framework for the toy model and the supersymmetric realisations of such a light hidden sector. For the latter, we discuss the two mechanisms by which the hidden gauge symmetry is considered to be broken. Further, we specify the two limiting scenarios of the NMSSM in which the CP-odd Higgs is light.

In **Chapter 2**, we present constraints derived on the light CP-odd Higgs A^0, allowing us to address the question of how light the A^0 can be in the NMSSM. We discuss the different types of meson decays through which one can search for the CP-odd Higgs and show the regions of parameter space which can be excluded using various measurements of such decays. Additionally, we consider the limits that can be obtained from the muon anomalous magnetic moment as well as beam dump and reactor experiments. These results are also published in [41] and quoted in the Review of Particle Physics by the Particle Data Group (PDG) [4].

Chapter 3 treats the analysis of several electron beam dump experiments and the resulting limits on the hidden photon mass and the kinetic mixing, as published in [42]. We discuss both the production of hidden photons in bremsstrahlung and the subsequent decay into electrons. For the predicted number of events in an experiment, we illustrate the dependence on the different parameters of the experimental set-up. We describe how we determine the acceptance of each experiment under consideration by using the results of the Monte Carlo simulations performed with MadGraph. Together with the constraints obtained from our analysis we summarise the status of all current constraints on hidden photons and briefly describe the various searches as well as future experiments.

Chapter 4 is concerned with the phenomenology of the different dark sector models in which the hidden photon mediates the interaction between the Standard Model and the dark matter particle in the hidden sector. We introduce the constraints that arise on these kind of scenarios and illustrate their application to our dark sector models. The resulting effects on the parameter space of the toy model and the supersymmetric models are examined in detail with emphasis on the signatures in direct detection experiments. Besides covering results published in [43], this chapter presents an update of the entire analysis taking into account recent developments in direct detection experiments.

In **Chapter 5**, we conclude and give an outlook on future work.

Chapter 1

Fundamentals

This chapter sets the stage for the analyses carried out in this thesis and the findings presented in the subsequent chapters. In Sec. 1.1, starting from the observational evidence for dark matter, the requirements that have to be met by a viable dark matter particle are summarised and WIMPs as appealing candidates are discussed. Additionally, the distribution of dark matter in the galaxy and possible detection methods are outlined. Sec. 1.2 introduces different extensions of the Standard Model which are of importance for the remainder of this thesis, in particular hidden sectors. The case where such sectors contain a hidden photon is then further examined in Sec. 1.3 in view of the analysis carried out in Chapter 3 to derive constraints on hidden photons. The possibility that the hidden sector additionally comprises a dark matter particle is considered in Sec. 1.4. There, the toy model and the supersymmetric dark sector models, for which we analyse the phenomenology in Chapter 4, are introduced. In Sec. 1.5, we discuss the light NMSSM CP-odd Higgs, for which the constraints are studied in Chapter 2.

1.1 Dark matter

There are many indications for the existence of a significant amount of non-luminous matter in the Universe. Different observations of large astrophysical systems show that the mass of an object (e.g. galaxy) determined from its gravitational effect does not match the one inferred from its visible contents like stars, gas and dust. This discrepancy can be solved by introducing an invisible, therefore called *dark*, form of matter that makes up for the missing mass. Alternative solutions, suggesting a modification of the laws of gravity on large scales, have also been proposed. While they can account for certain observations without the need for dark matter, they usually fail to reproduce all simultaneously and are therefore not studied further in this work. Especially the bullet cluster discussed in Sec. 1.1.1 is not well explained in those models and favours particle dark matter as solution.

In the following, we summarise the evidence for the existence of dark matter and certain requirements imposed on a valid candidate. Many reviews about dark matter exist in the literature, e.g. Refs. [1–7]. Since so far not much is known about the particle nature of dark matter, an additional discovery through some non-gravitational interaction is indispensable in order to discriminate between different models and finally identify a dark matter particle. An overview of different searches is given at the end of this section.

1.1.1 Evidence for dark matter

On galactic scales, rotation curves of several spiral galaxies show an unexpected behaviour. The circular velocities of stars and gas in a galaxy according to Newtonian mechanics should scale as $v(r) \propto \sqrt{M(r)/r}$ with the radius r from the centre and the mass $M(r)$ enclosed in the sphere of radius r [3]. Thus, at large enough distances, when most of the galaxy's visible mass is contained inside of r and $M(r)$ is constant, the velocities should fall off as $v(r) \propto 1/\sqrt{r}$ with increasing r. Instead, observations often yield a flat distribution as shown in Fig. 1.1, which suggest the presence of a non-luminous matter component in the galaxy. Therefore, in order to explain the flatness of the distribution, a halo of dark matter which extends beyond the radius of the visible disk is required.

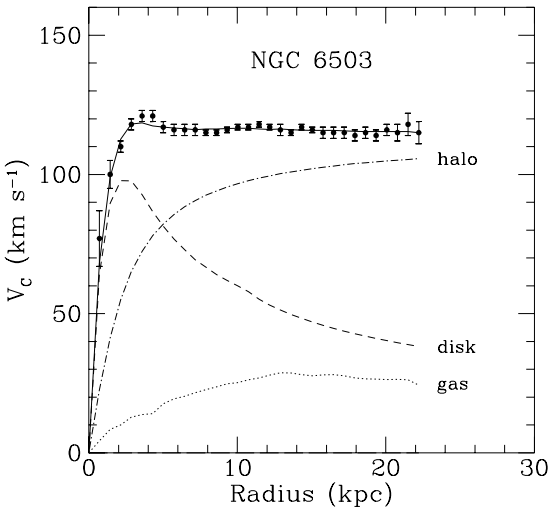

Figure 1.1: Typical rotation curve exhibiting the flat behaviour at large radius, here for the example of NGC 6503 from [3]. Different contributions arising from the gas, the disk and the dark matter halo are shown as dotted, dashed and dash-dotted lines, respectively.

In a similar way, dark matter also manifests its existence on the scale of galaxy clusters. Different methods can be applied to determine the mass of a cluster. They usually yield a discrepancy between the gravitational and the visible mass suggesting a contribution from dark matter. It is, for example, possible to deduce the mass from

weak gravitational lensing or from the circular velocities of galaxies by application of the virial theorem. Applying the latter method for the Coma cluster, F. Zwicky deduced in 1933 that the gravitational mass had to be much larger than the observed one and thus suggested the existence of dark matter for the first time. Weak gravitational lensing on the other hand uses the distortion of images of distant galaxies, which results from the bending of light when passing by the gravitational potential of a massive object, to infer the matter distribution along the line-of-sight. Other observations supporting the presence of dark matter from subgalactic to inter-galactic scales exist, see, e.g. [3], but are beyond the scope of this work.

A striking evidence for the existence of dark matter arises from the so-called Bullet cluster [44]. Observed by the Hubble space telescope in 2006, it is the result of two colliding galaxy clusters. The stellar components of both clusters behave collisionlessly and are not much slowed down in the collision in contrast to the interacting fluid-like gas and dust. This leads to the spatial separation shown in Fig. 1.2 between the stellar component in the left-hand plot and the decelerated plasma cloud in the right-hand plot. The mass distribution should then follow the gas which is known to form the main matter contribution of the cluster. This is, however, not the case, as shown by the green lines in Fig. 1.2. These lines depict the cluster's mass distribution as inferred from weak gravitational lensing. Instead of tracing the gas in the right-hand plot, the mass distribution shown by the green lines is similar to the one of the stars. Thereby, the presence of a non-luminous and collisionless component, which dominates the mass of the cluster, is revealed. This surprising behaviour observed in the Bullet cluster seems to be difficult to explain by employing modifications of gravity. It therefore demonstrates compelling evidence for the existence of dark matter.

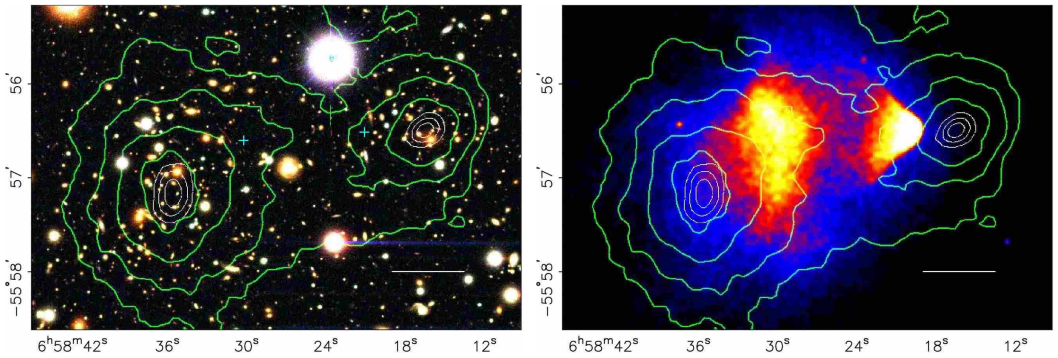

Figure 1.2: Observations of the Bullet cluster's different components from [44].
Left: Stellar component overlaid with green lines representing the mass distribution obtained from weak gravitational lensing. Blue crosses indicate the centre of the gas.
Right: X-ray image of the plasma cloud again overlaid with the mass distribution.

Finally, of great importance is the observation of the Cosmic Microwave Background (CMB) radiation since it allows to precisely determine the total amount of dark matter

in the Universe in the framework of the cosmological concordance model, the Lambda-Cold Dark Matter model (ΛCDM)[1]. This radiation emerges from the time when the early Universe became transparent for photons after it had cooled enough for electrons and protons to recombine in neutral atoms. The further expansion of the Universe caused these photons to redshift and cool. Observations today, by the COsmic Background Explorer (COBE), the Wilkinson Microwave Anisotropy Probe (WMAP) and most recently by the Planck satellite, show a near-perfect thermal black body spectrum with a temperature of 2.726 K that is isotropic to 1 part in 10^5. Analysing the power spectrum of temperature anisotropies in the CMB allows to determine different parameters of the cosmological model. The most important parameters in the context of the present work are the energy densities of different components in the Universe, in particular the overall, the baryonic and the non-baryonic matter component. Based on the measurements of the WMAP satellite the Review of Particle Physics by the PDG [4] quotes the density of the baryonic matter as

$$\Omega_{\mathrm{b}} h^2 = 0.022 \pm 0.001 \ , \tag{1.1}$$

and the one of cold (as explained in Sec. 1.1.2), non-baryonic dark matter as

$$\Omega_{\mathrm{DM}} h^2 = 0.112 \pm 0.006 \ , \tag{1.2}$$

where the abundances $\Omega_i = \rho_i/\rho_c$ are normalised to the critical density ρ_c for which the Universe is flat and are further multiplied by the scaled Hubble parameter h defined as $H_0 = 100h$ km s^{-1} Mpc^{-1}. The overall matter content $\Omega_{\mathrm{M}} = \Omega_{\mathrm{b}} + \Omega_{\mathrm{DM}}$ of the Universe is thus dominated by cold, non-baryonic dark matter since $\Omega_{\mathrm{M}} \gg \Omega_{\mathrm{b}}$. Some amount of $\Omega_{\mathrm{b}} h^2$ is also expected to serve as baryonic dark matter, e.g. in form of cold molecular gas clouds or MAssive Compact Halo Objects (MACHO) but their contribution to the mass of the galactic halo was found to be small [4]. Therefore, it is important to understand the nature of this cold, non-baryonic dark matter and to find viable particle candidates. Throughout this work, we simply refer to this as dark matter, implicitly assuming cold and non-baryonic, and require the corresponding relic density to lie within 3σ of the value given in Eq. (1.2). In March 2013, the Planck satellite [45] released their most recent data and found a slightly higher value of

$$\Omega_{\mathrm{DM}} h^2 = 0.1196 \pm 0.0031 \quad \text{(Planck only)}, \tag{1.3}$$

which is the most precise value obtained by one single experiment to date.

Altogether, nowadays the existence of a large amount of (cold, non-luminous) dark matter in the Universe is well-established. Its exact particle nature is still unknown and some candidates as well as necessary requirements are discussed in the following.

[1] This is the currently accepted cosmological model. It describes the expansion history of the Universe after the Big Bang in agreement with observations. The model includes a non-zero cosmological constant, called Lambda (Λ), together with Cold Dark Matter.

1.1.2 Dark matter candidates

For a particle to qualify as viable candidate for dark matter, it has to meet different requirements. As a first step, it is natural to check if the Standard Model provides such a particle.

According to the measurements of the CMB, discussed earlier, a *non-baryonic* dark matter component dominates the matter density of the Universe. The production of a good dark matter candidate should therefore yield a density in agreement with the measured relic abundance $\Omega_{\mathrm{DM}}h^2$ given by Eq. (1.2). Two possible mechanisms to obtain the required relic abundance are production from the decay of a heavier particle and thermal production in the early Universe. The latter is the most common one and gives rise to a large class of dark matter candidates, known as Weakly Interacting Massive Particles (WIMPs), which naturally obtain the correct relic abundance. This is discussed in more detail in Sec. 1.1.2.1.

Among the possible candidates within the Standard Model, all baryons are ruled out by definition when looking for non-baryonic dark matter. Also, for a particle to be dark, it should be non-luminous and thus *neutral* since it would have most likely been seen otherwise. This then further excludes among the Standard Model particles all charged leptons as dark matter candidates. Moreover, dark matter has to be *stable* or at least sufficiently long-lived on cosmological time scales (lifetime larger than the age of the Universe) not to have decayed by now. This requirement can, for example, be achieved if the dark matter carries an additional quantum number preventing it from decaying into Standard Model particles. This then eliminates also the Standard Model gauge bosons and the Higgs boson as dark matter candidates. Neutrinos are thus the only remaining potential candidate for dark matter in the Standard Model. They are, however, not a good candidate since the light neutrino contribution to Eq. (1.2) is limited to $\Omega_\nu h^2 < 0.0062$ [4], and since neutrinos form hot dark matter which is in conflict with structure formation, as discussed in the following.

For consistency with structure formation, dark matter is generally considered to be *cold*, as opposed to warm or hot. Cold dark matter is non-relativistic during structure formation, while hot dark matter is relativistic. Particles with velocity distributions between those two extrema are then denoted as warm. Because of these differences in their behaviour, the three classes (cold, warm, hot) have different effects on the structure formation and can be tested against observations. The general idea is that structure formation starts with the smallest structures which consecutively cluster into larger ones. This "bottom-up" formation is supported by observations of galaxies which are older than superclusters. It can be achieved by cold dark matter since these particles moving with non-relativistic velocities can clump on small scales. Large N-body simulations for structure formation with cold dark matter (in a ΛCDM Universe) are consistent with observations of the large-scale structure in the Universe. Hot dark matter, on the contrary, spoils this kind of structure formation since the relativistic dark matter particles

can not clump on small scales and thus wash out small-scale density fluctuations (below the free-streaming length). This is similar to the Silk damping [46] of small scales by free-streaming photons during recombination. Therefore, in the presence of hot dark matter, large structures form first and only later on in their fragmentation do the small structures emerge. This top-down formation is, however, in conflict with the observations of the older galaxies and therefore disfavours hot dark matter. This is the reason why Standard Model neutrinos are excluded as viable dark matter candidates. Warm dark matter, on the other hand, does not lead to the same contradictions as hot dark matter because of its smaller free-streaming length. It has been of interest since some disagreement between cold dark matter simulations and observations occurred regarding the small-scale structure of the Universe. One example, the so-called "missing satellite" problem, arose in cold dark matter simulations which predicted a larger number of dwarf-sized subhalos than found in observations [47,48]. Warm dark matter, in contrast to the cold one, suppresses the formation at small scales because of the larger free-streaming length and could solve this issue. However, recent discoveries of additional satellites indicate that the problem might not have originated from the cold dark matter simulations but was caused by incomplete observations. Another issue, referred to as the "core-vs-cusp problem", occurs since cold dark matter simulations predict cusps in the inner dark matter density profile of galaxies in contrast to the constant density cores expected from observations of dwarf galaxies [49]. Additionally, the simulations give too high densities for the most massive subhalos to host the brightest Milky Way satellites galaxies [50] which is known as the "too-big-to-fail problem". Even though the cold dark matter paradigm is generally adopted, warm dark matter can also be consistent with structure formation and only hot dark matter is in conflict.

Another common assumption is that dark matter besides being cold behaves also *collisionlessly*. This has already been inferred in Sec. 1.1.1 in view of the Bullet cluster. While collisionless cold dark matter successfully reproduces the large-scale structures, it is afflicted with the aforementioned small-scale problems. In this respect, warm dark matter is not the only way out, but also the collisionless nature has been questioned. One possible modification studied in this context is to allow the dark matter to self-interact. However, the strength of the self-interaction required to solve these problems seemed to be in tension with other observations and constraints, e.g. from the Bullet cluster. A revival of interest in these scenarios arose since some of these constraints weakened in improved simulations or could be avoided in new models with velocity-dependent self-interactions. Recently, viable scenarios in which the dark matter has Yukawa-like interactions mediated by a light messenger were suggested, e.g. in Refs. [51–53].

Further requirements arise since a viable dark matter candidate should *neither spoil the success of big bang nucleosynthesis (BBN) nor stellar evolution*. The impressive agreement between the predictions from BBN for the abundances of light elements (D, ^{3}He, ^{4}He, ^{7}Li) and their primordial abundances inferred from observations allows to constrain deviations from standard cosmology. Potential dangers arise, for example,

when increasing the relativistic degrees of freedom (often parametrised by the effective number of neutrinos N_ν) and causing a faster expansion or if particle decays during or after BBN produce high-energy photons capable of destroying the light elements. Note that since the predicted abundances depend on the baryon density, BBN also allows a determination of $\Omega_\mathrm{b}h^2$ which agrees well with the CMB measurement in Eq. (1.2). Details and a review on BBN can, for example, be found in [54]. Stellar evolution places limits on extra exotic energy losses, cf. e.g. [55], since they would, for example, change the lifetime or sound speed profile of stars and thereby can constrain certain dark matter candidates.

Finally, dark matter is also constrained by various negative results of different experimental searches. A viable dark matter candidate should therefore not produce a signal that would have been detected in any of these experiments. An overview of the different experiments is presented in Sec. 1.1.4.

In summary, this discussion showed, that the Standard Model does not provide a candidate for dark matter. A particle with the properties of a good dark matter candidate, outlined in this section, therefore has to be sought in new models of physics beyond the Standard Model. Many such extensions exist and provide viable dark matter candidates. Two possible scenarios are introduced in Sec. 1.2. To guarantee the stability of the dark matter particle, many models impose a symmetry and thereby forbid the decay into Standard Model particles. In several of these extensions, the dark matter candidate belongs to the aforementioned class of Weakly Interacting Massive Particles (WIMPs) which are described in the following.

1.1.2.1 Thermal relic abundance and WIMP dark matter

As mentioned earlier, thermal production is the most prominent mechanism to generate the relic abundance of dark matter. It assumes that the dark matter particle ψ is in thermal equilibrium with the primordial plasma in the early Universe. The annihilation of ψ into Standard Model particles and the inverse production of ψ out of Standard Model particles maintain the equilibrium density. Once the temperature T drops below the dark matter mass m_ψ, the energy in the plasma is not sufficient for Standard Model particles to efficiently produce ψ and it falls out of equilibrium. The evolution of the dark matter number density $n_\psi(t)$ with time t is described by the Boltzmann equation [1, 56]

$$\frac{dn_\psi}{dt} + 3Hn_\psi \;=\; -\langle\sigma_\mathrm{ann}v\rangle\left[(n_\psi)^2 - (n_\psi^\mathrm{eq})^2\right] \,, \tag{1.4}$$

where H is the Hubble parameter, $\langle\sigma_\mathrm{ann}v\rangle$ is the thermally averaged annihilation cross section and n_ψ^eq is the number density at thermal equilibrium. The expansion of the Universe causing a dilution of the number density is encoded in the second term on the left-hand side and the presence of interactions in the right-hand side. The equilibrium

density in the non-relativistic limit is Boltzmann suppressed by $n_\psi^{\rm eq} \propto \exp[-m_\psi/T]$. After falling out of equilibrium, the dark matter density decreases exponentially with T until the annihilation rate $\Gamma = \langle\sigma_{\rm ann} v\rangle n_\psi$ of ψ drops below the expansion rate H. This is referred to as *freeze out*. The number density per comoving volume $n_\psi a^3$ then stays constant since ψ stops to annihilate.

In order to determine the relic abundance of a self-annihilating dark matter particle in the simplest case, the Boltzmann equation (1.4) has to be solved (further complication can arise for example from coannihilations). For this purpose, the thermally averaged annihilation cross section has also to be calculated. There exist different codes, e.g. micrOMEGAs [57–61], which perform these tasks and numerically compute the relic abundance of a dark matter particle in a given theoretical model. Solving the Boltzmann equation, a rough estimate for the relic density of a dark matter particle with annihilation cross section $\langle\sigma_{\rm ann} v\rangle$ can be obtained as

$$\Omega_{\rm DM} h^2 \;=\; \frac{m_\psi\, n_\psi}{\rho_c} \;\simeq\; \frac{3 * 10^{-27}\ {\rm cm}^3\ {\rm s}^{-1}}{\langle\sigma_{\rm ann} v\rangle}\ , \tag{1.5}$$

in units of the critical density ρ_c. In this approximation, the abundance is inversely proportional to the annihilation cross section and independent of the dark matter mass. It shows that the appropriate abundance can be obtained for a massive particle with cross sections which are typical for weak interactions. Such particles are referred to as Weakly Interacting Massive Particles (WIMPs) and represent a prominent class of dark matter candidates. They freeze out when they are non-relativistic and thus constitute cold dark matter. The argument that a GeV- to TeV-scale particle with weak-scale annihilation cross section gets naturally produced with the right relic abundance is called the "WIMP miracle".

1.1.3 Dark matter spatial distribution

The presence of a large amount of dark matter in galaxies and galaxy clusters is inferred from several observations, as discussed in Sec 1.1.1. An important issue — especially regarding the effort described in Sec. 1.1.4 to detect other signs of dark matter than gravitational ones — is the distribution of dark matter in these galactic halos and notably the one of the Milky Way. The measured rotation curves of different galaxies can be reproduced over a large range of radii by a class of density distributions with the phenomenological form given by [2]

$$\rho(r) \propto \frac{\rho_c}{(r/a)^\gamma [1 + (r/a)^\alpha]^{(\beta-\gamma)/\alpha}} \tag{1.6}$$

and certain sets of the parameters (α, β, γ). One possible shape described by $(\alpha, \beta, \gamma) = (1, 3, 1)$ was found in 1996 by Navarro, Frenk and White [62] in N-body simulations and is known as the NFW profile. In a later simulation, Moore *et al.* [63] obtained a

profile with $(\alpha, \beta, \gamma) = (1.5, 3, 1.5)$, which predicts an even steeper cusp at the inner region of the galaxy than the NFW one. The isothermal profile, on the other hand, with parameters $(\alpha, \beta, \gamma) = (2, 2, 0)$ does not diverge as $r \to 0$ and gives a core at the galactic centre. Another example with finite central density is the Einasto profile [64] which is not described by Eq. (1.6) but was also found to provide good agreement with halos from N-body simulations.

In analyses of direct detection experiments (cf. Sec. 1.1.4.1), it is common to use the so-called Standard Halo Model (SHM) [65] which will also be considered in most of this work, though in some cases also the effects of changing to a different profile are illustrated. The SHM assumes a spherically symmetric and isothermal distribution of dark matter around the galactic centre as well as a Maxwellian distribution $F(\vec{v}, r) \propto \exp(-v^2/\bar{v}^2)$ for the dark matter velocities with a mean velocity $\bar{v} = 220$ km/s in the galactic frame and an escape velocity $v_{\text{esc}} = 544$ km/s. The density profile scales as r^{-2} and is often normalised to a local density of

$$\rho_{\text{DM}} = 0.3 \text{ GeV/cm}^3 \tag{1.7}$$

at the solar position.

N-body simulations are of great importance for our understanding of the growth of dark matter structure in the Universe in general and in particular regarding the distribution of dark matter in galactic halos. They simulate the evolution of a large number of dark matter "particles" under the influence of gravity starting from certain initial conditions (matter distribution inferred from the inhomogeneities in the CMB) until the formation of structures and galaxies. Because of the limited computational power, the mass and spatial resolution as well as the number of "particles" is limited so that, for example, the masses of the simulated "particles" are a multiple of the solar mass. Simulations have been improved with better computational possibilities, recent ones include the Via Lactea II simulation [66], the Aquarius project [67] and the Millennium-II simulation [68]. While the simulations agree qualitatively at large scales, the density profile in the inner region of galaxies as well as potential substructures in the halo are still subject to discussions as they lie beyond current resolution. In contrast to most simulations which only consider dark matter, recent ones also including baryons indicate that the stellar disk affects the accretion of satellites and leads to the formation of a co-rotating thick disc of stars and dark matter [69–71] referred to as dark disk. As claimed in [72], baryons could also affect the density of dark matter in the inner region of a galaxy and result in a spiked profile.

Another parameter of importance in this context is the above-mentioned local dark matter density ρ_{DM}. It is also afflicted with uncertainties and depends on the shape of the density profile [2]. While Eq. (1.7) is the generically used value, different studies found values ranging from 0.2 GeV/cm^3 to 0.6 GeV/cm^3 (e.g. 0.39 GeV/cm^3 in [73] for an NFW or an Einasto profile, 0.43 GeV/cm^3 in [74], 0.235 GeV/cm^3 in [75], 0.2 –

0.56 GeV/cm^3 in [76] for an NFW profile and very similar for an Einasto profile). Note that, as an observer within the Milky Way, it is in general more difficult to determine parameters for the dark matter halo of our own galaxy than for other galaxies.

1.1.4 Detection of dark matter

In order to confirm the existence of dark matter and determine its particle properties like its mass or couplings, a detection through another interaction besides the gravitational one is desirable. The three methods of currently employed experimental searches are direct detection, indirect detection and searches at colliders. For each, the relevant process is sketched in Fig. 1.3 by the arrows indicating the flow of time for the interactions of two dark matter and two Standard Model particles.

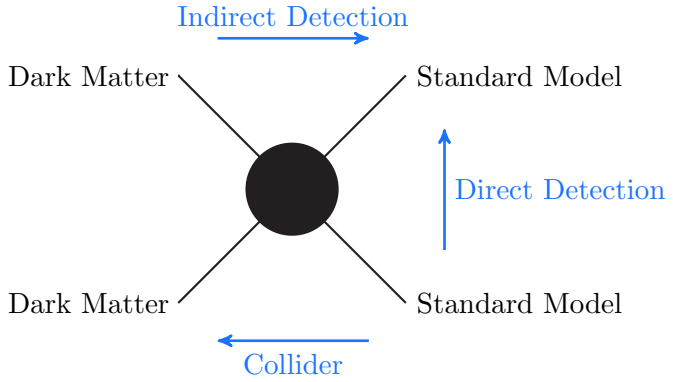

Figure 1.3: Diagram illustrating some unknown interaction (black disk) of two dark matter and two Standard Model particles. The blue arrows give the direction of the time flow for the respective process involved in the different dark matter detection methods.

In the following, the three searches are briefly summarised with emphasis on direct detection, which is the most relevant in the context of this work. We only briefly comment on the other two searches for completeness. Note, that they all rely on couplings of dark matter to other forces than gravity, which might not be present. The assumption that dark matter possesses other interactions is, however, well-justified for the class of thermal relics and in particular WIMPs which by definition have weak scale interactions, as discussed in Sec. 1.1.2.1. For the dark matter candidates studied throughout this work, this assumption is considered to be valid.

1.1.4.1 Direct detection

Since dark matter from the galactic halo should continuously pass by the Earth, its presence could be revealed once it interacts inside a detector with normal matter. Direct detection experiments aim at measuring the elastic scattering[2] of a dark matter

[2]Inelastic scattering on nuclei or electrons is in principle also possible, though usually less considered in experiments since rates are suppressed and a discrimination from the natural radioactive background is difficult. This possibility is therefore not discussed further in this work.

particle on a nucleus of the target material. Various experiments are carried out using different techniques to detect the resulting nuclear recoil. However, since dark matter interacts only weakly, such events are expected to be rare. Experiments therefore use large detectors placed far underground in order to suppress the background from cosmic rays (most importantly neutrons produced in interactions of cosmic rays since they give a similar signal as expected from dark matter). More details on the relevant calculations and direct detection techniques are given for example in [1, 8–11].

The differential rate of nuclear recoils per unit detector mass, time and energy (typically in units of counts/kg/day/keV) is given by [11]

$$\frac{dR}{dE_r} \;=\; N_{\mathcal{N}} \frac{\rho_{\mathrm{DM}}}{m_{\mathrm{DM}}} \int_{v_{\mathrm{min}}}^{v_{\mathrm{max}}} v\; f(v)\; \frac{d\sigma_{\mathcal{N}}}{dE_r}(v, E_r)\; dv \;, \tag{1.8}$$

in which $N_{\mathcal{N}}$ is the number of nuclei per kilogram of the target, ρ_{DM} is the local dark matter density, m_{DM} is the dark matter mass, v and $f(v)$ are the dark matter velocity and velocity distribution in the Earth rest frame and $d\sigma_{\mathcal{N}}/dE_R$ is the differential scattering cross section on a nucleus $\mathcal{N}$. The lower limit of the integration is given by the minimal velocity $v_{\mathrm{min}} = \sqrt{m_{\mathcal{N}} E_r / (2\mu_{\mathcal{N}}^2)}$, which can produce a recoil of energy E_r. The upper limit is set by the escape velocity v_{esc} of the galaxy in the Earth rest frame, cf. Sec. 1.1.3. The expected rate in an experiment thus requires to combine factors from particle physics, nuclear physics and astrophysics as well as a good understanding of the particular detector response. Interpretation of experimental results can thus be complicated especially since some of these factors are afflicted with uncertainties which can affect the derivation of limits.

Regarding the astrophysical factors, direct detection experiments usually assume the Standard Halo Model introduced in Sec. 1.1.3. They consider the canonical value of 0.3 GeV/cm^3 for the local dark matter density and a Maxwell–Boltzmann velocity distribution in the galactic frame. As mentioned above, different studies suggest deviations from these standard assumptions which would affect the direct detection limits. A variation in ρ_{DM} results in an overall factor in $\sigma_{\mathcal{N}}$ because of the proportionality $dR/dE_r \propto \rho_{\mathrm{DM}} \sigma_{\mathcal{N}}$ and is the same for all experiments. Changing the assumptions for the velocity distribution, e.g. varying the shape, the escape or the mean velocity, affects the limits of different experiments differently and in a more complicated way, depending also on the dark matter mass. This is caused by experiments being sensitive to different parts of the velocity distribution due to varying v_{min} for different target nuclei and energy thresholds. This effect is particularly important for light dark matter as discussed in more detail, for example, in [77]. In [70], it was shown that also the presence of a dark disk would have important consequences and enhance the rates in direct detection experiments. Because of those uncertainties, halo-independent analyses like Ref. [78–80], systematic studies of the uncertainties as in Ref. [81] and a better understanding of the astrophysical uncertainties are important and subject to continuous effort, see also [65] for a discussion.

The scattering cross section on a nucleus $\mathcal{N}$ can in general be separated into a spin-independent (SI) and a spin-dependent (SD) contribution, where the former results from scalar or vector and the latter from axial couplings between the dark matter and the nucleon. The dark matter-nucleus cross section can be written in terms of the cross sections in the zero momentum transfer limit $\sigma_0^{\rm SI}$ and $\sigma_0^{\rm SD}$ as

$$\frac{d\sigma_{\mathcal{N}}}{dE_r} = \frac{m_{\mathcal{N}}}{2\mu_{\mathcal{N}}^2 v^2}\left[\sigma_0^{\rm SI} F_{\rm SI}^2(E_r) + \sigma_0^{\rm SD} F_{\rm SD}^2(E_r)\right] , \tag{1.9}$$

in which $\mu_{\mathcal{N}} = m_{\rm DM} m_{\mathcal{N}}/(m_{\rm DM} + m_{\mathcal{N}})$ is the dark matter-nucleus reduced mass, and $F_{\rm SI}$ and $F_{\rm SD}$ are form factors which depend on the recoil energy E_r. Experiments are usually more sensitive to spin-independent scattering since it is coherently enhanced for a nucleus $\mathcal{N}$ compared to a single nucleon, unlike in the case of spin-dependent scattering, which even vanishes for nuclei with zero total spin (e.g. for even-even nuclei with an even number of protons and neutrons). Therefore, in most experiments the use of heavy target nuclei results generally in a larger spin-independent than spin-dependent scattering cross section.

For a dark matter particle ψ, the spin-independent scattering can arise from scalar or vector dark matter-quark interactions with the respective terms in the Lagrangian given by [1, 10]

$$\mathcal{L}^q_{\rm scalar} = a_q \bar{\psi}\psi\bar{q}q \qquad \text{and} \qquad \mathcal{L}^q_{\rm vec} = b_q \bar{\psi}\gamma_\mu\psi\bar{q}\gamma^\mu q\,, \tag{1.10}$$

where the presence of the couplings a_q and b_q to quarks depends on the particular dark matter model. The spin-independent part of the scattering cross section of Eq. (1.9) then receives a contribution from the scalar dark matter-nucleus cross section given by

$$\sigma^{\rm SI}_{0,\,\rm scalar} = \frac{4\mu_{\mathcal{N}}^2}{\pi}\big(Z f_p + (A-Z) f_n\big)^2 , \tag{1.11}$$

where Z and A are atomic number and atomic mass of the target nucleus and f_p (f_n) are effective couplings of the dark matter particle to protons (neutrons). These parameters f_p and f_n depend on the couplings a_q to light and heavy quarks and on the contributions of the light quarks to the mass of the nucleon (these contributions are measured experimentally but suffer from uncertainties, especially the s-quark contribution). The part in the spin-independent scattering cross section arising from the vector couplings only receives a contribution from the valence quarks and is given by

$$\sigma^{\rm SI}_{0,\,\rm vec} = \frac{\mu_{\mathcal{N}}^2 B_{\mathcal{N}}^2}{64\pi} , \tag{1.12}$$

where $B_{\mathcal{N}} = Z(b_u - b_d) + A(b_u + 2b_d)$.

The combined spin-independent contribution to the scattering cross section of dark matter on a nucleus $\mathcal{N}$ can then be written as

$$\frac{d\sigma_{\mathcal{N}}^{\mathrm{SI}}}{dE_r} \;=\; \frac{2m_{\mathcal{N}}}{\pi v^2}\left(\big(Zf_p+(A-Z)f_n\big)^2+\frac{B_{\mathcal{N}}^2}{256}\right)\,F_{\mathrm{SI}}^2(E_r)\;. \tag{1.13}$$

In the most commonly studied case of scalar interactions and for approximately equal couplings to protons and neutrons $f_p \approx f_n \equiv f_{\mathrm{N}}$, the spin-independent scattering cross section thus becomes

$$\left(\frac{d\sigma_{\mathcal{N}}^{\mathrm{SI}}}{dE_r}\right)_{\mathrm{scalar}}^{f_p\approx f_n} \;=\; \frac{2m_{\mathcal{N}}}{\pi v^2}A^2 f_{\mathrm{N}}^2\;F_{\mathrm{SI}}^2(E_r) \;=\; \frac{m_{\mathcal{N}}}{2v^2\mu_{\mathrm{N}}^2}\;\sigma_{\mathrm{N,\,scalar}}^{\mathrm{SI}}\;A^2\;F_{\mathrm{SI}}^2(E_r)\,, \tag{1.14}$$

where the cross section on a single nucleon N is expressed in analogy to the one given in Eq. (1.11) for $f_p \approx f_n$ by

$$\sigma_{\mathrm{N,\,scalar}}^{\mathrm{SI}} \;=\; \frac{4\mu_{\mathrm{N}}^2}{\pi}\;f_{\mathrm{N}}^2\,, \tag{1.15}$$

with the dark matter-nucleon reduced mass $\mu_{\mathrm{N}} = m_{\mathrm{DM}}m_{\mathrm{N}}/(m_{\mathrm{DM}}+m_{\mathrm{N}})$ for a nucleon with mass $m_{\mathrm{N}} \approx m_p \approx m_n$. The spin-independent scattering cross section in this particular case of Eq. (1.14) thus scales with the atomic mass squared A^2 and is dominant for heavy target nuclei, as mentioned above. Constraints from direct detection experiments are then usually presented on the cross section per nucleon for scalar interaction under the assumptions of $f_p \approx f_n$.

On the contrary, in a case where dark matter couples to the charge of Standard Model particles, the scattering occurs mostly on protons, while $f_n \approx 0$. Then, from Eq. (1.13), the spin-independent scattering cross section follows for scalar and vector interactions instead as

$$\begin{aligned}
\left(\frac{d\sigma_{\mathcal{N}}^{\mathrm{SI}}}{dE_r}\right)_{\mathrm{scalar}}^{f_n\approx 0} \;&=\; \frac{2m_{\mathcal{N}}}{\pi v^2}Z^2 f_p^2\;F_{\mathrm{SI}}^2(E_r) \;=\; \frac{m_{\mathcal{N}}}{2v^2\mu_{\mathrm{N}}^2}\;Z^2\;\sigma_{p,\,\mathrm{scalar}}^{\mathrm{SI}}\;F_{\mathrm{SI}}^2(E_r)\,,\\
\left(\frac{d\sigma_{\mathcal{N}}^{\mathrm{SI}}}{dE_r}\right)_{\mathrm{vec}}^{f_n\approx 0} \;&=\; \frac{m_{\mathcal{N}}}{\pi v^2}\frac{Z^2}{128}\;F_{\mathrm{SI}}^2(E_r) \;=\; \frac{m_{\mathcal{N}}}{2v^2\mu_{\mathrm{N}}^2}\;Z^2\;\sigma_{p,\,\mathrm{vec}}^{\mathrm{SI}}\;F_{\mathrm{SI}}^2(E_r)\,,
\end{aligned} \tag{1.16}$$

where for $m_{\mathrm{N}} \approx m_p$ the scalar cross section per proton is roughly the same as the one per nucleon of Eq. (1.15), i.e. $\sigma_{p,\,\mathrm{scalar}}^{\mathrm{SI}} \approx \sigma_{\mathrm{N,\,scalar}}^{\mathrm{SI}}$, and for vector interactions the cross section for scattering on a single proton is given by

$$\sigma_{p,\,\mathrm{vec}}^{\mathrm{SI}} \;=\; \frac{\mu_{\mathrm{N}}^2}{64\pi}\,, \tag{1.17}$$

in analogy to Eq. (1.12) for $B_{\mathcal{N}} = Z$, in the case where the coupling is to the charge. Thus, in the particular case where the scattering takes place exclusively on protons, both the vector and the scalar cross sections for spin-independent scattering scale with Z^2, instead of with A^2 in the case of $f_p \approx f_n$. This different scaling will become important in the analysis of the direct detection signatures in a specific model studied in Chapter 4.

Besides the astrophysical uncertainties in the computations of rates and cross sections for direct detection experiments, further uncertainties are introduced when converting the scattering cross sections between the partonic, the hadronic and the nuclear levels and also complicate the comparison between experiments using different target nuclei, cf. e.g. [10,82] and references therein. Another potentially problematic issue arises when translating the measured energy to the actual recoil energy since it depends on the detector response and can affect the comparison of experiments. In general, a dark matter signal is expected to be largest at low recoil energies near the energy threshold of the detector where it is most endangered to be affected by backgrounds, noise or a bad understanding of the detector response. This is particularly important for light dark matter for which the sensitivity decreases rapidly and low energy thresholds are crucial.

While most experiments want to observe an excess of nuclear recoil events produced from dark matter scattering above the expected background rate, few experiments are looking for a very particular feature in order to uniquely identify a signal of galactic origin. This method, first suggested in [83, 84], relies on the Earth's motion around the Sun which is expected to cause an annual modulation of the signal rate. Since the Earth's velocity in the galactic rest frame results from the rotation of the Earth around the Sun and the one of the Sun around the galactic centre as

$$v_\oplus \;=\; 220 \text{ km/s } \big(1.05 + 0.07 \cos[2\pi(t - t_m)/1 \text{ year}]\big) \tag{1.18}$$

it periodically fluctuates with a maximum when Earth and Sun move in the same ($t_m \approx$ June 2^{nd}) and a minimum when they move in opposite directions. In summer (winter), there are then more dark matter particles with high (low) speed so that the event rate peaks in summer for large recoil energies and in winter for small ones. This annual modulation is however expected to be small $\approx 7\%$ [9] since the orbital speed of the Earth is much smaller than the one of the Sun. Another signature caused by the Earth's motion through the galaxy would be a forward-backward asymmetry in an experiment capable of obtaining directional information on the recoiling nucleus [10,85]. Since backgrounds are unlikely to show such a behaviour and only few events would be needed, it could be an intriguing sign of dark matter, however, there are no directional experiments yet [11].

A large number of experiments have been constructed to look for signals originating from the scattering of dark matter on a nucleus inside the detector. The null results of these searches are continuously lowering the limits on the scattering cross sections as a function of the dark matter mass. A summary of current experiments and future plans is given in [11]. The XENON100 [86, 87] and CDMS-II [88, 89] experiments are the largest and most prominent ones providing currently the strongest constraints on spin-independent scattering. In Sec. 4.1.3, we give an overview of the limits which are of importance in this work. Besides these negative searches, there are also four experiments claiming the observation of a signal, two as an annual modulation and two as an excess in the low energy events. The first evidence for a modulation was presented by the DAMA

collaboration in 1998 [32] and has now reached a significance of 8.9σ by observing more than 13 annual cycles [33,34]. In 2011, the CoGeNT experiment has claimed indications of an annual modulation which is compatible with a light dark matter particle [35,36]. In 2012, the CRESST experiment found an excess of events above their known background which might be explained by a light dark matter particle [37,38]. While this work was being finished, the CDMS collaboration reported the observation of 3 events after cuts at an expected background of 0.4 events in a special analysis of their silicon detectors [39]. All experiments point towards a light dark matter particle, if the standard (most simple) astrophysical assumptions are made, but the exact masses and cross sections required to explain the signals differ somewhat. They are also in tension with the limits arising from the negative searches especially from XENON and CDMS. These experiments, however, are designed to look for heavier dark matter particles and are not the most sensitive in the relevant low mass range due to their high thresholds and heavy target nuclei (also the reliability of the detector performance close to the energy thresholds has been questioned and their limits were disputed, e.g. in [90,91]). In view of the different uncertainties and the limited knowledge in several ingredients needed to estimate the number of events, the signals should not be dismissed easily. For different assumptions on the astrophysical parameter or somewhat more exotic dark matter candidates, these signals can be brought in agreement with each another and with the limits, examples of which are given in Sec. 4.1.3.

1.1.4.2 Indirect detection

Besides direct detection it is also possible to search indirectly for dark matter by detecting the products of its annihilation (or decay which is not the focus here). It is in general possible to look for neutrinos, gamma rays, positrons, antiprotons or antideuterons arising either as primary products in the dark matter annihilation or as secondary ones, e.g. from successive decays of primary particles. The flux of produced particles is proportional to the square of the dark matter density ρ_ψ and the annihilation cross section times the relative velocity of the dark matter particles as $\phi \propto \rho_\psi^2 \sigma_{\mathrm{ann}} v$. For a thermal relic, the annihilation cross section would be linked to the one determining the relic density (cf. Sec. 1.1.2.1) though differences might arise due to the lower velocity today compared to the time of decoupling and since coannihilations could contribute to the relic abundance. Because of the quadratic dependence on ρ_ψ it is promising to look at places with high density like the galactic centre and the Sun or the Earth, which can capture and accumulate dark matter. Furthermore, the observation of a spectral feature like a line, for example, in the gamma ray spectrum would be a distinct signature pointing towards dark matter.

An overview of different annihilation products that are promising for indirect searches is, e.g. given in [3,12,13] and references therein. Charged cosmic rays like positrons or antiprotons can in general not be associated with a particular source and are instead

observed as a diffuse flux since they are deflected by the magnetic fields in the galaxy, undergo interactions with the interstellar medium and lose energy. Their interpretation in terms of a dark matter signal is, however, challenging as their propagation suffers from uncertainties, and background estimates are complicated since these particles are also produced by astrophysical sources. Neutrinos and gamma rays on the other hand are neutral and not deflected by magnetic fields so that they point back to their origin. The galactic centre is then a very promising source since the dark matter density is expected to be high. Neutrinos, due to their weak interactions, can additionally emerge from the centre of the Sun or the Earth but they require large detectors in order to be observed. Besides the galactic centre, the halo or dwarf galaxies are also interesting targets to look for gamma ray signals. More details on dark matter searches with neutrinos from the Sun/Earth are given, e.g. in [1], and with gamma rays, e.g. in [92].

In the past years, several experiments reported observations of unexpected phenomena which might originate from dark matter or point towards special unforeseen astrophysical features. Some of these anomalies disappeared with time and others got confirmed by additional experiments. The following listing is intended as a brief overview without attempt of completeness.

There has been much excitement after the PAMELA experiment presented in 2008 their measurement of an excess in the positron fraction [28] over the predicted background of cosmic rays. This excess was confirmed by the Fermi collaboration [29, 30] and in April 2013 also by the AMS experiment [31]. Since the first observation there have been many works dedicated to the explanation of the excess either with astrophysical sources like pulsars or with dark matter. In the latter case, the following obstacles have to be overcome by a successful dark matter model: the required annihilation cross section has in general to be larger than the standard thermal one needed to get the correct relic abundance, cf. e.g. [93, 94] (typical boosts range from a factor of $\mathcal{O}(1)$ to $\mathcal{O}(100)$); the dark matter annihilation should proceed dominantly into leptons and not produce many hadrons since the PAMELA measurement [95, 96] of the antiproton-to-proton flux ratio does not show a corresponding excess, cf. e.g. [94].

Different observations of photons exhibiting somewhat curious features also attracted attention and provoked interpretations in terms of dark matter. The INTEGRAL observation of a 511 keV line of photons from the galactic centre [97, 98] could arise from the annihilations of positrons produced in the annihilation of a light (MeV-scale) dark matter particle [99–102]. An unusual microwave emission in the region around the galactic centre seen by WMAP (referred to as the WMAP haze and confirmed by Planck [103]) might be due to the synchrotron emission of relativistic e^-/e^+ originating from dark matter annihilations at the galactic centre [104–106]. The existence of this haze has also been confirmed by the Fermi satellite's discovery of a corresponding gamma ray haze (also called Fermi bubbles). In [107–109], an unexpected spectrum and angular distribution of gamma rays from the galactic centre was found in the measurements of

the Fermi Gamma Ray Space Telescope and explained by the annihilation of dark matter, though astrophysical explanations are also possible. Non-thermal radio filaments which are characterised by their radio emission were found to exhibit a hard synchrotron emission of unknown origin. It was shown in [110, 111] that the synchrotron spectrum could be explained if dark matter annihilations within these filaments produce a nearly monoenergetic electron spectrum. The model studied in [111] as possible solution to the synchrotron emission from radio filaments can simultaneously account for the WMAP haze and the gamma ray spectrum observed from the galactic centre. It constitutes of a $\sim$ 10 GeV dark matter particle annihilating through a light gauge boson of an extra U(1) symmetry (this so-called hidden photon is discussed in Sec. 1.3 and this model is similar to the one of Sec. 1.4.2). However, note that there might of course also be astrophysical explanations to all these phenomena.

Finally, a special spectral feature indicating the presence of a gamma ray line around 130 GeV was found in the data of the Fermi satellite in 2012 [112,113]. This has attracted much attention since lines are considered to be a smoking gun signature for dark matter annihilation, but it is still subject to discussions.

Like direct detection, indirect detection requires input from astrophysics which can introduce uncertainties. Modifications in the dark matter density, e.g. at the galactic centre by the presence of a cusp or in the halo by the presence of higher density clumps, change the predicted fluxes of annihilation products. Deviations in the velocity distribution affect the capture rate of dark matter in the Sun or the Earth. The propagation and interactions of charged particles in the galaxy is difficult to model. The astrophysical background might differ from the expectations and mimic dark matter signatures. These and other obstacles complicate the interpretation of measurements in terms of dark matter.

1.1.4.3 Collider searches

Finally, dark matter might be accessible to collider searches. Again relying on the assumption that dark matter couples to Standard Model particles, it could in principle be produced in the interactions of the latter. This production could occur either directly in the collisions or in subsequent decay chains of other new particles which might be present in the Standard Model extension. In the case mentioned above, where a symmetry is introduced in order to prevent the dark matter from decaying, this very same fact avoids in return the production of a single dark matter particle from Standard Model particles. Dark matter or other new particles which might be contained in addition to dark matter in the extension of the Standard Model will then only be produced in pairs out of Standard Model particles at a collider. Since the dark matter does not interact much with ordinary matter, once produced it would appear as missing energy and momentum in the detector.

Dedicated searches at the Large Hadron Collider (LHC) were performed looking for signatures with missing transverse energy $\not{E}_T$ in combination with a single jet or photon. Supposing that dark matter couples indirectly to quarks or gluons and that the mediator of this interaction is heavy and can be integrated out, the coupling is treated in the analysis as a point interaction and different effective contact operators are studied. The results of this approach have also been translated into limits on the dark matter scattering cross section which compared to direct detection bounds are stronger at small masses. However, these limits can not always be applied since they rely on strong assumptions such as a heavy mediator and that the involved operators are the same at the energies relevant for LHC and those for direct detection. Both Atlas and CMS conducted searches for monojet + $\not{E}_T$ events in [114] and [115], respectively, as well as for monophoton + $\not{E}_T$ events in [116] and [117], respectively.

Specific signatures including other new particles, in general, depend on the details of the particular Standard Model extension. While collider searches do not suffer from astrophysical uncertainties, identifying a new stable particle produced in the laboratory as the true dark matter first requires to ensure that it indeed exists in the galaxy in sufficient numbers. An example of how dark matter properties could be determined at a collider is given in [118].

1.1.4.4 Complementarity of detection methods

The experimental searches for dark matter discussed in Secs. 1.1.4.1 to 1.1.4.3 can be used complementary. The strength with which a signal might be produced in one case can in a given model, in principle, be related to the other observations. In Fig. 1.3, the interactions which are relevant for the different searches are illustrated for two dark matter and two Standard Model particles (caveats arise since different interactions might not exhibit the same energy dependence and can involve couplings to different Standard Model particles). For each interaction, the direction for the flow of time is indicated by an arrow. The annihilation cross section connected to the thermal relic abundance in the early Universe can be linked to searches with indirect detection experiments (arrow from left to right), the scattering process relevant for direct detection (arrow from bottom to top) and the production of dark matter at colliders (arrow from right to left).

Therefore, combining data from different types of experiments is very useful, see e.g. [12,119,120]. It allows to cross-check results but also to circumvent the uncertainties a certain method might inevitably be afflicted with, for example arising from the dark matter velocity distribution in the case of direct detection or astrophysical backgrounds in indirect detection. Furthermore, specific properties of a dark matter particle might make it inaccessible to certain experiments while other could be better suited. Finally, in the case of positive signals, ambiguities could complicate the reconstruction of the dark matter properties like the mass or interaction strength while a combination of diverse datasets could allow to break the degeneracy.

1.1.4.5 Lessons from dark matter detection

Despite lots of experimental effort, the solution of the question of the particle nature of dark matter still lacks conclusive and consistent signals. The different features reported by indirect searches in cosmic rays might stem from the annihilation of dark matter but they could also have astrophysical origins. Potential positive observations of the scattering of dark matter in direct detection experiments seem to be in tension with negative searches in other similar experiments. In general, the comparison of results from different direct detection experiments is, however, problematic and relies on certain assumptions. Results can be more or less in tension or even allowed under different assumptions and therefore the signals should not be disregarded easily but rather might serve as a guide to point towards potentially interesting dark matter candidates. For such a candidate, it would be desirable if it could explain more than one and as many as possible of the claimed signals simultaneously. However, one should keep in mind that some of these signals might originate from dark matter while others might turn out to be false. Furthermore, a viable candidate should be consistent with the numerous limits obtained from null results in due consideration of the uncertainties and assumptions.

Interesting possibilities seem to arise for scenarios with light dark matter, having a mass of about 10 GeV [121]. As discussed in Sec. 1.1.4.1, in this mass range, dark matter may explain the signals observed by DAMA, CoGeNT, CRESST and CDMS and be (marginally) consistent with direct detection limits since these weaken at small masses and suffer from uncertainties (e.g. from astrophysical assumptions). According to Sec. 1.1.4.2, such a light dark matter particle might further account for the synchrotron emission from radio filaments, the WMAP haze and the gamma rays observed from the galactic centre (though there might be tensions e.g. with antiproton limits). It is, however, difficult to explain all these observed signals simultaneously with one dark matter particle. In the models, which are analysed in Chapter 4 of this thesis, we consider different dark matter candidates with a mass of $\mathcal{O}(10\text{ GeV})$. We also discuss the possible explanation of the signals found by DAMA and CoGeNT though they are not the primary motivation but rather a potential additional feature, when trying to find viable dark matter candidates in simple supersymmetric hidden dark sectors with a hidden U(1) symmetry (see Sec. 1.4 for details on the models).

1.2 Standard Model and extensions

The Standard Model of particle physics describes the known elementary particles and their interactions through the electromagnetic, strong and weak forces remarkably well. However, as discussed in Sec. 1.1.2, it does not contain a particle which could serve as viable candidate to explain dark matter. Various new physics models have been suggested and many of them also provide a candidate for dark matter. In the following,

we briefly introduce supersymmetry and hidden sectors, which are key ingredients of the appealing models considered in this work.

1.2.1 Supersymmetry

Supersymmetry (SUSY) is one of the most prominent and best studied extensions of the Standard Model. Relating bosons and fermions, this symmetry requires each Standard Model particle to possess at least one so-called superpartner with the same mass but a difference in spin of 1/2. Since superpartners have not been observed yet, supersymmetry has to be broken by some yet unknown mechanism. One then could hope to find superpartners with masses around a TeV since supersymmetry close to the TeV scale has several appealing features. For example, it stabilises the Higgs mass at the electroweak scale from being pulled towards the GUT or Planck scale by large quadratic divergences arising from loop corrections (hierarchy problem). Furthermore, compared to the situation in the Standard Model, it greatly improves the unification of the gauge couplings at a high energy scale. Most importantly in the spirit of the previous sections, it can provide stable neutral particles that can serve as dark matter candidates, the neutralino being the most prominent example.

Enlarging the Standard Model with the least particle content needed for a viable supersymmetric extension, leads to what is known as the Minimal Supersymmetric Standard Model (MSSM). It requires to double the number of Standard Model particles and to add an extra Higgs doublet in order to give masses to up- and down-type fermions and to keep the theory anomaly free. Despite solving the aforementioned problems of the Standard Model, the MSSM also possesses shortcomings that motivate further non-minimal extensions, an example of which is the Next-to-Minimal Supersymmetric Standard Model (NMSSM) discussed in Sec. 1.5.

1.2.2 Hidden sectors

A hidden sector is composed of a set of Standard-Model-neutral particles, which, in contrast with the particles of the Standard Model, are charged under an additional (Abelian or non-Abelian) gauge group. Such sectors are generically predicted in string theories [20, 21] and exist in various supersymmetric models as a source of SUSY breaking [4, 14, 15]. They are not directly connected to the Standard Model but could interact with it through messenger particles. The most simple and most prominent model is the one with an extra U(1) gauge symmetry in the hidden sector. In this case, the corresponding U(1) gauge boson, the hidden photon γ', acts as a messenger between the hidden and the visible sector. This scenario is discussed in detail in Sec. 1.3.

Since the interactions with the visible sector are very weak, so are the current experimental bounds. In fact, there might exist gauge fields and matter particles in the hidden sector with masses in the sub-GeV range that have so far escaped detection. These

particles belong to a class which in analogy to WIMPs is often referred to as Weakly Interacting Slim Particles (WISPs). Examples of WISPs are the aforementioned hidden U(1) gauge bosons, the CP-odd Higgs of the NMSSM introduced in Sec. 1.5, and other axion-like particles. For the CP-odd Higgs and the hidden photon, specific constraints are derived in Chapters 2 and 3, respectively.

Furthermore, because of their weak couplings to the Standard Model these sectors naturally provide a good hideout for dark matter. The possibility of dark matter interacting via a light messenger particle, sometimes called a dark force, received much interest as a potential explanation for some of the recent astrophysical observations mentioned in Sec. 1.1.4.2. The advantages of such a construction are discussed in Sec. 1.4 for the particular realisation of a hidden photon as a messenger.

1.3 Hidden sector with hidden photon

Models with an additional U(1) symmetry and the associated gauge boson, the hidden photon γ', in a hidden sector are of great interest from a top-down and a bottom-up perspective, as discussed in the following. In this work, it is assumed that the U(1) symmetry is broken at low energies by a Higgs or a Stückelberg mechanism. The corresponding hidden photon can be light and acts as a messenger with the visible sector. While in general the hidden photon can be as light as subelectronvolt, in this work we consider masses in the MeV to GeV range.

1.3.1 Motivation

By definition, hidden sectors have no direct coupling with the visible sector since they are neutral under the Standard Model gauge group and vice versa. At low energies, their only interactions with the visible sectors might arise from non-renormalisable effective operators of mass dimension larger than four and would possibly be unobservable since they are suppressed by some higher scale. However, the kinetic mixing of abelian gauge fields from the hidden and the visible sector is an exception. It corresponds to a renormalisable mass dimension four term in the low energy effective Lagrangian [22–25] and would therefore not be suppressed. Thus, the dominant interaction of the hidden photon γ' considered in this work with the Standard Model at low energies appears at the dimension four level through kinetic mixing with the visible sector hypercharge U(1) gauge boson, as discussed in Sec. 1.3.2. In fact, kinetic mixing is one of the few renormalisable interactions through which hidden sectors can be probed. There is a number of experiments capable of testing hidden photons with MeV- to GeV-scale masses. Certain constraints are derived in Chapter 3 where also an overview of all current constraints is given. A review of bounds for lighter masses is given in [122, 123].

From a top-down perspective, hidden sectors with an extra hidden U(1) symmetry appear naturally in well-motivated extensions of the Standard Model, see e.g. [124] and references therein. While one large-rank local gauge group is believed to unify the Standard Model interactions at high energies, it must be broken at low energies in order to describe the observed nature. This breaking of large gauge symmetries often yields, besides the Standard Model gauge group, also extra U(1)s which may remain unbroken down to low energies. If such U(1)s existed, they would remain undetected up to now as long as they belong to some hidden sector. Extra U(1) factors were predicted in the context of grand unified theories (GUTs) [125] and in supersymmetric models [16–19]. Furthermore, it was found that hidden U(1)s arise in various embeddings of the Standard Model in string theory: e.g. kinetic mixing was studied for the heterotic string in [19,126–129] and for type II strings in [20,130–136]; both hidden photon masses and kinetic mixing were considered in [20, 21, 137].

From a bottom-up point of view, the hidden photon is of great interest for various phenomenological reasons. For MeV-scale masses, it provides a solution to the discrepancy encountered in the muon anomalous magnetic moment between the Standard Model prediction and the experimentally measured value [26], cf. Sec. 1.3.3. Models in which an MeV- to GeV-scale hidden photon mediates the interaction between the visible sector and a dark matter particle have attracted much attention, see, e.g. [43, 100, 102, 111, 138–155]. These models with a hidden photon as a dark force mediator exhibit special features of interest in the context of the astrophysical observations listed above, as discussed in Sec. 1.4. Specific models of this kind and their phenomenology are then studied in Chapter 4. For masses much lighter than the ones considered in this work, it is also possible that the hidden photon itself forms super-weakly interacting dark matter [156–158]. Very light hidden photons in the milli-eV range could also account for the excess of dark radiation besides ordinary photons and neutrinos [159] which was present in former CMB data [160,161] though this indication has disappeared in the recent Planck measurement [45], which is now compatible at 1σ with the Standard Model value.

1.3.2 Low energy effective Lagrangian and kinetic mixing

At low energy, the dominant interaction of the hidden U(1) gauge boson (the hidden photon γ') with the visible sector is through kinetic mixing with the Standard Model hypercharge $\mathrm{U}(1)_Y$ gauge boson. The size of the kinetic mixing that can be generated in string theory models ranges over several orders of magnitude from values as small as $\sim 10^{-12}$ to $\sim 10^{-2}$ [19, 20]. From a field theory perspective, the kinetic mixing can be generated from loops of heavy particles charged under both U(1)s [22–25]. By integrating out these particles, the size of the kinetic mixing χ_Y can be estimated as a loop factor. For two heavy Dirac fermions with masses $m_1 > m_2$ and charges $(Q_v, Q_h)_1$

and $(Q_v, -Q_h)_2$ under $(\mathrm{U}(1)_v, \mathrm{U}(1)_h)$, i.e. the visible $\mathrm{U}(1)_v$ and the hidden $\mathrm{U}(1)_h$, the kinetic mixing is linked to the gauge coupling g_h in the hidden sector by [24]

$$\chi_Y \;=\; -\frac{4}{3}\,\frac{g_Y g_h}{16\pi^2}\,Q_v Q_h\,\ln\frac{m_1^2}{m_2^2}\;, \tag{1.19}$$

where g_Y is the hypercharge gauge coupling. The kinetic mixing can then typically be of the order of 10^{-3} for charges of order one and without a substantial hierarchy between the masses. Smaller values of χ_Y correspond to decreasing the hidden gauge coupling which may be extremely small in the case of hyperweak groups in D-brane models with LARGE bulk volume [20, 21, 162]. In any case, the kinetic mixing parameter is a small quantity and so we can often focus on the leading order effects, higher order corrections being negligible.

Throughout this work, results are presented in terms of the kinetic mixing χ with the ordinary photon which is linked to χ_Y via the cosine of the Weinberg angle by

$$\chi = c_W \chi_Y\;. \tag{1.20}$$

Furthermore, assuming that the kinetic mixing originates from a high-energy theory, in analogy to Eq. (1.19), we impose the relation

$$\chi \;=\; \frac{g_Y c_W g_h}{16\pi^2}\,\kappa \tag{1.21}$$

between the hidden sector gauge coupling g_h and the kinetic mixing χ. As SUSY contributions change (1.19), relation (1.21) with $\kappa = 1$ is exact for one pair of SUSY chiral multiplets and the logarithmic factor equal to one. The parameter κ depends on the masses of the particles in the loop and must, in principle, be derived from the high-energy model. Since κ only depends logarithmically on the mass splittings of the spectrum we usually assume it equal to one ($\kappa = 1$) or vary it by at most an order of magnitude from unity ($0.1 \leq \kappa \leq 10$). Note that all results studied in this work are only sensitive to the absolute value of κ, while the effects of different signs were studied in [163].

The most simple low energy effective Lagrangian describing the kinetic mixing with the ordinary photon in a hidden sector with just an extra U(1) symmetry and the corresponding hidden photon γ' is given by

$$\mathcal{L}_{\text{eff}} \;\supset\; -\frac{1}{4}\tilde{F}_{\mu\nu}\tilde{F}^{\mu\nu} - \frac{1}{4}\tilde{X}_{\mu\nu}\tilde{X}^{\mu\nu} + \frac{\chi}{2}\tilde{X}_{\mu\nu}\tilde{F}^{\mu\nu} + \frac{\tilde{m}_{\gamma'}^2}{2}\tilde{X}_\mu\tilde{X}^\mu + e j^\mu_{\text{em}}\tilde{A}_\mu, \tag{1.22}$$

where χ is the kinetic mixing parameter, $\tilde{F}_{\mu\nu} = \partial_\mu\tilde{A}_\nu - \partial_\nu\tilde{A}_\mu$ is the field strength tensor of the ordinary electromagnetic U(1) field $\tilde{A}_\mu$, similarly $\tilde{X}_{\mu\nu} = \partial_\mu\tilde{X}_\nu - \partial_\nu\tilde{X}_\mu$ is the field strength tensor of the hidden U(1) gauge field $\tilde{X}_\mu$ and $j^\mu_{\text{em}} = Q\bar{\psi}\gamma^\mu\psi$ is the usual electromagnetic current, cf. also Appendix A.1. The physical consequences of the kinetic mixing can be seen once the Lagrangian is written in the diagonal eigenbasis. Since the hidden U(1) is assumed to be spontaneously broken, the hidden photon gets a mass.

The mass $m_{\gamma'}$ of the hidden photon can be generated either by the Stückelberg mechanism or by the Higgs mechanism in the presence of a hidden Higgs field. Both mechanisms can produce hidden photon masses over a large range [20, 21] even down to subelectronvolt. They naturally also allow for GeV-scale masses. For example in certain string compactifications [20], the mass generated by the Stückelberg mechanism depends on the volume of the extra dimension and thus the string scale M_S as $m_{\gamma'} \sim M_S^2/M_{\mathrm{Pl}}$ which for intermediate string scales of $M_S \sim 10^9 - 10^{10}$ GeV and a Planck mass of $M_{\mathrm{Pl}} \sim 10^{18}$ GeV gives an MeV- to GeV-scale hidden photon mass.

Finally, diagonalizing the kinetic mixing term with the transformation

$$\tilde{A}_\mu = A_\mu + \frac{\chi}{\sqrt{1-\chi^2}} X_\mu \,, \qquad \tilde{X}_\mu = \frac{1}{\sqrt{1-\chi^2}} X_\mu \,, \tag{1.23}$$

the Lagrangian expanded to first order in χ reads

$$\mathcal{L}_{\mathrm{eff}} \supset -\frac{1}{4} F_{\mu\nu} F^{\mu\nu} - \frac{1}{4} X_{\mu\nu} X^{\mu\nu} + \frac{1}{2} m_{\gamma'}^2 X_\mu X^\mu + e j_{\mathrm{em}}^\mu A_\mu + e\chi j_{\mathrm{em}}^\mu X_\mu \,, \tag{1.24}$$

where it can be seen that the electromagnetic current acquires a charge under the hidden U(1), cf. also Appendix A.1. The last term couples the hidden photon to charged Standard Model particles and gives rise to a QED-like vertex $i\chi e Q \gamma^\mu$. This allows experiments to probe the hidden photon by producing it from charged fermions and looking for its decay back into those particles. Searches with electron beam dump experiments in which the hidden photon is emitted in bremsstrahlung from the initial electron beam are studied in detail in Chapter 3. There, we derive the corresponding constraints on the hidden photon mass $m_{\gamma'}$ and kinetic mixing parameter χ from the non-observation of the decay of the hidden photon. These results are also published in [42].

1.3.3 Discrepancy in anomalous magnetic moment

The anomalous magnetic moment of the muon is well measured and can be computed within the Standard Model to high precision. The Standard Model prediction takes into account a QED part which is computed up to 4 loops and estimated for 5 loops, an electroweak contribution which is suppressed by $\sim 10^{-9}$ and determined up to 2 loops (the 3-loop part is negligible) and a hadronic loop contribution at leading and next-to-leading order. This hadronic contribution gives rise to the main uncertainties in the theoretical calculation since it can not be calculated from first principles, cf. [4] for more details. A comparison of the prediction and the measurement thus probes the Standard Model at the quantum level and in case of disagreement might point towards new physics.

The value measured in 2006 by the E821 [164, 165] experiment at the Brookhaven National Laboratory (BNL) deviates from the Standard Model prediction. Currently,

the Review of Particle Physics by the PDG [4] gives the difference between experiment and theory as

$$\Delta a_\mu \;=\; a_\mu^{\mathrm{EXP}} - a_\mu^{\mathrm{SM}} \;=\; (28.7 \pm 8.0) \times 10^{-10}\,, \tag{1.25}$$

(errors combined in quadrature) where $a_\mu \equiv (g_\mu - 2)/2$. This corresponds to a discrepancy of 3.6σ. Other estimates of the hadronic contribution give slightly varying values but consistently show a mismatch, e.g. [166, 167].

This disagreement might have its origin in new physics beyond the Standard Model. If this new physics contribution adds up to the theoretical prediction from the Standard Model it could increase the theory estimate and make up for the higher measured value. Supersymmetry is one possible solution as, e.g. recently presented in [168] and can partly be probed at the LHC in the future.

The hidden photon with a mass in the MeV range, as considered in this work, is another possible explanation. Because of its coupling to charged particles of the Standard Model it gives an additional positive 1-loop contribution to the anomalous magnetic moment of the muon of $a_\mu^{\gamma'} \sim \alpha\chi^2/2\pi$ which can increase the theory value and solve the discrepancy for $\chi \sim 10^{-3}$ [26].

1.4 Dark force and dark matter

Hidden sectors, like the minimal one with just a hidden photon discussed in Sec. 1.3, can in general not only contain gauge but also matter fields. The possibility of a dark matter particle residing in the hidden sector and interacting via a hidden photon attracted much attention especially in the context of the astrophysical observations listed in Sec. 1.1.4. Different ranges of dark matter and hidden photon masses have been studied in various models, in particular, MeV- to GeV-scale hidden photons, often called a dark forces, [43, 100, 102, 111, 138–155] but even massless U(1)s [169–172].

1.4.1 Motivation

In general, scenarios with dark matter and a light mediator like the hidden photon have special features, which make them interesting from a phenomenological perspective, as discussed in the following. In order to explain the rise in the positron fraction, which has been observed by PAMELA [28] and was confirmed by Fermi [29, 30] and recently also AMS [31], in terms of dark matter, the annihilation cross section has to be significantly larger than the thermal one, as mentioned in Sec. 1.1.4.2. The required enhancement is sometimes assumed to be of astrophysical origin (e.g. halo substructure like a nearby clump with higher dark matter density) though large boost factors of this kind seem unlikely [173]. Another possible boost could arise from the particle physics side by the so-called Sommerfeld enhancement [27]. This increases the annihilation cross section at

low velocities, i.e. the present-day signals as desired for PAMELA [141, 142, 174–176], while leaving the one in the early Universe low enough to give the correct thermal relic abundance. Such an effect can occur in the presence of a light force carrier like the hidden photon which acts as a long-range attractive force and can enhance the cross section by distorting the wave functions of the incoming dark matter particles. This is discussed in more detail in [141, 177] and can be viewed as a repeated exchange of force carriers between the dark matter in a ladder Feynman diagram as illustrated in Fig. 1.4.

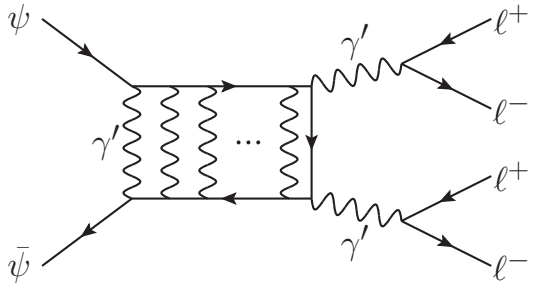

Figure 1.4: Feynman diagram for the annihilation of the hidden sector dark matter particle ψ in presence of a light hidden photon γ' (representative for a light mediator). The multiple exchange of the γ' in the ladder diagram leads to the Sommerfeld enhancement of the cross section. The annihilation through a hidden photon with $m_{\gamma'} \lesssim 1$ GeV is leptophilic because of kinematics.

Besides providing the boost factor, which is needed to get large enough cross sections to explain the PAMELA excess, models with a light messenger particle have another advantage. The dark matter annihilation into two hidden photons shown in Fig. 1.4 can well be the dominant channel if other couplings are absent. Then, the annihilation is naturally leptophilic (i.e. it proceeds dominantly into leptons) if the hidden photon is so light ($2m_e \lesssim m_{\gamma'} \lesssim 1$ GeV) that kinematics only allow for decays into leptons. This allows to reproduce the hard spectrum of positrons needed to fit the PAMELA excess without overproducing antiprotons and violating the measured flux [141].

In addition, the hidden photon plays an important role for direct detection as it mediates the scattering on nuclei. A light dark matter particle interacting via a hidden photon could potentially explain the signals reported by the direct detection experiments DAMA [33, 34], CoGeNT [35, 36], CRESST [37, 38] and CDMS [39]. Such scenarios were, for example, studied for elastic scattering in [102, 146] and for inelastic scattering in [141, 144, 146, 178, 179]. Furthermore, it was considered in [180, 181] that the scattering on nuclei mediated by the hidden photon can be isospin violating. This might alleviate the tension with the null results of the other searches, cf. also Sec. 4.1.3 for a discussion.

In view of the general benefits of hidden sectors, their phenomenologically interesting features and the potential indications for dark matter, these scenarios received much attention and various models have been studied. In this work, we construct and analyse different models with a light hidden sector dark matter particle interacting via

a hidden photon. Such a scenario could be of interest for the direct detection signals. Although we discuss the possible explanation of these signals in Chapter 4, these are not our primary motivation but instead we aim to explore which simple supersymmetric hidden dark sectors with an extra U(1) give viable models and how they can be constrained by observations. For this purpose, we have implemented our models in micrOMEGAs [57–61][3], which enables us to compute the relic abundance and the scattering cross sections of the dark matter particle. Comparing these observables with the measurements of the relic abundance Eq. (1.2) and the limits and signals from direct detection experiments discussed in Sec. 1.1.4.1 allows to determine the viable models and the interesting parameter space. These results are presented in Chapter 4 and are published in [43].

In the following, the models with light hidden sector dark matter, which are analysed in Chapter 4, are introduced and important specifics are highlighted. The most minimal set-up of Sec. 1.4.2 with just one additional Dirac fermion besides the hidden photon is used as a toy model to illustrate the different features and the phenomenology with the smallest possible number of parameters. More complete supersymmetric dark sector models are then presented in Sec. 1.4.3. The differences of the toy model to similar works of [102, 152, 154, 187] and the supersymmetric model to [146] are also highlighted.

1.4.2 Toy model

This model assumes the simplest possible dark sector with a Dirac fermion ψ, which carries unit charge under the (massive) hidden U(1), as dark matter candidate. Besides the hidden photon mass $m_{\gamma'}$ and the kinetic mixing χ as in Sec. 1.3, the dark matter mass m_ψ is another free parameter of this model. In contrast to the similar models, studied in [102, 152, 154, 187], we do not treat the kinetic mixing χ and the hidden gauge coupling g_h as two independent free parameters. Instead, based on the assumption that the kinetic mixing is generated from integrating out heavy particles, we fix g_h as a function of χ by the relation given in Eq. (1.21). This is a novel aspect of this work and leads to qualitatively different results for the cross sections, as discussed in Sec. 4.2. Most results for the toy model presented in Sec. 4.2 rely on the assumptions that the parameter κ is set to $\kappa = 1$, but we also consider the effect of varying it within $0.1 \leq \kappa \leq 10$.

The Lagrangian for this model is given by

$$\mathcal{L} \;=\; \mathcal{L}_{\mathrm{SM}} - \frac{1}{4}\tilde{X}_{\mu\nu}\tilde{X}^{\mu\nu} + \frac{\chi_Y}{2}\tilde{B}_{\mu\nu}\tilde{X}^{\mu\nu} + \frac{1}{2}\tilde{m}^2_{\gamma'}\tilde{X}_\mu\tilde{X}^\mu + g_h\bar{\psi}\gamma^\mu\psi\tilde{X}_\mu + m_\psi\bar{\psi}\psi, \quad (1.26)$$

where $\tilde{B}_{\mu\nu}$ and $\tilde{X}_{\mu\nu}$ are the field strength tensors for the hypercharge gauge field $\tilde{B}_\mu$ and the hidden photon gauge field $\tilde{X}_\mu$, respectively, ψ is the Dirac fermion dark matter

[3] As described in [43], LanHEP [182–186] was used to the generate the model-files for micrOMEGAs.

particle, m_ψ is its mass, $\chi_Y = \chi/c_W$ and $\tilde{m}^2_{\gamma'} \approx m_{\gamma'} + \mathcal{O}(\chi_Y^2)$, cf. Appendix A.4. We do not include a Higgs sector and do not consider how the dark matter particle becomes massive. A GeV-scale mass of the hidden photon could naturally be generated by the Stückelberg mechanism.

Because of the interaction with the hidden photon, the dark matter particle can annihilate into Standard Model particles and scatter off nuclei. In Chapter 4, we determine the regions of the parameter space which provide a viable dark matter candidate and study their signature in direct detection experiments as well as the corresponding constraints. The resulting phenomenology of the model is also published in [43].

1.4.3 Supersymmetric dark sectors

This section describes how the idea of the dark hidden sector, considered in the toy model of Sec. 1.4.2, can be embedded into a supersymmetric model. It sets the theoretical framework for the phenomenological analysis presented in Chapter 4. Similar to the toy model, we seek to construct a hidden sector that contains a light dark matter particle which interacts with the visible sector through kinetic mixing of a light hidden photon with the hypercharge gauge field.

Other elegantly simple supersymmetric models have been studied in [143–146, 149, 151]. However, these works emphasised that supersymmetry breaking effects in the visible sector would have to be dominated by gauge mediation in order to obtain small enough masses for such a light hidden sector. We therefore examine whether a scenario with light hidden sector dark matter is also possible in models with gravity mediation. In view of the direct detection signals, we search for a gravity-mediated spectrum of particles which can give the desired phenomenology. This is also of interest for the question if such a model can be embedded into string theory. While hidden sectors in general appear naturally there, cf. e.g. [20, 21, 128, 133, 136, 137, 188–190], it is difficult to achieve gauge mediation dominance over gravity mediation in globally consistent models.

The hidden sector models considered in the following and in Chapter 4, have a similar particle content and couplings to those in [146]. However, unlike argued in that work, we show that gravity mediation domination also allows for interesting phenomenological predictions under certain mild assumptions, without requiring additional sequestering relative to the visible sector. A possible explanation of the signals found by DAMA and CoGeNT together with constraints from different observations is then presented in Chapter 4. The following discussion summarises the one presented in [43] where more details can be found.

1.4.3.1 Supersymmetric kinetic mixing

In the models considered in this section, the dominant interaction between the visible and the hidden sector is through kinetic mixing of the hidden U(1) gauge field with the

hypercharge gauge field. A holomorphic kinetic mixing χ_h between hypercharge $\tilde{B}_\alpha$ with coupling g_Y (and gaugino the Bino, b) and hidden gauge superfield $\tilde{X}_\alpha$ with coupling g_h (and gaugino written as λ) appears in the Lagrangian density as [43]

$$\mathcal{L} \supset \int d^2\theta \left(\frac{1}{4g_Y^2}\tilde{B}^\alpha \tilde{B}_\alpha + \frac{1}{4g_h^2}\tilde{X}^\alpha \tilde{X}_\alpha - \frac{\chi_h}{2}\tilde{B}^\alpha \tilde{X}_\alpha \right) . \tag{1.27}$$

The physical kinetic mixing in the canonical basis [20, 134] is then given by

$$\chi_Y = g_Y g_h \mathrm{Re}(\chi_h) = \frac{\chi}{c_W} . \tag{1.28}$$

As discussed above, it is assumed that there is no matter which carries charges of both the hidden and the visible gauge groups. Therefore, this relationship is valid at all energy scales. Furthermore, we shall take the value of the holomorphic kinetic mixing parameter to be of the order of a loop factor [20]

$$\chi_h \equiv \frac{\kappa}{16\pi^2}. \tag{1.29}$$

In our analysis, we thus use the physical kinetic mixing χ and apply again the relation of Eq. (1.21) with the hidden gauge coupling g_h as in the case of the toy model.

1.4.3.2 Hidden matter fields

We construct the simplest anomaly free supersymmetric dark sector model which is possible without adding dimensionful supersymmetric quantities. The superpotential

$$W \supset \lambda_S S H_+ H_- \tag{1.30}$$

contains a dimensionless Yukawa coupling λ_S and three chiral superfields S, H_+, H_-, where H_+ and H_- carry charges ± 1 under the hidden U(1).

These scenarios are inspired from D-brane models and were derived e.g. in [188, 190] from string theory. In [146], such a model with gauge mediation was studied and denoted a "hidden sector NMSSM", although we have set the cubic singlet term in the superpotential to zero. The model possesses a global U(1) symmetry under which S and H_- are charged. This is, however, not respected by string theory and we consider that it is either broken at higher order in the superpotential or through non-perturbative effects so that it does not play a role in the following, cf. [43] for details.

Once soft supersymmetry-breaking terms are included, the potential for the hidden sector is roughly given by [43]

$$\begin{aligned} V_h &= |\lambda_S|^2(|SH_+|^2 + |SH_-|^2 + |H_+H_-|^2) + \frac{g_h^2}{2}(|H_+|^2 - |H_-|^2 - \xi)^2 \\ &\quad + m_{H_+}^2|H_+|^2 + m_{H_-}^2|H_-|^2 + m_S^2|S|^2 + (\lambda_S A_S S H_+ H_- + \frac{1}{2}M_\lambda \lambda\lambda + c.c.) , \end{aligned} \tag{1.31}$$

with $\xi = \chi g_Y/(g_h c_W)\frac{v^2}{4}\cos 2\beta$, the soft masses $m^2_{H_\pm}$ and m^2_S, the trilinear soft term A_S and the hidden gaugino mass M_λ.

The crucial difference for the phenomenology of the model, when considering gravity mediation, is that the gravitino is not the lightest supersymmetric particle (LSP). Therefore, the dark matter can consist of stable hidden sector particles. Depending on the mechanism by which the hidden gauge symmetry is broken, the models yield different dark matter particles. We study two breaking mechanisms, which are described in the following, and their respective implications on the particle content of the hidden sector. A complete analysis of the model including a determination of the dark matter relic abundance and the direct detection cross sections is then given in Chapter 4.

1.4.3.3 Symmetry breaking through running

One possibility is that the hidden gauge symmetry breaking is induced by the running of the Yukawa coupling λ_S. This is similar to the case in the MSSM where the top Yukawa coupling can, through running from the grand unified theory (GUT) scale, induce electroweak symmetry breaking. In this scenario, the independent supersymmetric parameters at the high-energy scale are then the kinetic mixing χ, the hidden sector gauge coupling g_h and the Yukawa coupling λ_S as well as the soft masses $m_{H_\pm}$, m_S, M_λ and A_S. Thereby, since the fields $H_\pm$ are a non-chiral pair, we set $m_{H_+} = m_{H_-}$ at the high-energy scale (note that there is no explicit Fayet–Iliopoulos term for the hidden $U(1)$ which would introduce a mass splitting).

The two-loop renormalisation group equations (RGEs) of the model, discussed in detail in [43][4], drive in the case of $m_S > m_{H_\pm}$ the soft masses for $m^2_{H_\pm}$ to be negative at low energies. This triggers the breaking of the hidden gauge symmetry. The coupling to the visible sector through kinetic mixing determines if H_+ or H_- condenses. Without loss of generality, we take χ to be negative and find that H_+ obtains a vacuum expectation value (vev). A stable minimum where $\langle H_+\rangle = \Delta/\lambda_S$ and all other expectation values vanish is obtained, according to [43], when Δ is real and

$$\begin{aligned} 0 &\leq m^2_{H_-} + m^2_{H_+} + m^2_S + 2\Delta^2 \,, \\ 0 &\leq (m^2_{H_-} + m^2_{H_+} + \Delta^2)(m^2_S + \Delta^2) - |A_S|^2\Delta^2, \end{aligned} \tag{1.32}$$

in which $\Delta \equiv \sqrt{\lambda^2_S\xi - m^2_{H_+}\lambda^2_S/g^2_h}$. The hidden photon mass induced by radiative hidden gauge symmetry breaking is then given by

$$m_{\gamma'} = \frac{\sqrt{2}g_h}{\lambda_S}\Delta. \tag{1.33}$$

[4]Note that the two-loop RGEs do not include the running of the kinetic mixing which is suppressed by $\mathcal{O}(\chi^2)$ [146] and therefore equivalent to *three*-loop order. This would also introduce a weak dependence on the visible sector parameters and is beyond the scope of this work.

Values for $m_{\gamma'}$ ranging from a few GeV to a hundred GeV can be obtained. In [43], possible results for $m_{\gamma'}$ are given as a function of m_S and $\alpha_S \equiv \lambda_S^2/4\pi$ for two scenarios with different hidden gaugino masses.

Choosing the soft masses and couplings at the MSSM GUT scale and running down, we find models at the low-energy scale with hidden gauge symmetry breaking. Since we apply a relation between χ and g_h, given by Eq. (1.21), we reduce the number of free parameters of the model by one if we fix $\kappa = 1$. However, as in the case of the toy model, κ will also be allowed to vary within the range $0.1 \leq \kappa \leq 10$, in the results of the analysis in Chapter 4. This does not strictly reduce the number of parameters but rather constrains them with important consequences. A scan over the remaining parameters then allows to find viable models at the low-energy scale which will turn out to give an interesting phenomenology. This search uses the RGE engine from SoftSUSY [191].

1.4.3.4 Symmetry breaking induced by the visible sector

Another possible mechanism to break the hidden gauge symmetry is via the effective Fayet–Iliopoulos term, which is induced in the hidden sector by the kinetic mixing with the visible Higgs D-term. This has been promoted in other works such as [146]. In this case, the squares of the soft masses $m_{H_+}^2$ and $m_{H_-}^2$ can be positive as long as they are small enough that the hidden gauge symmetry is broken and a stable minimum is obtained.

Though this scenario is more difficult to justify in models with gravity mediation, it is not implausible and can, for example, be achieved when the hidden sector is sequestered. Then, the gravitino is assumed to be much heavier than the hidden sector. Furthermore, the singlet mass-squared $m_S^2 > 0$ and the hidden gaugino mass-squared M_λ^2 are assumed to be of a similar order of magnitude than the hidden Higgs soft terms $m_{H_+}^2, m_{H_-}^2$ and the hidden A_S term is chosen to be small. This differs from the model of [146], where gauge mediation is considered and the masses squared are instead given by $m_S^2 \sim M_\lambda^2 \sim 0$.

1.4.3.5 Dark matter candidates

In these models, the dark matter particle can either be a Majorana fermion or a Dirac fermion and is kept stable by R-parity.[5] The fermion mass matrix in the basis of the hidden gaugino, hidden Higgsinos and hidden singlino ($\tilde{\lambda},\ \tilde{h}_+,\ \tilde{h}_-,\ \tilde{s}$) is given by

$$\mathcal{M}_f \ = \ \begin{pmatrix} M_\lambda & m_{\gamma'} & 0 & 0 \\ m_{\gamma'} & 0 & 0 & 0 \\ 0 & 0 & 0 & \Delta \\ 0 & 0 & \Delta & 0 \end{pmatrix}, \tag{1.34}$$

[5] Even though the model also contains stable scalars, we do not consider them as dark matter candidates since the protecting symmetries are expected to be broken at some higher order in the potential so that they can ultimately decay.

where the kinetic mixing with the visible neutralino is neglected. This mixing is taken into account in the complete analysis and described in detail in [43]. The Majorana fermion is obtained from diagonalising the $\tilde{\lambda}$, $\tilde{h}_+$ states and the Dirac fermion from $\tilde{h}_-$, $\tilde{s}$. We refer to the former as "$\tilde{o}_1$" due to the notation used in micrOMEGAs for the lightest odd particle and denote the latter as "$\tilde{o}_7$". According to Eq. (1.34), there is always a Majorana fermion lighter than the hidden gauge boson (in order to avoid this, a mass for the hidden singlino would have to be added). Therefore, in the supersymmetric dark sector models considered in this work, it is not possible to have a hidden photon lighter than the dark matter particle. The Dirac fermion can be the dark matter particle if the Yukawa coupling is $\lambda_S < \sqrt{2} g_h$ and the Majorana mass M_λ is rather small at the high-energy scale (this is possible, e.g. in a string model). While the Dirac fermion can not be the dark matter in radiative-breaking models it is an attractive candidate for models with visible sector induced breaking. It would also not be a good candidate in gauge mediation, where the singlet scalar is necessarily lighter than the fermion [146].

Note that in diagonalizing the mass matrix one always finds a Majorana fermion from the $\tilde{\lambda}$, $\tilde{h}_+$ states, which is lighter than the hidden photon. For the Dirac fermion to be the dark matter particle, its mass has to be even below the one of the Majorana fermion and is thus necessarily also smaller than $m_{\gamma'}$. Therefore, in these models the dark matter particle can never be heavier than the hidden photon. This is in contrast to the toy model and has phenomenological consequences which are discussed in Sec. 4.3.

1.5 The NMSSM

The Next-to-Minimal Supersymmetric Standard Model (NMSSM) is an attractive extension of the Minimal Supersymmetric Standard Model (MSSM) as mentioned in Sec. 1.2.1. Certain shortcomings of the MSSM can be solved in the NMSSM by enlarging the field content by an extra singlet superfield S.

1.5.1 Motivation

Historically, the NMSSM has been motivated as a solution to the so-called μ-problem of the MSSM [192]. This problem is linked to the dimensionful parameter μ in the supersymmetric mass term $\mu H_u H_d$ in the superpotential, which is the analogous to the Higgs mass term in the Standard Model. For different reasons [193, 194], this parameter is required to be of the order of the SUSY breaking scale $\mu \sim \mathrm{O}(100\ \mathrm{GeV})$. There is, however, in the MSSM no theoretical explanation why the μ-parameter is small compared to the Planck scale and at a similar scale than the unrelated soft SUSY breaking terms. This missing explanation is referred to as the μ-problem. It can be solved in the NMSSM by requiring a scale-invariant superpotential and generating the μ-term dynamically by the vev $\langle S \rangle$ of the extra singlet S instead of introducing an

arbitrary μ-term. This effective μ-term in the NMSSM is thereby connected to the mechanism of soft supersymmetry breaking and can easily be of the order of m_{soft} without having to be adjusted by hand.

More recently, it has been suggested that the fine-tuning problem of the MSSM could be alleviated or removed in the NMSSM when the CP-odd Higgs A^0 is light [195, 196]. This problem, also referred to as the little hierarchy problem, is caused by the discrepancy between the tree-level prediction for the lightest Higgs mass as $m_h \leq m_Z$ and the lower bound $m_h \geq 114$ GeV from LEP, which applies in most MSSM scenarios (the scalar boson discovered at LHC [197, 198] might correspond to the lightest Higgs with $m_h \simeq 125$ GeV and would emphasise this discrepancy). Then, in the MSSM, large soft supersymmetry breaking mass parameters are needed for the one-loop corrections to lift the Higgs mass sufficiently. The presence of a light CP-odd Higgs in the NMSSM allows for an additional decay channel $h \to 2A^0$ where the A^0s either escape detection or lead to exotic final states (four particle final states, e.g. 4τ) which would not appear in the standard search channels. This weakens the LEP limits on m_h [195, 196] and thereby alleviates the tension with the tree-level prediction. Although this scenario is now tightly constrained by the new ALEPH analysis [199] as well as BaBar data on $\Upsilon(3S)$ decays [200, 201], some parameter space remains available [202] and can further be probed by η_b-decays [203].

Further motivation for the NMSSM in general and a light A^0 in particular arises since it was found in [204] that NMSSM-like models can also be obtained from the heterotic string. These scenarios yield specific versions of the NMSSM such as the Peccei–Quinn (PQ) version. In this case, a light pseudo-Goldstone boson appears in the spectrum whose mass is generated by small PQ violating effects and can therefore be much below the GeV scale.

Moreover, the excitement in the course of the PAMELA observations also initiated studies of the NMSSM and a light A^0 in the context of dark matter, e.g. [176,187,205]. In these works, the neutralino dark matter annihilation proceeds via the light pseudoscalar which, for masses of a few hundred MeV, dominantly decays into leptons of the first and second generation. This large fraction of leptons in the final state can account for the observed positron excess in PAMELA. Hadronic decay modes are then naturally suppressed because of kinematics. Therefore, the annihilation does not produce an excess in antiprotons, which would be in contradiction with the antiproton spectrum observed by PAMELA.

Motivated by these considerations, it is important to study constraints on a very light A^0. This task is accomplished in Chapter 2 and the resulting limits are published in [41]. In the following, we review the theoretical framework for a light CP-odd Higgs in the NMSSM.

1.5.2 NMSSM and a light CP-odd Higgs

As mentioned in Sec. 1.5, the NMSSM is an extension of the MSSM with a gauge-singlet superfield S. In our analysis in Chapter 2, we focus on a particular version of the NMSSM which has no direct μ-term and is usually referred to as the $\mathbb{Z}_3$-symmetric NMSSM. The relevant part of the superpotential of this $\mathbb{Z}_3$-symmetric NMSSM is given by

$$W \supset \lambda S H_1 H_2 + \frac{1}{3}\kappa S^3 \,, \tag{1.35}$$

where λ and κ are dimensionless Yukawa couplings. The corresponding soft-breaking terms in the Higgs sector are

$$V_{\text{soft}} = m_1^2|H_1|^2 + m_2^2|H_2|^2 + m_S^2|S|^2 + \left(\lambda A_\lambda S H_1 H_2 + \frac{1}{3}\kappa A_\kappa S^3 + \text{h.c.}\right), \tag{1.36}$$

with the soft masses m_1, m_2, m_S, and the trilinear soft terms A_λ and A_κ. As discussed earlier, when S obtains a vev $s = \langle S \rangle$ of the order of the weak or supersymmetry breaking scale, this generates an effective μ-term with $\mu_{\text{eff}} = \lambda s$ [194]. Since this scale-invariant cubic superpotential possesses an accidental discrete $\mathbb{Z}_3$-symmetry when all superfields are transformed by $e^{i2\pi/3}$, it is called the $\mathbb{Z}_3$-symmetric NMSSM.

It was found that in the two limiting cases where the Higgs potential possesses either an approximate Peccei–Quinn or an approximate R-symmetry, a light pseudoscalar A^0 appears naturally [196, 206–210]. These two scenarios are sketched briefly in the following.

1.5.2.1 Peccei–Quinn limit

In the limit $\kappa \to 0$, where the term $\propto \lambda$ in Eq. (1.35) is the only one involving S, the Lagrangian is invariant under the transformation

$$H_{1,2} \to e^{i\alpha} H_{1,2} \quad \text{and} \quad S \to e^{-2i\alpha} S \,. \tag{1.37}$$

At the electroweak scale this global symmetry is spontaneously broken by the vevs of $H_{1,2}$ and S. This results in a massless Nambu–Goldstone boson, an axion-like particle, which is given by [194]

$$\begin{aligned} A^0 &= \frac{1}{N}\Big(v \, \sin 2\beta \; A^0_{\text{MSSM}} - 2s \; S_I\Big) \,, \\ N &= \sqrt{v^2 \sin^2 2\beta + 4s^2} \,, \end{aligned} \tag{1.38}$$

where $A^0_{\text{MSSM}} = \cos\beta \; H_{1I} + \sin\beta \; H_{2I}$ is the MSSM pseudoscalar and the subscript I refers to the imaginary part of the Higgs neutral component; as usual, $\tan\beta = v_1/v_2$ and $v = \sqrt{v_1^2 + v_2^2} = 174$ GeV, with the vevs v_1 and v_2 of the two Higgs SU(2)-doublets H_1 and H_2 which generate masses for the up-type quarks and the down-type quarks

and charged leptons, respectively. The mass of the pseudoscalar can be expressed in the large $\tan\beta$ regime according to [207] by

$$m_{A^0}^2 \simeq -3\kappa A_\kappa s \; . \tag{1.39}$$

Since the renormalisation of κ is proportional to κ itself, this coupling can be very small and lead to A^0 being very light. In the NMSSM example obtained from the heterotic string in Ref. [204], mentioned above, it was found that $\kappa < \mathcal{O}((\phi/M_{\rm Pl})^5)$, with ϕ being an average vev of certain Standard Model singlets. For ϕ being an order of magnitude below the Planck scale, the value of κ can be as small as 10^{-6}, therefore leading to a mass of ~ 100 MeV for the pseudoscalar. In other models, this mass can be even lighter. Since the PQ symmetry is anomalous, as in the DFSZ axion models (by Dine, Fischler, Srednicki [211] and Zhitnitsky [212]), the lower limit on m_{A^0} is set by the anomaly contribution and is of the order of 100 keV [211] (for $s \sim v$).

1.5.2.2 R-symmetry limit

In the limit $A_\kappa, A_\lambda \to 0$, the Higgs sector of the $\mathbb{Z}_3$-symmetric NMSSM is R-invariant, i.e. invariant under an R-symmetry under which the superfields transform as [194]

$$H_{1,2} \to e^{i\alpha_R} H_{1,2} \quad \text{and} \quad S \to e^{i\alpha_R} S \; . \tag{1.40}$$

Spontaneous breaking of this symmetry by the vevs of $H_{1,2}$ and S results in an "R-axion". Its composition is given by [194],

$$\begin{aligned} A^0 &= \frac{1}{N}\Big(v \;\sin 2\beta \; A^0_{\rm MSSM} + s \; S_I\Big) \; , \\ N &= \sqrt{v^2 \sin^2 2\beta + s^2} \; , \end{aligned} \tag{1.41}$$

with the same $A^0_{\rm MSSM}$ as in Eq. (1.38).

Unlike the Peccei–Quinn symmetry discussed above, the R-symmetry is not a (classical) symmetry of the full Lagrangian [194]. Even if $A_\kappa, A_\lambda \to 0$, the gaugino mass terms break the R-symmetry explicitly. Non-zero A-terms are induced by renormalisation, so their minimal value is a loop factor times the gaugino mass. The A^0 mass is then again approximated by (1.39).

In both PQ- and R-symmetric cases, the light pseudoscalar is in most of the parameter space singlet-like in the limit $s \gg v \;\sin 2\beta$. Its couplings to gauge bosons and Standard Model matter are suppressed in this limit. However, s cannot be too large, otherwise a large effective μ-term is induced. An exception is the case $\lambda \ll 1$, which corresponds to the "decoupling limit", i.e. when there is no communication between the singlet and the rest of the NMSSM.

Chapter 2

Constraints on the NMSSM CP-odd Higgs

In Chapter 1, we argued that light particles with masses in the sub-GeV range, which have not been detected so far because of their weak interactions with the Standard Model, might still exist. These particles are often referred to as WISPs. Examples of WISPs are axion-like particles, the hidden photon considered in Chapter 3 and the NMSSM CP-odd Higgs which is the focus of the present chapter. A light CP-odd Higgs in the NMSSM arises naturally from spontaneous breaking of approximate symmetries like the Peccei–Quinn or R-symmetry, and can be obtained in heterotic string models, as discussed in Chapter 1.

In this chapter, we study experimental constraints on the CP-odd Higgs with a mass below the two-muon threshold and its couplings to fermions. We specifically address the question how light a CP-odd Higgs can be. An introduction describing the relevant background and formulae used in the subsequent analysis is given in Sec. 2.1. We demonstrate how meson decays can be used to constrain the CP-odd Higgs. Using different precision measurements, we derive in Sec. 2.2 numerous constraints from rare and radiative meson decays as well as the anomalous magnetic moment of the muon. Additional complementary constraints from reactor and beam dump experiments are then presented in Sec. 2.3.

The obtained results apply more generally to the couplings of a light pseudoscalar to fermions. They are published in [41] and quoted in the Review of Particle Physics by the PDG [4]. This analysis was conducted in collaboration with Oleg Lebedev, Sául Ramos-Sánchez and Andreas Ringwald.

2.1 The light CP-odd Higgs of the NMSSM

As mentioned in Sec. 1.5, the NMSSM is an extension of the MSSM with a gauge-singlet superfield S. In this chapter, we focus on a particular version of the NMSSM which has

no direct μ-term and is usually referred to as the $\mathbb{Z}_3$-symmetric NMSSM. It is introduced in Sec. 1.5.2 and the superpotential and soft terms are given in Eqs. (1.35) and (1.36), respectively. There, it is also argued that the model naturally contains a light CP-odd Higgs in the two cases when the Higgs potential either has an approximate Peccei–Quinn or an approximate R-symmetry. Since the constraints derived in this chapter are based on interactions with fermions, the coupling of the CP-odd Higgs A^0 to fermions is the most important term of the Lagrangian for the following analysis. Adopting the notation of Ref. [202], this term is given by

$$\Delta\mathcal{L} \;=\; -\frac{g_2}{2m_W}\, C_{Aff} \left(m_d\, \bar{d}\gamma_5 d + \frac{1}{\tan^2\beta} m_u\, \bar{u}\gamma_5 u + m_\ell\, \bar{\ell}\gamma_5 \ell \right) A^0, \tag{2.1}$$

for down-type quarks d (mass m_d), up-type quarks u (mass m_u) and leptons ℓ (mass m_ℓ), where as usual $\tan\beta = v_1/v_2$ with vevs $v_1 = \langle H_1 \rangle$ and $v_2 = \langle H_2 \rangle$. In the NMSSM, the coupling C_{Aff} can according to [202] be expressed in terms of the singlet-doublet mixing angle θ_A and $\tan\beta$ by $C_{Aff} = \cos\theta_A \tan\beta$, with $\cos\theta_A = v \sin 2\beta / N$ and N given by Eq. (1.38) in the PQ-limit and by Eq. (1.41) in the R-symmetry limit. In what follows, we treat C_{Aff} as a free parameter and derive various particle physics constraints on it. In the NMSSM, very large ($> 10^2$) and very small ($< 10^{-2}$) values of C_{Aff} lead to violation of perturbativity and/or require finetuning. Therefore, it usually suffices to focus on the moderate C_{Aff} window. However, since our analysis applies more generally to the coupling of any pseudoscalar particle to matter, as long as the coupling C_{Aff} is universal for all fermions, we discuss constraints also outside of this window.

Various constraints, in particular from meson decays, have already been well studied for the A^0 masses beyond the two-muon threshold $m_{A^0} > 2m_\mu$. In the range $2m_\mu < m_{A^0} < 3m_\pi$, where A^0 decays predominantly into two muons, constraints arise from the two decays $K^+ \longrightarrow \pi^+ A^0$ and $B \longrightarrow K\ A^0$. The corresponding bound has been derived in [213] and excludes roughly $C_{Aff} > \mathcal{O}(10^{-2})$. However, the bound weakens somewhat for masses above the three-pion threshold since there the branching ratio for the decay into muons decreases. For even larger A^0 masses $m_{A^0} \geq 1$ GeV, the $\Upsilon \longrightarrow \gamma A^0$ decay imposes that $C_{Aff} < 0.5$ for $\tan\beta \sim 1$ [202]. This bound also weakens for increasing m_{A^0} till about $\mathcal{O}(1)$ for $m_{A^0} \sim m_\Upsilon$. Above 12 GeV, the DELPHI data on $e^+e^- \longrightarrow b\bar{b}A^0 \longrightarrow b\bar{b}b\bar{b}$ set a rather weak limit requiring that $C_{Aff} < \mathcal{O}(10)$ [202]. Further constraints, which are usually relevant at large $\tan\beta$, are summarised in Ref. [194].

On the contrary, the light mass territory with $m_{A^0} < 2m_\mu$ is less well explored. Only few constraints have been studied in Refs. [208, 213] in the framework of the NMSSM and in Refs. [214,215] for Two Higgs Doublet Models (see also [216]). In what follows, we study the $\{m_{A^0}, C_{Aff}\}$ parameter space with respect to various constraints arising from different meson decays, the muon anomalous magnetic moment as well as reactor and beam dump experiments. In particular, we discuss how light a CP-odd Higgs boson is allowed to be. Since we work in terms of the coupling C_{Aff} between the A^0 and fermions, most of our results are largely independent of $\tan\beta$ and specific features of the NMSSM.

2.1.1 Decay width of the A^0

In the mass range we are interested in, for m_{A^0} below the two-muon threshold, A^0 can only decay into an electron-positron pair or into two photons. Its total decay width is thus the sum

$$\Gamma_{A^0} = \Gamma_{A^0\to e^+e^-} + \Gamma_{A^0\to\gamma\gamma} \tag{2.2}$$

of the partial decay widths into e^+e^- and into $\gamma\gamma$. These are given by

$$\Gamma_{A^0\to f\bar{f}} = \frac{\sqrt{2}G_F}{8\pi}\, m_f^2\, m_{A^0}\, C_{Aff}^2 \sqrt{1-4\frac{m_f^2}{m_{A^0}^2}}\,, \tag{2.3}$$

$$\Gamma_{A^0\to\gamma\gamma} = \frac{\sqrt{2}G_F\alpha^2}{16\pi^3}\, m_{A^0}^3 \left|\sum_i r C_{Aii} Q_i^2 k_i F(k_i)\right|^2\,, \tag{2.4}$$

where the latter has been taken from [217] with the sum running over all Standard Model fermions in which $r = 1(N_c)$ for leptons (quarks), $k_i = m_i^2/m_{A^0}^2$, Q_i is the charge of the fermion in the loop; $C_{Aii} = C_{Aff}$ for the down-type fermions and $C_{Aii} = C_{Aff}/\tan^2\beta$ for the up-type fermions. Here, we neglect the contribution from chargino loops as the coupling is dominated by the Standard Model fermions. The loop function $F(k_i)$ is given in [217] as

$$F(k_i) = \begin{cases} -2\left(\arcsin\frac{1}{2\sqrt{k_i}}\right)^2 & \text{for } k_i \geq \frac{1}{4}\,, \\ \frac{1}{2}\left[\ln\left(\frac{1+\sqrt{1-4k_i}}{1-\sqrt{1-4k_i}}\right)+i\pi\right]^2 & \text{for } k_i < \frac{1}{4}\,, \end{cases} \tag{2.5}$$

and has the limits

$$k_i\, F(k_i) = \begin{cases} 0 & \text{for } k_i \ll 1\,, \\ -\frac{\pi^2}{8} & \text{for } k_i = \frac{1}{4}\,, \\ -\frac{1}{2} & \text{for } k_i \gg 1\,. \end{cases} \tag{2.6}$$

For a very light A^0, the only possible decay channel is the one into two photons. In this case, for example for $C_{Aff} = 1$ and $m_{A^0} = 0.5$ MeV, the total decay width is about $\Gamma_{A^0} \simeq 4\times10^{-12}$ eV according to Eq. (2.2) with $\Gamma_{A^0\to e^+e^-} = 0$. This corresponds to a decay length of $\tau c \sim 60$ km (for a boost factor $\gamma \sim 1$). Above the two-electron threshold, the total decay width increases since the decay into e^+e^- opens. Taking, for example, $m_{A^0} = 50$ MeV and $C_{Aff} = 1$, the total decay width becomes $\Gamma_{A^0} \simeq 10^{-5}$ eV, according to Eq. (2.2). Thus, the corresponding decay length decreases to $\tau c \sim 2$ cm. Both example parameter points assume that $\tan\beta = 1$.

The dependence of the branching ratio $\mathrm{BR}(A^0 \longrightarrow e^+e^-) = \Gamma_{A^0\to e^+e^-}/\Gamma_{A^0}$ on $\tan\beta$ is shown in Fig. 2.1 as a function of the mass of A^0. Increasing $\tan\beta$ reduces the up-type quark contributions to the decay width into photons $\Gamma_{A^0\to\gamma\gamma}$ in Eq. (2.4) and thereby increases $\mathrm{BR}(A^0 \longrightarrow e^+e^-)$. This dependence saturates for $\tan\beta \geq 3$. The decay channel

into an electron-positron pair $A^0 \longrightarrow e^+e^-$ dominates for masses m_{A^0} above the two-electron threshold and below ~ 80 MeV, when the decay into two photons $A^0 \longrightarrow \gamma\gamma$ becomes important. For masses above the two-muon threshold, the decay $A^0 \longrightarrow \mu^+\mu^-$ is dominant.

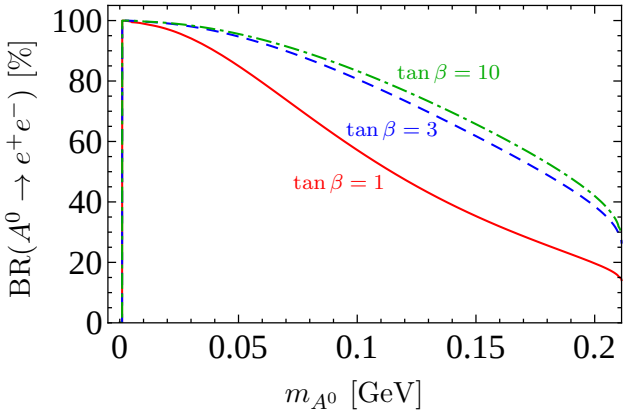

Figure 2.1: Dependence of the A^0 branching ratio into e^+e^- $\mathrm{BR}(A^0 \longrightarrow e^+e^-) = \Gamma_{A^0\to e^+e^-}/\Gamma_{A^0}$ on $\tan\beta$ as a function of the A^0 mass m_{A^0}. The lowest (solid red) curve corresponds to $\tan\beta = 1$, the higher (dashed blue) one to $\tan\beta = 3$ and the highest (dash-dotted green) curve to $\tan\beta = 10$.

2.1.2 Specifics of the A^0 in meson decays

In the following analysis in Sec. 2.2, an important set of constraints on the A^0 parameter space $\{m_{A^0}, C_{Aff}\}$ arises from the decay of a meson X in which an A^0 can be produced along with another meson Y by $X \longrightarrow Y + A^0$. For the decay $B^0 \longrightarrow K^0 A^0$, the decay width in the NMSSM was found in [213] as

$$\Gamma(B^0 \to K^0 A^0) = \frac{G_F^2\,|V_{tb}V_{ts}^*|^2}{2^{10}\pi^5}\,|C_A|^2\,\frac{|\vec{p}_K|}{m_{B^0}^2}\left|f_0^{B^0}(m_{A^0}^2)\right|^2\left(\frac{m_{B^0}^2 - m_{K^0}^2}{m_b}\right)^2, \quad (2.7)$$

where G_F is the Fermi constant, m_{B^0} is the B^0 mass, m_{K^0} is the K^0 mass, V_{tb} and V_{ts} are CKM matrix elements, cf. Tab. 2.1, $|\vec{p}_K| \simeq m_{B^0}/2$ is the three momentum of the kaon, the coupling C_A as well as the form factor f_0 are given in [213] and $f_0^{B^0}(0) \sim 0.3 - 0.4$ [218]. The decay width of the process $K^+ \longrightarrow \pi^+ A^0$ can be obtained from Eq. (2.7) with the replacements $b \to s$, $s \to d$, $K \to \pi$ and $B \to K$ as

$$\Gamma(K^+ \longrightarrow \pi^+ A^0) = \frac{G_F^2\,|V_{ts}V_{td}^*|^2}{2^{10}\pi^5}\,|C_A'|^2\,\frac{|\vec{p}_\pi|}{m_{K^+}^2}\left|f_0^{K^+}(m_{A^0}^2)\right|^2\left(\frac{m_{K^+}^2 - m_{\pi^+}^2}{m_s}\right)^2, \quad (2.8)$$

where now the form factor $f_0^{K^+}(0) \sim 1$ [219] has to be used and $|\vec{p}_\pi| \simeq m_{K^+}/2$ similar to the case above. A measurement of the branching ratio $\mathcal{B}^{\mathrm{EXP}}_{B^0\to K^0+x}$ or $\mathcal{B}^{\mathrm{EXP}}_{K^+\to\pi^++x}$ performed by an experiment for either of the two decays can thus be used to derive a

constraint on A^0 by requiring

$$BR(B^0 \longrightarrow K^0 A^0) \;\equiv\; \frac{\Gamma(B^0 \longrightarrow K^0 A^0)}{\Gamma_{B^0}} \;\stackrel{!}{\leq}\; \mathcal{B}^{\rm EXP}_{B^0 \to K^0 + x} \,, \tag{2.9}$$

or

$$BR(K^+ \longrightarrow \pi^+ A^0) \;\equiv\; \frac{\Gamma(K^+ \longrightarrow \pi^+ A^0)}{\Gamma_{K^+}} \;\stackrel{!}{\leq}\; \mathcal{B}^{\rm EXP}_{K^+ \to \pi^+ + x} \,, \tag{2.10}$$

with $\Gamma(B^0 \to K^0 A^0)$ and $\Gamma(K^+ \longrightarrow \pi^+ A^0)$ given by Eqs. (2.7) and (2.8), respectively, and the total decay widths Γ_{B^0} and Γ_{K^+}. The quantity C_A appearing in Eq. (2.7) was calculated in Ref. [213] in the large $\tan\beta$ regime to be $C_A \sim C_{Aff} \tan\beta \, m_b \, m_t$ for order one stop mixing and sparticles at the electroweak scale. Since the full NMSSM calculation at low $\tan\beta$ is not available, we estimate the order of magnitude of the resulting limits by rescaling the large $\tan\beta$ result and taking conservatively $\tan\beta \sim \mathcal{O}(1)$.[1] The limit from a measurement of $B^0 \longrightarrow K^0 + x$ on the coupling C_{Aff} can then be derived from Eq. (2.9) with Eq. (2.7) as

$$\begin{aligned}
|C_A|^2 \;&\leq\; \mathcal{B}^{\rm EXP}_{B^0 \to K^0 + x} \, \Gamma_{B^0} \, \frac{2^{10}\pi^5}{G_F^2 \, |V_{tb} V_{ts}^*|^2 \, |f_0^{B^0}(m_{A^0}^2)|^2} \, 2 m_{B^0} \, \left(\frac{m_b}{m_{B^0}^2 - m_{K^0}^2} \right)^2 , \\
C_{Aff} \tan\beta \;&\lesssim\; \sqrt{\mathcal{B}^{\rm EXP}_{B^0 \to K^0 + x} \, \Gamma_{B^0} \, m_{B^0}} \, \frac{2^5 \pi^2 \sqrt{2\pi}}{G_F \, |V_{tb} V_{ts}^*| \, |f_0^{B^0}(m_{A^0}^2)|} \, \frac{1}{m_t (m_{B^0}^2 - m_{K^0}^2)} \,, \\
C_{Aff} \tan\beta \;&\lesssim\; 1.9 \, \sqrt{\mathcal{B}^{\rm EXP}_{B^0 \to K^0 + x}} \,,
\end{aligned} \tag{2.11}$$

where the total B^0 decay width $\Gamma_{B^0} = 4.3 \times 10^{-13}$ GeV follows from the total lifetime given in Tab. 2.1. Analogously, using $C_A' \sim C_{Aff} \tan\beta \, m_s \, m_t$ in Eq. (2.8), the limit from a measurement of $K^+ \longrightarrow \pi^+ + x$ on C_{Aff} is found with Eq. (2.10) as

$$\begin{aligned}
C_{Aff} \tan\beta \;&\lesssim\; \sqrt{\mathcal{B}^{\rm EXP}_{K^+ \to \pi^+ + x} \, \Gamma_{K^+} \, m_{K^+}} \, \frac{2^5 \pi^2 \sqrt{2\pi}}{G_F \, |V_{ts} V_{td}^*| \, |f_0^{K^+}(m_{A^0}^2)|} \, \frac{1}{m_t (m_{K^+}^2 - m_{\pi^+}^2)} \,, \\
C_{Aff} \tan\beta \;&\lesssim\; 29.7 \, \sqrt{\mathcal{B}^{\rm EXP}_{K^+ \to \pi^+ + x}} \,,
\end{aligned} \tag{2.12}$$

with the total K^+ decay width $\Gamma_{K^+} = 5.32 \times 10^{-17}$ GeV obtained from the lifetime given in Tab. 2.1.

For the limits on the coupling C_{Aff} derived from these processes, it is important to distinguish the following two classes of measurements and their different sensitivities to complementary regions of the parameter space. In the first class of meson decays, only the final-state meson is observed while the other decay products are invisible, i.e.

$$X \;\longrightarrow\; Y \;+\; \text{invisible} \,, \tag{2.13}$$

with X and Y being mesons. Experimental limits on the branching ratios of such processes can be used to exclude parts of the parameter space in which the A^0 is sufficiently

[1] Essentially, this corresponds to the Standard Model contribution with an additional coupling (2.1). The $b_R - s_L$ transition is mediated by the $W-t$ loop with A^0 coupled to the top quark.

long-lived to escape the detector and thus remains invisible to the experiment. These limits, however, break down if the decay width of the A^0 is so large that it decays inside the detector and thus does not meet the criterion of an invisible decay product. This point in the parameter space where the exclusion region from processes of the type $X \longrightarrow Y + \text{inv.}$ ends is the starting point of the second class of meson decays, namely the ones where besides the final-state meson a pair of leptons is detected, i.e.

$$X \longrightarrow Y + \ell^+\ell^- . \tag{2.14}$$

Such measurements allow to derive limits on the A^0 since they get a contribution from the production of A^0 in $X \longrightarrow Y + A^0$ followed by the decay $A^0 \longrightarrow e^+e^-$. They therefore constrain the region of the parameter space where the A^0 has a short lifetime and the above-mentioned limits fail. The two classes give thus complementary constraints.

The limits on an invisible A^0 thus apply if the decay length in the laboratory frame is larger than the dimensions of the detector, i.e. as long as the lifetime τ of A^0 fulfils $\tau\gamma > d$ or equivalently the total decay width Γ_{A^0} meets the requirement $\Gamma_{A^0} < E_{A^0}/m_{A^0}d$ with Γ_{A^0} given by Eq. (2.2), γ being the boost factor, d the size of the detector (~ 10 m) and E_{A^0} the energy with which the A^0 is produced. As described above, the opposite of this requirement, i.e. $\Gamma_{A^0} > E_{A^0}/m_{A^0}d$, determines the lower bound of the constraints on a visible A^0. In a two-body decay $X \longrightarrow Y + A^0$, the energy of the A^0 decay product is given by

$$E_{A^0} = \frac{m_X^2 - m_Y^2 + m_{A^0}^2}{2m_X} , \tag{2.15}$$

where in the relevant cases $m_X^2 \gg m_Y^2, m_{A^0}^2$. Thus, the requirement for the first (second) class of measurements to be applicable, i.e. the upper (lower) reach of the limits on an invisible (visible) A^0 is then given by

$$\Gamma_{A^0} \quad \begin{matrix} < \\ (>) \end{matrix} \quad \frac{m_X^2 - m_Y^2 + m_{A^0}^2}{2m_X m_{A^0}\, d} , \tag{2.16}$$

which we refer to in the following as the invisibility- (visibility-) condition.

An estimate of this transition region between the applicability of the two different measurements can be obtained in the two mass ranges $m_{A^0} < 2m_e$ and $m_{A^0} \gtrsim 2m_e$. For the former, where the A^0 can only decay into two photons, the invisibility-condition Eq. (2.16) then translates with the decay width $\Gamma_{A^0\to\gamma\gamma}$ of Eq. (2.4) to an upper reach

$$m_{A^0}^4\, C_{Aff}^2 \lesssim \frac{4\sqrt{2}\pi^3 m_X}{G_F\alpha^2 d} \left| \sum_\ell k_\ell F(k_\ell) + \sum_d \frac{1}{3} k_d F(k_d) + \sum_u \frac{4}{3\tan\beta^2} k_u F(k_u) \right|^{-2} ,$$

where the sums run over leptons, down- and up-type quarks with $C_{Aii} = C_{Aff}$ for the first two and $C_{Aii} = C_{Aff}/\tan^2\beta$ for the latter. For a detector of size $d \sim 10$ m and $\tan\beta \sim 1$, the upper reach of the limits from measurements of the type $X \longrightarrow Y + \text{inv.}$

becomes roughly

$$m_{A^0}\sqrt{C_{Aff}} \lesssim 25\text{ MeV} \times \sqrt[4]{\frac{m_X}{\text{GeV}}} \qquad \text{for } m_{A^0} < 2m_e\,. \tag{2.17}$$

Above the threshold for the decay into an electron-positron pair, i.e. $m_{A^0} \gtrsim 2m_e$, this limit changes and an estimate can be derived from $\Gamma_{A^0} \sim \Gamma_{A^0\to e^+e^-}$ with Eq. (2.3) as

$$m_{A^0}^2\, C_{Aff}^2 \lesssim \frac{2\sqrt{2}\pi m_X}{G_F m_e^2 d}\left(1-4\frac{m_e^2}{m_{A^0}^2}\right)^{-\frac{1}{2}}.$$

Assuming again $d \sim 10$ m, the upper reach of the limits from measurements of the type $X \longrightarrow Y + \text{inv.}$ is then given by

$$m_{A^0}\, C_{Aff} \lesssim 8\text{ MeV} \times \sqrt{\frac{m_X}{\text{GeV}}} \qquad \text{for } m_{A^0} \gtrsim 2m_e\,. \tag{2.18}$$

Thus, the constraints arising from measurements of decays in which the A^0 is invisible in the detector have an upper limitation given by Eqs. (2.17) and (2.18) in the mass ranges $m_{A^0} < 2m_e$ and $m_{A^0} \gtrsim 2m_e$, respectively. Because of the different dependence of both equations on m_{A^0} and C_{Aff}, this upper limit is expected to show a different behaviour in the mass ranges below and above the threshold for the decay into e^+e^-. When shown in a log-log plot of C_{Aff} versus m_{A^0}, the limitation in the lower mass range exhibits a slope of -2 due to the invisibility-condition (2.17). For higher masses on the contrary, Eq. (2.18) leads to a slope of -1. In both cases, the dependence of the upper limitation of these constraints on the detector size is only square-root.

Parameters		Particle	Mass [GeV]
G_F	$\sqrt{2}g_2^2/(8m_W^2)$	m_{B^0}	5.27955
V_{td}	8.4×10^{-3}	$m_{B^\pm}$	5.27925
V_{ts}	42.9×10^{-3}	m_{K^0}	0.493677
V_{tb}	0.89	$m_{K^\pm}$	0.493677
f_π	0.093 [GeV]	m_{π^0}	0.1349766
τ_{B^0}	1.519×10^{-12} [s]	$m_{\pi^\pm}$	0.13957
$\tau_{B^\pm}$	1.641×10^{-12} [s]	$m_{\Upsilon(1S)}$	9.46030
$\tau_{K^\pm}$	1.238×10^{-8} [s]	$m_{\Upsilon(3S)}$	10.3552

Table 2.1: Parameters, particle masses and lifetimes from [4] used for the numerical results in this chapter.

2.2 Constraints from precision measurements

In this section, limits on the mass m_{A^0} and the coupling C_{Aff} of the CP-odd Higgs arising from meson decays as well as from the muon anomalous magnetic moment will be presented. As mentioned above, the A^0 can be produced in various meson decays and constraints can be derived from measurements of branching ratios for the two cases where the A^0 is invisible or visible through its decay into e^+e^-. Further bounds arise from the rare pion decay $\pi^0 \longrightarrow e^+e^-$ which occurs in the Standard Model only at the loop-level and receives a tree-level contribution of the A^0 and from the muon anomalous magnetic moment to which the A^0 contributes at the loop-level.

2.2.1 Rare B-decay B $\longrightarrow$ K + invisible

Limits on the production of A^0 in different rare B-meson decays [220–223] can be derived from measurements of the branching ratios

$$\begin{aligned} \mathcal{B}^{\text{CLEO}}(B^0 \longrightarrow K_S^0 + \text{invisible}) &< 5.3 \times 10^{-5} \,, \\ \mathcal{B}^{\text{BaBar}}(B^- \longrightarrow K^- \nu\bar{\nu}) &< 7.0 \times 10^{-5} \,, \end{aligned} \tag{2.19}$$

performed by CLEO [224] and BaBar [225], respectively. In the following, we will use the more constraining CLEO result, which with Eq. (2.11) gives $C_{Aff} < 0.02/\tan\beta$. Thus, taking conservatively $\tan\beta \sim \mathcal{O}(1)$, we find that the CLEO measurement requires that

$$C_{Aff} \;<\; 10^{-2} \,, \tag{2.20}$$

while values of C_{Aff} larger than 10^{-2} are excluded. This constraint is already strong at small $\tan\beta$ and gets even stronger at large $\tan\beta$. Since the experiments only detect the final-state meson while the other decay products are invisible, the A^0 has to remain invisible and the obtained bound of Eq. (2.20) is only applicable as long as A^0 is sufficiently long-lived to decay outside of the detector. According to the invisibility-condition Eq. (2.16) and the estimates Eqs. (2.17) and (2.18) with $m_X = m_{B^0} = 5.28$ GeV the limit is valid up to

$$\begin{aligned} m_{A^0}\sqrt{C_{Aff}} &\lesssim 37 \text{ MeV} \quad \text{for } m_{A^0} < 2m_e \,, \\ m_{A^0}\, C_{Aff} &\lesssim 18 \text{ MeV} \quad \text{for } m_{A^0} \gtrsim 2m_e \,, \end{aligned} \tag{2.21}$$

beyond which the A^0 becomes visible in the detector.

The resulting exclusion region based on the CLEO measurement (2.19) is plotted in Fig. 2.2 in brown and marked "$B^0 \longrightarrow K^0 + \text{inv.}$". Note that, in contrast to the lower boundary, the upper boundary of the exclusion contour is calculated quite reliably from Eq. (2.16) and is essentially independent of $\tan\beta$. In the plot, we use the full A^0-width Γ_{A^0} given by Eq. (2.2) in the determination of this upper boundary without restricting

to the approximation $\Gamma_{A^0} \sim \Gamma_{e^+e^-}$ for $m_{A^0} \gtrsim 2m_e$ as done in the estimate in Eq. (2.21). The kink in this upper line at $m_{A^0} \approx 2m_e$ is due to the rapid drop in the decay width as m_{A^0} falls below the threshold for the decay into e^+e^-. The smaller decay width causes an increase in the A^0 lifetime and thus the invisibility-condition is applicable up to larger values of the coupling C_{Aff}.

2.2.2 Rare K-decay $\mathbf{K \longrightarrow \pi +}$ invisible

Similarly to the process and constraint considered in Sec. 2.2.1, a light invisible A^0 can also be produced in K-decays. The corresponding branching ratio has been measured by E787 [226, 227] and E949 [228] to be[2]

$$\begin{aligned} \mathcal{B}^{\mathrm{E787}}(K^+ \longrightarrow \pi^+ + \text{invisible}) &< 4.5 \times 10^{-11}\,, \\ \mathcal{B}^{\mathrm{E949}}(K^+ \longrightarrow \pi^+ + \text{invisible}) &< 10^{-10}\,. \end{aligned} \tag{2.22}$$

Using the tighter E787 result, the limit can then be obtained from Eq. (2.12) as $C_{Aff} < 2 \times 10^{-4}/\tan\beta$. For $\tan\beta \sim \mathcal{O}(1)$, the E787 measurement thus demands that

$$C_{Aff} \;<\; 10^{-4}\,. \tag{2.23}$$

As in the previous section, the A^0 has to be invisible for these measurements to be applicable. Therefore, the upper reach of this constraint is again determined by the invisibility-condition Eq. (2.16). For $m_X = m_{K^+} = 494$ MeV, it can be estimated with Eqs. (2.17) and (2.18) that the limit is valid up to

$$\begin{aligned} m_{A^0}\sqrt{C_{Aff}} &\lesssim 21 \text{ MeV} \quad \text{for } m_{A^0} < 2m_e\,, \\ m_{A^0}\, C_{Aff} &\lesssim 5 \text{ MeV} \quad \text{for } m_{A^0} > 2m_e\,. \end{aligned} \tag{2.24}$$

In Fig. 2.2, this limit is shown as green shaded region, labelled "$K^+ \longrightarrow \pi^+ + \text{inv.}$". As in the B-decays discussed in Sec. 2.2.1, the lower boundary of the exclusion contour only gets stronger with increasing $\tan\beta$ and its precise value is not important for us. Furthermore, its upper boundary caused by the invisibility-requirement shows a similar behaviour as the one of "$B^0 \longrightarrow K^0 + \text{inv.}$".

2.2.3 Rare decays $\mathbf{B \longrightarrow K\ e^+e^-}$ and $\mathbf{K \longrightarrow \pi\ e^+e^-}$

In contrast to the cases of an invisible A^0 studied in the previous two sections, A^0 contributes to the processes $B \longrightarrow K\, e^+e^-$ and $K \longrightarrow \pi\, e^+e^-$ if it decays inside the detector. As discussed in Sec. 2.1.2, measurements of those decays can thus be used to constrain the A^0 in the region of the parameter space where the earlier limits fail, namely

[2] Note that these measured bounds become significantly weaker at the pion pole, $m_{A^0} = m_\pi$.

at high couplings where the decay width is large and the lifetime is short. However, in the experiments considered in this section, a cut on the invariant mass $m_{\ell^+\ell^-} > 140$ MeV of the lepton pair (i.e. the absolute value of the sum of the impulses of the outgoing leptons) is adopted in order to suppress backgrounds like conversion of photons and $\pi^0 \longrightarrow e^+e^-\gamma$. Therefore, the resulting bounds only apply to masses $m_{A^0} > 140$ MeV. The BELLE experiment reported in [229] their finding of

$$\mathcal{B}^{\text{BELLE}}(B \longrightarrow K\ \ell^+\ell^-) \ \simeq\ 4.8 \times 10^{-7}\,, \tag{2.25}$$

where ℓ includes muons and electrons with $m_{\ell^+\ell^-} > 140$ MeV. Assuming lepton universality, we will use a conservative bound on the branching ratio into electrons $\text{BR}(B \to KA^0 \to K\ e^+e^-) < 2.4 \times 10^{-7}$ in our analysis. The resulting constraint from the BELLE measurement on the A^0 under the assumption that

$$\text{BR}(B \longrightarrow KA^0 \longrightarrow K\ e^+e^-) \ \simeq\ \text{BR}(B \longrightarrow K\ A^0) \times \text{BR}(A^0 \longrightarrow e^+e^-)\,, \tag{2.26}$$

follows then similarly to Eq. (2.11) as

$$C_{Aff} \tan\beta \ \lesssim\ 1.9 \sqrt{\frac{\mathcal{B}^{\text{EXP}}_{B^0 \to K^0 + \ell^+\ell^-}}{\text{BR}_{A^0 \to e^+e^-}}}\,. \tag{2.27}$$

For $\tan\beta \sim 1$, the branching ratio $\text{BR}(A^0 \longrightarrow e^+e^-)$ is about $20 - 40\%$ in the relevant mass range so that the limit requires that $C_{Aff} < 2 \times 10^{-3}$.

However, at such small couplings, the decay length of A^0 is much larger ($\sim \mathcal{O}(\text{km})$) than the size of the detector, so that the A^0 is invisible and would not appear in the measured process. Therefore, the limit can only be applied at larger couplings once the A^0 decays inside the detector. Applying the visibility-condition of Eq. (2.16), we get a reduced requirement of

$$C_{Aff} \ <\ 8 \times 10^{-2}\,, \tag{2.28}$$

which excludes the thin stripe 140 MeV $< m_{A^0} < 2m_\mu$ shown in Fig. 2.2 in cyan and labelled "$B \longrightarrow Ke^+e^-$". Note that here Eq. (2.17) gives a better estimate than Eq. (2.18) since for this mass range the decay channel into $\gamma\gamma$ is the dominant one. In the plotted exclusion curves, we always use the exact result with the full decay width.

Similarly, the same region of the parameter space for a visible A^0 can be constrained by another process which was measured by the NA48/2 experiment at CERN in different K-decays [230] as

$$\mathcal{B}^{\text{NA48/2}}(K^\pm \longrightarrow \pi^\pm\ e^+e^-) \ \simeq\ 3.11 \times 10^{-7}\,, \tag{2.29}$$

where also the same kinematic cut $m_{e^+e^-} > 140$ MeV is employed. Using Eq. (2.12) and an analogue of Eq. (2.26), we find that this measurement requires

$$C_{Aff} \;<\; 3 \times 10^{-2}\,. \tag{2.30}$$

Since the visibility-condition Eq. (2.16) demands that $C_{Aff} > 2 \times 10^{-2}$ for A^0 to be visible in the detector, this constraint can be applied without restrictions. It is plotted in pink in Fig. 2.2 and marked "$K \longrightarrow \pi e^+e^-$".

It is noteworthy that the window 140 MeV $< m_{A^0} < 2m_\mu$ is eliminated simultaneously by the limits obtained from the two different processes presented in this section. There are additional NMSSM contributions to $B \longrightarrow K\ e^+e^-$ and $K \longrightarrow \pi\ e^+e^-$ apart from the one of A^0 which could, in principle, lead to cancellations. However, considering two independent processes makes this possibility less likely and this window can be excluded.

There is another measurement of BR($B \longrightarrow K\ \ell^+\ell^-$) performed by BaBar [231] which is sensitive to lower A^0 masses since it imposes a lower kinematic cut of $m_{e^+e^-} >$ 30 MeV. Because of the larger low-energy backgrounds caused by this lower cut, their result loses somewhat in efficiency [213] and was reported as

$$\mathcal{B}^{\text{BaBar}}(B \longrightarrow K\ \ell^+\ell^-) \;\simeq\; 0.34 \times 10^{-6}. \tag{2.31}$$

According to Eq. (2.27), this would lead to a constraint of $C_{Aff} < 1.3 \times 10^{-3}$ which is, however, again in the region where A^0 is invisible. Therefore, in order for A^0 to decay inside the detector, the limit is determined by the visibility-condition Eq. (2.16) and excludes for $m_{A^0} > 30$ MeV the region with $C_{Aff} \gtrsim 10^{-1} - 10^{0}$ depending on the A^0 mass. The exact shape of the limit is drawn in red in Fig. 2.2 and labelled "$B \longrightarrow Ke^+e^-$". Although one may question the reliability of this result at low e^+e^- invariant masses, another experiment, to be discussed in the next subsection, excludes a similar region of parameter space.

2.2.4 Rare K-decay $\mathbf{K \longrightarrow \pi + X}$

A byproduct of the $K_{\mu 2}$ experiment at KEK in Japan originally looking for heavy neutrinos was a measurement of the 2-body decay $K^+ \longrightarrow \pi^+ + X$, where X is any particle [232]. The analysis was performed searching for a peak in the π^+ momentum for 10 MeV $< m_X <$ 300 MeV. The resulting bound was found as

$$\mathcal{B}^{K_{\mu 2}}(K^+ \longrightarrow \pi^+ + X) \;<\; 10^{-6}\,, \tag{2.32}$$

at 90% C.L. for the mass range $m_X < 60$ MeV and relaxes for larger m_X to 10^{-5} at $m_X \sim 120$ MeV.

The exclusion limit on C_{Aff} obtained with Eq. (2.12) is plotted in black in Fig. 2.2 and marked "$K^+ \longrightarrow \pi^+ X$". The constraint amounts approximately to the requirement that

$$C_{Aff} \;<\; 4 \times 10^{-2}\,, \tag{2.33}$$

for masses $m_{A^0} > 10$ MeV.

Note that for masses close to the pion mass $m_{A^0} \simeq m_{\pi^0}$ the limit (2.33) becomes weaker. However, this region is constrained by $\pi^0 \longrightarrow e^+e^-$, as discussed in Sec. 2.2.6. Additionally, it is disfavoured by the $\pi^+ - \pi^0$ mass difference which would be affected in the presence of an A^0 due to the shift in the π^0 mass when $\pi^0 - A^0$ mixing is taken into account. Furthermore, a similar region of the parameter space up to $m_{A^0} = 100$ MeV is excluded by the process $\pi^+ \longrightarrow e^+\nu\, A^0$ with the subsequent decay $A^0 \longrightarrow e^+e^-$ [233] (for applications to axion models, see [234]).

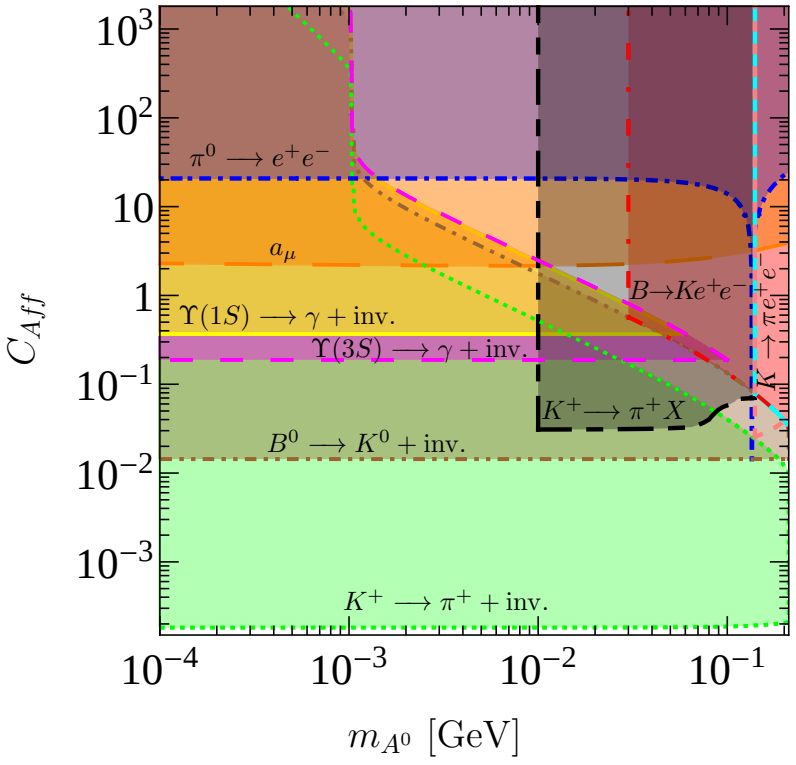

Figure 2.2: Constraints from various precision measurements on the mass m_{A^0} of the light NMSSM CP-odd Higgs A^0 and its coupling to fermions C_{Aff}. Limits arise from different meson decays in which the A^0 either is sufficiently long-lived to be invisible in the detector or appears via its decay into e^+e^-, from the tree-level contribution of the A^0 to the rare pion decay $\pi^0 \longrightarrow e^+e^-$ and from the loop-level contribution of the A^0 to the muon anomalous magnetic moment a_μ. The coloured regions are excluded. All bounds include the effect of varying BR($A^0 \longrightarrow e^+e^-$) with m_{A^0}.

2.2.5 Radiative Upsilon-decays $\Upsilon \longrightarrow \gamma$ + invisible

Further bounds arise from the production of A^0 in radiative Υ-decays, where the relevant measurements

$$\mathcal{B}^{\text{BABAR}}(\Upsilon(1S) \longrightarrow \gamma + \text{invisible}) \;<\; 1.3 \times 10^{-5}, \tag{2.34}$$

$$\mathcal{B}^{\text{BABAR}}(\Upsilon(3S) \longrightarrow \gamma + \text{invisible}) \;<\; 3 \times 10^{-6}, \tag{2.35}$$

have been performed by CLEO [235] and BABAR [236,237], respectively. The branching ratio for the process $\Upsilon \longrightarrow \gamma A^0$ is given in [213, 238, 239] as

$$\text{BR}(\Upsilon \longrightarrow \gamma A^0) \;=\; \mathcal{B}_{\Upsilon\to\mu^+\mu^-}\, \frac{G_F m_b^2}{\sqrt{2}\pi\alpha}\, C_{Aff}^2 \left(1 - \frac{m_{A^0}^2}{m_\Upsilon^2}\right) F_{\text{QCD}}\,, \tag{2.36}$$

where $F_{\text{QCD}} \sim 0.5$ is a factor taking into account QCD corrections and the branching ratios into muons are given in [4] as $\mathcal{B}_{\Upsilon(1S)\to\mu^+\mu^-} \simeq 0.025$ and $\mathcal{B}_{\Upsilon(3S)\to\mu^+\mu^-} \simeq 0.022$. Demanding that the branching ratio into γA^0 does not exceed the values measured in the experiments, the constraint on the coupling follows from expression (2.36) as

$$C_{Aff}^2 \;<\; \frac{\mathcal{B}^{\text{EXP}}(\Upsilon \longrightarrow \gamma + \text{invisible})}{\mathcal{B}_{\Upsilon\to\mu^+\mu^-}}\, \frac{\sqrt{2}\pi\alpha}{G_F m_b^2 F_{\text{QCD}}} \left(1 - \frac{m_{A^0}^2}{m_\Upsilon^2}\right)^{-1}, \tag{2.37}$$

and leads to the requirements

$$\begin{aligned} C_{Aff} \;&<\; 0.37 \quad (\text{CLEO})\,, \\ C_{Aff} \;&<\; 0.19 \quad (\text{BABAR})\,, \end{aligned} \tag{2.38}$$

which are independent of $\tan\beta$. In Fig. 2.2, the former is shown in yellow and marked as "$\Upsilon(1S) \longrightarrow \gamma + \text{inv.}$" and the latter in magenta labelled "$\Upsilon(3S) \longrightarrow \gamma + \text{inv.}$".

Since both experiments do not detect any final-state particles else than the photon, the measurements apply only if the A^0 decays outside the detector. The invisibility-conditions Eqs. (2.17) and (2.18) give for $m_X = m_{\Upsilon(3S)} = 10.4$ GeV an estimate of the upper reach of the obtained BABAR limit as

$$\begin{aligned} m_{A^0}\sqrt{C_{Aff}} \;&\lesssim\; 44 \text{ MeV} \quad \text{for } m_{A^0} < 2m_e\,, \\ m_{A^0}\, C_{Aff} \;&\lesssim\; 25 \text{ MeV} \quad \text{for } m_{A^0} \gtrsim 2m_e\,, \end{aligned} \tag{2.39}$$

which is roughly the same for the CLEO limit, where $m_X = m_{\Upsilon(1S)} = 9.5$ GeV.

2.2.6 Pion decay $\pi^0 \longrightarrow e^+e^-$

A light A^0 provides a pseudoscalar decay channel for the rare pion decay into e^+e^- as shown in the left diagram of Fig. 2.3 (see, e.g. [240]). This chirality-suppressed decay

proceeds in the Standard Model only through a loop diagram with a $\pi^0\gamma^*\gamma^*$ vertex as shown in Fig. 2.3 on the right and has a very small branching ratio. The recent KTeV measurement of this process [241] as

$$\mathcal{B}^{\text{KTeV}}(\pi^0 \longrightarrow e^+e^-) \;\simeq\; 7.48 \times 10^{-8} \tag{2.40}$$

is somewhat (3σ) above the Standard Model prediction [242,243]. To be conservative in deriving a constraint on the A^0, we require that the tree-level contribution from A^0 does not exceed the central experimental value, thus $\mathcal{B}(\pi^0 \longrightarrow A^0 \longrightarrow e^+e^-) < 7.5 \times 10^{-8}$.

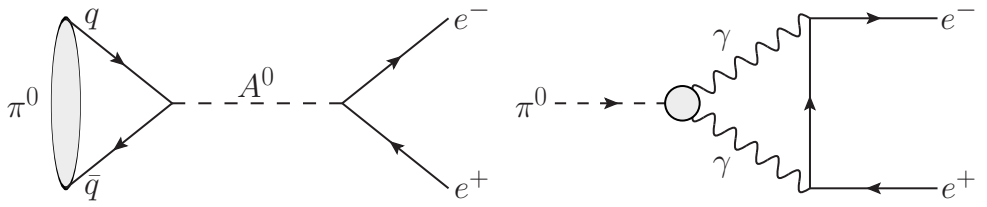

Figure 2.3: Feynman diagrams for the rare pion decay $\pi^0 \longrightarrow e^+e^-$.
Left: Tree-level contribution from the CP-odd Higgs A^0 in the NMSSM.
Right: Loop-level contribution in the Standard Model.

For the decay width in the NMSSM, we find

$$\Gamma(\pi^0 \longrightarrow A^0 \longrightarrow e^+e^-) \quad \simeq \quad \frac{G_F^2}{4\pi} \, \frac{m_e^2 m_\pi^5 f_\pi^2}{|m_\pi^2 - m_{A^0}^2 + i\Gamma_{A^0} m_{A^0}|^2} \, C_{Aff}^4 \;, \tag{2.41}$$

where the up-quark contribution is neglected and $\langle 0|m_d \bar{d}\gamma^5 d|\pi^0\rangle \simeq -im_\pi^2 f_\pi$ is assumed.[3] The total decay width Γ_{A^0} of the A^0 is given by Eq. (2.2), the pion mass is $m_\pi = 135$ MeV and the pion decay constant $f_\pi = 93$ MeV [244]. We neglect the $\pi^0 - A^0$ mixing effects which are of order $\delta m^2/m_\pi^2 \sim f_\pi/M_W \sim 10^{-3}$ and relevant only very close to the pion mass.

The total width of the π^0 is given by [244]

$$\Gamma(\pi^0 \longrightarrow \gamma\gamma) \;=\; \frac{\alpha^2}{64\pi^3} \, \frac{m_\pi^3}{f_\pi^2} \;, \tag{2.42}$$

so that the limit on C_{Aff} follows as

$$C_{Aff}^4 \;<\; \mathcal{B}(\pi^0 \longrightarrow A^0 \longrightarrow e^+e^-) \, \frac{\alpha^2}{16\pi^2 G_F^2} \, \frac{|m_\pi^2 - m_{A^0}^2 + i\Gamma_{A^0} m_{A^0}|^2}{m_e^2 m_\pi^2 f_\pi^4} \;. \tag{2.43}$$

Therefore, the KTeV result requires

$$C_{Aff} \;<\; 20 \;, \tag{2.44}$$

[3] Our bound on C_{Aff} is not sensitive to this approximation since it scales as the square root of this matrix element.

for m_{A^0} away from the pion resonance region while the constraint becomes stronger at $m_{A^0} \simeq m_\pi$. A more precise bound including the proper m_{A^0}-dependence is shown in blue in Fig. 2.2 marked "$\pi^0 \longrightarrow e^+e^-$". This constraint is complementary to those of the $X \longrightarrow Y +$ invisible decays discussed in the previous sections, in that it excludes the parameter space above $C_{Aff} \simeq 20$ regardless of the A^0 mass. It is also a reliable tree-level constraint and essentially independent of $\tan\beta$.

2.2.7 Muon anomalous magnetic moment

The A^0 contributes at the loop-level to the anomalous magnetic moment of the muon a_μ. This quantity is well measured and calculated in the Standard Model, cf. Sec. 1.3.3. Currently, there is, however, a 3.6σ discrepancy Δa_μ between the Standard Model prediction $a_\mu^{\rm SM}$ and the measurement $a_\mu^{\rm EXP}$ preformed by E821 [164, 165] at BNL. This discrepancy is given by [4]

$$\Delta a_\mu \;=\; a_\mu^{\rm EXP} - a_\mu^{\rm SM} \;=\; (28.7 \pm 8.0) \times 10^{-10} \tag{2.45}$$

(errors combined in quadrature) and may be considered as a hint for new physics.[4]

In the NMSSM, a_μ receives significant one- and two-loop contributions $a_\mu^{\rm 1L}(A^0)$ and $a_\mu^{\rm 2L}(A^0)$ due to the CP-odd Higgs A^0. They have been computed, for example, in [246] and can be written as

$$\begin{aligned}
\delta a_\mu(A^0) \;&=\; \delta a_\mu^{\rm 1L}(A^0) + \delta a_\mu^{\rm 2L}(A^0)\,, \qquad (2.46)\\
\delta a_\mu^{\rm 1L}(A^0) \;&=\; -\frac{\sqrt{2}G_F}{8\pi^2}\; m_\mu^2\; |C_{Aff}|^2\; f_1\Big(\frac{m_{A^0}^2}{m_\mu^2}\Big)\,,\\
\delta a_\mu^{\rm 2L}(A^0) \;&=\; \frac{\sqrt{2}G_F\alpha}{8\pi^3}\; m_\mu^2\; |C_{Aff}|^2\; \left[\frac{4}{3}\frac{1}{\tan^2\beta} f_2\Big(\frac{m_t^2}{m_{A^0}^2}\Big) + \frac{1}{3} f_2\Big(\frac{m_b^2}{m_{A^0}^2}\Big) + f_2\Big(\frac{m_\tau^2}{m_{A^0}^2}\Big)\right],
\end{aligned}$$

where the functions f_1 and f_2 are defined as

$$\begin{aligned}
f_1(z) \;&=\; \int_0^1 dx \frac{x^3}{x^2 + z(1-x)}\,,\\
f_2(z) \;&=\; z\int_0^1 dx \frac{1}{x(1-x) - z} \ln\frac{x(1-x)}{z}\,. \qquad (2.47)
\end{aligned}$$

The one-loop contribution $a_\mu^{\rm 1L}(A^0)$ is negative and therefore worsens the discrepancy between the theoretical prediction and the measured value of a_μ. The two-loop contribution $a_\mu^{\rm 2L}(A^0)$, on the contrary, is positive and can resolve this discrepancy since it may be dominant for m_{A^0} above roughly 1 GeV. This does, however, not occur in the mass range we are interested in.

[4] The discrepancy of 4σ quoted in our work [41] was based on an earlier result of [245]. The updated Δa_μ does not affect the conservative constraint derived on A^0.

Since there are other NMSSM contributions of both signs to the muon anomalous magnetic moment, the contribution coming from the CP-odd Higgs A^0 can be cancelled. We therefore derive a constraint by requiring that the latter does not worsen the discrepancy beyond 5σ as

$$\delta a_\mu(A^0) \;\leq\; a_\mu^{\rm EXP} - a_\mu^{\rm SM} \;\simeq\; 40\times 10^{-10} \quad (5\sigma)\,. \tag{2.48}$$

The corresponding bound on C_{Aff} taking into account the full m_{A^0}-dependence of Eq. (2.46) is shown in orange and marked "a_μ" in Fig. 2.2 for $\tan\beta \sim 1$. It roughly demands that

$$C_{Aff} \;<\; 2\,, \tag{2.49}$$

for $m_{A^0} \lesssim m_\mu$ and weakens slightly with increasing A^0 mass. The $\tan\beta$-dependence is very mild in the region of interest since it stems only from the 2-loop contribution, which is subdominant. Once this bound is imposed, the constraint from the electron anomalous magnetic moment is satisfied automatically.

2.2.8 Other constraints

A summary of further (model-dependent) constraints is presented in Refs. [194, 213]. These are, however, weaker than the bounds derived in the previous sections and furthermore require assumptions about the NMSSM spectrum. For instance, there are contributions from all neutral Higgses to the decay $B_s \longrightarrow \mu^+\mu^-$ and the $B-\bar{B}$ mixing which allow to eliminate parts of parameter space with $C_{Aff} \gtrsim \mathcal{O}(10)$ depending on their specific masses and $\tan\beta$ [213].

There are further possible constraints from flavour physics, for example, arising from J/Ψ decays. The measurement reported by CLEO of the process $\mathcal{B}^{\rm CLEO}(J/\Psi \longrightarrow \gamma + \text{invisible}) < 4.3\times 10^{-6}$ [247] is somewhat weaker than the analogous $\Upsilon(3S)$ bound from BaBar, considered in Sec. 2.2.5. Since the A^0 coupling to up-type quarks relevant in the J/Ψ decays falls very quickly with $\tan\beta$, the potential limit is less constraining and we do not use this result in our analysis.

Another limit follows from the missing-energy process $B \longrightarrow K A^0 A^0$. Since it is driven by the hA^0A^0 coupling [248] it sets a mild constraint on the SH_1H_2 coupling in the superpotential given by $\lambda < 0.7$.

For a light CP-odd Higgs, LEP data do not impose relevant constraints. Since the A^0 couples to the Z-boson at tree-level through the $A^0 H_i^0 Z_\mu$ vertex [194], the (invisible) Z-width does not set a limit on the mass of A^0 . Electroweak oblique corrections are suppressed by the mass of the heavier pseudoscalar (see, e.g. [205]) and thus also not relevant. For the same reason, the production of A^0 at LEP through $e^+e^- \longrightarrow h\ A^0$ is suppressed. The associated production with bottom quarks $e^+e^- \longrightarrow b\bar{b}\ A^0$ is also insignificant [205]. Finally, the constraints from $Z \longrightarrow \gamma\ A^0$ are also weak [249, 250].

Further bounds from astrophysics have been summarised in Ref. [208]. They are usually relevant for pseudoscalar particles with sub-MeV masses. These are, however, in the range $10^{-4} < C_{Aff} < 10^3$ already excluded by meson decays in which an invisible A^0 due to its long lifetime appears as missing energy as shown in Fig. 2.2. An additional constraint for very small couplings $C_{Aff} < 10^{-4}$ and masses $m_{A^0} < 30$ MeV has been derived from the supernova SN1987A [208].

Altogether, the combination of various constraints presented in this section requires the CP-odd Higgs to be heavier than two muons (210 MeV) or have very small couplings $C_{Aff} < 10^{-4}$ to fermions. The derivation of this bound does not rely on the specifics of the NMSSM. It is only based on the coupling (2.1) of the A^0 to fermions at $\tan\beta \sim \mathcal{O}(1)$ and is therefore much more general. This coupling is sufficient to induce the $b - s$ and $s - d$ transitions (with a change of flavour resulting from Standard Model loops) which were used in the processes like $B \longrightarrow K\ A^0$ and $K \longrightarrow \pi\ A^0$. Similarly, Υ decays, $\pi^0 \longrightarrow e^+e^-$ and the muon anomalous magnetic moment are generated directly by the coupling to fermions given by Eq. (2.1).

For completeness, we discuss in the next section further complementary constraints arising from reactor and beam dump experiments. Those experiments were performed in the past to constrain axion models and can now be reanalysed to limits on the CP-odd Higgs as presented in the following.

2.3 Bounds from reactor and beam dump experiments

Even though the constraints derived in the previous section exclude an A^0 with a mass below 210 MeV and couplings to fermions larger than $C_{Aff} \sim 10^{-4}$, we present here additional limits that rely on a different kind of physics compared to the meson decays of Sec. 2.2. The following constraints from reactor and beam dump experiments are therefore in this sense complementary.

2.3.1 Reactor experiments

The CP-odd Higgs, like other axion-like particles, can be emitted in place of photons from excited nuclear levels. This makes nuclear reactors a source of pseudoscalar particles with masses up to 10 MeV. Therefore, the results obtained in searches for axion-like particles from nuclear power reactors carried out in the past can be used to derive constraints on the parameter space of the CP-odd Higgs. Here, we consider two representative experiments which employ the nuclear power reactors Bugey in France and Kuo-Sheng in Taiwan.

The detector used in [251] to look for axions was placed at a distance of 18.5 m from the Bugey reactor core. The experiment searched for the decays $a \longrightarrow e^+e^-$ of an axion-like particle a into an electron-positron pair. Since no excess of e^+e^- events has been observed, a constraint on the axion decay constant f_a was derived for axion masses above the two-electron threshold $2m_e$ and below ~ 9.5 MeV. The corresponding exclusion region for the CP-odd Higgs can be read off from Fig. 5 of [251] using the conversion

$$C_{Aff} \;=\; \frac{1}{f_a}\,\frac{2m_W}{g_2}\,, \tag{2.50}$$

from the coupling f_a of an axion to fermions to the coupling C_{Aff} of the A^0. The resulting limit on the A^0 covers the range $10^{-3} \lesssim C_{Aff} \lesssim \mathrm{O}(1)$ for masses $2m_e \leq m_{A^0} \lesssim 9.5$ MeV and is shown in Fig. 2.4 in red.

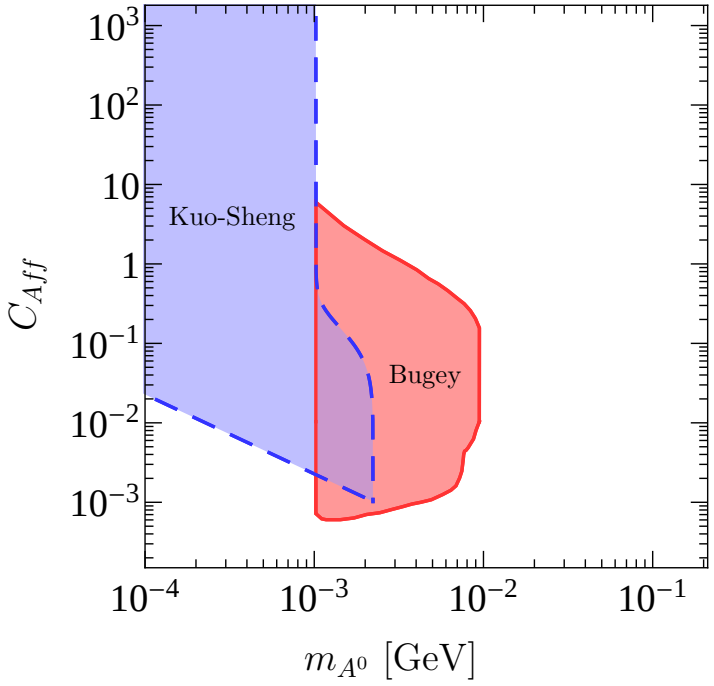

Figure 2.4: Constraints on the mass m_{A^0} of the light NMSSM CP-odd Higgs A^0 and its coupling C_{Aff} to fermions from the nuclear power reactors Bugey (France) and Kuo-Sheng (Taiwan).

Another experiment performed at the Kuo-Sheng nuclear reactor searched for axions via Compton conversion on electrons [252]. For this purpose, a Germanium detector was placed 28 m away from the reactor to measure the ionization energy resulting from the axion-photon conversion in the detector. This experiment also did not observe a signal and placed a limit on the axion's coupling to electrons for masses from $\mathcal{O}$(eV) up to $\mathcal{O}$(MeV). The exclusion region can be read off from Fig. 7 of [252] and their Eq. (31), which limits $g_{aee}\, g^1_{aNN} < 1.3 \times 10^{-10}$ for axion masses below ~ 1 MeV. Using $g_{aee} = C_{Aff}\, g_2\, m_e/(2m_W)$ and $g^1_{aNN} = 3 \times 10^{-8} m_{A^0}/\mathrm{eV}$, this translates into a bound

for the A^0 given by

$$m_{A^0}\, C_{Aff} \;<\; 2 \times 10^{-3}\ \text{MeV}, \tag{2.51}$$

for $m_{A^0} < 2m_e$. This corresponds to the blue exclusion region at $m_{A^0} < 2m_e$ shown in Fig. 2.4. The experiment has also some sensitivity to somewhat higher masses since an A^0 can be produced like an axion in the neutron capture process $pn \longrightarrow d\gamma$ in place of the photon. The transition energy of 2.23 MeV of this process defines the highest A^0 mass that can be produced and thus limits the reach to $m_{A^0} < 2.23$ MeV. Requiring that the A^0 does not decay before it reaches the detector, an expression equivalent to the invisibility-condition Eq. (2.18) leads to a constraint of $m_{A^0} C_{Aff} < 0.3$ MeV for $m_{A^0} > 2m_e$ and $m_{A^0} < 2.23$ MeV. The resulting bulge at $m_{A^0} > 2m_e$ is also shown in blue in Fig. 2.4.

2.3.2 Beam dump experiments

Another class of constraints arises from beam dump experiments in which axion-like particles in general and the CP-odd Higgs in particular can be emitted via bremsstrahlung or Primakoff production (see, e.g. [40]). These experiments and their techniques are described in detail in Sec. 3.1 and 3.2 in the context of the hidden photon. Like the CP-odd Higgs, hidden photons can be produced in bremsstrahlung and the corresponding constraints are given in Sec. 3.3.

In brief, the basic idea of these experiments is as follows. An intense beam of particles (electrons or protons) is dumped onto a thick target which absorbs the beam and all the Standard Model background produced by the beam. However, very weakly interacting particle such as axions, the CP-odd Higgs or the hidden photon might also be produced by the beam. These exotic particles traverse the dump because of their weak interactions and can then possibly decay into Standard Model particles. These decay products are then collected by the detector which is typically placed some meters behind the target and well shielded from it.

In our analysis, we consider the following four representative examples of beam dump experiments[5] (in Sec. 3.2, additional ones and further details are given):

- E141 experiment at the Stanford Linear Accelerator Center (SLAC) in 1987 [254]: 2×10^{15} electrons at an energy of 9 GeV dumped onto a 12 cm tungsten target with a detector placed 35 m behind the target;
- E774 experiment at Fermilab in 1991 [255]: 0.52×10^{10} electrons with 275 GeV dumped onto a 30 cm target with a detector at the end of a 7.25 m long decay volume;

[5] We are not displaying the results of the electron beam dump experiment SLAC E137 [40] and the proton beam dump experiment Fermilab 605 [253] since the corresponding exclusion regions are already largely covered by the limits of the experiments displayed in Fig. 2.5.

- CHARM experiment at CERN in 1985 [256]:
  2.4×10^{18} protons at 400 GeV dumped onto a thick copper target and a detector placed in a distance of 480 m;

- Orsay experiment in France in 1989 [257]:
  2×10^{16} electrons with an energy of 1.6 GeV dumped onto a 1 m target followed by a detector in a distance of 2 m.

We derive the corresponding exclusion regions presented in Fig. 2.5 by reading off the limits on axions from the plots published in these papers and either using the conversion factor for the axion decay constant given in Eq. (2.50) or calculating the decay time according to Eq. (2.2).

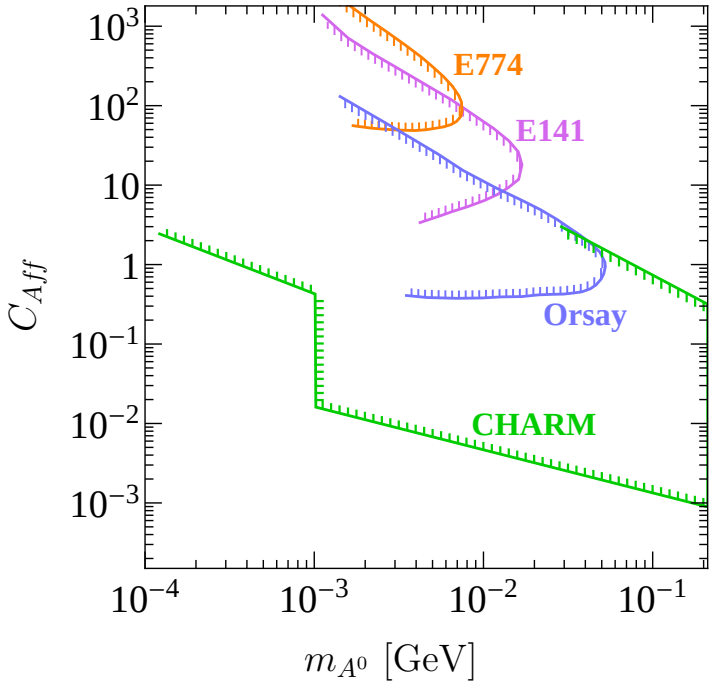

Figure 2.5: Constraints on the mass m_{A^0} of the light NMSSM CP-odd Higgs A^0 and its coupling C_{Aff} to fermions from different beam dump experiments. In the CHARM experiment (CERN), a proton beam is dumped. The other experiments E774 (Fermilab), E141 (SLAC) and Orsay (France) use an electron beam.

Altogether, this section shows that the reactor and beam dump experiments by themselves already eliminate most of the parameter space of the CP-odd Higgs, as shown in Figs. 2.4 and 2.5. Since these experiments make use of a different kind of physics compared to the limits from meson decays shown in Fig. 2.2, their bounds can be considered as complementary ones.

2.4 Summary

In this chapter, it was shown that high precision measurements and experiments exploiting high intensities are able to probe light particles even if their couplings are weak. By deriving constraints from meson decays, the muon anomalous magnetic moment and reactor as well as beam dump experiments, the CP-odd Higgs with a mass $m_{A^0} < 2m_\mu$ was found to be excluded for couplings $C_{Aff} > 10^{-4}$. Smaller couplings can hardly be achieved in the NMSSM and therefore require the A^0 to be heavier than 210 MeV. Most parts of the parameter space are even constrained by more than one experiment so that the bound is based on independent processes. As the analysis did not use specific features of the NMSSM and was performed in terms of the mass and the coupling to fermions $\{m_{A^0}, C_{Aff}\}$, the obtained results apply as well to the couplings of a light pseudoscalar particle to matter. Note that unlike meson decays, electron beam dump experiments as well as the muon anomalous magnetic moment probe directly the coupling to leptons, which could be the only coupling to matter in exotic ("leptophilic") scenarios. The electron beam dump experiments are further analysed in the next chapter in order to derive constraints on another WISP candidate, the hidden photon.

Our constraints on the light CP-odd Higgs affect the analysis which was performed in [187] and which explained the PAMELA excess in the NMSSM in the presence of a light A^0. This analysis considered a heavy neutralino as dark matter particle and masses for the A^0 ranging from a few MeV to 250 MeV. The PAMELA excess was then explained by the annihilation of the neutralino into hA^0 followed by $h \longrightarrow A^0A^0$ and subsequently $A^0 \longrightarrow e^+e^-$ or $A^0 \longrightarrow \mu^+\mu^-$. In the cases in which the decay into e^+e^- was studied, the A^0 possessed a mass below the two-muon threshold and is therefore severely constrained by our results. Our constraints are thus of importance for scenarios in which a light A^0 with $A^0 \longrightarrow e^+e^-$ is consider in order to obtain leptophilic dark matter annihilations and, for example, essentially rules out the corresponding cases in [187].

Another consequence of our findings is that the decay channel of the CP-odd Higgs into $\mu^+\mu^-$ is open since we showed that the A^0 is heavier than twice the muon mass. This implies that the CP-odd Higgs can be searched for at the LHC through the decay into $\mu^+\mu^-$, see, e.g. [258–260]. This decay of the A^0 into $\mu^+\mu^-$ further allows the lightest NMSSM CP-even Higgs h to be probed by searching for four muons via the decay $h \longrightarrow 2A^0 \longrightarrow 4\mu$ [261, 262] or, in the case of an even heavier A^0, for 4τ [263].

Chapter 3

Constraints on Hidden Photons

Hidden sectors with light extra U(1) gauge bosons, so-called hidden photons, are well motivated, as discussed in Chapter 1. They arise naturally in various Standard Model extensions like supersymmetry or string theory. MeV- to GeV-scale hidden photons are phenomenologically of interest as they exhibit features which are desirable in the context of dark matter, especially in view of recent astrophysical observations, as discussed in Chapter 4. In addition, an MeV-scale hidden photon might explain the long-standing discrepancy observed in the muon anomalous magnetic moment. Similar to the CP-odd Higgs studied in Chapter 2, a light hidden photon could have escaped detection until now due to its weak interactions and thus presents another example of a WISP.

As explained in Sec. 1.3, the kinetic mixing of the hidden photon with the ordinary photon gives rise to a coupling of the hidden photon to the electromagnetic current of the Standard Model. The coupling strength of this interaction is reduced by the size of the kinetic mixing χ with respect to the electromagnetic one and a QED-like vertex $i\chi eQ\gamma^\mu$ arises (cf. also Appendix A). Experiments can then search for the hidden photon via its interaction with charged fermions.

In this chapter, we study the possibility to probe hidden photons at electron beam dump experiments and present the constraints obtained from this analysis. In these experiments, the hidden photon can be produced in a process similar to ordinary bremsstrahlung off an initial electron beam. It can traverse the dump and then be observed through its decay into charged leptons. In the following analysis, we assume that there are no other particles in the hidden sector which are charged under the extra U(1) and lighter than the hidden photon, so that the hidden photon can only decay into Standard Model particles. In Sec. 3.1, we examine these processes and summarise the most important formulae and computational steps needed to derive the number of events expected in an experiment from the decay of the hidden photon (more details are given in Appendix B). We further show how the corresponding exclusion contour arises and how it depends on the specifics of the experimental set-up. The different experiments under consideration are then introduced in Sec. 3.2. There, we also discuss in detail the

determination of the experimental acceptances from the use of Monte Carlo simulations. The resulting constraints from the analysed electron beam dump experiments are then presented in Sec. 3.3. An up-to-date overview of all current limits on hidden photons and a summary of future searches are given in Secs. 3.4 and 3.5.

Our analysis includes two new limits from experiments at the High Energy Accelerator Research Organization in Japan (KEK) and the Laboratoire de l'accelérateur linéaire (LAL, Orsay) which were not considered before. An additional innovation is that all our constraints take into account the experimental acceptances obtained from Monte Carlo simulations. These results were done in collaboration with Carsten Niebuhr and Andreas Ringwald and are published in [42].

3.1 Principles of hidden photons in electron fixed-target experiments

Hidden photons with masses in the MeV to GeV range can be tested and constrained by experiments through their interaction with charged Standard Model particles. As described in Sec. 1.3.2, the coupling of the hidden photon to the electromagnetic current arises from the kinetic mixing of the hidden photon with the ordinary photon and is given by a QED-like vertex $i\chi eQ\gamma^\mu$ (cf. also Appendix A). Among possible experimental searches, electron beam dump experiments are particularly well suited for kinetic mixing values $\chi \lesssim 10^{-3}$. In these experiments, the basic idea is that hidden photons are emitted from an electron beam incident on a target and are then observed in a detector behind the dump through their decay into, e.g. e^+e^-, as sketched in Fig. 3.1. The emission process is similar to bremsstrahlung of ordinary photons as illustrated in the left-hand diagram of Fig. 3.2.

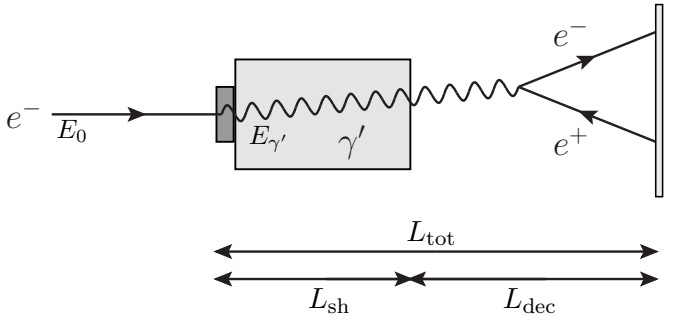

Figure 3.1: Sketch of the set-up of an electron beam dump experiment. An incident electron beam of energy E_0 hits the target and produces a hidden photon γ' with energy $E_{\gamma'}$ in bremsstrahlung. The hidden photon traverses the shield and can be observed in the detector via its decay, e.g. into e^+e^-. The definitions of the lengths L_{sh}, L_{dec} and L_{tot} used in the text are illustrated in the set-up.

In the range of low masses and small kinetic mixing, where the hidden photon production rates are low, searches at fixed-target experiments are better suited than those at colliders. One reason is that a fixed-target set-up can collect larger luminosities then achieved at a collider. Assuming the same beam, consisting of N_e electrons in one bunch, being either dumped onto a target or collided head-on with a second identical beam one can relate the luminosity of both respective set-ups. We roughly estimate the luminosity $\mathcal{L}^{\text{ft}}$ at the fixed-target set-up and the luminosity $\mathcal{L}^{\text{coll}}$ at a collider as

$$\mathcal{L}^{\text{ft}} \simeq N_e \frac{N_0 \rho_{\text{sh}} l_{\text{sh}}}{A} \qquad \text{versus} \qquad \mathcal{L}^{\text{coll}} \simeq \frac{N_e^2}{\mathcal{A}_{\text{b}}} , \tag{3.1}$$

where the target has density ρ_{sh}, number density n_{sh}, atomic mass A and effective shield thickness l_{sh}, while the second beam has cross-sectional area $\mathcal{A}_{\text{b}}$ and bunch length l_{b}. Thus, the luminosity at a fixed-target experiment could in principle be by a factor $(N_0 \rho_{\text{sh}} l_{\text{sh}} \mathcal{A}_{\text{b}})/(A N_e) \simeq n_{\text{sh}}/n_e \times l_{\text{sh}}/l_{\text{b}} \simeq \mathcal{O}(10^6)$ larger than at a collider. However, the actual experiments under consideration typically collect $\mathcal{O}(\text{ab}^{-1})$ per day so that the difference compared to state-of-the-art e^+e^- machines like Belle, which collects $\mathcal{O}(\text{ab}^{-1})$ per decade, is only $\mathcal{O}(10^3)$. Another advantage of fixed-target experiments over colliders arises from the cross sections for the hidden photon production processes in both cases, sketched in Fig. 3.2, which scale as

$$\sigma^{\text{ft}}_{\gamma'} \sim \frac{\alpha^3 Z^2 \chi^2}{m^2_{\gamma'}} \qquad \text{versus} \qquad \sigma^{\text{coll}}_{\gamma'} \sim \frac{\alpha^2 \chi^2}{E^2} . \tag{3.2}$$

For typical values of $\chi \simeq 10^{-4}$ and $m_{\gamma'} \simeq 50$ MeV, the cross section $\sigma^{\text{ft}}_{\gamma'}$ can be roughly $\mathcal{O}(\text{pb})$ at a fixed-target experiment with a tungsten target. It is therefore considerably larger than $\sigma^{\text{coll}}_{\gamma'}$ of $\mathcal{O}(\text{fb})$ which is achieved for the same parameters at a collider with an energy of 1 GeV.

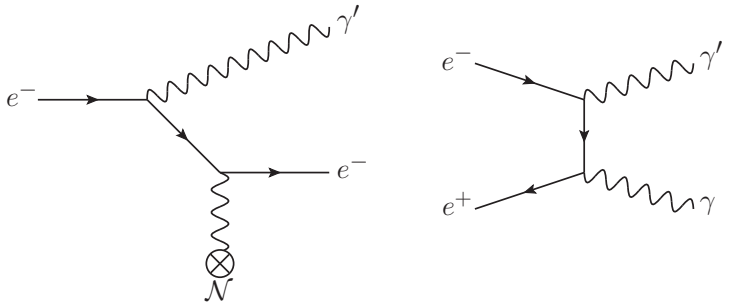

Figure 3.2: Different production processes for hidden photons.
Left: Production in bremsstrahlung off the initial electron beam at a fixed-target experiment.
Right: Production at an e^+e^- collider.

In the 1980s and early 1990s, several electron beam dump experiments have been carried out to search for light metastable pseudoscalar (axion-like) or scalar (Higgs-like) particles. In this way, it was, for example, possible to rule out an axion-like particle with

a mass of 1.8 MeV as explanation for the monoenergetic positron peak observed in heavy-ion collisions at the Gesellschaft für Schwerionenforschung (GSI) in 1983 [264]. Like hidden photons, such new particles could be produced in a process similar to ordinary bremsstrahlung, could subsequently traverse the dump and then be detected via the decay into Standard Model particles. The non-observation of the expected events had then been used to derive limits on the mass and coupling strength of such hypothetical particles [40, 254, 255, 257, 265]. The same considerations also lead to the constraints on the CP-odd Higgs derived in Sec. 2.3.2. Following a similar line of thought, the data of these experiments that were taken about two decades ago can nowadays also be reused to derive constraints on other particles like the hidden photon. This task was accomplished quite exhaustively in Ref. [266] for the past electron beam dump experiments E141 [254] and E137 [40] at SLAC as well as E774 at Fermilab [255]. In [42], we derived new constraints from two other experiments at KEK [265] and in Orsay [257] that had not been considered so far. In extension of the earlier analysis, our results include the different acceptances which we obtained with Monte Carlo simulations for each experiment depending on the specific set-up, the detector geometry and possible energy cuts. Additionally, we reanalysed the earlier limits by taking the corresponding acceptances into account.

The following subsections summarise the analytic calculations performed in order to derive the exclusion limits from electron beam dump experiments. We study the hidden photon production in the Weizsäcker–Williams approximation following the discussion of Ref. [266] and the probability for the subsequent decay into leptons. This allows to derive an estimate for the number of events expected in an electron beam dump experiment. Comparing this number with the measurement of a toy experiment illustrates how limits from beam dump experiments are obtained. The shape of the exclusion contours and their dependence on the different parameters of the set-up are discussed in detail.

3.1.1 Hidden photon production in bremsstrahlung

As mentioned above, analogous to ordinary photon bremsstrahlung, hidden photons can be produced by initial- or final-state radiation off an electron (or positron) beam incident on a fixed target. The corresponding production cross section has been calculated in [266] in the Weizsäcker–Williams approximation based on the results of [267–269] for axion bremsstrahlung. In this approximation, the target particle, i.e. a nucleus $\mathcal{N}$ in our case, which is moving with great velocity in the frame of the electron, is replaced by a flux of effective photons. This is known as the pseudophoton-flux of the Weizsäcker–Williams method. The incident electron from the beam with energy E_e can then scatter off those photons and radiate a hidden photon γ', as illustrated in Fig. 3.3. Since the photons are relatively soft, the cross section for the one-photon exchange process of the hidden photon production can be written as a product of the pseudophoton-flux and the cross

section for real photon scattering according to [266] as

$$\begin{aligned}&\frac{d\sigma_{\gamma'}(e^-(p_i)+\mathcal{N}(P_i)\to e^-(p_f)+\mathcal{N}(P_f)+\gamma'(k))}{dE_{\gamma'}\ d\cos\theta_{\gamma'}} \\ &\quad=\left(\frac{\alpha\ \xi}{\pi}\right)\left(\frac{E_e x_e}{1-x_e}\sqrt{1-\frac{m_{\gamma'}^2}{E_e^2}}\right)\left.\frac{d\sigma(e^-(p_i)+\gamma(q)\to e^-(p_f)+\gamma'(k))}{d(p_i\cdot k)}\right|_{t=t_{\min}},\end{aligned} \tag{3.3}$$

where $x_e \equiv E_{\gamma'}/E_e$ is the fraction of the incoming electron's energy carried by the hidden photon, p_i (P_i) and p_f (P_f) are the initial and final state momenta of the electron e^- (nucleus $\mathcal{N}$), $\theta_{\gamma'}$ is the labframe angle between the incident beam and the emitted hidden photon, k is the hidden photon momentum, $q = P_i - P_f$ is the photon momentum and $t \equiv -q^2$ its virtuality. Taking into account the form factors of the target, the effective photon flux ξ was originally determined for the similar case of axion bremsstrahlung and is given in [268, 269] as

$$\xi(E_e, m_{\gamma'}, Z, A) \ = \ \int_{t_{\min}}^{t_{\max}} dt\ \frac{t-t_{\min}}{t^2}\ G_2(t)\ , \tag{3.4}$$

where for small emission angles one can approximate $t_{\min} \simeq (m_{\gamma'}^2/2E_e)^2$ and $t_{\max} \simeq m_{\gamma'}^2$. According to [266], their quadratic dependence on $\theta_{\gamma'}$ can be neglected to excellent approximation. The electric form factor $G_2(t) = G_{2,\mathrm{el}}(t) + G_{2,\mathrm{in}}(t)$ consists of an elastic and an inelastic contribution [266]. The elastic one, given by

$$G_{2,\mathrm{el}}(t) \ = \ \left(\frac{a^2 t}{1+a^2 t}\right)^2\left(\frac{1}{1+t/d}\right)^2 Z^2\ , \tag{3.5}$$

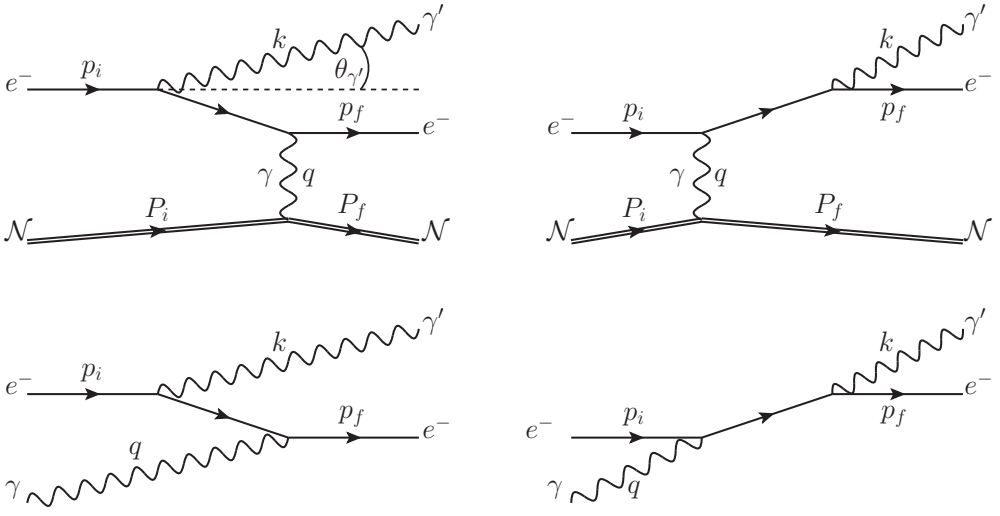

Figure 3.3: Diagrams and kinematic variables for the hidden photon production. The upper two graphs show the full process of bremsstrahlung in electron nucleon scattering. The lower two give the corresponding production in real photon scattering considered in the Weizsäcker–Williams approximation to be convoluted with the pseudophoton flux, cf. [267].

consists of an elastic atomic form factor and an elastic nuclear form factor, which describe electron screening and the finite nuclear size, respectively. For a target nucleus of atomic number Z and mass number A, the parameters are given by $a = 111\ Z^{-1/3}/m_e$ and $d = 0.164\ \text{GeV}^2\ A^{-2/3}$. The inelastic contribution parametrises the inelastic atomic and nuclear form factor as

$$G_{2,\text{in}}(t) = \left(\frac{a'^2 t}{1+a'^2 t}\right)^2 \left(\frac{1+\frac{t}{4m_p^2}(\mu_p^2-1)}{(1+\frac{t}{0.71\ \text{GeV}^2})^4}\right)^2 Z\ , \tag{3.6}$$

where $a' = 773\ Z^{-2/3}/m_e$, $\mu_p = 2.79$ and m_p is the proton mass. For the mass range of interest, the effective photon flux ξ scales roughly as Z^2 independent of $m_{\gamma'}$, as shown in Appendix B.1 and Fig. B.1.

The differential cross section for the bremsstrahlung production of hidden photons can then be estimated in the Weizsäcker–Williams approximation as

$$\begin{aligned}\frac{d\sigma_{\gamma'}}{dx_e\ d\cos\theta_{\gamma'}} &= 8\alpha^3\chi^2 E_e^2 x_e\ \xi(E_e, m_{\gamma'}, Z, A)\ \sqrt{1-\frac{m_{\gamma'}^2}{E_e^2}} \\ &\quad \left[\frac{1-x_e+\frac{x_e^2}{2}}{U^2} + \frac{(1-x_e)^2 m_{\gamma'}^4}{U^4} - \frac{(1-x_e)x_e m_{\gamma'}^2}{U^3}\right],\end{aligned} \tag{3.7}$$

where

$$U(x_e, E_e, m_{\gamma'}, \theta_{\gamma'}) = E_e^2\ x_e\ \theta_{\gamma'}^2 + m_{\gamma'}^2 \frac{1-x_e}{x_e} + m_e^2\ x_e\ , \tag{3.8}$$

is derived from the kinematics at the minimum t_{min} of the virtuality t in [266]. The function U describes the virtuality of the intermediate electron in the initial-state bremsstrahlung. The approximations leading to these results are valid for

$$m_e \ll m_{\gamma'} \ll E_e \quad \text{and} \quad x_e\theta_{\gamma'}^2 \ll 1. \tag{3.9}$$

Integrating Eq. (3.7) over the emission angle $\theta_{\gamma'}$ of the hidden photon from 0 to some maximum angle θ_{max} set by the geometry of the experiment (in all experiments under consideration it is $\theta_{\text{max}} < 0.5$ rad), we obtain

$$\frac{d\sigma_{\gamma'}}{dx_e} \simeq 4\alpha^3\chi^2\ \xi\ \sqrt{1-\frac{m_{\gamma'}^2}{E_e^2}}\ \frac{1-x_e+\frac{x_e^2}{3}}{m_{\gamma'}^2\frac{1-x_e}{x_e} + m_e^2 x_e}\ , \tag{3.10}$$

cf. also Appendix B.2 for details. Note that our result for the cross section (3.10) includes a factor 1/2 which has erroneously been omitted in the results presented in Ref. [266].

It can be seen from Eqs. (3.8) that in most of the parameter space U is dominated by the term $\propto m_{\gamma'}^2$. The production rate thus scales as $\alpha^3\chi^2 Z^2/m_{\gamma'}^2$ which is also apparent in Eq. (3.10) and already anticipated in Eq. (3.2). The produced hidden photons are highly boosted and emitted at a small angle in forward direction. This is shown in Fig. 3.4, in which the distributions of the emission angle $\theta_{\gamma'}$ in the lab-frame with respect to the

direction of the initial electron (left-hand plot) and the energy $E_{\gamma'}$ (right-hand plot) are given. Both histograms are based on data obtained from Monte Carlo simulations with MadGraph for a typical parameter point with $m_{\gamma'} = 50$ MeV and $\chi = 10^{-5}$. Because of the small emission angles, an expansion to few or even zeroth order in $\theta_{\gamma'}$ is usually a good approximation. The maximum emission angle $\theta_{\gamma' \max} \sim \max(\sqrt{m_{\gamma'} m_e}/E_0,\ m_{\gamma'}^{3/2}/E_0^{3/2})$ estimated in [266] is also smaller than the opening angle $\theta_\ell \sim m_{\gamma'}/E_0$ of the decay leptons. For those small emission angles, the production is largest when U of Eq. (3.8) is minimised. This is the case when $x_e \approx 1$, i.e. when the hidden photon carries most of the beam energy.

After being produced in the target, the hidden photons traverse potential shields due to their tiny interactions with Standard Model particles. They can then be observed in the detector through their decay back into Standard Model particles as described in the following section.

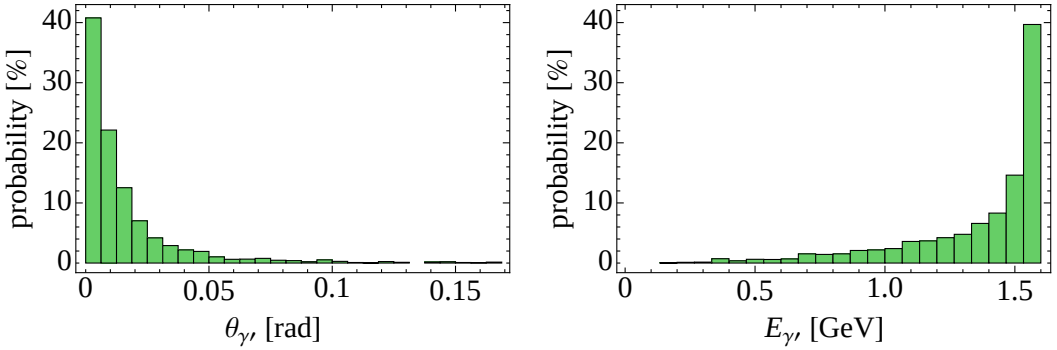

Figure 3.4: Distribution obtained from Monte Carlo simulations with MadGraph for a beam energy of 1.6 GeV and a total of 3200 hidden photons produced with a mass of 50 MeV and for a kinetic mixing value $\chi = 10^{-5}$.
Left: Hidden photon emission angle $\theta_{\gamma'}$ with respect to the beam direction in the lab-frame.
Right: Energy E_0 with which the hidden photon is emitted.

3.1.2 Hidden photon decay

The only possible decay channels of the hidden photon are those into Standard Model particles through kinetic mixing, since it is assumed throughout this chapter that there are no other particles in the hidden sector which are charged under the extra U(1) and lighter than the hidden photon. In most of the parameter space covered by electron beam dump experiments, the hidden photon mass is $m_{\gamma'} \lesssim 2m_\mu$ so that the only available decay channel is the one into e^+e^-. Above the two-muon threshold also $\gamma' \to \mu^+\mu^-$ opens and at even higher masses the decay into hadrons gets accessible. For our purpose, the total decay width $\Gamma_{\gamma'}$ is given by

$$\Gamma_{\gamma'} \ = \ \Gamma_{\gamma' \to e^+e^-} \ + \ \Gamma_{\gamma' \to \mu^+\mu^-} \left[1 + R(m_{\gamma'})\right], \tag{3.11}$$

where the second term is only present for $m_{\gamma'} \geq 2m_\mu$ and $R(\sqrt{s})$ is defined as the energy dependent ratio $\sigma(e^+e^- \to \text{hadrons}, \sqrt{s})/\sigma(e^+e^- \to \mu^+\mu^-, \sqrt{s})$ taken from Ref. [4] (see Appendix B.5 for more information). We find that the partial decay width into leptons is given by

$$\Gamma_{\gamma' \to \ell^+\ell^-} = \frac{\alpha\chi^2}{3} m_{\gamma'} \left(1 + 2\frac{m_\ell^2}{m_{\gamma'}^2}\right) \sqrt{1 - 4\frac{m_\ell^2}{m_{\gamma'}^2}} \,, \tag{3.12}$$

where m_ℓ is the mass of the lepton.

The decay length $l_{\gamma'}$ in the lab-frame, i.e. the distance after which the γ'-population is reduced by a factor e, is defined as

$$l_{\gamma'} \equiv \gamma\beta\tau_{\gamma'} = \frac{E_{\gamma'}}{m_{\gamma'}} \sqrt{1 - \frac{m_{\gamma'}^2}{E_{\gamma'}^2}} \, \frac{1}{\Gamma_{\gamma'}} \,, \tag{3.13}$$

with the mean lifetime $\tau_{\gamma'} = 1/\Gamma_{\gamma'}$ and the total decay width $\Gamma_{\gamma'}$ of Eq. (3.11). For typical values of χ and $m_{\gamma'} \lesssim 2m_\mu$ and with $\Gamma_{\gamma' \to e^+e^-}$ given by Eq. (3.12), this can be estimated as

$$l_{\gamma'} \simeq \frac{3E_{\gamma'}}{\alpha\chi^2 m_{\gamma'}^2} \simeq 8 \text{ cm} \, \frac{E_{\gamma'}}{1 \text{ GeV}} \left(\frac{10^{-4}}{\chi}\right)^2 \left(\frac{10 \text{ MeV}}{m_{\gamma'}}\right)^2 \,, \tag{3.14}$$

where $m_e \ll m_{\gamma'}$ has been used. Since the region of interest both for $m_{\gamma'}$ and χ spans several orders of magnitude, so does the decay length, ranging from $\mathcal{O}(\text{mm})$ to $\mathcal{O}(\text{km})$. In order for the decay products to be observable in an electron beam dump experiment, the hidden photon has to decay in the open decay region between the end of the shield and before or within the detector, i.e., in the area labelled L_{dec} in Fig. 3.1. Thus, comparing the hidden photon decay length with the dimensions of the set-up gives an indication for the reach of the experiments. For large values of χ and/or $m_{\gamma'}$, the decay length is much shorter than the minimum extension of the shield required to suppress the Standard Model background. The corresponding region of the parameter space is therefore not accessible with electron beam dump experiments as will be discussed in more detail below.

3.1.3 Number of expected events

In order to derive constraints on a new particle from the absence of a signal in a certain experiment, we need to determine the number of events expected if this particle was to exist. In general, the number of hidden photons produced in a fixed target experiment from N_e electrons with initial energy E_0 dumped on a target can be written as

$$N_{\gamma'} = \sigma_{\gamma'} \, N_e \, n_{\text{sh}} \, L_{\text{sh}} = \sigma_{\gamma'} \, N_e \, \frac{N_0}{A} \, \rho_{\text{sh}} \, L_{\text{sh}} \,, \tag{3.15}$$

where n_{sh}, ρ_{sh} and A are the number density, density and atomic mass of the target, respectively, L_{sh} is the length of the target plus shield, N_0 is Avogadro's number and

$\sigma_{\gamma'}$ is the cross section for hidden photon production in bremsstrahlung discussed in Sec. 3.1.1.

One has to take into account that the electrons, in passing through the target, might interact with the material. In this way, their initial energy E_0 becomes degraded before they undergo the interaction producing a hidden photon at an energy $E_e \leq E_0$. This is described by the energy distribution of the electron beam as a function of the penetration depth t measured in units of the radiation length. According to [267], the electron energy distribution can be estimated as

$$I_e(E_0, E_e, t) = \frac{1}{E_0} \frac{\left[\ln\left(\frac{E_0}{E_e}\right)\right]^{\frac{4}{3}t-1}}{\Gamma(\frac{4}{3}t)} , \tag{3.16}$$

where Γ is the Gamma function. The behaviour of I_e as a function of E_e for different values of t is discussed in Appendix B.3 and shown in Fig. B.2. Depending on whether the target is longer or much shorter than one radiation length, this expression can be simplified to the two limiting cases of a thick or a thin target experiment as

$$I_e(E_0, E_e, t) \approx \begin{cases} \frac{1}{E_0}\left(\frac{E_0 - E_e}{E_0}\right)^{\frac{4}{3}t-1} \frac{4}{3}t & t \gtrsim 1 \text{ – “thick target”} , \quad (3.17) \\ \delta(E_e - E_0) & t \ll 1 \text{ – “thin target”} . \quad (3.18) \end{cases}$$

This electron energy distribution has to be convoluted with the bremsstrahlung cross section and integrated over the length l_{sh} up to the total length L_{sh} of the target plus shield. Expressing all distances in terms of the unit radiation length X_0 as $t_{\text{sh}} = \rho_{\text{sh}} l_{\text{sh}}/X_0$ (see Appendix B.4 for details), the number of hidden photons with energy $E_{\gamma'} = x_0 E_0$ produced per incident electron can be written as

$$\frac{dN_{\gamma'}}{dx_0} = N_e \frac{N_0 X_0}{A} \int_0^{T_{\text{sh}}} dt_{\text{sh}} \int_{E_{\gamma'}+m_e}^{E_0} dE_e \; I_e(E_0, E_e, t_{\text{sh}}) \frac{E_0}{E_e} \left.\frac{d\sigma}{dx_e}\right|_{x_e = \frac{E_{\gamma'}}{E_e}} , \tag{3.19}$$

when a target of $T_{\text{sh}} \equiv \rho_{\text{sh}} L_{\text{sh}}/X_0$ radiation lengths is used.

In order to be observed in an experiment, the hidden photons must decay behind the shield and in front of, or within, the detector according to the differential decay probability

$$\frac{dP(l)}{dl} = \frac{1}{l_{\gamma'}} e^{-l/l_{\gamma'}} , \tag{3.20}$$

with the decay length $l_{\gamma'}$ defined in (3.13).

Finally, the total number of expected events from hidden photons, that are produced in the target via bremsstrahlung off the electron beam and that decay at a distance z

behind the front edge of the target, is given by

$$\frac{dN_{\gamma'}}{dx_0\, dz} = N_e \frac{N_0 X_0}{A} \int_{E_{\gamma'}+m_e}^{E_0} dE_e \int_0^{T_{\rm sh}} dt_{\rm sh} \left[I_e(E_0, E_e, t_{\rm sh})\, \frac{E_0}{E_e}\, \frac{d\sigma}{dx_e}\bigg|_{x_e=\frac{E_{\gamma'}}{E_e}} \frac{dP(z - \frac{X_0}{\rho_{\rm sh}} t_{\rm sh})}{dz} \right], \tag{3.21}$$

where N_e and E_0 are the number and energy of the incident electrons, respectively, $N_0 \simeq 6 \times 10^{23}$ mole^{-1} is Avogadro's number, $\rho_{\rm sh}$ and X_0 are the density and unit radiation length of the target, respectively. The differential cross section $d\sigma/dx_e$ is given in Eq. (3.10) (cf. also Appendix B.2 and Eq. (B.7)), the electron energy distribution $I_e(E_0, E_e, t)$ in Eq. (3.16) and the differential decay probability dP/dz in Eq. (3.20).

3.1.4 Special case: thick target beam dump experiment

For the thick target experiments we are interested in, most of the hidden photon production takes place within the first radiation length. Therefore, the dependence of the hidden photon decay probability on $t_{\rm sh}$ can be neglected and Eq. (3.21) simplifies to

$$\frac{dN_{\gamma'}}{dx_0\, dz} \simeq N_e \frac{N_0 X_0}{A} \int_{E_{\gamma'}+m_e}^{E_0} dE_e \int_0^{T_{\rm sh}} dt_{\rm sh} \left[I_e(E_0, E_e, t_{\rm sh}) \frac{E_0}{E_e}\, \frac{d\sigma}{dx_e}\bigg|_{x_e=\frac{E_{\gamma'}}{E_e}} \frac{dP(z)}{dz} \right]. \tag{3.22}$$

Since only hidden photons that decay between the end of the shield and before, or within, the detector can be observed, z has to be integrated from $L_{\rm sh}$ to the total length $L_{\rm tot}$ of the experiment. This leads to

$$\frac{dN_{\gamma'}}{dx_0} \simeq N_e\, \frac{N_0 X_0}{A}\, \int_{E_{\gamma'}+m_e}^{E_0} dE_e\, \int_0^{T_{\rm sh}} dt_{\rm sh} \left[I_e(E_0, E_e, t_{\rm sh})\, \frac{E_0}{E_e}\, \frac{d\sigma}{dx_e}\bigg|_{x_e=\frac{E_{\gamma'}}{E_e}} \left(e^{-L_{\rm sh}/l_{\gamma'}} - e^{-L_{\rm tot}/l_{\gamma'}} \right) \right], \tag{3.23}$$

where $L_{\rm tot} \equiv L_{\rm sh} + L_{\rm dec}$ with the length of the decay region $L_{\rm dec}$, as sketched in Fig. 3.1. The total number of events behind the dump, resulting from the decay of the hidden photon, is thus obtained by integrating over x_0 or equivalently over $E_{\gamma'}$ as

$$N_{\gamma'} \simeq N_e \frac{N_0 X_0}{A} \int_{m_{\gamma'}}^{E_0 - m_e} dE_{\gamma'} \int_{E_{\gamma'}+m_e}^{E_0} dE_e \int_0^{T_{\rm sh}} dt_{\rm sh} \left[I_e(E_0, E_e, t_{\rm sh})\, \frac{1}{E_e}\, \frac{d\sigma}{dx_e}\bigg|_{x_e=\frac{E_{\gamma'}}{E_e}} e^{-L_{\rm sh}/l_{\gamma'}} \left(1 - e^{-L_{\rm dec}/l_{\gamma'}} \right) \right] {\rm BR}_{\rm detect}\,, \tag{3.24}$$

where ${\rm BR}_{\rm detect}$ is the branching ratio into those decay products that the detector is sensitive to, i.e. electrons, muons or both.

For a specific experimental set-up, a constraint as a function of $m_{\gamma'}$ and χ can be derived by comparing the upper limit on the number of events observed in an experiment

with the one expected from (numerically) integrating Eq. (3.24), cf. also Appendix B.6 for details. The exclusion region depends on the dimensions of the experiment L_{sh} and L_{dec}, the number N_e and energy E_0 of dumped electrons, the target material and the 95% C.L. upper limit $N_{95\%\mathrm{up}}$ of the number of events observed in the experiment. An example exclusion limit is illustrated in grey in Fig. 3.5*(a)* for a fictitious toy experiment with $E_0 = 4$ GeV, $L_{\mathrm{sh}} = 200$ cm and $L_{\mathrm{dec}} = 200$ cm which dumped $N_e = 1 \times 10^{14}$ electrons and obtained a limit of $N_{95\%\mathrm{up}} = 10$ events. The shape of the exclusion contour can be understood by the following arguments.

As mentioned in Sec. 3.1.2, the upper reach of the experiments in the $m_{\gamma'}$-χ plane is set by the extension of the shield compared to the hidden photon decay length: if $l_{\gamma'}$ gets much shorter than L_{sh}, the exponential factor $e^{-L_{\mathrm{sh}}/l_{\gamma'}}$ in Eq. (3.24) drops rapidly. This causes the number $N_{\gamma'}$ of expected events to decrease quickly since most hidden photons decay inside the shield. Therefore, the sensitivity of the experiment breaks down. The estimate of the decay length (3.14) indicates that in a log-log plot of χ versus $m_{\gamma'}$ this upper limit is given by a straight line with slope of -1. This behaviour and the rapid decline of the exponential factor is shown in Fig. 3.5*(a)* by the green lines which demonstrate how the value of $e^{-L_{\mathrm{sh}}/l_{\gamma'}}$ decreases quickly from 10^{-1} at the lowest line in steps of 10^{-5} to 10^{-51} at the upper most line. Thus, changing in a set-up either the decay length $l_{\gamma'}$ via E_0 or the length L_{sh} of the shield, moves the upper boundary of the exclusion limit accordingly as illustrated in Fig. 3.5*(b)*. Therein, the central solid orange line gives the exclusion contour for the settings of the original toy experiment, the line to the left (short-dashed) results from either increasing L_{sh} or decreasing E_0 by a factor of 4 and the line to the right (long-dashed) from either decreasing L_{sh} or increasing E_0 by the same factor. Note that, in all plots of Fig. 3.5*(b–d)*, the interior of each contour, i.e. the part enclosed with the χ-axis, is excluded and the coloured shaded region symbolises the range in which the exclusion contour changes when varying a certain parameter in the specified range.

The lower boundary of the exclusion contour on the other hand is for small hidden photon masses almost horizontal, i.e. roughly independent of $m_{\gamma'}$. In this part of the parameter space, the decay probability, which is contained in Eq. (3.23) in the part enclosed in parenthesis, can be approximated as $P \propto L_{\mathrm{dec}}/l_{\gamma'}$ by expanding the exponentials for a large decay length $l_{\gamma'} \gg L_{\mathrm{sh}}, L_{\mathrm{dec}}$. In this limit, both the decay probability and the production rate decrease $\propto \chi^2$. The former scales as $P \propto 1/l_{\gamma'} \propto \chi^2 m_{\gamma'}^2$ because of (3.14) and the latter as $\sigma_{\gamma'} \propto \chi^2/m_{\gamma'}^2$, cf. (3.2). The number of hidden photons then follows as $N_{\gamma'} \propto \sigma_{\gamma'} L_{\mathrm{dec}}/l_{\gamma'} \propto \chi^4 L_{\mathrm{dec}}$ and is therefore roughly independent of $m_{\gamma'}$. This is indicated by the yellow band in Fig. 3.5*(a)* for an estimate of $N_{\gamma'}$. Since $N_{\gamma'}$ falls of very quickly with the fourth power of χ, the lower reach of the exclusion contour is limited by statistics. For decreasing kinetic mixing, too few hidden photons are produced and many of them do not decay before the detector because of their long decay length. The dependence of this lower boundary of the exclusion contour on L_{dec} is illustrated in Fig. 3.5*(c)*. Increasing or decreasing the length of the decay volume by a factor of 5 thus

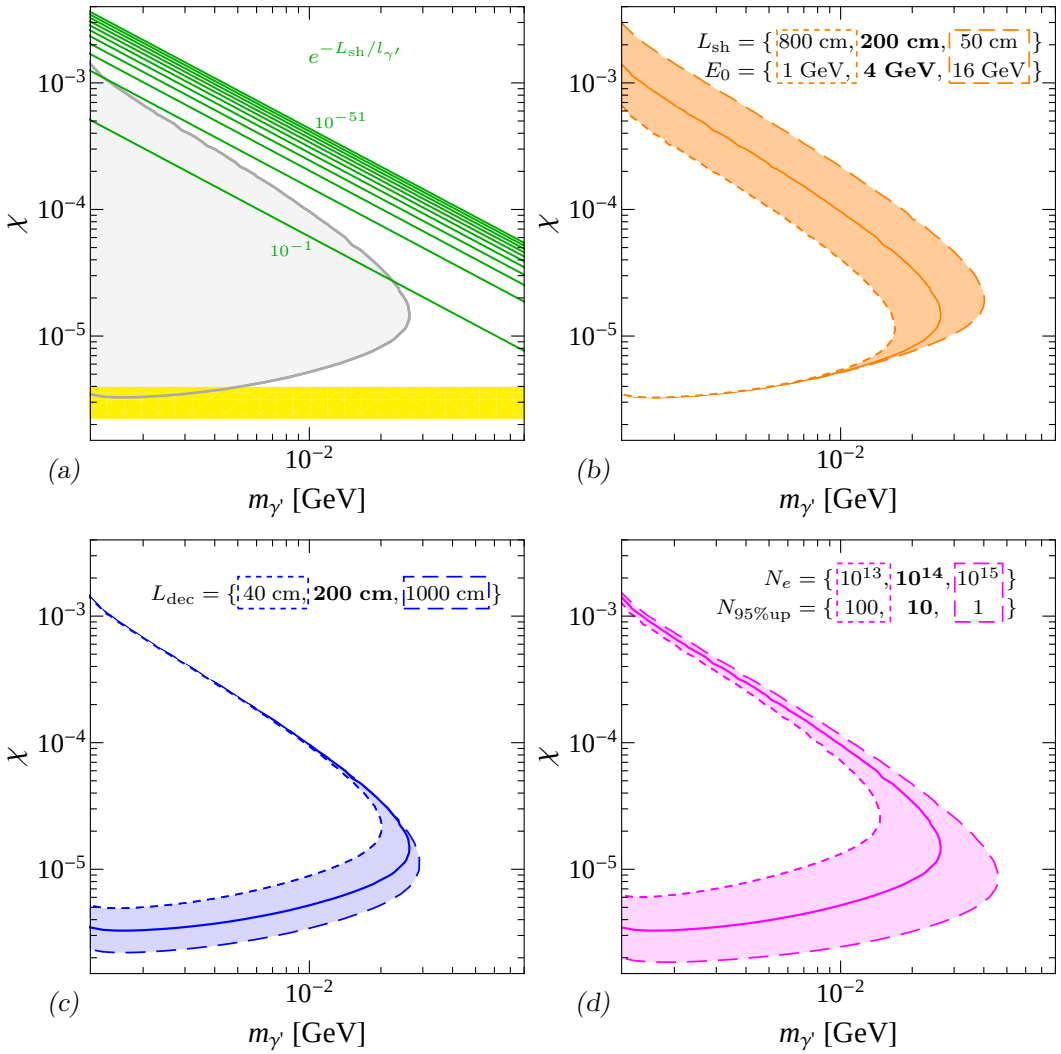

Figure 3.5: *(a)* Grey exclusion contour of the toy experiment together with the experiment's upper and lower estimated reach. The green lines give the variation of the exponential factor $e^{-L_{\rm sh}/l_{\gamma'}}$ which multiplies $N_{\gamma'}$ from 10^{-1} in steps of 10^{-5} to 10^{-51} (upper reach). In the log-log plot they have a slope of -1. The yellow band shows the lower reach for $l_{\gamma'} \gg L_{\rm sh}, L_{\rm dec}$ which is caused by too few statistics and roughly independent of $m_{\gamma'}$.

(b–d) Dependence of the exclusion contour on different factors of the experimental set-up: $L_{\rm sh}$, E_0, $L_{\rm dec}$, N_e and $N_{95\%\rm up}$. The parameters given in bold are the ones of the original toy experiment. They represent the central values and result in the solid contours. The other parameters correspond to the outermost values of the range which leads to the shaded areas.
(b) Variation of the shield length $L_{\rm sh}$ or the beam energy E_0 by a factor of 4 gives a similar shift of the upper contour line. The short-dashed line corresponds to increasing $L_{\rm sh}$ or decreasing E_0, the long-dashed line to decreasing $L_{\rm sh}$ or increasing E_0.
(c) Change in the exclusion limit originating from a reduction (short-dashed) or an increase (long-dashed) of the length of the decay region $L_{\rm dec}$ by a factor of 5.
(d) Identical but opposite rescaling of the contour caused by a modification of the number N_e of incident electrons or the upper limit of observed events $N_{95\%\rm up}$ by a factor of 10. Decreasing (increasing) N_e or increasing (decreasing) $N_{95\%\rm up}$ gives the short-dashed (long-dashed) purple line.

extends or diminishes the exclusion limit as shown by the long-dashed and short-dashed blue lines, respectively. The increased reach in case of a longer decay volume holds as long as losses due to the smaller solid angle resulting from the more distant detector can be neglected.

Lastly, both the number N_e of electrons dumped by the experiment and the upper limit $N_{95\%\text{up}}$ on the observed number of events control the overall scaling of the exclusion contour in a reciprocal way. The effect of changing both by a factor of 10 is illustrated in Fig. 3.5*(d)*. There, the stronger exclusion bound, shown as long-dashed purple line, corresponds to an increase (decrease) of N_e ($N_{95\%\text{up}}$) and the weaker bound, given as short-dashed purple line, results from a decrease (increase) in N_e ($N_{95\%\text{up}}$).

3.2 Application to electron beam dump experiments

3.2.1 Overview of existing electron beam dump experiments

In the following, we give a brief overview of the different experiments that we used to derive constraints. A summary of the most important parameters is also given in Tab. 3.1.

KEK

An experiment looking for neutral penetrating particles was conducted in 1986 at the National Laboratory for High Energy Physics (KEK) in Japan [265]. The interest in such particles was fuelled by the aforementioned monoenergetic positron peak observed at the Gesellschaft für Schwerionenforschung (GSI) in 1983 [264] which could result, for example, from a light axion-like particle. At KEK, a 2.5 GeV electron linear accelerator injected a total of 27 mC (1.69×10^{17} electrons) into a tungsten target. In front of a 220 cm long decay volume, a dump of iron, lead and plastic was used as shield against the background. The detector system, which was looking for e^+e^- pairs, consisted of multiwire proportional chambers, scintillation counters and a lead-glass Čerenkov counter. It was combined with a pair magnet providing a horizontal momentum kick of 13.5 MeV in 70% of the running time and of 40.5 MeV in the rest of the time. No energy cuts were used.

The experiment did not observe any signal and concluded that the GSI observation is unlikely caused by an axion. Thus, following Appendix B.7 we deduce the corresponding 95% C.L. upper limit $N_{95\%\text{up}}$ of 3 events for a Poisson signal.

SLAC E141

Also motivated by the GSI anomaly, this search for short-lived axions was performed at SLAC in 1987 [254]. The experiment used an electron beam of $E_0 = 9$ GeV which was dumped onto a 12 cm tungsten target. Following an evacuated beam pipe, a

spectrometer was placed 35 m downstream of the dump to look for positrons with secondary energy E' in the range between 70% and 90% of E_0. A large part of the beam pipe was surrounded by lead and concrete shielding to reduce the background. In the last 5 m, the pipe had a diameter of 7.5 cm defining the angular acceptance of 1.1 mrad. With a total of 2×10^{15} electrons (0.32 mC) dumped, the experiment concluded that a pseudoscalar decaying to e^+e^- is ruled out as solution to the GSI phenomenon.

From the background-subtracted number of positrons observed at different energies and reported by the experiment in Fig. 1c of Ref. [254], we extract for $x \equiv E'/E_0 \geq 0.7$ a total of 1126^{+1312}_{-1126} events. As described in Appendix B.7, we find that the corresponding 95% C.L. upper limit, assuming a Gaussian signal, then has to be taken as $N_{95\%\text{up}} = 3419$ events.

SLAC E137

Another experiment to look for neutral metastable penetrating particles was carried out at SLAC in 1988 [40] with a 20 GeV electron beam dumped onto an aluminium target. A 179 m thick hill served as earth shielding and was followed by a 204 m wide open valley as decay region. The experiment dumped in total 1.86×10^{20} electrons in two phases, a first one consisting of 9.5 Coulomb and a second one of 20.4 Coulomb. The detector was an electromagnetic shower counter of dimensions 2 m $\times$ 3 m perpendicular to the beam axis in the first and 3 m $\times$ 3 m in the second phase. It recorded either electron or positron events with an energy higher than 3 GeV.

The experiment reported that no candidate events were observed above 3 GeV in their search for axion-like particles. Thus, according to Appendix B.7, the 95% C.L. upper limit, assuming a Poisson signal, is given by $N_{95\%\text{up}} = 3$ events.

Orsay

In a search for light Higgs bosons, in 1989, a total of 2×10^{16} electrons (3.2 mC) with an energy of 1.6 GeV provided by the Orsay linac was dumped onto a tungsten target [257].[1] Surrounded by lead shielding the dump had a total length of 1 m. It was placed in front of a 2 m long and 10 cm wide decay volume inside a concrete wall. Behind this, a combination of scintillation counters and lead-glass Čerenkov counters was used to detect either electrons or positrons with an energy larger than 0.75 GeV.

The experiment concluded that the data which were taken within only a few hours, did not contain any events. Therefore, the experiment ruled out a Standard Model

[1] Note that another beam dump experiment was performed in Orsay in 1986 [270] which we do, however, not consider because it only reaches up to masses of about 15 MeV. In [271], it was suggested that this experiment could be used to constrain U-bosons. This U-boson is similar to the hidden photon but contains additional axial couplings. Constraints on this particle were studied in [18, 272–276], and its connection to dark matter was considered in [100, 138, 139].

Higgs between 1.2 and 52 MeV. Again following Appendix B.7, this translates to a 95% C.L. upper limit $N_{95\%\text{up}}$ of 3 events for a Poisson signal.

Fermilab E774

In 1991, a 275 GeV electron beam at Fermilab was exploited in a search for short-lived neutral bosons decaying to e^+e^- [255]. A total of 0.52×10^{10} electrons (0.83 nC) were dumped onto a 30 cm tungsten electromagnetic calorimeter used as target. Behind the shield a 2 m long decay space opened and was followed by four scintillation counters. Another electromagnetic calorimeter was placed in a distance of 7.25 m downstream from the dump and used for trigger. The experiment required two charged particles in the detector, i.e. both the electron and the positron from the decay. The final multiplicity-2 electromagnetic spectrum published in Fig. 4c of the analysis in [255] was obtained by subtracting the background of, for example, misidentified multiplicity-2 hadronic final states like $K_S^0 \to \pi^+\pi^-$.

From this plotted spectrum, we find a total of zero events with excess multiplicity-2. As this results from a subtraction of the background from the original multiplicity-2 spectrum, the statistical error is dominated by the total number of events in Fig. 4b of their publication [255]. We read off this plot a total of 89 events and infer the corresponding statistical error as $\sqrt{89}$ events. According to Appendix B.7, the 95% C.L. upper limit is given by $N_{95\%\text{up}} = 18$ events.

	target	E_0	N_{el}		L_{sh}	L_{dec}	N_{obs}	$N_{95\%\text{up}}$
		[GeV]	$\#_{\text{electrons}}$	Coulomb	[m]	[m]		
KEK	$^{183.84}_{74}$W	2.5	1.69×10^{17}	27 mC	2.4	2.2	0	3
E141	$^{183.84}_{74}$W	9	2×10^{15}	0.32 mC	0.12	35	1126^{+1312}_{-1126}	3419
E137	$^{26.98}_{13}$Al	20	1.87×10^{20}	30 C	179	204	0	3
Orsay	$^{183.84}_{74}$W	1.6	2×10^{16}	3.2 mC	1	2	0	3
E774	$^{183.84}_{74}$W	275	5.2×10^{9}	0.83 nC	0.3	2	0^{+9}_{-0}	18

Table 3.1: Overview of the different beam dump experiments analysed in this work and their specifications. The target materials are labelled by their mass number A, atomic number Z and chemical symbol ^A_ZW/Al, where W stands for tungsten and Al for aluminium. The number of observed events N_{obs} have directly been extracted from the experiment's papers. They differ in the case of E141 and E137 slightly from the estimates used in Ref. [266] as do the corresponding 95% C.L. values obtained according to Appendix B.7.

3.2.2 Acceptance of analysed experiments

The calculation of the expected number of hidden photons in a beam dump experiment in Sec. 3.1 relies on the assumption of an ideal experimental layout in which all decay products are seen in the detector. This is, however, not the case in a real experiment. Because of possible energy cuts in the analysis as well as the geometry of the set-up and the finite detector size compared to the angles under which the hidden photon and the decay-leptons are emitted, not all events predicted by Eq. (3.24) are detected. To estimate these effects, we simulate the hidden photon production and decay for all experiments discussed in Sec. 3.2.1 (see also Tab. 3.1) with the Monte Carlo generator MadGraph [277, 278]. Comparing the results of these simulations with the specifics of the set-up enables us to determine the acceptance of each experiment. This is discussed in detail in the following and explained with illustrative examples of the Orsay experiment. Note that we consider here only events where the hidden photon decay occurs behind the shield and before/within the detector, since this criterion is already accounted for in our theoretical estimate (3.24).

The production of the hidden photon in bremsstrahlung as well as its subsequent decay into e^+e^- can be simulated with MadGraph for different hidden photon masses and kinetic mixing values. Both processes were implemented for a fixed-target set-up into MadGraph by Rouven Essig, Philip Schuster and Natalia Toro [278] for use in the APEX experiment. We adopt this code to generate events for the electron beam dump experiments listed in Sec. 3.2.1 and set the beam energy E_0, the target atomic number Z and mass number A according to the specifications given in Tab. 3.1. We simulate for every experiment data samples with various combinations of hidden photon mass and kinetic mixing. At each of those parameter points we generate about $\mathcal{O}(3000)$ events providing us with the four-momenta of the hidden photon and of its decay products.

The collected events are then further analysed with Mathematica. There, we implement the energy cuts and three-dimensional layout of each experiment, i.e. the size of the target and the decay volume (not only the extension in the z-direction of the beam, but also possible boundaries in x- and y-direction) as well as the different detector components with their respective positions and sizes. In order to estimate the acceptance of the experiment, we need to find the number of decay products that are produced by a hidden photon within the decay volume, hit all required components of the detector and fulfil the selection criteria. The three different conditions c-1 to c-3 for a valid event can thus be summarised as:

c-1) The hidden photon decay position must lie within the decay volume. Since the acceptance only takes into account the decays that occur behind the dump and before/within the detector, this criterion refers only to potential lateral boundaries of the decay volume in x and y.

c-2) Depending on the requirements of the experiment either one or both decay products have to pass through certain relevant detector components.

c-3) The energy of the hidden photon and/or the decay product(s) has to fulfil the respective energy cuts.

The remaining number of valid events after applying *c*-1 to *c*-3 compared to the total number of simulated events then gives the acceptance according to

$$\frac{\#\text{events}|_{\{c\text{-}1\ \wedge\ c\text{-}2\ \wedge\ c\text{-}3\}}}{\#\text{events}}\,. \tag{3.25}$$

Since the Monte Carlo only generates four-momenta, we first have to construct the decay position of the hidden photon according to the decay length given by Eq. (3.13), determine the subsequent path of the decay products from this point on and compare it with the lay-out of the detector. Assuming that the hidden photon is produced by an electron with energy E_0 at the impact point of the beam on the target, its trajectory continues in the direction set by its four-momentum through the target. These assumptions are usually quite good since most of the hidden photon production takes place early in the target where the electrons carry a large fraction of the initial beam energy. With the distribution of an exponential decay, we random-generate the decay length of the hidden photon from (3.13) as a function of its energy, mass and kinetic mixing. The decay length must be corrected so that only decays behind the dump and before/within the detector are taken into account. The repeated use of one generated Monte Carlo event with various decay lengths allows us to artificially increase the data sample and the statistics.

A three-dimensional example of the distribution of hidden photon decay positions obtained for the settings of the Orsay experiment is shown in the left-hand plot of Fig. 3.6. As described in Sec. 3.2.1, the decay region in this particular case is a 2 m long and 10 cm wide volume passing through a concrete wall. It is represented as a transparent grey cuboid in the left-hand plot of Fig. 3.6. The green points in this plot indicate hidden photon decay positions within this volume, while brown points are not valid since the decay takes place inside the surrounding wall. For the other experiments under consideration, the decay volume is not limited in the x- and y-direction, so that all hidden photon decays are allowed.

In the next step, out of all decays within the decay volume the fraction of leptons that pass the detector has to be determined. For each decay position, we construct the path of both leptons according to the four-momenta generated with MadGraph. In the case of the KEK experiment, an additional momentum-kick resulting from the pair magnet has to be taken into account. Depending on the requirements of the experiment either both or only one of the two leptons have to traverse certain parts of the detector. This is shown in the set-up of the Orsay experiment for three different events in the

left-hand plot of Fig. 3.7. The grey cuboid again represents the decay volume and the green panels to the right illustrate the three detector components through which at least one of the decay-leptons has to pass. The tracks of the hidden photons are shown in green for two events classified as valid and in brown for an event that must be rejected. Note that those three trajectories have different origins since the plane at $z = 0$ corresponds to the end of the dump and not the production point. The paths of the two leptons indicated by orange dashed lines, originating from the hidden photon shown as brown line, do not hit all the three detector parts so that this event is not valid. The intersections of the trajectories of the leptons with the detector plane are given as grey dots when outside and as coloured dots when inside the detector area. Both decay-leptons of the hidden photon with the longest green track cross the entire detector as shown by the red lines and the corresponding red dots. From the hidden photon with the shorter green track one lepton does and one does not pass the detector as represented by the solid and dashed purple lines, respectively. The right-hand plot of Fig. 3.7 shows a green square, representing the topview of the first detector component behind the decay volume. It contains the penetration points of all leptons resulting from

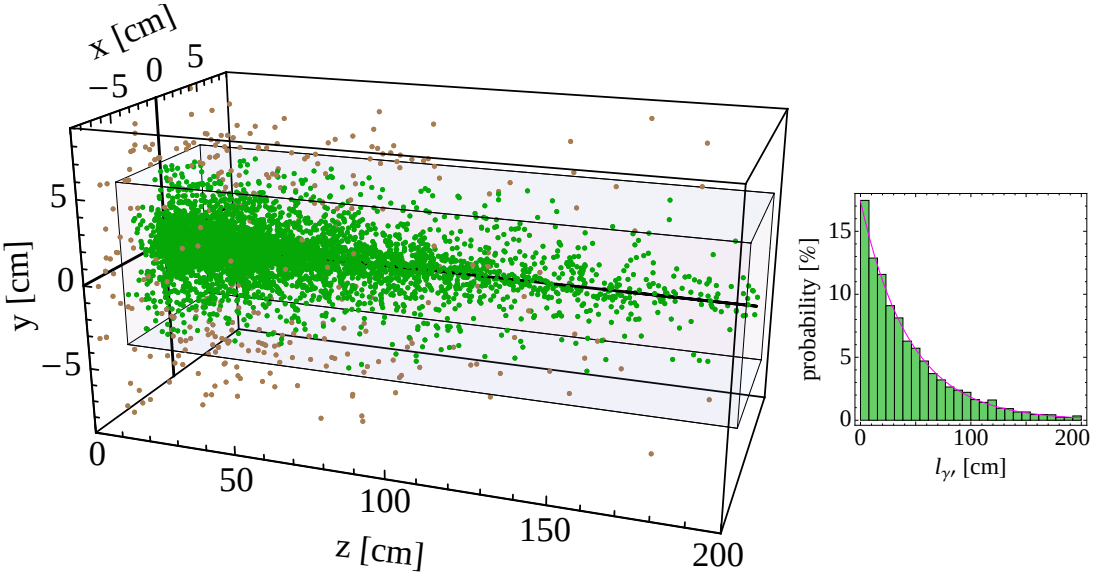

Figure 3.6: Visualisation of the hidden photon decay position *(left)* and length *(right)* for a total of 6400 events with a mass of $m_{\gamma'} = 50$ MeV and a kinetic mixing of $\chi = 1 \times 10^{-5}$.
Left: Hidden photon decay positions computed according to the four-momenta obtained from MadGraph simulations and the decay lengths randomly generated following the distribution of an exponential decay. The dump is placed at the left end of the plotted region and ends at $z = 0$. Points in green lie inside the 200 m long and 10 cm wide decay volume of the Orsay experiment which is represented as a grey cuboid. Points in brown are not valid since the decay occurs inside the wall surrounding the decay volume. Out of all events, about 91% ($\sim$ 5800 events) lie inside and 9% ($\sim$ 600 events) outside the decay volume.
Right: Distribution of the hidden photon decay length compared to the curve of an exponential distribution $e^{-l/l_{\gamma'}}$ with the decay length given by Eq. (3.13) where the mean hidden photon energy of the data sample was used.

6400 simulated hidden photon decays. Again, red and purple is used to distinguish the cases where both or one decay-lepton, respectively, traverse the entire detector. Grey implies that the lepton does not cross all parts of the detector.

In the last step, the energy of those leptons which pass the detector has to be compared to the energy cuts applied in the experiment. Then, the acceptance can be computed according to (3.25) as the ratio of the number of events for which the hidden photon decays inside the decay volume and the required number of decay-leptons traverse all detector components while passing the energy cuts, i.e. events fulfilling c-1 to c-3, with respect to the total number of simulated events. In this way, we determine the acceptance of each experiment for different combinations of $m_{\gamma'}$ and χ. The acceptance decreases slightly with increasing hidden photon mass but has very little dependence on χ. This is expected since the acceptance relies on kinematics in comparing the mass-dependent angles of emission and decay to the solid angle covered by the detector. Since both the hidden photon emission angle and the opening angle of the decay-leptons increase with $m_{\gamma'}$, as discussed in Sec. 3.1.1, the acceptance gets smaller at larger masses.

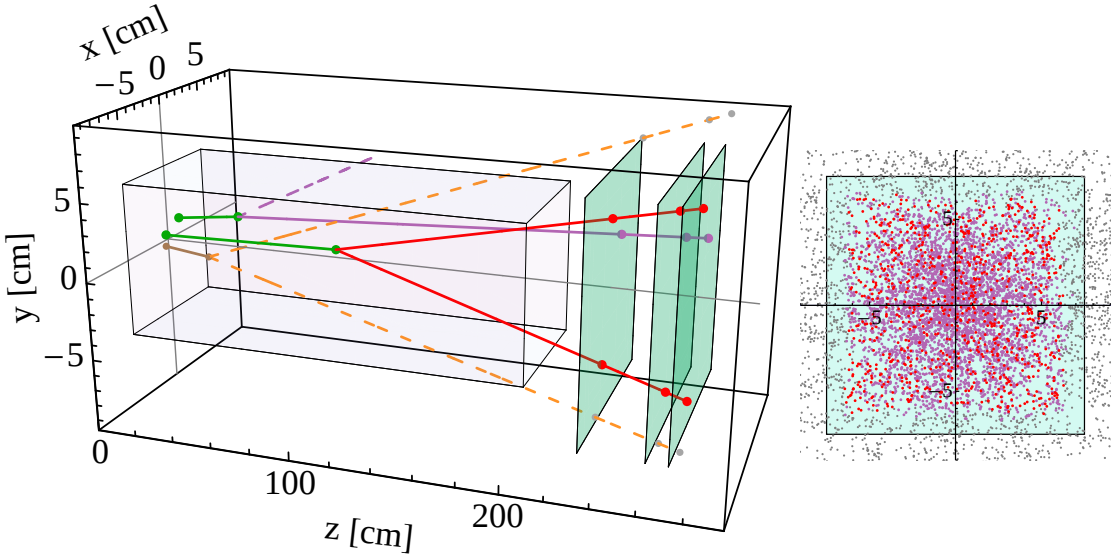

Figure 3.7: Left: Illustration of three hidden photon decay events from Monte Carlo simulations with MadGraph in the set-up of the Orsay experiment. The grey cuboid represents the decay volume and is followed by the three detector components shown as green panels. Both decay-leptons (dashed orange lines) from the hidden photon with the brown track miss the detector. For the hidden photon with the longest green track, both leptons (solid red lines) pass the detector. For the hidden photon with the shorter green track, only the lepton shown by the solid purple line hits the detector while the one given by the dashed line misses. *Right:* Topview of the first detector panel with impact points of the decay-leptons: red represents events where both, purple where only one and grey where none of the leptons traverse the entire detector. The plot contains the ~ 5800 events for which the hidden photon decays inside the decay volume, cf. Fig. 3.6. Among those, 17% are not valid (grey dots) as they violate c-2 or c-3. The other 83% are detected (75% by one lepton and 8% by both as indicated by purple and red, respectively) and pass the energy cuts, i.e. they fulfil c-2 and c-3.

3.3 Limits on hidden photons from electron beam dump experiments

Combining the results of the last two sections allows us to determine the 95% C.L. exclusion limits on hidden photons from electron beam dump experiments. In Sec. 3.1, the process of hidden photon production in bremsstrahlung and the subsequent decay into leptons was studied. This analysis took the pseudophoton-flux of the Weizsäcker–Williams approximation, nuclear and atomic size effects as well as the energy distribution of electrons in the target into account. Those considerations condensed in the final formula (3.24) giving the theoretical prediction for the number of expected events from hidden photon decays in an ideal experiment which detects all produced leptons, see also Appendix B.6. The limitations of a real experimental set-up like the geometry and finite detector size demand a scaling down of this estimate. Comparing the kinematics, emission angles and trajectories obtained using MadGraph Monte Carlo simulations with the layout of the experiments presented in Sec. 3.2.1 allows to determine the actual acceptance, as discussed in Sec. 3.2.2.

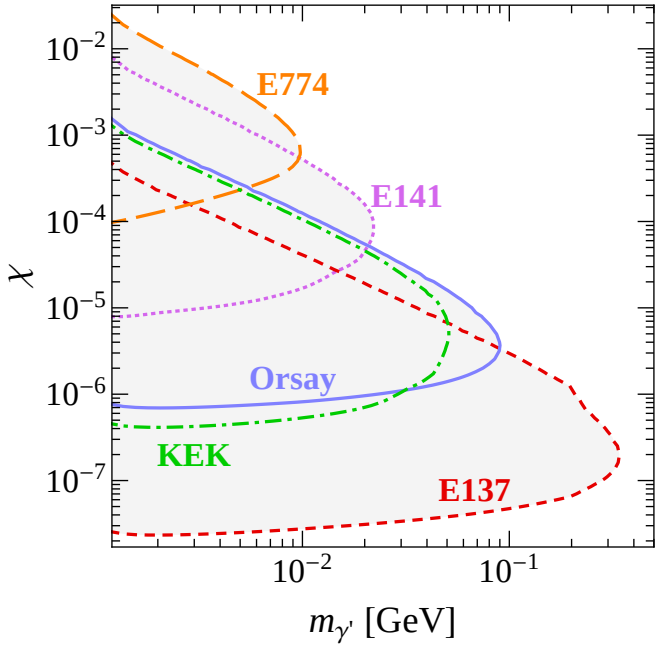

Figure 3.8: Limits on the hidden photon mass $m_{\gamma'}$ and the kinetic mixing χ from different electron beam dump experiments. The limits from the experiments at KEK (dash-dotted green line) and in Orsay (solid blue line) have been presented for the first time in the context of this work. The limits from E141 (dotted purple line), E137 (dashed red line) and E774 (long-dashed orange line), which were already considered in Ref. [266], have been reanalysed in the present work. Our analysis of all these limits takes the experimental acceptances determined with MadGraph into account.

Each experiment then excludes those points in the $m_{\gamma'}$-χ-parameter space for which the number of theoretically predicted events according to Eq. (3.24) multiplied with the experimental acceptance from Sec. 3.2.2 is larger than the experiments upper limit $N_{95\%\text{up}}$ given in Tab. 3.1. The resulting limits for the different experiments are shown in Fig. 3.8. The shape of the exclusion contours is as expected according to the discussion in Sec. 3.1.4 and the estimates of Fig. 3.5. Our limits for the previously analysed experiments at SLAC (E141 as dotted purple line and E137 as dashed red line) and at Fermilab (E774 as long-dashed orange line) are comparable to those presented in [266]. However, the constraints we find are generally a bit weaker because of the factor 1/2 discrepancy in Eq. (3.10), the slightly varied numbers of events $N_{95\%\text{up}}$ used for our 95% C.L. contours and the somewhat different experimental acceptances which we obtained from Monte Carlo simulations with respect to the rough estimates assumed in [266]. We find that the limits for the experiments at KEK and in Orsay, which are analysed in our work for the first time, cover a similar region, though Orsay extends to slightly higher masses. These new limits from KEK and Orsay allow us to exclude a region of the parameter space which so far has not been constrained by any other electron beam dump experiment, as shown in Fig. 3.8 by the dash-dotted green and solid blue lines, respectively.

3.4 Current limits on hidden photons

Besides the limits from electron beam dump experiments derived in the previous sections, various other constraints arise on the hidden photon mass $m_{\gamma'}$ and the kinetic mixing χ. They are discussed in the following and summarised in Fig. 3.9 in comparison to those presented in Fig. 3.8.

Beam dump experiments with protons probe a similar region of the parameter space as those with electrons. The general idea is that hidden photons can be produced in the radiative decays of neutral pseudoscalar mesons which are generated by a proton beam. Like in the case of electron beam dumps the hidden photon can traverse the shield and be observed through its decay in the detector. The shape of their exclusion contours is very similar to the one from electron beam dump experiment which was discussed in Sec. 3.1.4. The upper limit again results from a too short decay length with respect to the extension of the shield and thus features because of $1/l_{\gamma'} \propto \chi^2 m_{\gamma'}^2$ the same slope of -1 in the log-log plot. For the lower limit, the production cross section here is for small masses roughly $\propto \chi^2$, instead of $\propto \chi^2/m_{\gamma'}^2$ in the case of electron beam dumps. Therefore, multiplied with $1/l_{\gamma'} \propto \chi^2 m_{\gamma'}^2$, the slope of the lower limits is $-1/2$ and no longer independent of $m_{\gamma'}$. A first limit was obtained in [279] by reanalysing proton beam dump data from the ν-Cal I experiment which were taken with a ~ 70 GeV proton beam provided by the U70 accelerator at the Institute of High Energy Physics (IHEP) in Serpukhov. The original purpose of this experiment was to search for axions and

light Higgs bosons. The decay of π^0 mesons generated by the proton beam can produce hidden photons in a similar way as ordinary photons in $\pi \to \gamma\gamma$. Since the analysis only considered production from π^0 decays, hidden photon masses up to $m_{\pi^0} \simeq 134$ MeV can be probed. This is possible by searching for electromagnetic showers from the only available decay channel of the hidden photon into e^+e^-. The limit derived in [279] from the absence of a signal above the background overlaps with the one obtained from KEK and Orsay as shown by the line labelled "ν-Cal I" in Fig. 3.9. Further limits, denoted "NOMAD", "PS191" and "CHARM" in Fig. 3.9, were derived from neutrino experiments at CERN originally performed to search for the decay $\nu_h \to \nu e^+e^-$ of a heavy neutrino. The NOMAD experiment with a 450 GeV proton beam and PS191 with a 12.2 GeV proton beam were reanalysed in terms of hidden photons originating from π^0 decays in [280]. The former is limited to masses up to 95 MeV due to selection cuts in the analysis but the combined mass coverage is similar to the one of ν-Cal I. In the CHARM experiment with a 400 GeV proton beam, hidden photons originating from η and η' decays can be constrained up to about 500 MeV [281].

For the region with low mass and large kinetic mixing, the strongest constraints arise from the anomalous magnetic moment of the muon and the electron labelled "a_μ" and

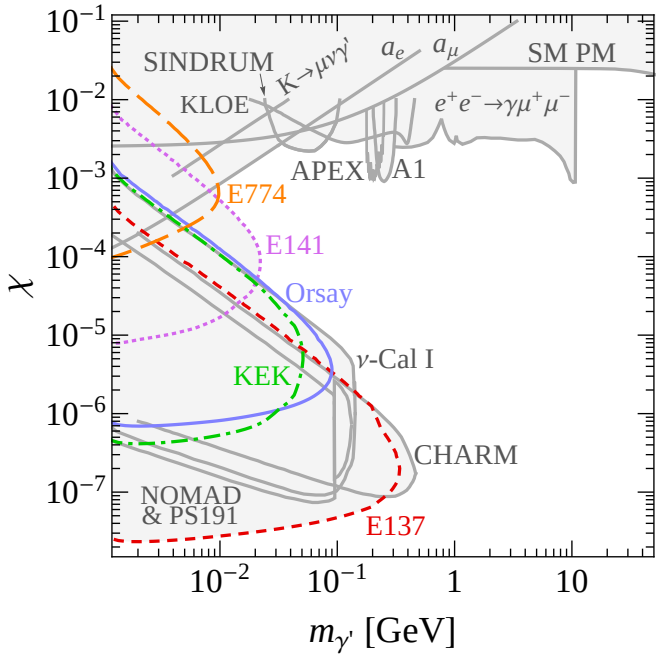

Figure 3.9: Collection of all current limits on hidden photons: from the electron beam dump experiments of the present work (coloured lines, cf. Fig. 3.8, all other limits as grey lines), Standard Model precision measurements, muon and electron anomalous magnetic moment, a reinterpretation of the BaBar search $e^+e^- \to \gamma\mu^+\mu^-$ for pseudoscalars, the electron fixed target experiments A1 and APEX, the ν-Cal I experiment at the Serpukhov proton beam dump, the KLOE experiment, the neutrino experiments NOMAD, PS191 and CHARM, the Kaon decay $K \to \mu\nu\gamma'$ and a search for rare decays by SINDRUM, cf. text for details.

"a_e", respectively. The one-loop contribution of the hidden photon to the anomalous magnetic moment of a lepton was calculated in [26]. As discussed in Sec. 1.3.3, there is a discrepancy between the measured value of the muon anomalous magnetic moment and the Standard Model prediction which could be resolved by the positive contribution arising from the hidden photon. A constraint can be derived demanding that this contribution does not exceed the measured value by more than 5σ and was presented in [26]. In the same analysis, a limit from the electron anomalous magnetic moment was found by comparing the measurement to the Standard Model value. This limit has recently been updated and strengthened in [282, 283].

Another limit for this region of the parameter space was announced in [284] around the same time as the update on a_e. The decay $K^+ \to \mu^+\nu_\mu\gamma'$ was analysed using data from the rare kaon decay $K^+ \to \mu^+ +$ invisible where the muon is the only final-state particle detected while all others are invisible neutral states. The obtained limit would have improved the former a_e bound but is not competitive with the improved one.

In the first analysis of the electron beam dump limits [266], a search for hidden photons using electron fixed-target experiments with a thin target was suggested. The idea is to exploit the same process of hidden photon production in bremsstrahlung followed by the decay into leptons, used in the beam dump case, but to overcome the limitation to the lower left corner of the parameter space $\{m_{\gamma'}, \chi\}$ by using instead a thin target. This then allows to probe shorter decay lengths and thus larger values of χ. The challenge is then to find a narrow resonance arising from the hidden photon decay in the e^+e^- invariant mass spectrum over the large QED background from so-called trident processes.[2] The experiments A1 at MAMI in Mainz [285] and APEX at JLab [286–288] are designed to search for such a resonance by placing two spectrometers at a small angle off the beam axis behind the target. Both experiments were already able to set new constraints in their first test runs, as shown in Fig. 3.9. They will further probe the parameter space in the near future.

Higher masses and larger kinetic mixing values can be probed with collider experiments. The KLOE-2 experiment [289] is carried out at the Frascati DAϕNE ϕ-factory, an e^+e^- collider. It searches for hidden photons produced in the decay of vector (V) to pseudoscalar (P) mesons analogous to $V \to P\gamma$. Decaying further to e^+e^- the hidden photon would appear as a peak in the e^+e^- invariant mass distribution. A first limit from ϕ decays to ηe^+e^- was derived in [289]. It was recently improved by using larger statistics [290] to the one shown in Fig. 3.9. The strongest constraint for masses beyond $\sim$ 300 MeV arises from a search for a pseudoscalar a^0 performed by BaBar around the $\Upsilon(3S)$ resonance [291] in the process $\Upsilon(3S) \to \gamma a^0$ with the subsequent decay $a^0 \to \mu^+\mu^-$. Because of identical final states this analysis was reinterpreted to $e^+e^- \to \gamma\gamma' \to \gamma\mu^+\mu^-$ and used to set a limit on hidden photons [286, 292–294] labelled

[2] The radiative trident process in which the hidden photon is replaced by an off-shell photon γ^* is an irreducible background. The larger Bethe–Heitler trident process, however, can be suppressed by appropriate cuts because to the different kinematics. This is discussed in detail in Ref. [266].

$e^+e^- \to \gamma\mu^+\mu^-$ in Fig. 3.9. Higher masses are only very little constrained for kinetic mixing values above $\sim 10^{-2}$. In [293], a bound was derived from the effect of a virtual hidden photon on precision Standard Model observables. The strongest limit results from the shift of the Z mass caused by the kinetic mixing. When combined with other measurements around m_Z, it leads to the curve labelled "SM PM".

The most recent limit presented in January 2013 [295] was obtained reanalysing data from a search for rare particle decays performed by the SINDRUM experiment at the Paul Scherrer Institute (PSI) in 1992. The experiment studied decays $\pi^0 \to \gamma e^+ e^-$ in a magnetic spectrometer. A short-lived hidden photon produced in $\pi^0 \to \gamma\gamma'$ and quickly decaying to e^+e^- would appear as a peak in the experiment's continuous e^+e^- invariant mass distribution. The absence of such an excess allows to constrain a region at large kinetic mixing where the hidden photon is short-lived.

An up-to-date overview of all those constraints on the mass $m_{\gamma'}$ and kinetic mixing χ of the hidden photon together with the ones from electron beam dump experiments presented in Sec. 3.3 is shown in Fig. 3.9. For a larger range of masses and kinetic mixing values 10^{-9} GeV $\leq m_{\gamma'} \leq 10^3$ GeV and $10^{-15} \leq \chi \leq 1$, a summary of various constraints on hidden photons from cosmology (including BBN), astrophysics and laboratory searches is given, for example, in [122, 123] and references therein. Not included there is a very recent limit for masses of $\mathcal{O}(100$ GeV) obtained in [296] from LHC data. Using searches for a narrow Z'-like resonances in the electron and muon channels ATLAS [297, 298] excludes masses above $\sim$ 170 GeV and CMS [299] above $\sim$ 300 GeV but only for rather large kinetic mixing values $\gtrsim 0.02$.

3.5 Future searches for hidden photons

Despite the numerous existing constraints on hidden photons with masses in the MeV to GeV range a large part of the parameter space is not covered. The region discussed in Sec. 1.3.3 in which the hidden photon could explain the discrepancy between the measured and the predicted value for the muon anomalous magnetic moment is also still partly allowed. This region was derived in the analysis of [26] and is shown as a light green band in Fig. 3.10. Much effort was and is currently dedicated to probe the open regions of the parameter space with future experiments. Various possibilities and potential sensitivities of different searches have been examined for accelerator based experiments like B-factories [292, 300, 301], electron fixed-target experiments [266, 302] and proton beam dump experiments like long-baseline neutrino experiments [179, 303], cf. also Ref. [304] for a recent overview.

The electron fixed-target experiments A1 at MAMI in Mainz [285] and APEX [286–288] at JLab already placed first limits from their test runs, as discussed in Sec. 3.4. Using different beam energies they are going to further extend their exclusion regions in

the near future. Their projected sensitivity is indicated by the purple and pink line in Fig. 3.10.

In addition, other possible search strategies were suggested [266,302,305], for example, by using a low energy and high intensity electron beam and an internal hydrogen gas target or by looking for displaced vertices in electron thin target experiments. The DarkLight [306] experiment at JLab and a similar one at MESA in Mainz are using the first technique. They plan to reach a sensitivity roughly sketched by the blue and cyan line in Fig. 3.10 [302]. The yellow line is an estimate of the region accessible to the second method and will be employed by the HPS [307] experiment at JLab.

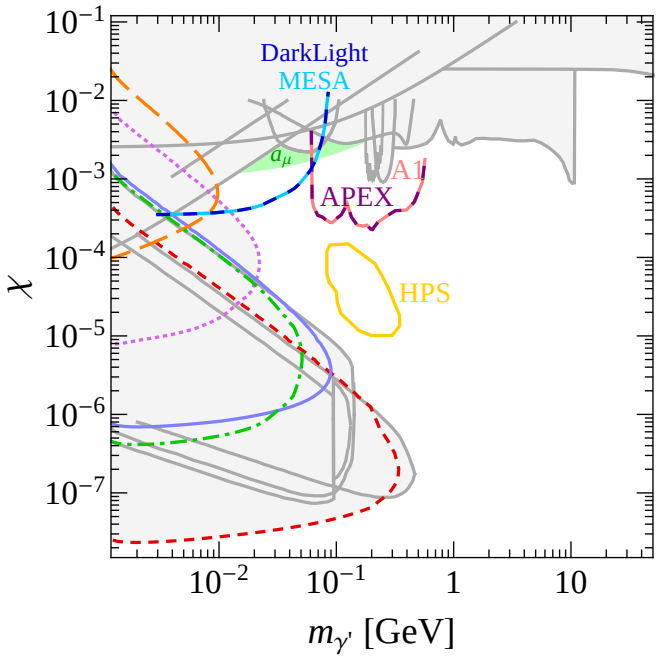

Figure 3.10: Projected sensitivities of future searches for hidden photons. The purple and pink line display the reach of A1 in Mainz and APEX at JLab. Blue and cyan represents the reach of DarkLight at JLab and MESA in Mainz. The yellow circle gives a rough estimate for HPS at JLab. The light green band indicates the region in which the hidden photon can account for the observed deviation in the muon anomalous magnetic moment from predictions. Grey areas are the limits shown in Fig. 3.9.

3.6 Summary

This chapter presented an analysis of the search for hidden photons with electron beam dump experiments, based on the production of hidden photons in bremsstrahlung and the detection of their decay. The obtained results allowed us to derive constraints on the mass $m_{\gamma'}$ of the hidden photon and the strength of the kinetic mixing χ with the ordinary photon for five different experiments. These high-intensity experiments exclude

the lower left corner of the parameter space $\{m_{\gamma'}, \chi\}$ up to masses of about 300 MeV. New limits from experiments at KEK and in Orsay exclude a previously unconstrained region of the parameter space. These limits and the other reanalysed ones from the experiments E141, E137 and E774 take the experimental acceptances from Monte Carlo simulations into account. Various other constraints on hidden photons exist but a large part of the parameter space is unconstrained and will partly be probed in the future. This region, where the hidden photon is still allowed by experimental limits, is also of interest for hidden sectors containing in addition a dark matter candidate, as studied in the next chapter.

Chapter 4

Dark Forces and Dark Matter in a Hidden Sector

We argued in Chapter 1 that there is overwhelming evidence for the existence of a non-luminous, non-baryonic type of matter and that the understanding of the particle nature of this dark matter requires physics beyond the Standard Model. It was also discussed that models in which the dark matter particles resides in a hidden sector and interacts through a hidden photon as a dark force are theoretically well motivated and possibly exhibit interesting phenomenological features. In this context, we introduced in Sec. 1.4 a specific toy model with minimal particle content (a Dirac fermion as dark matter candidate) and very few parameters. Additionally, we presented a string-inspired supersymmetric framework for a dark sector with gravity mediation domination. In this case, we allowed the hidden gauge symmetry to be broken either radiatively or induced by the visible sector.

The dark sectors models which we will consider throughout this chapter contain a dark matter particle in the hidden sector which interacts with the visible sector through kinetic mixing of the light hidden photon with the hypercharge gauge boson. We focus on hidden sectors in which both the dark matter particle and the hidden photon are light, with masses in the MeV to GeV range. Such a scenario is of interest in view of the signals claimed by the direct detection experiments DAMA and CoGeNT (later on also CRESST and very recently CDMS reported signals). Moreover, as discussed in Chapter 3, hidden photons in the MeV range are accessible to different experiments and are not only already subject to numerous constraints but will further be probed by new searches in the future.

In this chapter, we study the phenomenology of the toy model and the supersymmetric dark sector models. We investigate if and in which cases these models provide viable dark matter candidates. Therefore, we examine if they produce the correct relic abundance and are consistent with observations, in particular the results from direct

detection experiments. The various constraints that have to be taken into account both on the hidden photon and on the dark matter particle are summarised in Sec. 4.1. The discussion for hidden photons is based on the results obtained in Chapter 3. The consequences of all constraints on the parameter space and the reach of future searches for hidden photons are then illustrated in Sec. 4.2 by their application to the toy model. There, we analyse in detail the annihilation process of the Dirac fermion dark matter candidate and the resulting relic abundance as well as its scattering on nuclei together with the implications for direct detection. In Sec. 4.3, we then present the results of the parameter scan over our supersymmetric dark sector models. Depending on the breaking mechanism for the hidden gauge symmetry, the dark matter particle can be a Dirac fermion or a Majorana fermion which exhibit distinct signatures in direct detection experiments. We highlight the differences to the toy model and the phenomenological consequences. For all analysed scenarios, we show in Sec. 4.4 how the recently updated limits from direct detection experiments affect our findings.

A crucial novel aspect of our results with respect to other dark sector models is that we apply the relation given in Eq. (1.21) between the kinetic mixing χ and the hidden gauge coupling g_h instead of keeping them independent, as discussed in Sec. 4.2. This work was done in collaboration with Mark Goodsell and Andreas Ringwald and the results presented in Secs. 4.2 and 4.3 are published in [43].

4.1 Constraints on hidden sectors

Hidden sectors containing a hidden photon are, despite their weak interaction with the Standard Model, already subject to various constraints as discussed in Chapter 3 (cf. also Fig. 3.9). However, those limits which were derived on the models with only a hidden photon do not necessarily apply in the same way to the hidden sectors with an increased particle content considered in this chapter. Extending the earlier studied simple sector with hidden matter fields requires that additional bounds have to be considered, as discussed in the following. The hidden photon is no longer the only particle subject to constraints since also the dark matter has to fulfil certain requirements. This section gives a summary of the different limits that have to be taken into account in the search for viable models with dark matter and dark forces. Their implications are then illustrated in Sec. 4.2 by application to the toy model introduced in Sec. 1.4.2. We also comment on the reach of future experiments that have the potential to probe parts of the parameter space and possibly rule out further models.

4.1.1 Limits on the hidden photon

An overview of the constraints from different laboratory experiments for a hidden sector with an MeV- to GeV-scale hidden photon γ' is given in Sec. 3.4 and shown in Fig. 3.9.

Further limits for a larger range of masses and values of kinetic mixing, including bounds from cosmology and astrophysics, have been reviewed in [122, 123].

Since the supersymmetric models considered in the following analysis typically contain hidden photons with masses in the GeV range, out of the constraints summarised in Fig. 3.9 the following three are the most important ones. The only limit which applies to the entire mass range of interest arises from Standard Model precision measurements, in particular of the Z mass [293]. It excludes kinetic mixing values of roughly $\chi \gtrsim 3 \times 10^{-2}$. The limit is shown as an approximately horizontal long-dashed cyan line in most plots of χ versus $m_{\gamma'}$ throughout this chapter (e.g. Figs. 4.3, 4.4, 4.5, 4.7 and 4.8). Another limit restricted to much smaller masses comes from the requirement that the one-loop contribution of the hidden photon to the muon anomalous magnetic moment a_μ should not increase it beyond 5σ of the measured value [26]. This constraint dominates for $m_{\gamma'} < 1$ GeV and is drawn in the above-mentioned plots of this chapter as a dash-dotted brown line. Furthermore, BaBar data taken on the $\Upsilon(3S)$ resonance to search for a pseudoscalar in the process $\Upsilon(3S) \to \gamma a^0 \to \gamma\mu^+\mu^-$ can be reinterpreted because of the same final state to $e^+e^- \to \gamma\gamma' \to \gamma\mu^+\mu^-$ and therefore set a model-dependent bound on hidden photons [286, 292–294]. For masses in the range 0.2 GeV $\lesssim m_{\gamma'} \lesssim$ 10 GeV, this limit would be the strongest by excluding $\chi \gtrsim 2 \times 10^{-3}$, but it is model dependent and only holds if the γ' can not decay into hidden sector particles. In the plots throughout this chapter, we give the limit as it has been published in [293] by a short-dashed orange line. This limit corresponds to the case that the hidden photon decays with a branching ratio of 100% into the visible sector. In models in which decays into the hidden sector are possible, this branching ratio decreases and the limit becomes weaker. Since smaller branching ratios have not been considered in Refs. [286,292–294], the limit given in these references can not be applied in such a case. In the supersymmetric models, which we are considering, the hidden photon has often a similar mass to the dark matter particle, cf. Sec. 1.4.3.5. If this is the case, it can not decay within the hidden sector and the limit has to be respected. In this chapter, the limits from Standard Model precision measurements, the muon anomalous magnetic moment and BaBar are drawn in colour in most plots except for the log-log plots (Figs. 4.2 and 4.13) in which they are shown in grey and labelled SM PM, a_μ and $e^+e^- \to \gamma\mu^+\mu^-$, respectively.

In the cases where the BaBar limit is not applicable since the hidden photon can decay within the hidden sector, a different but much weaker constraint from the Z invisible width has to be taken into account. We require the contribution of the Z decay into hidden sector particles via the mixing with the hidden photon to be[1]

$$\frac{\Gamma(Z \to \text{hidden})}{\Gamma(Z \to \nu\overline{\nu})} \lesssim 0.008\,. \tag{4.1}$$

[1]The number of light neutrinos is according to the LEP results $N_\nu = (\Gamma_\nu + \Gamma_{\text{other inv.}})/\Gamma_\nu = 2.984 \pm 0.008$ [4]. Thus, an extra contribution of 0.008 to N_ν from decay into hidden sector particles leads to a 3σ discrepancy with the LEP measurement, instead of 2σ for the Standard Model.

The coupling of the Z to the hidden sector current $j_h^\mu = \bar{\psi}\gamma^\mu\psi$ is according to Eq. (A.61)

$$\mathcal{L} \supset -\frac{g_h s_\phi}{\sqrt{1-\chi_Y^2}} j_h^\mu Z_\mu \ , \tag{4.2}$$

where $s_\phi \simeq s_W \chi_Y/(1-x)$, $\chi_Y = \chi/c_W$, $x \simeq m_{\gamma'}^2/M_Z^2$ and c_W, s_W are the usual cosine and sine of the weak mixing angle. The decay width of the Z to hidden sector fermions ψ is then given by

$$\Gamma_{Z\to\psi\bar{\psi}} \ = \ \frac{1}{3}\alpha_h \left(\frac{s_\phi}{\sqrt{1-\chi_Y^2}}\right)^2 M_Z \left(1+2\frac{m_\psi^2}{M_Z^2}\right)\sqrt{1-4\frac{m_\psi^2}{M_Z^2}} \ , \tag{4.3}$$

where $\alpha_h = g_h^2/4\pi$ contains the hidden sector gauge coupling g_h. Together with the decay width into neutrinos

$$\Gamma_{Z\to\nu_i\bar{\nu}_i} \ = \ \frac{G_F M_Z^3}{6\sqrt{2}\pi} g^{\nu_i} \ = \ \frac{e^2 M_Z}{48\pi s_W^2 c_W^2} g^{\nu_i} \ , \tag{4.4}$$

where $G_F = \sqrt{2}g^2/8M_W^2$, $g = e/s_W$, $c_W = M_W/M_Z$ and $g^{\nu_i} \approx 0.5$ the constraint translates to

$$8 c_W^2 s_W^2 \left(\frac{s_\phi}{\sqrt{1-\chi_Y^2}}\right)^2 \left(\frac{g_h}{e}\right)^2 \left(1+2\frac{m_\psi^2}{M_Z^2}\right)\sqrt{1-4\frac{m_\psi^2}{M_Z^2}} \ \lesssim \ 0.008 \ , \tag{4.5}$$

for a single hidden Dirac fermion of mass $m_\psi < M_Z$ and unit charge under the hidden U(1) (see also [301]). In the models under consideration, where $m_\psi \ll M_Z$, Eq. (4.5) then simplifies to $\chi g_h \lesssim 0.04$. For a small number of hidden sector particles (and $g_h < 1$), this constraint is weaker than the one from the Standard Model precision measurements of the Z mass discussed above (SM PM).

For lighter hidden photons in the MeV range, also the limits from the electron beam dump experiments at Orsay [257], KEK [265], SLAC (E141 [254] and E137 [40]) and at Fermilab (E774 [255]) which were derived in Sec. 3.3 and are shown in Fig. 3.8 have to be applied in the models considered in this chapter. However, since they rely on the detection of the decay of the hidden photon to Standard Model particles (mostly electrons) and assume that this is the only decay possible (i.e. mostly BR($\gamma' \to e^+e^-$) = 100%), they have to be treated with caution here. These limits weaken if an additional decay channel opens into hidden sector particles since such a decay stays unobserved and lowers the branching ratio for the detectable channels. The same restriction applies to most other constraints which were presented in Sec. 3.4 for hidden photons with masses in the MeV range. With the exception of the limit from the rare kaon decay $K \to \mu +$ inv. [284] and those from the anomalous magnetic moment of the electron and the muon a_e and a_μ [26, 282, 283] all limits from fixed-target or collider searches assume that the hidden photon can not decay within the hidden sector. All these constraints

are shown in Fig. 4.2 for one specific toy-model with emphasis on the low mass range. Besides these limits which were already mentioned, there are further constraints by the proton beam dumps experiments ν-Cal I [279], CHARM, NOMAD and PS191 [280,281], the electron fixed-target experiments A1 [285] and APEX [287] as well as bounds arising from the production of hidden photons in different meson decays (KLOE [289] and SINDRUM [295]). Details of all limits on hidden photons are given in Sec. 3.4.

As described in Sec. 3.5, there are not only limits on these light hidden photons, but excitingly also dedicated experiments planned to search for these particles in other regions of the parameter space. Some of those experiments are already running and were able to set the first limits mentioned above. In the near future, the experiments A1 [285], APEX [286–288], MESA, DarkLight [302, 306] and HPS [307] can further probe parts of the parameter space that have not been constrained by other searches yet. This is indicated by the rough estimates of the different sensitivities which are shown in Fig. 4.2 together with the results from the toy model.

4.1.2 Constraints from big bang nucleosynthesis

In order for our models to be viable, it is important that they do not produce too many high-energy photons in the early Universe since these could dissociate nuclei (for example lithium) and spoil the predictions from big bang nucleosynthesis. As the thresholds for these processes are typically of the order of a few MeV, photons produced at higher energies are potentially dangerous. This might impose constraints on the hidden sector models, in which visible photons could arise, for example, from decays of particles in the hidden sector, the occasional annihilation of the frozen-out dark matter particles or oscillations of hidden photons into photons.

While BBN constraints on hidden sector matter which acquires a small charge under the visible photon (therefore called "minicharged" particles) in the presence of a *massless* hidden photons are summarised in [122], the massive case is studied in [43]. There, it is concluded that for the massive hidden photon considered in this work, the hidden sector states do not couple to the visible photon, cf. the diagonalisation of the physical states in Eq. (A.60) and also (A.61). Moreover, once a hidden photon is produced, the physical state does not oscillate into visible photons since for the kinetic mixing and mass ranges of interest in this work the hidden photon is much heavier than the plasma mass m_P of the photon during BBN ($m_P \lesssim 10^{-8}$ MeV) so that their mixing is negligible as it is proportional to $\chi c_W m_P^2/m_{\gamma'}^2$. Furthermore, because of the coupling to visible sector matter the hidden photon decays with a width of $\Gamma \simeq \frac{1}{3}Q^2\alpha\chi^2 c_W^2 m_{\gamma'} > 10^{-2}\chi^2$ GeV and a lifetime $\tau_{\gamma'} < \left(10^{-11}/\chi\right)^2 \left(\mathrm{GeV}/m_{\gamma'}\right)$ s, i.e., for $\chi > 10^{-5}$ immediately on any cosmological timescales without leaving a relic density of hidden photons. Therefore, BBN constraints do not affect our dark matter models as discussed in more detail in [43].

4.1.3 Limits on the dark matter particle

Finally, there are several constraints on the mass and interaction strength of the dark matter particle itself which have to be taken into account. In the following, the various limits applied in the later analysis are summarised and discussed regarding their relevance for the different dark matter particles obtained in our models. Our results which were derived in 2011 assume the experimental data available at that time. Especially the limits from direct detection experiments on spin-independent scattering of dark matter are based on the results of an analysis carried out in [81] in mid 2011. There, a systematic treatment of various uncertainties in direct detection experiments was performed. Due to the continuous progress in these experiments, limits have been updated since then. We study in Sec. 4.4 the implications of those recent achievements on our models and present in the following the different limits as they are applied in our analysis. Note that the searches for dark matter at the LHC mentioned in Sec. 1.1.4.3 do not apply here since they rely on the assumption that the mediator is heavy and can be integrated out. This is, however, not the case for the light hidden photon considered in this work.

Dark matter annihilation cross section and relic abundance

Like for any viable dark matter particle, the relic abundance Ωh^2 should not exceed the value determined from cosmological data as given in Eq. (1.2) in order not to overclose the Universe. In fact, we make the more loose requirement that the relic abundance be within 3σ of the measured value since the error of this measurement is smaller than the grid we can scan over in our supersymmetric models. This strict upper limit on the relic abundance translates to a lower limit on the thermally averaged dark matter annihilation cross section $\langle\sigma_{\text{ann}}v\rangle$ because of the dependence $\Omega h^2 \propto 1/\langle\sigma_{\text{ann}}v\rangle$, cf. Eq. (1.5). On the other hand, there is in principle no objection to having a dark matter candidate whose abundance is lower than the measured one. In this case, however, the particle under consideration would only constitute a part of the total dark matter in the Universe while other particle(s) would make up the remaining part. We refer to this scenario as subdominant dark matter. The supplementary dark matter component could, for example, be an axion or an axion-like particle. Their phenomenology is not the subject of this work and we shall simply assume that both their direct detection cross sections and their interactions with the hidden sector are negligible. The relic abundance of our hidden sector dark matter candidate is computed with micrOMEGAs [57–61] where we have implemented our different models. In the subsequent plots with our results, we will always indicate in dark green those dark matter candidates which provide the entire relic abundance and in light green those which contribute a subdominant part.

Dark matter scattering cross section and direct detection limits

Constraints on the scattering cross section of the dark matter particle on nuclei arise from the non-observation of a signal in direct detection experiments. A large number of such experiments are conducted and continuously lower their limits on the allowed elastic scattering cross sections on protons or neutrons. For those limits, one has to distinguish between spin-dependent (SD) and spin-independent (SI) scattering and the corresponding direct detection experiments. As discussed in Sec. 1.1.4.1, the constraints on the spin-independent scattering cross section are generally stronger than the ones on the spin-dependent one, since the former increases proportional to the mass of the target nuclei and most experiments use heavy target atoms. Depending on the nature of the dark matter particle, one or the other class of direct detection experiments is more sensitive. If the dark matter particle is a Dirac fermion it will appear mostly in spin-independent searches while a Majorana fermion because of its axial couplings can be searched for in spin-dependent experiments. In both cases, it will be shown that current limits are already able to exclude parts of the parameter space of our models. Furthermore, because of their constant progress in lowering the limits they continue to probe the dark matter candidates predicted by our models. The effect of these updated constraints is then presented in Sec. 4.4.

In our later analysis, as for the relic abundance, we again use micrOMEGAs to compute the different scattering cross sections of the dark matter particles. We then apply the corresponding constraints from the direct detection experiments to the obtained cross sections of the different dark matter particles. Two caveats have to be taken into account when comparing these cross sections with the experimental limits.

The first caveat arises for the case of spin-independent scattering of the hidden sector Dirac fermion with nuclei. This scattering takes place mostly due to γ' exchange. However, since especially at low $m_{\gamma'}$, the mixing of the hidden photon can be treated as being effectively only with the ordinary photon (see Appendix A.4 and Eq. (A.62)) this scattering interaction with the nucleus mostly results from the coupling of the photon to the proton's electric charge. Therefore, the spin-independent scattering of the Dirac fermion occurs almost exclusively on the proton inside the nucleus and it is thus strongly isospin-dependent. However, as discussed in Sec. 1.1.4.1, for a better comparison between limits from different direct detection experiments using different targets, the bounds on spin-independent scattering are usually presented on the cross section per nucleon under the assumption of equal effective couplings f_p and f_n to protons and neutrons. In this case of $f_p \approx f_n$, the cross sections scale with the square of the atomic mass of the nucleus, i.e. $\propto A^2$, as shown in Eq. (1.14). This case can, however, not be applied to the Dirac fermion, which scatters solely on protons so that $f_p \neq f_n \approx 0$. In this case, the cross section instead scales with the square of the charge of the nucleus, i.e. $\propto Z^2$, cf. Eq. (1.16). Therefore, the corresponding limits from direct detection experiments on

$\sigma_{\rm N}^{\rm SI,\ DD}$ have to be rescaled to a constraint on the cross section $\sigma_p^{\rm SI}$ on protons only. For each experiment this needs to be done individually by

$$\sigma_p^{\rm SI} \;=\; \frac{A^2}{Z^2}\,\sigma_{\rm N}^{\rm SI,\ DD}, \tag{4.6}$$

where Z and A are the atomic number and the mass number of the element in the target on which the scattering takes place. The spin-dependent interactions, on the contrary, are dominated by Z exchange and thus have only a rather weak isospin dependence. For all models analysed in the following, the results on the spin-independent direct detection cross sections will be presented for scattering on protons $\sigma_p^{\rm SI}$ since this is the dominant interaction for the Dirac fermion dark matter candidate.

The second caveat arises since the constraints from direct detection experiments on the scattering cross section assume that the local density of the dark matter particle is given by the generic value of $\rho_{\rm DM} = 0.3$ GeV/cm^3, cf. 1.1.3 and Eq. (1.7). Therefore, the limits strictly apply only to those dark matter particles that provide the entire relic abundance. In the cases where the dark matter makes up only a subdominant contribution of the total dark matter density, the bounds on the scattering cross section have to be rescaled accordingly and thus become weaker. For this rescaling, it is reasonable to assume that the dark matter in our local neighbourhood has the same content of different dark matter contributions as when averaged over the whole Universe. Then, the local density ρ_ψ of a dark matter candidate ψ relates to the local total dark matter density $\rho_{\rm DM}$ in the same way as their abundances

$$\frac{\rho_\psi}{\rho_{\rm DM}} \;=\; \frac{\Omega_\psi h^2}{\Omega_{\rm DM} h^2}. \tag{4.7}$$

The generic direct detection bounds on a dark matter particle that constitutes the entire local density therefore need to be multiplied by $\Omega_{\rm DM}h^2/\Omega_\psi h^2$ (which is > 1). This gives the weaker limit on the cross section of a subdominant candidate. Instead of scaling the limit for each dark matter particle as a function of its relic density up, we choose to keep the limits universal and rather scale the particle's real cross section σ^ψ down by

$$\sigma_{\rm resc}^\psi \;=\; \sigma^\psi\,\frac{\Omega_\psi h^2}{\Omega_{\rm DM} h^2}\ , \tag{4.8}$$

to the effective cross section $\sigma_{\rm resc}^\psi$ with which it appears in direct detection experiments (note that $\sigma_{\rm resc}^\psi < \sigma^\psi$, since $\Omega_\psi h^2 < \Omega_{\rm DM} h^2$ so that direct detection limits are less constraining for subdominant dark matter).

Spin-independent direct detection experiments

For spin-independent scattering and for the low dark matter masses ($\sim$ 10 GeV) we are interested in, the strongest constraints are set by XENON100 [86] and the silicon

run of CDMS [308][2] (referred to as CDMSSi hereafter). However, there is a long-standing tension between those exclusion limits on the one hand and the signal claims by DAMA [33,34] and later on also by CoGeNT [35,36] on the other hand (further claims by CRESST [37,38] and very recently by CDMS [39] also exist[3]). This tension caused a large debate on the reliability and comparability of these constraints. Especially the low dark matter masses, which might explain the signals, are close to the energy threshold of the experiments and therefore subject to many discussions. As mentioned in Sec. 1.1.4.1, the general comparison of the cross section per nucleon between experiments is also often considered problematic since these results are obtained with different techniques and target materials. They might furthermore suffer from nuclear physics uncertainties. In addition, the limits and claims are subject to astrophysical uncertainties (halo model, dark matter velocity distribution and local dark matter density) that can affect the results from different experiments in a different way and thereby increase or decrease the tension, cf. Sec. 1.1.4.1. In any case, although continuously improved limits more and more rule out most (or all) of the DAMA and CoGeNT preferred regions, those positive signals remain and should not be discarded carelessly.

In the last years, there have been numerous studies of how to reconcile those different results both depending on a particle physics model and in a model-independent way. We adapt the analysis of [81] which made a systematic scan of the various results taking into account specific uncertainties of the experiments and their backgrounds. Additionally, the effects emerging from different astrophysical assumptions were studied. They showed that for standard astrophysics the DAMA preferred region is in conflict with the XENON100 and CDMSSi limits while CoGeNT is still allowed. The compatibility of CoGeNT with the limits mainly results from taking into account the uncertainty in the strongly disputed scintillation efficiency of XENON100 at low recoil energies. This scenario considers the so-called Standard Halo Model (SHM, cf. Sec. 1.1.3) where the dark matter is assumed to have a spherically symmetric and isothermal distribution, a local density $\rho_\odot = 0.3$ GeV cm^{-3} and a Maxwellian velocity distribution with mean $\bar{v} = 220$ km/s and escape velocity $v_{\text{esc}} = 544$ km/s. For different assumptions on the halo density profile, it is shown that also the DAMA preferred region can be consistent with the exclusion limits. In our analysis, we will usually use the SHM and show in a few cases the differences that arise when changing for example to an Einasto [64] or a Navarro–Frenk–White [62] (NFW) profile. A discussion of dark matter density profiles is given in Sec. 1.1.3 and details on the considered halo models in Ref. [81].

Another interesting possibility considered in [180, 181, 309–313] to reconcile the disagreement between the signal claims and the limits is to allow for isospin-dependent

[2] Another special CDMS analysis of the germanium data [89] with low energy threshold gives a very similar exclusion limit and will therefore not be considered separately.

[3] We have not explicitly included the CRESST and CDMS signals in our analysis. One of CRESST's two signal regions [37,38] roughly agrees with the regions preferred by the DAMA and CoGeNT signals, although this is still subject to astrophysical uncertainties. A similar region is also compatible with the excess of events observed by CDMS [39], which was released while this thesis was being finalised.

interactions with just the right behaviour to suppress the interaction cross section with xenon nuclei. Thereby, it is possible to circumvent the most stringent limit arising from XENON100. However, a recent analysis [314] found that constraints from cosmic ray antiproton data can be important for isospin violating scenarios though their limits from an effective operator approach do not directly apply in cases with a light mediator. In our models, as mentioned above, the interaction of the Dirac fermion dark matter particle is almost entirely with protons rather than neutrons and thus also isospin-dependent. However, in contrast to the other works, in our case the isospin-dependence can not be tuned to give the desired effect, so we do not pursue this direction further.

In our analysis, we strictly apply the limits from XENON100 and CDMSSi derived in [81] to the spin-independent scattering cross sections of the different dark matter candidates. The resulting plots of the parameter space will thus only contain points for which the dark matter particle is not excluded by any of these two experiments. For those points, we further indicate in purple or red if the dark matter particle possesses the right cross sections to explain the signal claim of CoGeNT or DAMA, respectively. In the plots of σ_p^{SI} versus m_{DM} in Sec. 4.3 (see Figs. 4.6 and 4.9), the CDMSSi limit is shown as a dashed turquoise line and XENON100 as a dash-dotted blue line. CDMSSi sets the stronger constraint at the low dark masses in most halo models while XENON100 is only for the Einasto profile more constraining. The CoGeNT preferred region is shown in purple and the DAMA one in red/orange.

Spin-dependent direct detection experiments

The spin-dependent scattering both on protons and on neutrons, for the low dark matter masses we are interested in, is constrained by a number of direct detection experiments listed in the following. Note for completeness, that there have also been attempts to explain the DAMA signal by spin-dependent scattering either exclusively from neutrons [315] or from protons [316]. However, the former case is not applicable here, since in our models the cross sections of the Majorana fermion, which is the only dark matter candidate with sizeable spin-dependent scattering, are always of the same order of magnitude for protons and neutrons. It is thus impossible for the Majorana fermion to scatter only on neutrons like in [315]. In the second analysis [316], it was shown by analysing neutrinos coming from the annihilation of dark matter in the Sun that for scattering on protons, Super-Kamiokande rules out the DAMA preferred region almost independently of the specific dark matter model and annihilation channel. In addition, the largest spin-dependent cross sections that can be obtained in our models are more than one order of magnitude below the ones required in both scenarios to accommodate DAMA. Therefore, if spin-dependent scattering is confirmed as explanation of the DAMA (and CoGeNT) signals, it would rule out the models considered in this paper as they can not accommodate the required cross sections. Hence, we do not study these possibilities in more detail.

In our analysis, we use all results from the various direct detection experiments to constrain the cross sections σ_p^{SD} and σ_n^{SD} for spin-dependent scattering on protons and on neutrons in our models. The strongest limits on spin-dependent scattering on protons were provided by PICASSO [317] for the lightest and COUPP2011 [318] for the slightly larger masses until June 2011. The SIMPLE experiment [319] more recently published a constraint which is in the low mass region one order of magnitude stronger than the previous ones. However, the reliability of this limit has been questioned, due to the criticism concerning the limited lifetime of the used detectors as well as the background discrimination and subtraction methods [320] (see also the collaboration's response [321] for details). Further but much weaker limits are set by COUPP2007 [322] and KIMS [323]. Using Super-Kamiokande data on the neutrino fluxes from the Sun, another constraint can be derived on the spin-dependent cross section on protons since this scattering causes the dark matter to be captured inside the Sun, where its annihilation can produce neutrinos [324]. However, this limit should be considered as an estimate since it can vary depending on the model specific annihilation channel and branching ratios. Furthermore, it is limited to dark matter masses above 20 GeV because the experiment's analysis only considered such events where the muon, which is produced from the neutrino, traverses the entire detector in the upward direction (called upward through-going muon); this leads to a quite high threshold on the initial neutrino energy and causes the experiment's sensitivity to be restricted to larger dark matter masses.[4]

The cross section σ_n^{SD} for spin-dependent scattering on neutrons, on the other hand, is constrained by XENON10 [325], Zeplin [326] and CDMS [88, 89, 327]. For the mass range of interest in this paper, the strongest of those limits is set by XENON10. It is, however, weaker then the limit from SIMPLE on σ_p^{SD}. Since the Majorana fermion in our models has very similar cross sections for spin-dependent scattering on protons and neutrons, the SIMPLE limit constrains the parameter space more than XENON10.

In the following analysis, we apply to the cross sections for spin-dependent scattering on protons and to the ones for spin-dependent scattering on neutrons all direct detection bounds with the exception of the one from SIMPLE [319] as strict exclusions. The presented parameter points are all consistent with those limits. Because of the criticism of the result from the SIMPLE experiment, we do not apply this bound universally but rather show the effect on our results when taking it into account. In Sec. 4.3, the cross sections both for scattering on protons and on neutrons obtained by scanning over the parameter space in the different models are shown together with the corresponding limits. Figures of σ_p^{SD} versus m_{DM} contain the exclusions from SIMPLE as short-dashed brown line, Super-K as dashed black line, PICASSO as long-dashed orange line, COUPP2011 as dash-dotted turquoise line, COUPP2007 as dotted blue line

[4] There is another more recent analysis [316] of Super-Kamiokande data on neutrino fluxes where the limits for different annihilation channels also extend to smaller dark matter masses. Application of these constraints, however, requires to take into account the annihilation details and branching ratios and is left for future works.

and KIMS as solid green line. In the corresponding plots of $\sigma_n^{\rm SD}$ versus $m_{\rm DM}$, the limit from XENON10 is shown as dash-dotted blue, the one from Zeplin as dotted pink and the one from CDMS as dashed turquoise line.

4.2 Application to the toy model

Before studying the complex supersymmetric models, the phenomenology of hidden sector dark matter will be illustrated in this section by the minimal toy model introduced in Sec. 1.4.2. The application of the different constraints discussed in the previous section is demonstrated and potential viable models are presented. The toy model assumes the simplest possible dark sector which contains besides the (massive) hidden photon discussed in Chapter 3 only one additional Dirac fermion ψ with unit charge under the hidden U(1). The model does not include a Higgs sector and so we do not consider how the dark matter particle becomes massive. In any case, the hidden photon could naturally have a GeV-scale mass generated by the Stückelberg mechanism [20, 21] and does not require a Higgs sector. This minimal particle content allows us to focus on the essence of the dark matter phenomenology in a reasonably large parameter space without the benefits and downsides of further tunable parameters. This is essentially the model considered also in other works [102, 152, 154, 187] with the difference that we insist on the relation between the hidden gauge coupling g_h and the kinetic mixing χ given in Eq. (1.21). The parameters of the model are then the dark matter mass m_ψ, the hidden photon mass $m_{\gamma'}$, the kinetic mixing χ and the $\mathcal{O}(1)$ parameter κ that relates χ with the hidden sector gauge coupling g_h.

4.2.1 Constraints and future searches

The relic abundance of the Dirac fermion dark matter candidate was computed with micrOMEGAs where we have implemented the toy model. The annihilation of our dark matter candidate can proceed via the two processes shown in Fig. 4.1 either through a virtual hidden photon into Standard Model fermions or into two real hidden photons. While the s-channel annihilation (diagram on the left) is possible for the full range of dark matter masses, the t-channel process (diagram on the right) is kinematically only accessible for dark matter masses $m_\psi \geq m_{\gamma'}$ for which it is also dominant. The thermally averaged annihilation cross section for both channels is given by, cf. Appendix C,

$$\langle \sigma_{\rm ann} v \rangle_{\psi\bar{\psi}\to f\bar{f}} \approx \frac{\chi^2 e^2 g_h^2}{2\pi} \frac{m_\psi^2}{(4m_\psi^2 - m_{\gamma'}^2)^2} , \tag{4.9}$$

$$\langle \sigma_{\rm ann} v \rangle_{\psi\bar{\psi}\to\gamma'\gamma'} \approx \frac{\pi\alpha_h^2}{m_\psi^2} , \tag{4.10}$$

where $\alpha_h = g_h^2/4\pi$.

The s-channel leads to a resonant enhancement of the annihilation cross section for $m_{\gamma'} = 2m_\psi$. Accordingly, the relic abundance drops at this resonance since it is inversely proportional to the annihilation cross section. This behaviour can be seen in Fig. 4.2 in which the relic abundance as determined with micrOMEGAs is shown in green as a function of the kinetic mixing χ and the hidden photon mass $m_{\gamma'}$ for two different dark matter masses of 6 GeV (left-hand plot) and 7 GeV (right-hand plot). The thin dark green bands represent the regions in which the correct relic abundance of Eq. (1.2) is obtained. In the left-hand plot, this is shown for three different values of κ ($\kappa = 10$, $\kappa = 1$ and $\kappa = 0.1$ from top to bottom) and in the right-hand one for $\kappa = 0.1$. These bands exhibit the expected resonances at 12 GeV and 14 GeV, respectively. In the light green areas, the dark matter candidate gives a subdominant contribution to the total relic abundance. The white regions, on the other hand, are excluded since the annihilation is too weak at such small kinetic mixing values or large hidden photon masses and the dark matter becomes overabundant.

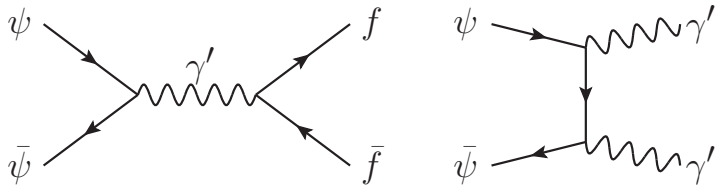

Figure 4.1: Feynman diagrams for the annihilation of the hidden sector dark matter particle ψ via its interaction with the hidden photon γ'.
Left: The s-channel annihilation via a virtual γ' into Standard Model fermions f is possible for the entire range of dark matter and hidden photon masses and is resonant at $m_{\gamma'} = 2m_\psi$.
Right: The t-channel process into two real hidden photons is kinematically only accessible when $m_\psi \geq m_{\gamma'}$. In this range, it is the dominant channel.

For hidden photon masses much smaller than the dark matter mass, the annihilation is dominated by the t-channel process (right-hand diagram in Fig. 4.1) and is essentially independent of $m_{\gamma'}$, cf. Eq. (4.10). In this case, for a given dark matter mass, this cross section and thus the relic abundance are fixed solely by the hidden gauge coupling g_h, which itself is determined via Eq. (1.21) by the kinetic mixing χ up to a factor κ, i.e. $\langle \sigma_{\text{ann}} v \rangle_{\psi\bar{\psi}\to\gamma'\gamma'} \propto \chi^4/\kappa^4$. Therefore, in Fig. 4.2, the green lines indicating the correct relic abundance are horizontal at small $m_{\gamma'}$ and their position in χ depends on κ. For larger values of κ, the cross section of Eq. (4.10) decreases and the correct relic abundance is obtained at larger values of χ. This is also apparent by the three lines in the left-hand plot of Fig. 4.2 which move upwards with increasing κ: the lowest line corresponds to $\kappa = 0.1$, the middle one to $\kappa = 1$ and the highest one to $\kappa = 10$. Because of the relation (1.21) a change by one order of magnitude in κ changes χ by the same amount.

The grey areas in Fig. 4.2 are excluded by the limits on hidden photons discussed in Secs. 3.4 and 4.1.1. All constraints can be applied in their original form and do not have to be modified to account for the additional presence of the dark matter particle

in the hidden sector. This would only be necessary if the hidden photon could decay invisibly inside the hidden sector and thus applies to the right side of the resonance, where $m_{\gamma'} \geq 2m_{\psi}$. In this range, the only existing bound is the one from Standard Model precision measurements (SM PM) which is, however, independent of the γ' decay channels. The coloured lines (with labels in the right-hand plot) represent the future searches for hidden photons as described in Secs. 3.5 and 4.1.1. It can be seen from the plot that those experiments will probe interesting parts of the parameter space.

Not only does the hidden photon enable the dark matter particle to annihilate it also mediates its elastic scattering on nuclei. Since the dark matter particle of the toy model considered in this section is a Dirac fermion, this scattering process is spin-independent. The corresponding cross sections obtained with micrOMEGAs have to be in agreement with the limits from CDMSSi and XENON100 and can be compared to the positive observations of DAMA and CoGeNT. As discussed in Sec. 4.1.3, the spin-independent cross sections per nucleon quoted by direct detection experiments need to be rescaled with Eq. (4.6) to the cross section per proton of the Dirac fermion dark matter particle. Furthermore, if the dark matter is subdominant the scattering cross sections have to be rescaled according to Eq. (4.8) for comparison with the direct detection results which rely on the generic value of the total local dark matter density. The resulting exclusions and regions of interest for DAMA and/or CoGeNT are shown in Fig. 4.2 for $\kappa = 0.1$ and two different settings of dark matter masses and halo models: the left-hand plot assumes $m_{\mathrm{DM}} = 6$ GeV and a Standard Halo Model (SHM) while the right-hand one uses $m_{\mathrm{DM}} = 7$ GeV and an Einasto profile. For the former settings, some of the CoGeNT preferred region is neither excluded by CDMSSi nor by XENON100 and scattering cross sections matching the ones preferred by CoGeNT can be obtained in the region of the parameter space shown in purple (90% and 99% contour are shown in lighter and darker shades) in the left-hand plot. For the latter settings, besides CoGeNT, also a part of the DAMA preferred region is in agreement with the limits and in addition overlaps with CoGeNT. Accordingly, cross sections in the red band in the right-hand plot can explain the DAMA signal, those in the purple band the CoGeNT signal and those in the blue band can explain both DAMA and CoGeNT at the same time. At the place where these bands coincide with the dark green stripe, the dark matter candidate not only possess a cross section which can explain the respective direct detection signals but also provides all of the dark matter in the Universe. In the largest part, however, the coloured bands lie on top of the light green areas and thus the corresponding direct detection signal is explained by a subdominant dark matter particle.

The constraints from CDMSSi and XENON100 on the spin-independent scattering cross section do not apply to the low dark matter mass of 6 GeV used in the left-hand plot of Fig. 4.2. However, for an Einasto profile, the dark matter particle with a mass of 7 GeV is constrained by XENON100 but still below the reach of CDMSSi, as shown in the right-hand plot. The XENON100 limit excludes the parameter space above the blue line as indicated by the dashed vertical lines. At the place where the XENON100

limit enters the region of subdominant dark matter (light green area), the scattering cross sections are rescaled as described in Sec. 4.1.3 to account for the smaller local dark matter density. This causes the kink in the exclusion line of XENON100. In the white overabundant region, the limit is not rescaled and the straight line there exhibits the behaviour obtained for a constant dark matter density equal to the observed one.

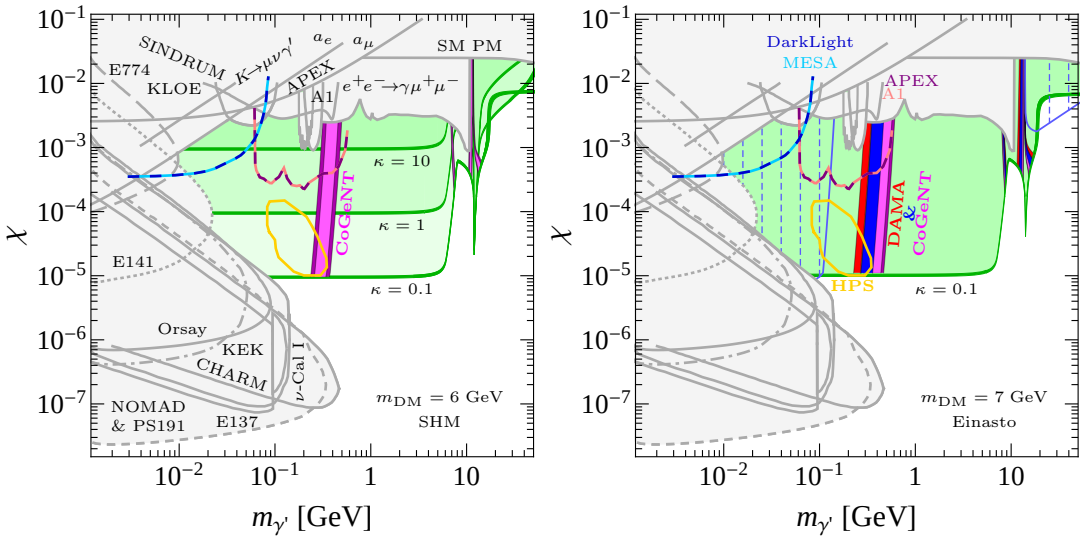

Figure 4.2: Allowed parameter space for the toy model with a Dirac fermion dark matter candidate for two different scenarios. In both plots, the dark green lines correspond to regions where the correct relic abundance is obtained, the light green areas give only a subdominant dark matter particle and the white ones are excluded because the dark matter is overabundant. The scattering cross sections in the subdominant areas are rescaled by the relic abundance according to Eq. (4.8) and the spin-independent limits and signals regions are rescaled by Eq. (4.6) to scattering on protons only. All grey shaded areas are constraints on hidden photons and the coloured lines indicate sensitivities of future searches.
Left: Model with a 6 GeV dark matter candidate assuming the Standard Halo Model (SHM). The dark green lines with the correct relic abundance are given for three different values of κ: the lowest corresponds to $\kappa = 0.1$, the middle to $\kappa = 1$, the upper to $\kappa = 10$. The purple band indicates where the cross sections for the case of $\kappa = 0.1$ could explain the CoGeNT signal. The grey regions give the limits from the electron beam dump experiments E774, E141 E137, Orsay and KEK, the proton beam dumps ν-Cal I, CHARM, NOMAD & PS191, the electron fixed target experiments A1 and APEX, the anomalous magnetic moment of the electron and the muon a_e and a_μ, the KLOE experiment at the DAϕNE e^+e^- collider, the decay $K \to \mu\nu\gamma'$, a search for rare meson decays by SINDRUM, a model-dependent BaBar search in $e^+e^- \to \gamma\mu^+\mu^-$ as well as Standard Model precision measurements SM PM (cf. Secs. 3.4 and 4.1.1 for details).
Right: Model with a 7 GeV dark matter candidate assuming an Einasto profile and $\kappa = 0.1$. The scattering cross sections can explain the CoGeNT signal in the purple band, DAMA in the red band and both at the same time in the blue band. The blue line represents the XENON100 bound which excludes all the hatched area. The coloured lines indicate the sensitivities of the hidden photon searches DarkLight, MESA, APEX, A1 and HPS (see Secs. 3.5 and 4.1.1).

The shape of all those contours — limits like the XENON100 line as well as allowed regions like DAMA and CoGeNT — which represent certain cross sections are not only influenced by the rescaling of the local dark matter density but also significantly affected by the application of the relation $g_h \propto \chi/\kappa$ of Eq. (1.21). For a dark matter particle with the correct relic abundance, the spin-independent scattering cross section of the Dirac fermion behaves as

$$\sigma^{\mathrm{SI}} \propto \frac{\chi^2 g_h^2}{m_{\gamma'}^4} \overset{(1.21)}{\propto} \frac{\chi^4}{m_{\gamma'}^4} , \tag{4.11}$$

for a constant dark matter mass and fixed κ. Thus, the XENON100 limit scales as $\chi \propto m_{\gamma'}$ and the corresponding line in the white areas has a slope of 1 in the log-log plot of Fig. 4.2. On the contrary, if g_h was kept constant instead of being determined by relation (1.21) the contour would follow $\chi \propto m_{\gamma'}^2$, i.e. possess a slope of 2 in a log-log plot. These characteristics change dramatically once rescaling is taken into account. For a subdominant dark matter particle, the scattering cross section has to be multiplied by the relic abundance, cf. Eq. (4.8), which is proportional to $1/\langle\sigma_{\mathrm{ann}} v\rangle$. The thermal-averaged ψ-$\bar{\psi}$ annihilation cross section times velocity $\langle\sigma_{\mathrm{ann}} v\rangle$ of the s- and t-channel is given in Eqs. (4.9) and (4.10), respectively. For fixed dark matter and hidden photon mass, they are proportional to $g_h^2\chi^2$ and g_h^4, respectively, and both translate with relation (1.21) to $\langle\sigma_{\mathrm{ann}} v\rangle \propto \chi^4$. In the region of interest, where the direct detection bands enter the subdominant area at $m_{\gamma'} \ll m_\psi$, the t-channel annihilation is the dominant process. Thus, when applying the relation $g_h \propto \chi/\kappa$ and rescaling with $\langle\sigma_{\mathrm{ann}} v\rangle \propto \chi^4$ the scattering cross section becomes

$$\sigma^{\mathrm{SI}}_{\mathrm{resc}} \propto \frac{\chi^4}{m_{\gamma'}^4} \frac{1}{\langle\sigma_{\mathrm{ann}} v\rangle} \propto \frac{1}{m_{\gamma'}^4} , \tag{4.12}$$

for a constant dark matter mass and fixed κ. The rescaled cross sections are thus approximately independent of χ. Therefore, both the XENON100 exclusion bound as well as the allowed regions for DAMA and CoGeNT are represented by almost vertical lines and bands in the subdominant region of Fig. 4.2.

As discussed in detail in this section, the Dirac fermion dark matter particle has large spin-independent scattering and some of the corresponding cross sections are in the reach of current or next generation direct detection experiments. Therefore, parts of the parameter space are already excluded, for example, by XENON100 as shown by the blue line and the hatched area in the right-hand plot of Fig. 4.2. Since the direct detection experiments continuously improve their limits, they will further probe the parameter space of the model and push, for example, the blue line in this plot towards the lower right corner of the parameter space. The impact of the latest bounds on the allowed parameter space of the toy model is discussed in Sec. 4.4.1.

4.2.2 Toy model example data point

For a better understanding of the above results and the toy model, a concrete example set of explicit values is discussed in view of the different experimental observables. This set of values is chosen such that the model satisfies all constraints and gives a cross section within the CoGeNT allowed region while constituting all of the dark matter. Fixing $\kappa = 0.1$, as in the left-hand plot of Fig. 4.2, and assuming a dark matter mass of 6 GeV, we find that the model gives a dark matter relic abundance within three standard deviations of the measured value (1.2) for $\chi \simeq 1 \times 10^{-5}$. According to relation (1.21) this kinetic mixing corresponds to a hidden gauge coupling of $g_h \simeq 0.05$.

The scattering of the Dirac fermion dark matter candidate is almost entirely spin-independent and on protons. Scattering cross sections in agreement with CoGeNT are possible for hidden photon masses in the range between 0.24 and 0.31 GeV. The corresponding cross sections σ_p^{SI} range from 1.4×10^{-39} cm^2 for the smaller hidden photon masses to 4.9×10^{-40} cm^2 for the larger ones. The cross sections of the direct detection limits and signal regions have to be rescaled by Eq. (4.6) to cross sections for scattering solely on protons in order to be comparable with σ_p^{SI}. Then, the cross sections of the dark matter particle can explain the CoGeNT signal for a Standard Halo Model and in the case of an Einasto profile fit both DAMA and CoGeNT [81].

In this range compatible with CoGeNT, the hidden photon is much lighter than the dark matter and the annihilation is almost entirely through the t-channel process (right-hand diagram in Fig. 4.1), which compared to the s-channel process is not suppressed by the kinetic mixing. This t-channel annihilation is almost independent of the hidden photon mass. Therefore, the dark green region in Fig. 4.2 in which the dark matter relic abundance matches the observed one is approximately horizontal up to hidden photon masses close to the dark matter mass. The width of the hidden photon in the given mass range lies between 1.9×10^{-13} GeV and 2.6×10^{-13} GeV.

4.2.3 Toy model parameter scan

Since the dark matter mass m_ψ is a free parameter of the toy model, we perform a scan over m_ψ in the range between 0.8 GeV and 25 GeV. In this way, we find viable models for the entire parameter space of kinetic mixing χ versus hidden photon mass $m_{\gamma'}$, as shown in Fig. 4.3. We refrain from running also over κ since the parameter space is already covered and instead fix it to its central value $\kappa = 1$. The obtained scatter plots in the plane χ versus $m_{\gamma'}$ are shown again for the Standard Halo Model in the left-hand and the Einasto profile in the right-hand plot (for details of the halo models, see [81]).

The colouring indicates by darker shades those models in which the dark matter candidate has the total relic abundance and by lighter shades those were it is subdominant. For the models in green, the dark matter particle is viable and in agreement with all

constraints but possesses scattering cross sections which can not fit any of the signals in the direct detection experiments. In the purple regions, the scattering cross sections are able to explain the CoGeNT signal while the dark matter is either subdominant (lighter purple) or gives the correct relic abundance (darker purple). The red and the blue regions are only present for the Einasto profile in the right-hand plot. The red ones correspond to scattering cross sections in agreement with DAMA, while in the blue regions the scattering cross sections explain simultaneously DAMA and CoGeNT. In both cases, the darker and lighter shades again reflect the dark matter abundance. Since for the Standard Halo Model the DAMA region does not overlap with the CoGeNT one and is excluded by the other direct detection constraints, there are neither blue nor red areas in the left-hand plot. The overlap in the mass-cross section space of the signal regions of DAMA and CoGeNT leading to the blue region for an Einasto profile is also possible for an NFW profile. This scenario is not plotted since it looks very similar to

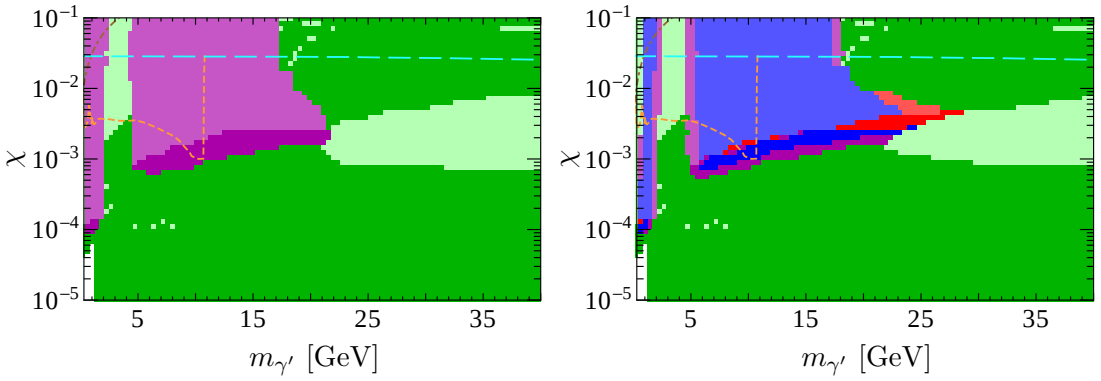

Figure 4.3: Allowed parameter space for the toy model with a Dirac fermion dark matter candidate ψ in the plane of kinetic mixing χ versus hidden photon mass $m_{\gamma'}$ when scanning over m_ψ in the range from 0.8 GeV to 25 GeV and fixing κ to 1. Darker shades of a certain colour indicate regions in which the correct relic abundance is obtained and lighter shades correspond to parts where the dark matter candidate is subdominant. The green areas in both plots are in agreement with the relic density and all direct detection constraints but the scattering cross sections do not explain any of the signal claims (all scattering cross sections are rescaled for subdominant dark matter and all limits as well as signal regions from [81] are rescaled to scattering on protons only). In both plots, the constraint from Standard Model precision measurements is shown as the almost horizontal long-dashed cyan line, the (model-dependent) BaBar limit is shown as a short-dashed orange line and the muon anomalous magnetic moment constraint is given as dash-dotted brown line at the top left corner.
Left: Assuming the Standard Halo Model (SHM), the cross sections for spin-independent scattering on protons obtained in the purple areas can explain the CoGeNT signal and are consistent with the other direct detection constraints.
Right: For an Einasto profile, parts of both the DAMA and CoGeNT preferred regions are consistent with the direct detection constraints. The cross sections obtained in the purple area again can explain the CoGeNT signal, those in the red one the DAMA signal and those in the blue one both at the same time.

the Einasto case. In the following analysis of the supersymmetric models, we shall use mostly the Standard Halo Model since the choice of halo model has a more dramatic effect on the presence (or absence) of an overlap of the signal regions than it has on the allowed parameter space of our models.

In Sec. 4.2.2, we presented concrete parameter sets for models with very light hidden photons ($m_{\gamma'} <$ GeV) and a Dirac fermion dark matter candidate with a mass of a few GeV. These models were consistent with all constraints and provided the total relic abundance in the Universe. In addition, the dark matter particle possessed scattering cross sections able to explain the direct detection signals. As can be seen in Fig. 4.3, such a scenario is also possible in a region of the parameter space at higher hidden photon masses. For $m_{\gamma'} \gtrsim 6$ GeV and $\chi \sim 10^{-3}$, the purple area in the left-hand plot and also the red and blue areas in the right-hand plot are shown in darker shades. Since the direct detection signals are only in agreement with the other limits for dark matter masses between 5.5 and 8.9 GeV, the hidden photon is in all these models heavier than the dark matter $m_{\gamma'} \gtrsim m_{\mathrm{DM}}$. Therefore, the annihilation proceeds only via the s-channel diagram of Fig. 4.1 since the t-channel is not accessible in this region. When decreasing the hidden photon mass, the t-channel opens and significantly enhances the annihilation rate which causes a drop in the abundance. Because of (4.8), this reduces the rescaled scattering cross sections accordingly and leads to the disappearance of the allowed region and the interruption of the purple band. An example model constituting the entirety of the dark matter while obeying all constraints and explaining DAMA and CoGeNT (in the case of an Einasto profile) is obtained for $m_\psi = 6$ GeV, $m_{\gamma'} = 14.1$ GeV, $\chi = 0.0016$ and $\kappa = 1$ (thus, $g_h = 0.72$). It gives a spin-independent scattering cross section of 5.1×10^{-40} cm^2 which fits the direct detection signals. For these settings, the hidden photon is quite wide with a width of 0.17 GeV and decays almost entirely into two dark matter particles.

4.3 Analysis of a supersymmetric dark sector

In this section, we discuss how the phenomenology changes when the basic toy model is replaced by a hidden sector which is embedded into a more complex supersymmetric model. We present the results of a scan over the parameter space of the models introduced in Sec. 1.4.3. The phenomenology is different for the two mechanisms considered in Secs. 1.4.3.3 and 1.4.3.4 by which the hidden gauge symmetry is broken. Both scenarios are confronted with constraints on the relic abundance of the dark matter particle and results from direct detection experiments.

We implement our models in micrOMEGAs [57–61] in order to obtain in each model predictions for different parameters which can be compared to experimental data. MicrOMEGAs automatically computes all of the required annihilation cross sections and

integrates the Boltzmann equations to give the relic abundance. Furthermore, it calculates the different direct detection cross sections for scattering on protons and neutrons. All the interactions between the hidden and visible sector are taken into account including the neutralino mixing and Higgs portal term which are described in [43] and which we believe to be novel results. Because of these interactions, there is a connection to specific particles in the visible sector and consequently a mild dependence on the spectrum and couplings assumed in the visible sector. Since we are investigating the effects of gravity mediation, and for minimality, we chose the visible sector to consist of the MSSM with a Higgs mass above the LEP bound and the lightest visible sector neutralino in the range 100 to 200 GeV. Changing the spectrum within these ranges leads to quantitative changes of a few percent in the hidden sector phenomenology, but not to qualitative ones.

As mentioned in Sec. 1.4.3, we take the kinetic mixing parameter $\chi < 0$ so that the field H_+ rather than H_- obtains a vacuum expectation value (vev). Because of the symmetry of the model, the sign of χ is entirely a matter of choice, and the physical results are unchanged when considering the opposite sign. Therefore, and for ease of comparison with the findings derived in Sec. 4.2 for the toy model, the magnitude of χ is used in the plots presenting our results.

The phenomenology of the supersymmetric hidden sector models is presented in the following separately for the two breaking mechanisms since their different dark matter candidates exhibit rather distinct features. Wherever comparison is possible, the differences and similarities with the toy model are emphasised.

4.3.1 Models with radiative breaking domination

In the following, the hidden gauge symmetry is assumed to be broken radiatively through the running of the Yukawa coupling λ_S, as described in Sec. 1.4.3.3. The dark matter candidate in this scenario is, as mentioned in Sec. 1.4.3.5, exclusively the Majorana fermion $\tilde{o}_1$ so that the scattering on nuclei is dominantly spin-dependent. We start with presenting the results for the relic abundance and the scattering cross sections for a complete parameter scan and then give detailed numbers obtained for one specific viable model.

4.3.1.1 Parameter scan for radiative breaking domination

We perform a scan over the kinetic mixing χ and the hidden photon mass $m_{\gamma'}$ in order to find parameter combinations which give a light dark matter candidate with a mass in range between 0.8 and 20 GeV. We insist that λ_S and the hidden gauge coupling g_h inferred from χ remain perturbative and thereby obtain via Eq. (1.21) an upper limit on χ. Since we are most interested in light hidden gauge bosons, we limit the

scans to a maximum value of 40 GeV for $m_{\gamma'}$. The low-energy parameters are found by choosing boundary conditions at the high-energy scale (10^{16} GeV) and running down. In practice, we fix at the high-energy scale $m_{H_\pm} = 100$ GeV, consider for κ different values $\in \{0.1, 0.5, 1, 2, 4, 6, 8, 10\}$ and scan over λ_S, m_S, M_λ, A_S and χ. This procedure ensures that we get consistent models at the low-energy scale, rather than having chosen the parameters completely *ad hoc*.

The details of those low-energy models obtained from the parameter scan are then used as input for micrOMEGAs. This further allows us to determine the corresponding relic abundances and scattering cross sections of the dark matter particle in each model. The results of this analysis projected on the plane of the absolute value of the kinetic mixing χ versus the hidden photon mass $m_{\gamma'}$ are shown in Figs. 4.4 and 4.5. Both figures demonstrate the effect of either fixing $\kappa = 1$ (left-hand plots) or scanning over it in the range $0.1 \leq \kappa \leq 10$ (right-hand plots). Clearly, allowing for a variation in κ seriously increases the parameter space in which viable models are found. This is in stark contrast to the toy model of Sec. 4.2 in which the parameter space was already filled for fixed $\kappa = 1$ (cf. Fig. 4.3). The green colour in the plots encodes again the dark matter relic abundance. Dark green points correspond to models that give the correct relic abundance while light green points represent a subdominant dark matter candidate. The coloured lines indicate the limits from the muon anomalous magnetic moment (dash-dotted brown), the BaBar search (short-dashed orange) and the Standard Model precision measurements (long-dashed cyan). All points shown in both figures are in agreement with the various direct detection constraints with the exception of the one from the SIMPLE experiment which is not taken into account in Fig. 4.4. The effect of including the SIMPLE limit is then illustrated in Fig. 4.5 where in comparison to Fig. 4.4 some of the dark green models, providing the correct relic abundance at larger hidden photon masses, disappeared since they violate the SIMPLE bound.

The direct detection cross sections for spin-dependent and spin-independent scattering obtained with micrOMEGAs are plotted in Fig. 4.6 as a function of the dark matter mass m_{DM}. For comparison, the different limits and signal regions discussed in Sec. 4.1.3 are also shown. For those plots, we scanned over the hidden photon mass $m_{\gamma'}$, the kinetic mixing χ as well as the parameter κ in the range $0.1 \leq \kappa \leq 10$. The cross sections are again rescaled for subdominant dark matter according to Eq. (4.8). The top plot contains the cross sections σ_p^{SD} for spin-dependent scattering on protons and the corresponding experimental bounds. At the bottom, the cross sections σ_p^{SI} for spin-independent scattering on protons are shown in the left-hand plot and those for spin-dependent scattering on neutrons σ_n^{SD} in the right-hand plot.

As the dark matter particle considered in this subsection is the Majorana fermion $\tilde{o}_1$ it dominantly possesses spin-dependent scattering. In the top and in the right-hand plot of Fig. 4.6, it can be seen that the cross sections σ_p^{SD} and σ_n^{SD} turn out to be quite large

and are partly even already excluded by current experiments. In fact, the plot at the top visualises that the most stringent constraint arises on the spin-dependent scattering on protons from the SIMPLE experiment, which is sketched as short-dashed brown line.

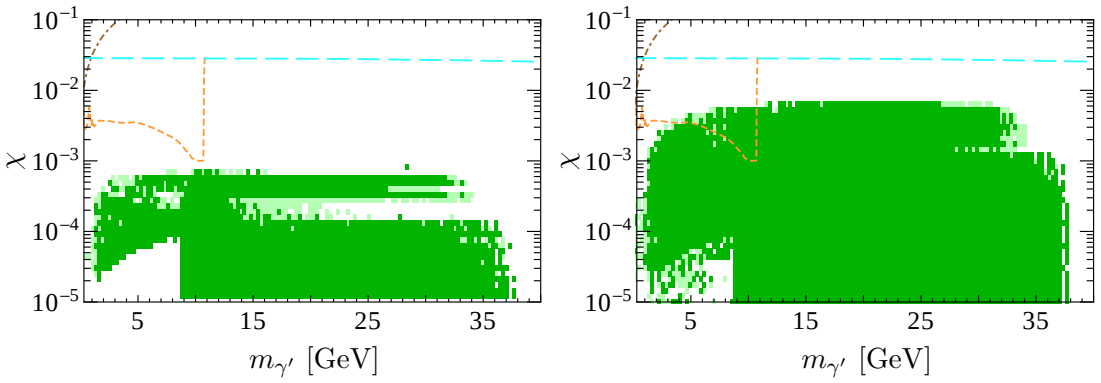

Figure 4.4: Viable models with radiatively induced breaking of the hidden gauge symmetry in the parameter space of the magnitude of the kinetic mixing χ versus the hidden photon mass $m_{\gamma'}$. Dark green areas correspond to models that provide the correct dark matter relic density, and light green regions give a subdominant dark matter candidate. Lines represent the constraints from Standard Model precision measurements (long-dashed cyan), a model-dependent reinterpretation of a BaBar search (short-dashed orange) and the muon anomalous magnetic moment (dash-dotted brown). All points contained in the plot correspond to viable models that are in agreement with all direct detection constraints **except for** the SIMPLE exclusion limit. The Standard Halo Model (SHM) has been used.
The two plots illustrate the effect from either keeping the parameter κ fixed or allowing it to vary by one order of magnitude in each direction:
Left: $\kappa = 1$. *Right:* $0.1 \leq \kappa \leq 10$.

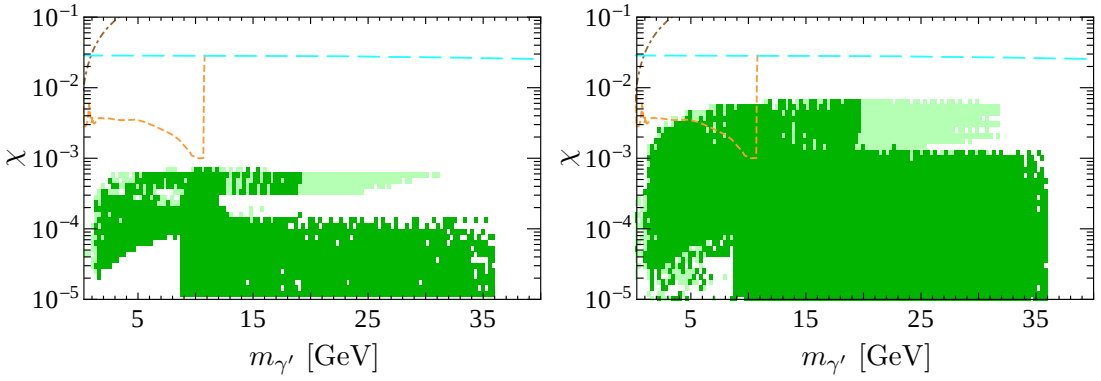

Figure 4.5: Viable models with radiatively induced breaking of the hidden gauge symmetry in the plane of the magnitude of the kinetic mixing χ versus the hidden photon mass $m_{\gamma'}$. Same colouring and exclusion lines as in Fig. 4.4. Again, all points correspond to viable models that are in agreement with all direct detection constraints, while now we are **including** the SIMPLE exclusion limit. The SHM has been used.
Again the effect of keeping κ fixed or allowing it to vary is illustrated:
Left: $\kappa = 1$. *Right:* $0.1 \leq \kappa \leq 10$.

If taken at face value it excludes many parameter points for dark matter masses above $\sim$ 7 GeV. Since the different cross sections are related, the inclusion of the SIMPLE limit on scattering on protons directly removes also large portions of the parameter space with large cross sections for *spin-independent* scattering on protons σ_p^{SI} as well as spin-dependent scattering on *neutrons* σ_n^{SD}. This is illustrated for both cases in the two plots at the bottom of Fig. 4.6, where yellow and orange points indicate those models that lie above the SIMPLE exclusion limit for spin-dependent scattering on protons in the top plot (hereby points in yellow have a subdominant and those in orange the total dark matter abundance). As can be seen from the right-hand plot at the bottom, the SIMPLE limit for spin-dependent scattering on protons is more constraining than limits for scattering on neutrons for which XENON10 excludes only very few models. The effect on the parameter space of allowed models when including the SIMPLE limit is also illustrated in Figs. 4.4 and 4.5. There, the former figure shows the viable models when this limit is not taken into account and the latter one contains those models that remain after the limit is applied.

As mentioned above, the fact that the hidden sector dark matter candidate in the models with radiative breaking domination is a Majorana fermion leads to extremely small cross sections for spin-independent scattering, as shown in the left-hand plot of Fig. 4.6. They do, however, obtain a contribution from the Higgs portal term, which is always present in supersymmetric theories. This is described in detail in [43], where also a simple approximation for the contribution of the Higgs portal term is derived as

$$\sigma_{\mathrm{N}}^{\mathrm{SI,\,Portal}} \;\sim\; 10^{-45}\mathrm{cm}^2 \times \left(\frac{m_{\tilde{o}_1}}{m_{\mathrm{N}} + m_{\tilde{o}_1}}\right)^2 \left(\frac{\chi}{0.002}\right)^2 \left(\frac{\mathrm{GeV}}{m_{\gamma'}}\right)^2 \,, \tag{4.13}$$

where $m_{\tilde{o}_1}$ is the mass of the Majorana fermion $\tilde{o}_1$ and m_{N} the one of the nucleon. This result agrees with the cross sections from micrOMEGAs plotted in the left-hand plot of Fig. 4.6. There is also a contribution from squark exchange, which is, however, somewhat smaller and more spectrum-dependent. These spin-independent scattering cross sections of the Majorana fermion are, in contrast to the Dirac fermion of the toy model, very similar for scattering on protons and on neutrons since the Higgs portal term is not isospin-violating. This is different to the scattering of the Dirac fermion which is essentially only on protons since it is mediated by the hidden photon which mixes with the photon. Therefore, we labelled in Eq. (4.13) the cross section as $\sigma_{\mathrm{N}}^{\mathrm{SI,\,Portal}}$ with "N" denoting Nucleons. In the left-hand plot of Fig. 4.6, we give the cross sections $\sigma_p^{\mathrm{SI,\,Portal}}$ for scattering on protons rather than on nucleons since this allows direct comparison with the results of the Dirac fermion in the other models. The signal regions of DAMA and CoGeNT as well as the limits are shown for a Standard Halo Model (SHM). Despite the contribution from the Higgs portal term, it can been seen that the cross sections σ_p^{SI} for scattering on protons are several orders of magnitude below the reach of current experiments. Consequently, these models are not able to provide the large cross sections needed to explain the DAMA or CoGeNT signals. We do not study other halo profiles

since they only allow potentially excluded signals to be marginally consistent but are of no interest for models that can not give the required cross sections.

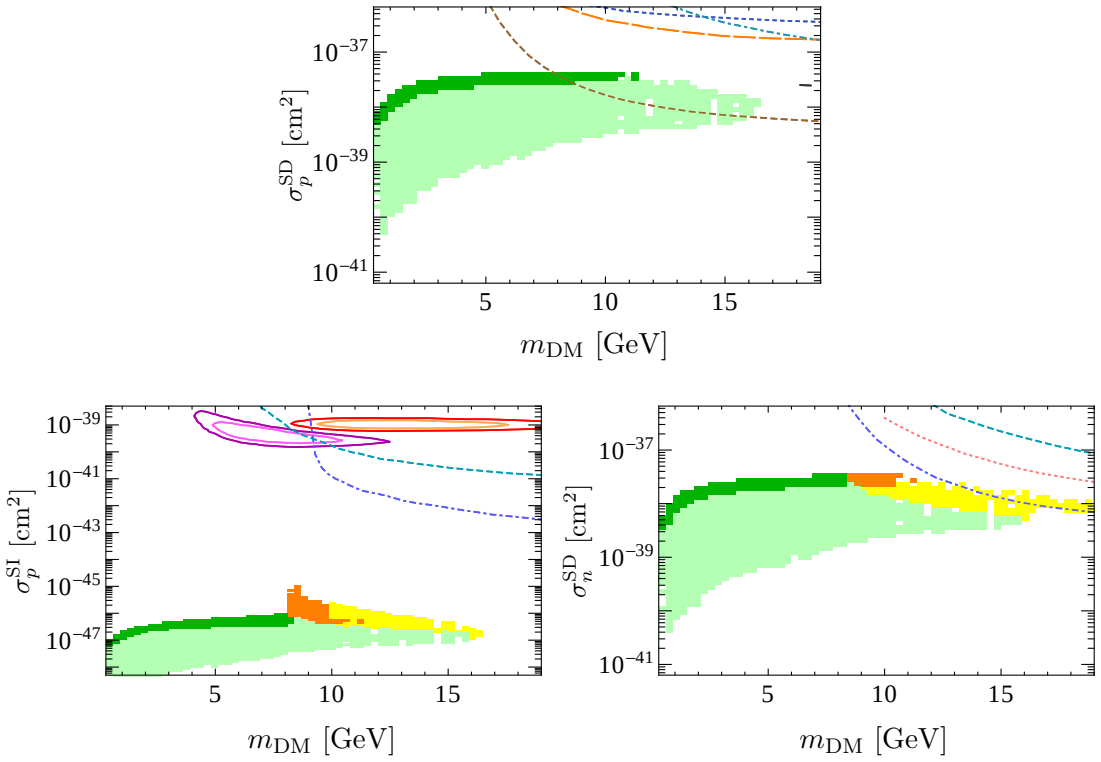

Figure 4.6: Direct detection cross sections of the Majorana fermion dark matter candidate $\tilde{o}_1$ obtained with micrOMEGAs for models with radiatively induced breaking. All plots are scanned over κ in the range $0.1 \leq \kappa \leq 10$. Models in dark green give the correct dark matter relic abundance while for those in light green the dark matter particle is subdominant and the cross sections have to be rescaled accordingly.
Top: Spin-dependent scattering cross sections σ_p^{SD} on protons and corresponding constraints from the direct detection experiments SIMPLE (lowest-lying, short-dashed brown curve), PICASSO (long-dashed orange line), COUPP2011 (dash-dotted turquoise limit), COUPP2007 (dotted blue line) and Super-K (dashed black line at the right edge of the plot).
Left bottom: Spin-independent scattering cross sections σ_p^{SI} on protons together with signal contours from DAMA (red/orange lines) and CoGeNT (purple lines) as well as exclusion limits from CDMSSi (dashed turquoise line) and XENON100 (dash-dotted blue line). Limits and signal regions are rescaled to cross sections for scattering on protons only and shown for the SHM.
Right bottom: Spin-dependent scattering cross sections σ_n^{SD} on neutrons together with the limits by XENON10 (dash-dotted blue line), Zeplin (dotted pink line) and CDMS (dashed turquoise line) from bottom to top.
In both plots at the bottom, points in yellow and orange lie above the SIMPLE limit on σ_p^{SD} and give a subdominant and total dark matter abundance, respectively.

4.3.1.2 Example model with radiative breaking domination

For a better understanding and for complementarity to the plots which can only show two-dimensional projections of the parameter space, we give in the following a concrete example of one model. This model satisfies all experimental constraints and provides the entire dark matter relic abundance. We take κ to be unity and the soft masses $m_{H_\pm}$ approximately 100 GeV at the high-energy scale. We then run the parameters down and make adjustments at the high scale in order to find appropriate values at low energies. It turns out that m_S is somewhat larger and drives the soft hidden Higgs masses to become tachyonic. The parameters at the low- (10 GeV) and high-energy (10^{16} GeV) scales are given in Tab. 4.1 together with the particle spectrum at low energies after hidden gauge symmetry breaking.

The dark matter candidate is the Majorana fermion $\tilde{o}_1$ and has a mass of 5.2 GeV. With a relic density of $\Omega_{\tilde{o}_1} h^2 = 0.112$ it provides the entire dark matter in the Universe. As expected, the cross section for spin-independent scattering on protons is with $\sigma_p^{\mathrm{SI}} = 3.8 \times 10^{-47}$ cm^2 very small. It is several orders of magnitude below the reach of current direct detection experiments. The cross section for spin-dependent scattering on protons is $\sigma_p^{\mathrm{SD}} = 2.8 \times 10^{-38}$ cm^2 and very similar to the one for scattering on neutrons $\sigma_n^{\mathrm{SD}} = 2.2 \times 10^{-38}$ cm^2. The hidden photon and the hidden Higgs both have a mass of 11.6 GeV. Their widths are 6.8×10^{-8} GeV and 4.8×10^{-8} GeV, respectively, and both decay mostly invisibly into two Majorana fermions $\tilde{o}_1$.

Considering in the visible sector for the MSSM the parameters at the SPS1b benchmark point [328][5], the full neutralino mass matrix in the basis (B_0, W_0, h_u^0, h_d^0, $\tilde{\lambda}$, $\tilde{h}_+$) is given by

$$\mathcal{M}_{\mathrm{neutralino}} = \begin{pmatrix} 166 & 0 & -2.73 & 43.8 & -0.01 & -0.01 \\ 0 & 310 & 2.73 & -79.9 & 0 & 0 \\ -2.73 & 2.73 & 0.00 & -512 & 0 & 0 \\ 43.8 & -79.9 & -512 & 0 & 0 & 0 \\ -0.01 & 0 & 0 & 0 & 20.7 & 11.6 \\ -0.01 & 0 & 0 & 0 & 11.6 & 0 \end{pmatrix}, \tag{4.14}$$

in which all masses are expressed in GeV. The eigenmasses of this matrix are 5.2, 25.9, 164, 298, 516 and 530 GeV. For the same data point, we can compute the mixing between

[5]This benchmark point is disfavoured by the LHC results and gives a too small mass for the lightest Higgs, but the dependence of our results on the visible sector parameters is small. Changing to another benchmark point is left for future work.

the original Higgs eigenstates and the mass eigenstates to be

$$\begin{pmatrix} H_+ \\ h \\ H \end{pmatrix} = \begin{pmatrix} 1.0 & -3.6 \times 10^{-5} & 1.2 \times 10^{-7} \\ 3.6 \times 10^{-5} & 1.0 & 0 \\ -1.2 \times 10^{-7} & 0 & 1.0 \end{pmatrix} \begin{pmatrix} h_1 \\ h_2 \\ h_3 \end{pmatrix}. \quad (4.15)$$

High scale parameters		Low scale parameters		Particle	Mass [GeV]
κ	-1.0	κ	-1.0	$\tilde{o}_7$	14.0
χ	-0.0008	χ	-0.0005	$\tilde{o}_1$	5.2
α_h	0.0031	α_h	0.003	$\tilde{o}_2$	25.9
α_S	0.011	α_S	0.010	γ'	11.6
M_λ	21.4 GeV	M_λ	20.7 GeV	H_+	11.6
$m^2_{H_+}$	101^2 GeV^2	$m^2_{H_+}$	-66.8 GeV^2	H_-	7.7
$m^2_{H_-}$	101^2 GeV^2	$m^2_{H_-}$	-68.9 GeV^2	S	406
m^2_S	418^2 GeV^2	m^2_S	406^2 GeV^2		
A_S	-0.2 GeV	A_S	-1.5 GeV		

Table 4.1: Parameters and particle masses of an example gravity mediated hidden sector model in which the hidden sector gauge symmetry is broken radiatively. The Majorana fermion dark matter particle $\tilde{o}_1$ has a mass of 5.2 GeV and constitutes with $\Omega_{\tilde{o}_1} h^2 = 0.112$ the total relic abundance. The model is consistent with all direct detection constraints. The scattering cross sections are $\sigma_p^{\mathrm{SI}} = 3.8 \times 10^{-47}$ cm^2, $\sigma_p^{\mathrm{SD}} = 2.8 \times 10^{-38}$ cm^2 and $\sigma_n^{\mathrm{SD}} = 2.2 \times 10^{-38}$ cm^2 and thus beyond the reach of current experiments.

4.3.2 Models with visible sector induced breaking

In the following, the gauge symmetry in the hidden sector is assumed to be broken by the effective Fayet–Iliopoulos term, as described in Sec. 1.4.3.4. In this scenario, the dark matter particle can be either a Dirac fermion or a Majorana fermion, cf. Sec. 1.4.3.5. The direct detection signature of both candidates is quite different since the scattering of the former is expected to be mostly spin-independent while it is dominantly spin-dependent for the latter. Therefore, the cases in which the Dirac fermion constitutes the dark matter particle resemble to some extend the toy model of Sec. 4.2. The cases in which the dark matter is provided by the Majorana fermion have some similarities to the models with radiative breaking domination of Sec. 4.3.1. The details and differences will become clear in the following discussion of the parameter space and the results for

the relic abundance and the scattering cross sections. Again, we give also a concrete example of one viable model with explicit numbers.

4.3.2.1 Parameter scan for visible sector induced breaking

We search for viable models with visible sector induced breaking by scanning over the parameters at the low-energy scale. Thereby, we again insist on the perturbativity for the Yukawa coupling λ_S and the hidden sector gauge coupling g_h, like in the models with radiative breaking domination. The soft supersymmetry breaking masses are chosen to be small which is, for example, possible when they are induced in gauge mediation or by sequestering of the hidden sector. We are again interested in a light hidden sector with hidden photon mass and dark matter mass up to 40 GeV. Phenomenologically, the results of this subsection can be considered to be a detailed examination of the model of [146] with the following two differences. In our models, in contrast to [146], the gravitino mass is large and the kinetic mixing χ is linked to the gauge coupling g_h via the relation in Eq. (1.21).

As discussed in Sec. 1.4.3.5, depending on the particular low-energy parameters, the dark matter candidate in these models can be either the Majorana fermion $\tilde{o}_1$ or the Dirac fermion $\tilde{o}_7$. With the different low-energy parameters obtained from the scans, we again use micrOMEGAs to compute for both dark matter particles the relic abundance and the various scattering cross sections which are relevant for direct detection. Applying all constraints discussed in Sec. 4.1, yields the viable models shown in Fig. 4.7, in the plane of the absolute value of the kinetic mixing χ versus the hidden photon mass $m_{\gamma'}$. In this figure, both plots contain only points which are in agreement with all direct detection limits specified in Sec. 4.1.3 including the one from the SIMPLE experiment. The colour code in both plots and in all other plots throughout this section is identical to the one used in Fig. 4.3 for the scatter plots of the toy model. The dark matter candidate in the dark green regions possesses the correct relic abundance and in the light green areas it is subdominant. As in Fig. 4.3, the coloured lines represent the constraints from Standard Model precision measurements (long-dashed cyan line), the muon anomalous magnetic moment (dash-dotted brown line) as well as the model-dependent BaBar limit (short-dashed orange line). In the two plots of Fig. 4.7, the effect of allowing for a variation in κ is illustrated. The parameter space expands quite strongly from keeping $\kappa = 1$ fixed in the left-hand plot to scanning over κ the range $0.1 \leq \kappa \leq 10$, as shown in the right-hand plot.

Even though in the models of this section the dark matter candidate can also be a Dirac fermion just like in the toy model, there are no viable models with parameters in the lower right area of the plots in Fig. 4.7. This is in strong contrast to the scatter plot of the toy model in Fig. 4.3. This contrast arises since in the models here the dark matter particle can never be heavier than the hidden photon. It can be seen from

Eq. (1.34) that there is always a Majorana fermion with mass equal or less than $m_{\gamma'}$. For the Dirac fermion to be the dark matter particle, it is required to be even lighter than the Majorana fermion. It is then necessarily also lighter than the hidden photon. Thus, in the models with visible sector induced breaking, the dark matter particle can never annihilate via the t-channel diagram shown on the right side of Fig. 4.1. The lower right part of the parameter space is therefore empty, in contrast to the toy model, where it was filled by dark green points obtaining the correct relic abundance from the t-channel annihilation (like those in the horizontal band in Fig. 4.2). The coarser grid and small holes in the scatter plots of this section, compared to the ones of the toy model, is caused by the fact that the parameter space here can not be scanned as continuously as for the toy model.

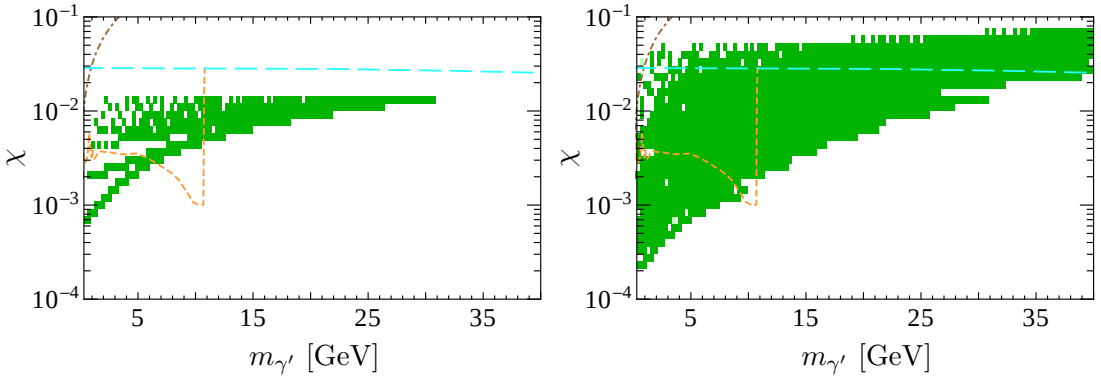

Figure 4.7: Viable models with visible sector induced breaking of the hidden gauge symmetry for fixed $\kappa = 1$ *(left)* or scanned over κ in the range $0.1 \leq \kappa \leq 10$ *(right)*. In the plane of the magnitude of the kinetic mixing χ versus the hidden photon mass $m_{\gamma'}$, dark green points represent models that give the correct relic abundance and light green ones provide a subdominant dark matter candidate. All models are in agreement with all constraints from direct detection including SIMPLE. Lines represent limits from Standard Model precision measurements (long-dashed cyan line), a model-dependent BaBar search (short-dashed orange line) and the muon anomalous magnetic moment (dash-dotted brown line).
Left: $\kappa = 1$. *Right:* $0.1 \leq \kappa \leq 10$.

Since the Dirac fermion dark matter candidate is expected to show in the direct detection experiments which are looking for spin-independent scattering, we can compare its cross sections to the signal claims of DAMA and CoGeNT. As in the toy model, the scattering cross sections obtained with micrOMEGAs have to be rescaled by Eq. (4.8) for subdominant dark matter particles. Additionally, the experimental limits and signal regions for the spin-independent case have to be rescaled by Eq. (4.6) to take into account that the Dirac fermion scatters exclusively on protons. The models in which the dark matter particle can explain the direct detection signals are represented in different colours in Fig. 4.8 in the plane of the magnitude of kinetic mixing versus the hidden photon mass. As in the right-hand plot of Fig. 4.7, the parameter space is scanned over $0.1 \leq \kappa \leq 10$ and all direct detection constraints are applied. Again, dark and

light green colours indicate models which give a dark matter candidate with the total or a subdominant relic abundance, respectively. Overlaid on the green areas, we present in different colours the regions of interest for the different direct detection claims. In the left-hand plot, the purple points correspond to models where the scattering cross section is in agreement with the CoGeNT signal for the Standard Halo Model (SHM). The effect of changing the halo model is then displayed in the right-hand plot where the Einasto profile is used (a similar picture is obtained for an isothermal or an NFW profile, cf. [81] for details on the halo models). In this scenario, also a part of the DAMA favoured region is allowed by the direct detection constraints and the models with the corresponding cross sections are represented in red. The models shown in blue provide scattering cross sections that simultaneously fit the DAMA and the CoGeNT signals. In both plots, the dark matter particle explaining the direct detection signals is always a subdominant Dirac fermion independent of the halo model, as will become evident from the following discussion and Fig. 4.9.

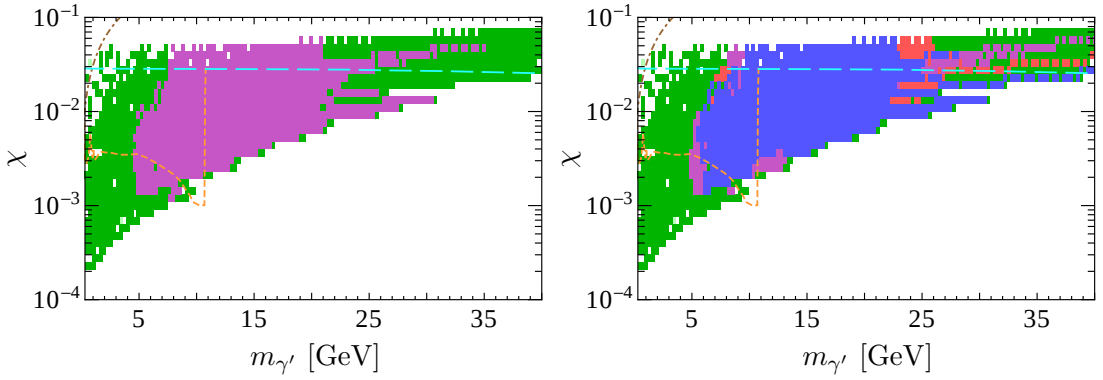

Figure 4.8: Viable models with visible sector induced breaking overlaid with coloured regions in which the scattering cross sections can explain the different direct detection claims (rescaled to scattering on protons). Both plots are scanned over $0.1 \leq \kappa \leq 10$ and shown in the plane of the magnitude of the kinetic mixing χ versus the hidden photon mass $m_{\gamma'}$. As in Fig. 4.7, all points are in agreement with all direct detection limits including SIMPLE and coloured lines give constraints. Green areas again indicate the relic abundance.
Left: Cross sections in the purple areas fit the CoGeNT signal for the SHM. In these regions, the dark matter is subdominant and the cross sections are rescaled with the relic abundance.
Right: For an Einasto profile, cross sections can explain CoGeNT in the purple regions, DAMA in the red ones and both simultaneously in the blue regions. Again the dark matter is subdominant and the cross sections are rescaled accordingly.

In Fig. 4.9, the spin-independent scattering cross sections σ_p^{SI} on protons, computed with micrOMEGAs, are plotted as a function of the dark matter mass, scanned over the kinetic mixing χ, the hidden photon mass $m_{\gamma'}$ and the parameter κ in the range $0.1 \leq \kappa \leq 10$. Dark green colours correspond again to models providing the correct relic abundance and light green ones to subdominant dark matter candidates. For the latter, the scattering cross sections have been rescaled with the relic abundance by Eq. (4.8)

to account for the lower local dark matter density. The coloured lines represent the limits and signal regions of the direct detection experiments discussed in Sec. 4.1.3. For these limits and signal regions, the original cross sections for scattering per nucleon have been rescaled to those on protons according to Eq. (4.6). In the left-hand plot, the Standard Halo Model (SHM) has been used and in the right-hand plot an Einasto profile. It can be seen that for the SHM only the CoGeNT region (purple) is allowed by the XENON100 (dash-dotted blue) and CDMSSi (dashed turquoise) limits while the DAMA region (red/orange) is excluded. For the Einasto profile, also a part of DAMA is allowed and overlaps with CoGeNT. This explains that there are solely purple regions in the left-hand plot of Fig. 4.8 while the right-hand plot contains in addition red and blue ones. Furthermore, it can be seen that the dark matter particle responsible for explaining the direct detection signals is subdominant since the signal regions lie in a light green area.

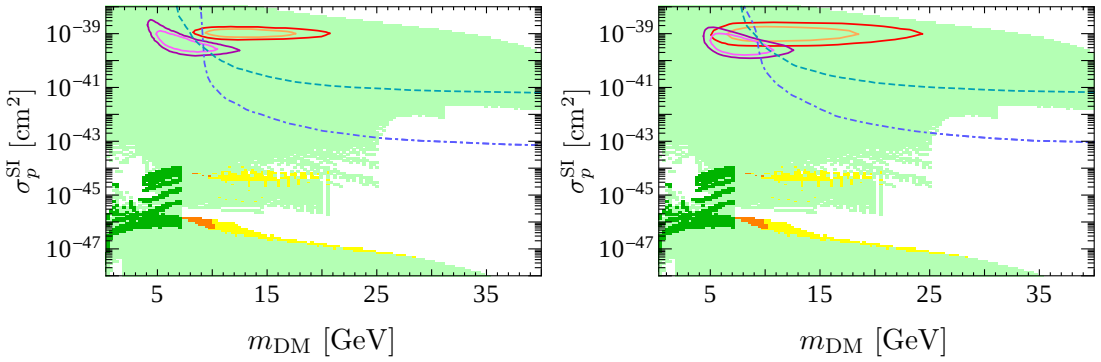

Figure 4.9: Cross sections σ_p^{SI} for spin-independent scattering on protons for models with visible sector induced breaking scanned over $0.1 \leq \kappa \leq 10$. In the light green regions, the cross sections are rescaled to account for the smaller local density of the subdominant dark matter candidate. Both plots split into two disjoint green areas: the dark matter particle is the Dirac fermion $\tilde{o}_7$ in the upper region and the Majorana fermion $\tilde{o}_1$ in the lower one. Points in yellow and orange lie above the SIMPLE limit of Fig. 4.10 on σ_p^{SD} and give a subdominant and the total relic abundance, respectively. Signal contours from CoGeNT (purple lines) and DAMA (red/orange lines) are shown together with exclusion limits from CDMSSi (dashed turquoise line) and XENON100 (dash-dotted blue line). All have been rescaled to scattering on protons and are given for two different halo models.
Left: The Standard Halo Model (SHM) as define in [81] is assumed.
Right: The Einasto profile has been used.

The plots showing the spin-independent scattering cross section in Fig. 4.9 appear to be split into two disjoint regions. These regions are caused by the two dark matter candidates which are possible in the different models with visible sector induced breaking. The Dirac fermion $\tilde{o}_7$ on the one hand has large spin-independent scattering cross sections and corresponds to the upper light green region. These cross sections are, as in the toy model scenario, in the range of current direct detection experiments and may explain

the signals in DAMA and CoGeNT. In contrast to the toy model, this is, however, only possible with a subdominant dark matter candidate. Similar to the radiatively-induced breaking case discussed in Sec. 4.3.1, the Majorana fermion $\tilde{o}_1$ on the other hand has very small spin-independent scattering cross sections despite the contribution from the Higgs portal term and squark exchange. They are below $\sim 10^{-45}$ cm^2 and correspond to the lower region in the plots (light green area and thin stripe of dark green). The plots only show the cross sections for scattering on protons since they are the dominant ones for the Dirac fermion. For the Majorana fermion, those for scattering on neutrons are roughly of the same size since they arise from the Higgs portal term which is not isospin-violating. The yellow and orange points in both plots of Fig. 4.9 show the effect of including the constraint from the SIMPLE experiment. In contrast to the green areas which are in agreement with this bound, those regions indicate models for which the spin-dependent scattering cross section on protons is in conflict with the SIMPLE limit. The models shown in yellow contain a subdominant dark matter candidate and those in orange provide the correct relic abundance.

The cross sections σ_p^{SD} and σ_n^{SD} for spin-dependent scattering on protons and on neutrons, respectively, are presented in Fig. 4.10. They were again obtained with micrOMEGAs and have been scanned over $0.1 \leq \kappa \leq 10$. As in Fig. 4.6, the lines illustrate the limits from the direct detection experiments described in Sec. 4.1.3. In the

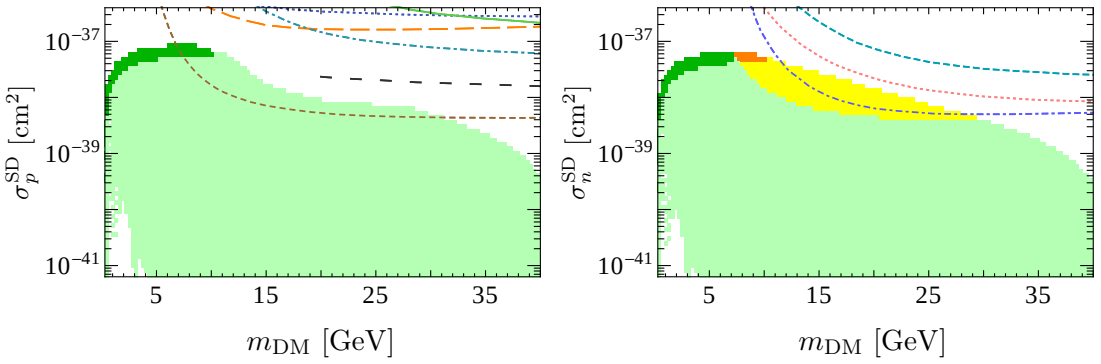

Figure 4.10: Cross sections for spin-dependent scattering in models with visible sector induced breaking, scanned over $0.1 \leq \kappa \leq 10$. Exclusion contours from the corresponding direct detection experiments are as described in Fig. 4.6. Cross sections in the light green areas are rescaled because the dark matter particle is subdominant. The plots only contain models in which the Majorana fermion $\tilde{o}_1$ is the dark matter candidate since the spin-dependent scattering cross sections of the Dirac fermion $\tilde{o}_7$ are too small to appear.
Left: Cross sections σ_p^{SD} for spin-dependent scattering on protons. Besides the limits given in Fig. 4.6, the KIMS limit is shown as solid green line (note that the lowest lying, short-dashed brown line is the SIMPLE limit).
Right: Cross sections σ_n^{SD} for spin-dependent scattering on neutrons. Points in yellow and orange lie above the SIMPLE limit and give a subdominant and total relic density, respectively.

left-hand plot for scattering on protons, the different limits on σ_p^{SD} arise from SIMPLE (short-dashed brown line), PICASSO (long-dashed orange line), COUPP2011 (dash-dotted turquoise line), COUPP2007 (dotted blue line), Super-K (dashed black line) and KIMS (solid green line). In the right-hand plot, the cross sections σ_n^{SD} for scattering on neutrons are given together with the limits from XENON10 (dash-dotted blue line), Zeplin (dotted pink line) and CDMS (dashed turquoise line). The left-hand plot shows which models lie above the SIMPLE limit on σ_p^{SD} and are potentially excluded. These models correspond to the above-mentioned yellow and orange regions, which are shown in the right-hand plot for σ_p^{SD} and in Fig. 4.9 for σ_p^{SI}. All points contained in Fig. 4.10, represent models where the Majorana fermion $\tilde{o}_1$ is the dark matter candidate since the Dirac fermion $\tilde{o}_7$ possesses almost no spin-dependent scattering on nuclei. Therefore, in the plots for spin-independent scattering in Fig. 4.9, the effect of the SIMPLE exclusion limit only matters for the lower regions in which the Majorana fermion is the dark matter particle. Like in the case of spin-independent scattering, the Majorana fermion also exhibits roughly the same cross sections for spin-dependent scattering on protons and on neutrons. The limit on σ_p^{SD} from SIMPLE (left-hand plot) is, however, more constraining than the limit on σ_n^{SD} from XENON10 (right-hand plot). Each plot in Figs. 4.9 and 4.10 contains only those models which are in agreement with all the limits shown in the other plots.

4.3.2.2 Example model with visible sector induced breaking

In the following, we present the specific parameters, cross sections and other relevant quantities for one particular model that can explain the CoGeNT signal for a Standard Halo Model and both DAMA and CoGeNT signals for an Einasto profile. The low scale parameters and the resulting particle spectrum is given in Tab. 4.2. We take, at the low-energy scale, $\kappa = -10$ and $\alpha_h = 0.040 \equiv g_h^2/4\pi$, which corresponds according to Eq. (1.21) to $\chi = -0.016$, and set $\alpha_S = 0.027 \equiv \lambda_S^2/4\pi$. The soft masses are given by sequestered values $M_\lambda = m_{H_+} = m_{H_-} = m_S = 1$ GeV and the hidden A-term vanishes, $A_S = 0$.

The Dirac fermion $\tilde{o}_7$ is the lightest hidden sector particle with a mass of 6.4 GeV. It has a relic abundance of $\Omega_{\tilde{o}_7} h^2 = 0.0023$ and is thus a subdominant dark matter candidate. Its spin-independent scattering is as expected almost entirely on protons. We find the corresponding effective scattering cross section of $\sigma_p^{\mathrm{SI}} = 5.5 \times 10^{-40}$ cm^2 after rescaling with the dark matter abundance according to Eq. (4.8). The hidden photon and the hidden Higgs both have a mass of 10.7 GeV. Their widths are 3.4×10^{-5} GeV and 1.6×10^{-10} GeV, respectively. The hidden photon decays mostly into light leptons and quarks and the hidden Higgs dominantly to $b\bar{b}$, $c\bar{c}$ and $\tau^+\tau^-$.

Using in the visible sector for the MSSM the parameters at the SPS1b benchmark point [328], the full neutralino mass matrix in the basis ($B_0,\ W_0,\ h_u^0,\ h_d^0,\ \tilde{\lambda},\ \tilde{h}_+$) reads

$$\mathcal{M}_{\text{neutralino}} = \begin{pmatrix} 166 & 0.00 & -2.73 & 43.8 & -0.02 & -0.17 \\ 0.00 & 310 & 2.73 & -79.9 & 0.00 & 0.00 \\ -2.73 & 2.73 & 0.00 & -512 & 0.00 & 0.00 \\ 43.8 & -79.9 & -512 & 0.00 & 0.00 & 0.00 \\ -0.02 & 0.00 & 0.00 & 0.00 & 1.00 & 10.7 \\ -0.17 & 0.00 & 0.00 & 0.00 & 10.7 & 0.00 \end{pmatrix}, \tag{4.16}$$

with all numbers expressed in GeV. The eigenmasses are 10.2, 11.2, 164, 298, 516 and 530 GeV. The mixing between the original Higgs eigenstates and the mass eigenstates is at the same data point found to be

$$\begin{pmatrix} H_+ \\ h \\ H \end{pmatrix} = \begin{pmatrix} 1.0 & -1.1 \times 10^{-3} & 3.7 \times 10^{-6} \\ 1.1 \times 10^{-4} & 1.0 & 0 \\ -3.7 \times 10^{-6} & 0 & 1.0 \end{pmatrix} \begin{pmatrix} h_1 \\ h_2 \\ h_3 \end{pmatrix}. \tag{4.17}$$

Low scale parameters		Particle	Mass [GeV]
κ	-10.0	$\tilde{o}_7$	6.4
χ	-0.016	$\tilde{o}_1$	10.2
α_h	0.038	$\tilde{o}_2$	11.2
α_S	0.027	γ'	10.7
M_λ	1.0 GeV	H_+	10.7
$m^2_{H_+}$	1.0 GeV^2	H_-	6.5
$m^2_{H_-}$	1.0 GeV^2	S	6.6
m^2_S	1.0 GeV^2		
A_S	0.0		

Table 4.2: Hidden sector low scale parameters and particle masses for an example sequestered model in which the hidden gauge symmetry breaking is induced by the visible sector. The Dirac fermion $\tilde{o}_7$ has a relic density of $\Omega_{\tilde{o}_7}h^2 = 2.3 \times 10^{-3}$ and is thus a subdominant dark matter particle. The rescaled direct detection cross section for spin-independent scattering on protons is $\sigma_p^{\text{SI}} = 5.5 \times 10^{-40}$ cm^2. The model is consistent with all direct detection limits. It can explain the CoGeNT signal for a SHM and also DAMA for an Einasto profile.

4.3.2.3 Low mass region

In contrast to the previous section, in which we studied hidden photons in the GeV range, the following results for models with visible sector induced breaking are focused on masses below 1 GeV. Such light masses are of particular interest in view of the searches for hidden photons that are already running or planned for the near future, as discussed in Sec. 3.5. To obtain such light masses in these models, however, requires some amount of fine-tuning. Scanning over the low-energy parameters, as in Sec. 4.3.2.1, we again compute the relic abundance and scattering cross sections of the dark matter particle with micrOMEGAs. The allowed models, scanned over κ in the range $0.1 \leq \kappa \leq 10$, are shown in Fig. 4.11 in the plane of the absolute value of the kinetic mixing χ versus the hidden photon mass $m_{\gamma'}$. The same colour code as in the previous sections is used to discriminate between dark matter candidates with the total relic abundance (dark green) and subdominant ones (light green). The grey areas are the constraints on hidden photons presented in Secs. 3.3 and 3.4. The coloured lines indicate the sensitivities of future searches for hidden photons, as discussed in Sec. 3.5. Numerous models are found to contain a viable dark matter candidate and possess a hidden photon in the region of interest for these experiments.

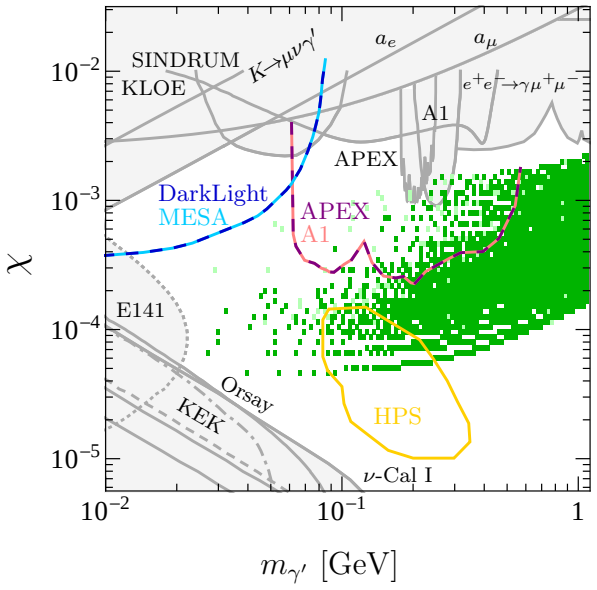

Figure 4.11: Viable models with visible sector induced breaking and a light hidden photon in the plane of the magnitude of the kinetic mixing χ versus the hidden photon mass $m_{\gamma'}$, scanned over $0.1 \leq \kappa \leq 10$. Dark green points represent models which give the correct relic abundance, light green ones provide a subdominant dark matter candidate. As in Fig. 4.2, grey areas and coloured lines are constraints and sensitivities of future searches for hidden photons, respectively.

As in Sec. 4.3.2.1, the dark matter particle can be either a Dirac fermion or a Majorana fermion. Furthermore, in the considered models with visible sector induced breaking, the dark matter particle can never be heavier than the hidden photon, as discussed earlier. Since we focus on models with a very light hidden photon, the mass of the dark matter particle is then always below 1 GeV throughout this section. Such small masses are, however, below the threshold of direct detection experiments. Therefore, the corresponding limits of these experiments, which are summarised in Sec. 4.1.3, do not apply here. The direct detection cross sections, obtained with micrOMEGAs and rescaled according to Eq. (4.8), are shown in Fig. 4.12 for spin-independent (left-hand plot) and spin-dependent (right-hand plot) scattering on protons. Similar to the results obtained at higher masses in Sec. 4.3.2.1, cf. Fig. 4.9, the spin-independent scattering cross sections split again into two distinct regions. In the upper one, the dark matter candidate is the Dirac fermion and in the lower one it is the Majorana fermion. For the spin-dependent case, the cross sections for scattering on protons and on neutrons are again roughly the same and only the former ones are displayed in the right-hand plot of Fig. 4.12. This plot contains models in which the Majorana fermion is the dark matter particle since the Dirac fermion has negligible spin-dependent scattering.

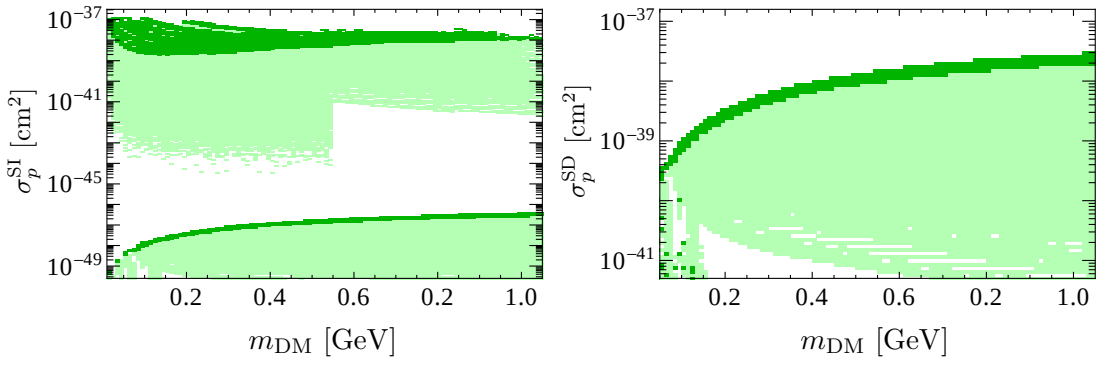

Figure 4.12: Scattering cross sections for a light dark matter candidate in models with visible sector induced breaking for $0.1 \leq \kappa \leq 10$. Points in dark green correspond to models that provide the total relic abundance. For points in light green, which give a subdominant dark matter candidate, the cross sections have been rescaled to account for the lower local density. All dark matter masses are below the threshold of direct detection experiments.
Left: Cross sections σ_p^{SI} for spin-independent scattering on protons.
Right: Cross sections σ_p^{SD} for spin-dependent scattering on protons. Cross sections σ_n^{SD} for spin-dependent scattering on neutrons are similar.

For the considered models with a very light hidden sector, it is not possible to probe the dark matter particle with conventional direct detection experiments. Since the dark matter is so light, its scattering on the heavy target nuclei produces a nuclear recoil energy which is well below the energy threshold of these experiments. Other detection methods are therefore required to probe such light dark matter particles. The DAMIC experiment [329] searches for low mass dark matter with Charge Coupled

Devices (CCDs) detectors and released a first limit for masses down to 1.2 GeV and cross sections $\sim 3 \times 10^{-39}$ cm^2, cf. also Sec. 4.4. The next run of this experiment will not only reach lower cross sections but might also probe even smaller masses like the ones obtained in our models. Another possibility suggested in [330] is to search for the scattering of light dark matter on electrons rather than on nuclei. According to [330], this scattering on electrons would allow experiments with xenon, argon, helium, or germanium targets to probe dark matter with masses in the MeV range. The light dark matter particle of our models scatters on electrons mediated by the hidden photon and could then also be searched for by those experiments. Finally, for these light hidden sectors, the hidden photon may instead be detected in the fixed target experiments shown in Fig. 4.11, particularly if the hidden photon cannot decay to hidden matter (as in the reasonably generic case when the dark matter particle has mass near that of the hidden photon).

4.4 Implications of updated direct detection data

Some of the direct detection experiments, used in the previous sections to constrain the dark matter scattering cross sections, improved their limits since our analysis was performed. In this section, the effect of these new constraints on the different models is studied. We present updated versions of the results which were derived for the toy model in Sec. 4.2 and for the supersymmetric models with radiative breaking domination in Sec. 4.3.1 and with visible sector induced breaking in Sec. 4.3.2. In addition, we change the requirement on the relic abundance to the most recent Planck [45] measurement of $\Omega_{\rm DM}h^2 = 0.1196 \pm 0.0031$, cf. Eq. (1.3). Models giving an abundance within 3σ of this result are considered to provide the entire dark matter in the Universe, those with a lower abundance yield a subdominant dark matter candidate.

For the direct detection experiments sensitive to spin-independent scattering of dark matter, for which we used the limits derived in [81], the strongest additional bounds arise from the following three experiments:

- The DAMIC experiment [329] places a constraint on dark matter masses in the range $1.2 \lesssim m_{\rm DM} \lesssim 10$ GeV and cross sections for scattering on nucleons of about $\sigma_{\rm N}^{\rm SI} \sim 3 \times 10^{-39}$ cm^2.
- A special search for light dark matter enabled XENON10 [331] to constrain masses down to 4 GeV with scattering cross sections on nucleons of $\sigma_{\rm N}^{\rm SI} \sim 10^{-39}$ cm^2, while the limit weakens to about $\sigma_{\rm N}^{\rm SI} \sim 10^{-42}$ cm^2 for masses $\mathcal{O}(10$ GeV$)$.[6]

[6] The limit which was originally published by XENON10 and has been used throughout this section was changed in an erratum of [331] when this thesis was about to be finished. The corrected limit is weaker and therefore less constraining for the parameter space of our models. Some of the signal regions might also still be allowed. These changes will be included in future work [332].

- The limit from XENON100 used in the previous sections was based on data from 100 live days of the experiment. The newer limit [87] with 225 live days of data provides currently the strongest bound for dark matter masses above 8 GeV.

For the Dirac fermion dark matter candidate of our models, these limits again have to be rescaled according to Eq. (4.6) to cross sections for scattering on protons. These improved bounds further increase the tension with the signal claims by DAMA and CoGeNT, which were considered in the previous sections. Most of their preferred regions (if not all) are in contradiction with these limits, especially with XENON100 (the same applies also to the signal claims by CRESST and CDMS). Therefore, in this section, we do no longer study if our models can reproduce the cross sections required to explain those signals but instead only apply the updated limits. We assume that the signals are excluded when the most simple settings for the standard dark matter halo are considered. We then do not anymore plot the DAMA and CoGeNT regions from [81] as in the previous sections, but instead the DAMA, CoGeNT and CRESST regions as given in [87].

On the spin-dependent side, new limits were released by PICASSO2012 [333] and COUPP2012 [334] for scattering on protons. The former constrains masses down to $\sim$ 4 GeV and is for light dark matter stronger than the SIMPLE limit, which was partly included in our previous analysis. The latter has a similar but slightly weaker exclusion curve as SIMPLE. The previous bounds for scattering on neutrons were significantly improved to cross sections of $\sigma_{\mathrm{n}}^{\mathrm{SD}} \sim 10^{-40}$ cm^2 for masses of 10 GeV by the XENON100 [335] experiment. In the same analysis, XENON100 published also a limit on spin-dependent scattering on protons which is stronger than the ones used in our previous analysis (except for the one by SIMPLE) but not competitive to the updates of PICASSO2012 and COUPP2012. We then apply these four recent bounds to the spin-dependent scattering cross sections in our new analysis. As a consequence of this, the effect of including or neglecting the SIMPLE limit, which was displayed in our analysis by the yellow and orange colouring (cf. Figs. 4.6, 4.9 and 4.10) is reduced, as shown in the subsequent figures.

In the following, we present the new results for the toy model and the supersymmetric models with radiative breaking domination and visible sector induced breaking. They take into account all the updated limits from direct detection experiments.

4.4.1 Toy model

The toy model has been introduced in Sec. 1.4.2 and analysed in detail in Sec. 4.2. Since its dark matter candidate is a Dirac fermion it has only spin-independent scattering on protons. The relevant new constraints on the corresponding cross sections are thus the ones from DAMIC, XENON10 and XENON100. The cross sections obtained with micrOMEGAs have again to be rescaled by Eq. (4.8) for subdominant dark matter

particles. The direct detection limits must be rescaled by Eq. (4.6) to limits for scattering on protons. For the case considered in Fig. 4.2, i.e. $m_\psi = 6$ GeV, the analogous picture with the improved limits is shown in Fig. 4.13. Instead of the three green lines giving the correct abundance for different values of κ, we here only show the case for $\kappa = 0.1$ corresponding to the lowest green line. In the light green area, the dark matter particle is subdominant Again, the grey areas give constraints and the coloured lines sensitivities of future searches for hidden photons. The purple band indicates the region where the cross sections are able to explain the CoGeNT signal. However, as indicated by the coloured lines and the hatched area, this region is entirely excluded by the recent limit from XENON10 (black line). This is in contrast to the earlier case of Fig. 4.2 where a dark matter mass of 6 GeV was still unconstrained and the CoGeNT preferred region was in agreement with the direct detection limits.

A scan over the dark matter mass in the range 0.8 GeV to 25 GeV is then shown for $\kappa = 1$ in Fig. 4.14, again in the plane of kinetic mixing χ versus hidden photon mass $m_{\gamma'}$. This plot is equivalent to the left one of Fig. 4.3. As expected, the new plot does no longer contain purple points since the CoGeNT region is excluded by the updated direct detection limits. Furthermore, a large part of the parameter space which was displayed in dark green is now shown in light green. The reason for this is that the corresponding models, which gave the correct relic abundance and were shown in

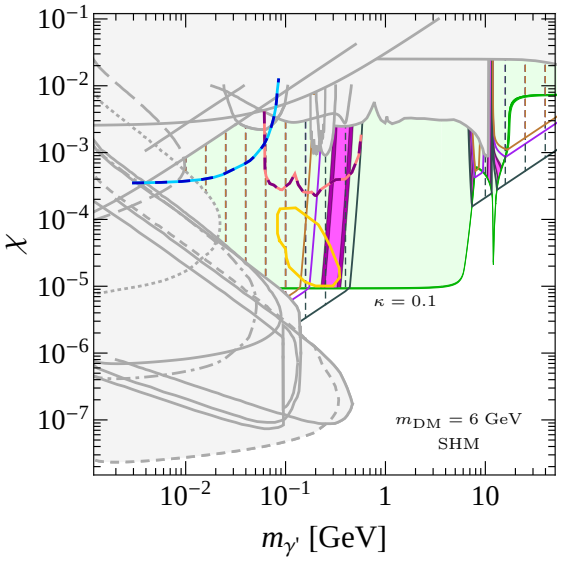

Figure 4.13: Allowed parameter space for the toy model with $m_\psi = 6$ GeV and $\kappa = 0.1$ when taking into account the updated direct detection limits. The thin dark green line gives the correct relic abundance, in the light green area the dark matter particle is subdominant. As in Fig. 4.2, the grey areas are excluded and the coloured lines represent the sensitivities of future searches for hidden photons. The coloured lines and hatched regions show the limits from the recent direct detection experiments: DAMIC in brown, XENON10 in black and XENON100 in purple. In contrast to Fig. 4.2, the purple band indicating the CoGeNT preferred region is now excluded by XENON10 for the Standard Halo Model.

dark green, are now excluded since they do not fulfil the improved direct detection bounds. Then, the only remaining viable scenarios in this region of the parameter space correspond to subdominant dark matter candidates. There are, however, still many viable models that survive the new limits and give the correct relic abundance or a subdominant dark matter candidate.

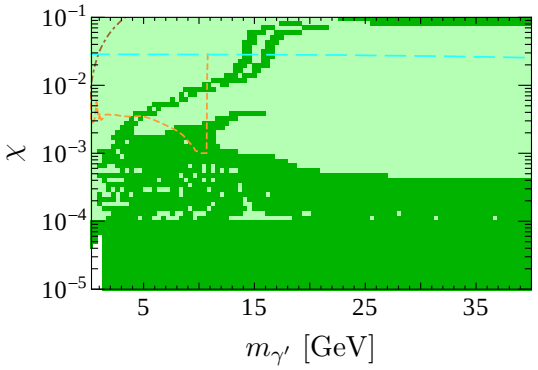

Figure 4.14: Allowed parameter space for the toy model when taking into account the updated direct detection limits, for $\kappa = 1$ and scanned over the dark matter masses in the range from 0.8 GeV to 25 GeV. As in Fig. 4.3, points in green (light green) give the correct (subdominant) relic abundance and the lines represent different limits. In contrast to the left-hand plot of Fig. 4.3, the purple CoGeNT region has disappeared since it is not allowed by the new direct detection constraints.

4.4.2 Models with radiative breaking domination

For the supersymmetric models with radiative breaking domination, the dark matter candidate is a Majorana fermion. As discussed in Sec. 4.3.1, the Majorana fermion has tiny spin-independent scattering so that only direct detection experiments which are sensitive to spin-dependent scattering can probe these models. Therefore, the relevant updates are the ones on the spin-dependent side by PICASSO2012, COUPP2012 and XENON100. Taking these new limits into account, the parameter space with the viable models is shown in Fig. 4.15, in the plane of the magnitude of the kinetic mixing χ versus the hidden photon mass $m_{\gamma'}$. These displayed models are in agreement with all direct detection constraints and either provide the correct relic abundance (dark green) or a subdominant dark matter candidate (light green). Again, the different direct detection cross sections have been computed with micrOMEGAs and rescaled according to Eq. (4.8) for subdominant dark matter candidates.

Compared to the analysis of Sec. 4.3.1, we find that more models are excluded than in Fig. 4.4, where the SIMPLE limit was not applied. The current result is, however, essentially the same as the one in Fig. 4.5, in which the SIMPLE limit was taken into account. Thus, the updated limits do not constrain the parameter space significantly stronger

than the SIMPLE limit did. This becomes also apparent in the plots with the corresponding direct detection cross sections for spin-dependent scattering on protons and on neutrons, shown in Fig. 4.16. Besides the previous limits presented in Fig. 4.6, lines for the updated ones from PICASSO2012 (long-dashed orange), COUPP2012 (dash-dotted turquoise) and XENON100 (long-dashed purple) on σ_p^{SD} are contained in the left-hand plot and from XENON100 (long-dashed purple) on σ_n^{SD} in the right-hand plot. COUPP2012 and PICASSO2012 almost close the gap to the SIMPLE limit. Therefore, the effect of including or disregarding the SIMPLE limit is reduced. There are then fewer yellow or orange models which represent the ones in conflict with SIMPLE (yellow indicating subdominant dark matter and orange the correct relic abundance). Since the SIMPLE limit remains the strongest one on σ_p^{SD}, the updates by COUPP2012 and PICASSO2012 do not improve compared to the previous situation when SIMPLE was included. However, the XENON100 limit on σ_n^{SD} does exclude a few models which were previously allowed by all limits (also SIMPLE), as shown in the right-hand plot by the light green points which lie above the long-dashed purple line.

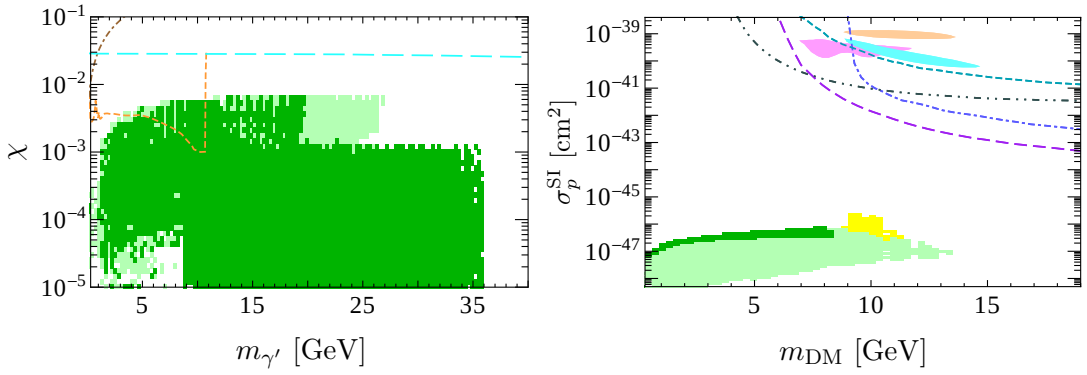

Figure 4.15: Viable models with radiative breaking domination after taking into account the updated direct detection limits and scanned over $0.1 \leq \kappa \leq 10$. Points in green (light green) give the correct (subdominant) relic abundance.
Left: Models in the plane of the magnitude of the kinetic mixing χ versus the hidden photon mass $m_{\gamma'}$. Coloured lines are constraints as in Fig. 4.5.
Right: Cross sections σ_p^{SI} for spin-independent scattering on protons together with lines for new limits from XENON10 (dash-double dotted black) and XENON100 (long-dashed purple) as well as the shaded signal regions from DAMA (orange), CoGeNT (pink) and CRESST (cyan). Old exclusion lines from CDMSSi (dashed turquoise) and XENON100 (dash-dotted blue) are as in Fig. 4.6. Points in yellow lie above the SIMPLE limit and are subdominant.

For spin-independent scattering, the corresponding cross sections for the Majorana fermion are, as expected, very small since they only arise from the Higgs portal term, which gives a small cross section. They are shown in the right-hand plot of Fig. 4.15. Similar to the situation in Fig. 4.6, the cross sections are much below the reach of current experiments. Therefore, they are not affected by the new limits from XENON10 (dash-double dotted black line) and XENON100 (long-dashed purple line).

Altogether, many models with radiative breaking domination are still allowed after including the updated limits. Future direct detection experiments can further probe the spin-dependent scattering of the Majorana fermion dark matter candidate.

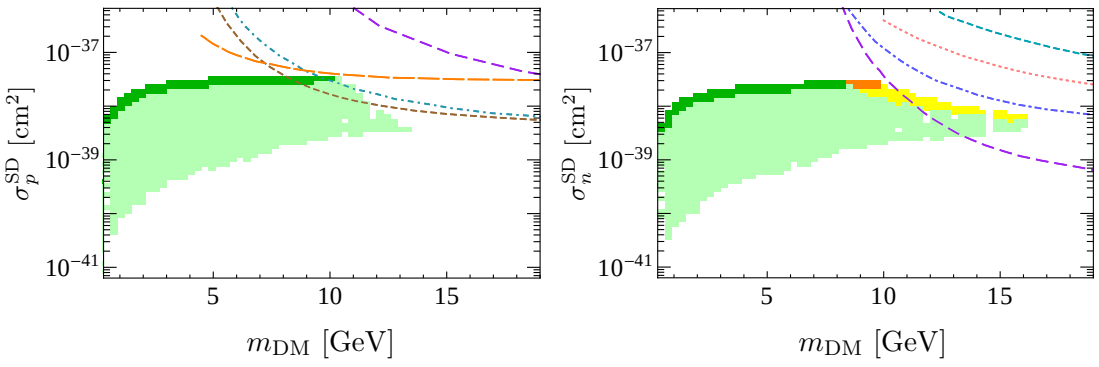

Figure 4.16: Cross sections for spin-dependent scattering in models with visible sector induced breaking together with updated direct detection limits for $0.1 \leq \kappa \leq 10$. As in Fig. 4.6, points in green (light green) are allowed with all other constraints and give the correct (subdominant) relic abundance, orange (yellow) ones give the correct (subdominant) abundance but lie above the SIMPLE limit.
Left: Cross sections σ_p^{SD} for scattering on protons and lines for new limits from COUPP2012 (dash-dotted turquoise), PICASSO2012 (long-dashed orange) and XENON100 (long-dashed purple) as well as the old limit from SIMPLE (short-dashed brown).
Right: Cross sections σ_n^{SD} for scattering on neutrons together with the lines for the new limit from XENON100 (long-dashed purple) as well as the old limits from XENON10 (dash-dotted blue), Zeplin (dotted pink) and CDMS (dashed turquoise).

4.4.3 Models with visible sector induced breaking

In the supersymmetric models with visible sector induced breaking, the results presented in Sec. 4.3.2 illustrated the differences with which the two possible dark matter candidates, the Dirac fermion and the Majorana fermion, appear in direct detection experiments. The Dirac fermion shows mostly in spin-independent scattering, similar to the scenario in the toy model. The Majorana fermion has very little spin-independent and dominantly spin-dependent scattering, as in the models with radiative breaking domination. Thus, different direct detection experiments probe the two particles and therefore all aforementioned updates have to be included in order to determine the allowed models. In the plane of the magnitude of the kinetic mixing χ versus the hidden photon mass $m_{\gamma'}$, the region where viable models can be found then reduces to the one shown in the left-hand plot of Fig. 4.17. This plot is the updated equivalent to the right-hand plot of Fig. 4.7, when all new constraints are taken into account. Again, points in dark green give the correct relic abundance and those in light green provide a subdominant dark matter candidate. Several models, which gave the correct relic abundance and were shown in dark green in the right-hand plot of Fig. 4.7, are no longer present in the

left-hand plot of Fig. 4.17. These models are excluded once the updated direct detection constraints are taken into account and only subdominant dark matter candidates are still viable in this region of the parameter space, as discussed in the following.

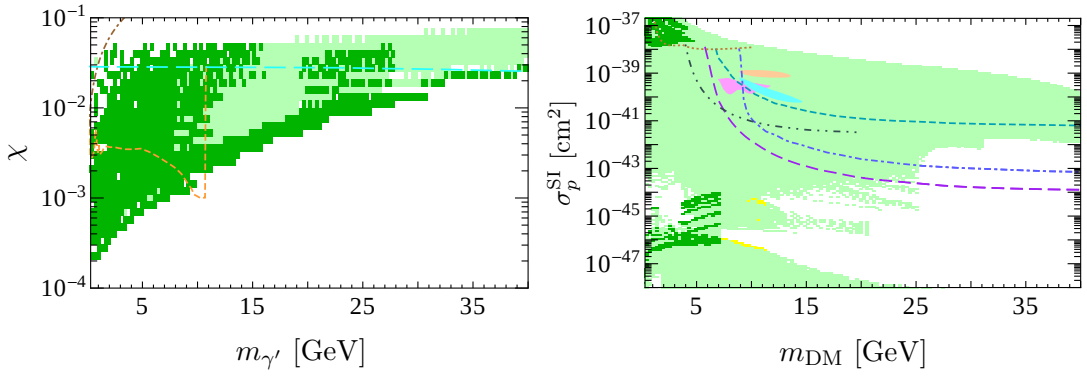

Figure 4.17: Viable models with visible sector induced breaking after taking into account the updated direct detection limits and scanning over $0.1 \leq \kappa \leq 10$. Points shown in green (light green) give the total (subdominant) relic density.
Left: Models in agreement with all direct detection limits in the plane of the magnitude of the kinetic mixing χ versus the hidden photon mass $m_{\gamma'}$. Lines show limits as in Fig. 4.7.
Right: Cross sections σ_p^{SI} for spin-independent scattering on protons together with lines for new limits by DAMIC (dotted brown), XENON10 (dash-double dotted black) and XENON100 (long-dashed purple) as well as old limits by CDMSSi (dashed turquoise) and XENON100 (dash-dotted blue), cf. Fig. 4.9. Shaded areas indicate preferred regions of the signals by DAMA (orange), CoGeNT (pink) and CRESST (cyan). Points in yellow are subdominant and in conflict with SIMPLE.

The direct detection cross sections obtained from micrOMEGAs are again rescaled according to Eq. (4.8) for subdominant dark matter. They are shown together with the respective direct detection limits in the right-hand plot of Fig. 4.17 for spin-independent scattering on protons (σ_p^{SI}) and in Fig. 4.18 for spin-dependent scattering on protons and on neutrons (σ_p^{SD} and σ_n^{SD}). Each plot in both figures contains only models which fulfil all the constraints shown in the other plots. For spin-independent scattering, the experimental limits on the cross section $\sigma_{\mathrm{N}}^{\mathrm{SI}}$ per nucleon have again been rescaled according to Eq. (4.6) to limits on σ_p^{SI} for scattering exclusively on protons. Besides the old limits from CDMSSi (dashed turquoise line) and XENON100 (dash-dotted blue line), which were shown in Fig. 4.9, the plot contains the new limits from DAMIC (dotted brown line), XENON10 (dash-double dotted black line) and XENON100 (long-dashed purple line). They exclude the preferred regions of the signal claims by DAMA (orange shade), CoGeNT (pink shade) and CRESST (cyan shade). The new plot of σ_p^{SI} shows again that the cross sections obtained in the models with visible sector induced breaking cluster in two disjoint regions. The upper region corresponds to the dark matter particle being the Dirac fermion and the lower one to the Majorana fermion.

The disappearance of dark green points in the left-hand plot of Fig. 4.17 is mostly due to the DAMIC limit on σ_p^{SI} which extends the earlier limits to much lower masses. In this way, it eliminates many models which gave the correct relic abundance at small masses, as shown by the dotted brown line in the right-hand plot of the same figure. Therefore, for some parts of the parameter space only models which give a subdominant dark matter candidate are still viable. Furthermore, since the preferred regions for the signals claims by DAMA or CoGeNT are excluded by the new limits, there are no longer areas coloured in purple, red or blue, as they were shown in Fig. 4.8.

The cross section for spin-dependent scattering on protons and on neutrons are given in Fig. 4.18 together with the corresponding direct detection limits, which are updated compared to the ones of Fig. 4.10. Both plots only contain models in which the Majorana fermion is the dark matter particle since the Dirac fermion has little spin-dependent scattering. The left-hand plot for σ_p^{SD} contains the new limits from PICASSO2012 (long-dashed orange line), COUPP2012 (dash-dotted turquoise line) and XENON100 (long-dashed purple line) together with the older limit from SIMPLE (dashed brown line). For σ_n^{SD}, the right-hand plot shows the new XENON100 bound (long-dashed purple line) along with the older limits from XENON10 (dash-dotted blue line), Zeplin (dotted pink line) and CDMS (dashed turquoise line). Compared to the corresponding plots in Fig. 4.10, the new XENON100 limit on σ_n^{SD} for scattering on neutrons has the most significant impact. It excludes many models as shown by the long-dashed purple

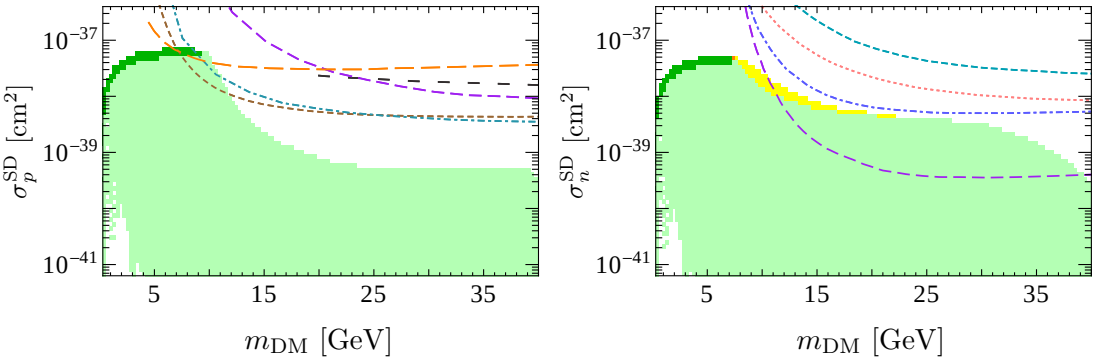

Figure 4.18: Cross sections for spin-dependent scattering in models with visible sector induced breaking together with updated direct detection limits for $0.1 \leq \kappa \leq 10$. As in Fig. 4.10, points in green (light green) are allowed with all other constraints and give the correct (subdominant) relic abundance, orange (yellow) points give the correct (subdominant) abundance but are in conflict with SIMPLE.
Left: Cross sections σ_p^{SD} for scattering on protons and lines for new limits from COUPP2012 (dash-dotted turquoise), PICASSO2012 (long-dashed orange) and XENON100 (long-dashed purple) as well as old ones from SIMPLE (short-dashed brown) and Super-K (dashed black).
Right: Cross sections σ_n^{SD} for scattering on neutrons together with the lines for the new limit from XENON100 (long-dashed purple) as well as the old limits from XENON10 (dash-dotted blue), Zeplin (dotted pink) and CDMS (dashed turquoise).

line in the right-hand plot of Fig. 4.18. This results in the large indentation in the left-hand plot. Furthermore, together with the new PICASSO2012 and COUPP2012 bounds, it reduces the effect on the parameter space caused by including or disregarding the SIMPLE limit. Since the new bounds have almost the same reach as SIMPLE, there are less models which are in conflict with SIMPLE but allowed by all other constraints. The yellow and orange regions, corresponding to these models, therefore diminish, as already discussed in Sec. 4.4.2 for the scenario with radiative breaking domination.

Even after the new constraints are taken into account, there are still many viable models with visible sector induced breaking. They can provide the correct relic abundance or give a subdominant contribution for either a Dirac fermion or a Majorana fermion as dark matter candidate. Future direct detection experiments can further probe the former through its spin-independent and the latter via spin-dependent scattering.

4.5 Summary

In this chapter, the dark matter relic abundance and direct detection cross sections of a toy dark sector model and complete string-inspired supersymmetric dark sector models were examined. The analysis emphasised the natural relationship between the kinetic mixing parameter and the hidden gauge coupling. For the supersymmetric models, the cases of radiative and visible sector induced breaking of the hidden gauge symmetry were distinguished and a stark phenomenological contrast between the two scenarios was established. Different signatures of a Dirac fermion and a Majorana fermion dark matter particle arise since the former scatters spin-independently and the latter spin-dependently. Our results show that the toy model as well as the supersymmetric dark force models with gravity mediation give viable light dark matter candidates. The Dirac fermion dark matter particle in the toy model and the models with visible sector induced breaking can furthermore obtain the scattering cross sections that might explain the signals in DAMA and CoGeNT (though not specifically analysed this would also be possible for CRESST and CDMS). The tension with the direct detection limits is not alleviated by the models and can only be reduced by non-standard assumptions for the dark matter halo. Signatures and constraints from indirect detection for these dark sector models have not been studied and are left for future work.

Chapter 5

Conclusions and Outlook

The question regarding the particle nature of dark matter is one of the great challenges of present-day particle physics. Since the Standard Model does not provide an appropriate candidate, it is well established that finding an answer requires an extension of the Standard Model. Numerous models have been proposed to solve this puzzle and provide a dark matter candidate. Many of these models involve new physics at the TeV scale and great experimental effort is being made at the high-energy frontier, searching for new heavy particles. Other models, on the contrary, predict new light particles which are very weakly coupled to the Standard Model and have therefore not been detected yet. The search for these particles — often referred to as WISPs — presents a complementary approach to uncovering new physics and requires high-intensity experiments.

An interesting concept in this context is that of hidden sectors. They contain particles that lack a direct connection with the Standard Model since they are neutral under the corresponding gauge groups. Consequently, they might only interact weakly with the visible sector through a messenger particle. This makes them an ideal environment not only for accommodating WISPs but also for dark matter. Furthermore, they are often predicted in string theories and can be contained in various supersymmetric models. One particular example that arises frequently is the case of a hidden sector with an extra U(1) symmetry. The corresponding gauge boson, the hidden photon, may be light and couples weakly to the Standard Model through kinetic mixing with the ordinary photon. Such scenarios also provide interesting phenomenological features and have received much attention in connection with dark matter.

In this thesis, we examined whether MeV-scale WISPs can be probed experimentally despite interacting only weakly with the Standard Model. Using the example of two candidates, the aforementioned hidden photon γ' and the CP-odd Higgs A^0 of the NMSSM, we found that current experimental data constrain the mass and the couplings of these particles. Furthermore, in view of the connection with dark matter, we studied different models with dark sectors in which a light dark matter particle interacts with the visible sector through the hidden photon. We showed that these models provide viable dark matter candidates with interesting prospects for direct detection.

Constraints on a light CP-odd Higgs in the NMSSM

The NMSSM is an attractive extension of the MSSM and was originally introduced to solve the so-called μ-problem. A light CP-odd Higgs A^0 can arise from the spontaneous breaking of approximate symmetries (Peccei–Quinn or R-symmetry) and is motivated by string theory. In the work performed with Oleg Lebedev, Sául Ramos-Sánchez and Andreas Ringwald, we focused on the mass range where the CP-odd Higgs is lighter than two muons since larger masses have already been studied. The analysis and the constraints which we derived on the mass m_{A^0} of the light A^0 and its coupling C_{Aff} to fermions were presented in Chapter 2.

We used various flavour physics precision measurements to place limits on the CP-odd Higgs in Sec. 2.2. The A^0 can be produced from the radiative decays $X \longrightarrow \gamma + A^0$ of a meson X or via the rare decays $X \longrightarrow Y + A^0$ to another meson Y. The branching ratio of such a process is constrained by experimental measurements of the type $X \longrightarrow Y/\gamma$+invisible or $X \longrightarrow Y/\gamma+\ell^+\ell^-$, according to the detected final states. The A^0, which can decay into $\gamma\gamma$ or e^+e^- in the mass range of interest, can contribute to either of these processes. Therefore, we distinguished between the two possibilities that, depending on its decay width, the A^0 decays either outside or inside the detector. We compared both cases to the corresponding measurements and in this way probed complementary regions of the A^0 parameter space. The search for an invisible A^0 only applies at small masses and couplings where the decay width is large and the lifetime is long enough for the A^0 to escape the detector. The measurements where the leptons in the final state are detected come into play once the lifetime is sufficiently short so that the A^0 can be observed through its decay into e^+e^-. Since in both cases the derived limits depend on the decay width of the A^0, we found that the exclusion contours for masses lighter and heavier than twice the electron mass exhibit a different behaviour. While below the two-electron threshold the A^0 only decays into two photons, the additional decay into electrons severely reduces the lifetime for heavier masses. Furthermore, we considered the rare pion decay into e^+e^- which is only a loop process in the Standard Model, while it proceeds through the CP-odd Higgs at tree-level. The measured branching ratio allowed us to exclude large couplings of the A^0. We also included another limit obtained from requiring that the loop contribution of the A^0 to the muon anomalous magnetic moment does not worsen the observed discrepancy beyond 5σ. In Sec. 2.3, we studied further limits from reactor and beam dump experiments, which are based on a different kind of physics and can therefore be considered as complementary.

In summary, we have addressed the question of how light the CP-odd Higgs of the NMSSM can be. We found that masses below 210 MeV and couplings to fermions larger than 10^{-4} are excluded, usually even by more than one experiment. This is shown in Fig. 2.2 for the constraints arising from meson decays. Since smaller couplings can scarcely be achieved in the NMSSM, we conclude that the A^0 has to be heavier than about 210 MeV. Our constraints on the CP-odd Higgs are published in [41] and quoted

in the Review of Particle Physics by the PDG [4]. They show that even very small couplings, like the ones of the CP-odd Higgs, can be constrained, e.g. with precision measurements from flavour physics or high-intensity beam dump experiments. In general, all our constraints apply to the couplings of a light pseudoscalar (axion-like) particle to matter since our analysis did not assume details of the NMSSM. Instead, the constraints have been derived solely in terms of the mass and the coupling strength. While the limits from meson decays require a coupling to quarks, those from electron beam dump experiment and the muon anomalous magnetic moment only rely on the coupling to leptons. They therefore also apply to leptophilic scenarios, where the pseudoscalar can only couple to leptons.

Our results severely constrain NMSSM scenarios in which the PAMELA excess is explained by leptophilic neutralino annihilations via a light CP-odd Higgs which subsequently decays to e^+e^-, as discussed in Sec. 2.4. According to our analysis, the CP-odd Higgs in the NMSSM should be heavier than two muons and might therefore be searched for at the LHC through the decay into $\mu^+\mu^-$.

Constraints on a light hidden photon

The hidden photon can be probed in experiments through its coupling to charged Standard Model particles. This coupling is generated by kinetic mixing with the photon and has a strength which is suppressed by the kinetic mixing parameter χ compared to the electron charge. In the work done in collaboration with Carsten Niebuhr and Andreas Ringwald, we studied constraints from electron beam dump experiments on the hidden photon mass $m_{\gamma'}$ and the kinetic mixing χ. Our analysis is described in Chapter 3 and the resulting limits on hidden photons with masses in the MeV range are published in [42].

In Sec. 3.1, we studied the production of the hidden photon in bremsstrahlung off an initial electron beam. Requiring that the hidden photon subsequently decays behind the beam dump and in front of the detector, we derived the number of events predicted to arise in an electron beam dump experiment. This enabled us to explore the characteristic shape of the expected exclusion contour as a function of the hidden photon mass $m_{\gamma'}$ and the kinetic mixing χ. We also studied the dependence of this contour on the specifications of a particular experimental set-up. From these considerations, we found that these kind of experiments can only access the lower left corner of the parameter space, i.e. small hidden photon masses and small kinetic mixing values. We stressed that the reach of electron beam dump experiments is limited at small values of χ by statistics and in the direction of large $m_{\gamma'}$ and/or large χ by the need for a long enough lifetime for the hidden photon to traverse the dump. We then introduced the five experiments labelled KEK, E141, E137, Orsay and E774, which were used in our analysis in Sec. 3.2. For each of these experiments, we generated events with MadGraph and constructed the path

of the hidden photon from the production to the decay, followed by the trajectories of its decay products. Comparing the results of these simulations with the three-dimensional layout and geometry of the experiments and taking into account potential energy cuts applied in the experiments' data analysis, we determined the actual acceptance of each experiment.

Finally, our resulting exclusion contours on the hidden photon mass $m_{\gamma'}$ and the kinetic mixing χ were presented in Fig. 3.8 for the five electron beam dump experiments that were analysed. For the first time the limits were obtained by combining the theoretical estimate for the number of events with the experimental acceptance from Monte Carlo simulations. The exclusion contours exhibit the behaviour which was anticipated in light of the above-mentioned considerations. Including the results of experiments at KEK and Orsay which had not been considered before, we were able to exclude a part of the parameter space which had not been constrained previously by any other similar experiment. Finally, we gave an overview of all current constraints on hidden photons from various searches in Sec. 3.4 and summarised plans for future experiments in Sec. 3.5.

Since large parts of the parameter space are still allowed, it is interesting to further check whether it is possible to probe as yet unexplored regions with potential future electron beams. While the region which is typically accessible for these kind of experiments is mostly excluded, pushing the limits further towards small χ or towards the upper right corner of the parameter space $\{m_{\gamma'}, \chi\}$ might require rather extreme measures, like severely shortening the shield or dumping a very large number of electrons. These considerations of how to extend the reach of a new experiment have to take into account the dependence of the limit on the experimental set-ups since, for example, collecting ten times more electrons would only result in lowering the reach in χ by a factor of $\sqrt[4]{10} \simeq 1.8$. For the ongoing 2013 Snowmass Study, as part of the Intensity Frontier working group, we currently also investigate if and how one can extend and improve the search and limits for hidden photons. Another open issue is whether the present limits can be improved by taking into account the fact that not only the initial electron from the beam but also the secondary electrons, produced in the thick target by the showering of the first one, might emit a hidden photon. An interesting question, which was not addressed in this thesis, concerns the modification of our limits in the presence of hidden sector particles that are lighter than the hidden photon and charged under the hidden U(1). As we assumed that the hidden photon can only decay into Standard Model particles, our constraints become weaker once the hidden photon can also decay within the hidden sector. A study of the modified limits is left for future works.

Hidden sector models with dark matter and a hidden photon

The phenomenology of different models which, besides a hidden photon, also contain a light dark matter particle in the hidden sector was studied in Chapter 4. In these models,

the dark matter particle can annihilate either into a real hidden photon or through a virtual one in an s-channel exchange into Standard Model fermions. Additionally, because of kinetic mixing, the hidden photon can mediate the scattering of dark matter on nuclei. These processes are relevant for the determination of the dark matter relic abundance and the prospects at direct detection experiments. In view of the signals claimed by certain direct detection experiments, we focused on models with a GeV-scale dark matter particle. We considered a toy model as well as simple string-inspired supersymmetric models with gravity mediation for which we allowed the hidden gauge symmetry to be broken either radiatively or by the visible sector. For these different scenarios, we addressed the question whether viable dark matter candidates can be obtained in agreement with observations. The results of this analysis, performed together with Mark Goodsell and Andreas Ringwald, are published in [43].

In the dark sector models, in addition to the constraints on the hidden photon which were discussed in Chapter 3, we also had to take into account limits on the accompanying dark matter particle. In Sec. 4.1, we summarised all relevant constraints, especially emphasizing the various limits from direct detection experiments. We discussed the application of these constraints to our models. It is necessary to distinguish whether the dark matter particle is a Dirac fermion or a Majorana fermion since the former scatters spin-independently and the latter spin-dependently. Therefore, different direct detection experiments have to be taken into account for both particles. Our analysis did not only consider dark matter particles which provide the entire relic abundance but also those which constitute a subdominant part of the total dark matter in the Universe. In the case of subdominant dark matter, the scattering cross sections had to be rescaled compared to those from direct detection experiments to account for the lower local dark matter density. Due to recent improvements in direct detection limits, we also performed an update of our analysis in Sec. 4.4. There, we studied the implications of these new limits on the parameter space of our models.

For the Dirac fermion dark matter particle, we argued that the spin-independent scattering mostly involves protons, i.e. it is strongly isospin-dependent, since it is mediated by the hidden photon which couples only to charged particles. In our analysis, the cross sections for spin-independent scattering from direct detection experiments, which are generally normalised to scattering on nucleons, therefore had to be rescaled accordingly. Then, the Dirac fermion dark matter particle turned out to be mostly constrained by XENON100 and CDMSSi as well as DAMIC and XENON10 in the updated analysis. We further found that the Dirac fermion can obtain scattering cross sections in the range required to fit the DAMA and CoGeNT signals. Even though we did not consider the CRESST and CDMS signals explicitly, these suggest cross sections and masses in a range similar to DAMA and CoGeNT and could also be accommodated by our models. While the signals by DAMA and CoGeNT were still in agreement with the limits applied in our first analysis, they are in tension with the newer limits when making the standard assumptions for the dark matter halo.

The Majorana fermion dark matter particle, which undergoes mostly spin-dependent scattering, turned out to receive the strongest constraint from SIMPLE for scattering on protons. Because of discussions questioning the reliability of this constraint, we highlighted the effect which arises from applying or disregarding this limit. In the updated analysis, the newer limits by COUPP and PICASSO as well as the one by XENON100 for scattering on neutrons turned out to be almost as constraining as SIMPLE.

Based on these considerations we examined whether a certain model could predict a viable dark matter candidate with the correct (or a subdominant) relic abundance and still be in agreement with the constraints from direct detection experiments. For the toy model with minimal particle content, we performed a scan over the parameter space and computed the relic abundance and spin-independent scattering cross sections of the Dirac fermion dark matter particle with micrOMEGAs in Sec. 4.2. Analysing the results with respect to the above-mentioned experimental requirements, we obtained viable models in most of the parameter space with hidden photon masses ranging from $\mathcal{O}(100\text{ MeV})$ to 40 GeV and kinetic mixing values from 10^{-5} to 10^{-2}. Dark matter particles having a mass between 0.8 GeV and 25 GeV were found to provide either the correct or a subdominant relic abundance in this parameter space. In some regions, the scattering cross section turned out to be in agreement with those explaining the DAMA and/or CoGeNT signal for different halo models. The updated direct detection constraints eliminated these signal regions, but we still found viable dark matter candidates for the same parameter space of hidden photon mass and kinetic mixing.

For the supersymmetric dark force models, we discussed, in Sec. 4.3, the phenomenology of the two scenarios which we obtained by considering two different mechanisms to break the hidden gauge symmetry. In the case of radiatively induced breaking, in contrast to the case of the toy model, we found that the dark matter particle is a Majorana fermion. The resulting direct detection cross sections, computed with micrOMEGAs, are very small for spin-independent scattering and beyond the reach of experiments. The spin-dependent scattering dominates and was shown to be partly constrained by experiments. The different low-energy models, which were obtained by scanning over the high-energy parameters and running down to the low scale, were therefore confronted with bounds from the direct detection experiments which are sensitive to spin-dependent scattering. Models providing viable dark matter candidates with a mass of a few GeV up to ~ 15 GeV were obtained but did not populate as much of the parameter space as in the toy model.

In the case where the breaking of the hidden gauge symmetry is induced by the visible sector, we searched for models by scanning over the low-energy parameters. The dark matter particle in these scenarios can either be a Dirac fermion or a Majorana fermion. The former was found to exhibit a phenomenology similar to the toy model with the following two differences. First, in all the supersymmetric dark sector models under consideration, the dark matter particle can never be heavier than the hidden photon.

Therefore, a large region of the parameter space at large hidden photon masses and small kinetic mixing values does, in contrast to the toy model, not provide any viable dark matter candidates since the t-channel annihilation into two hidden photons is not possible. Second, while the Dirac fermion dark matter particle can again obtain the scattering cross sections required to explain the direct detection signals, its contribution to the relic abundance in these cases is always subdominant. In the scenarios in which the Majorana fermion constitutes the dark matter particle, the phenomenology resembles the one in models with radiative breaking domination. The Majorana fermion can again be probed by direct detection experiments sensitive to spin-dependent scattering. A particular scan for very light hidden sectors yielded viable models with an MeV-scale hidden photon which may be detected by the future experiments discussed in Chapter 3.

In summary, our results on dark sectors showed that both our toy model as well as the supersymmetric dark force models with gravity mediation predict viable light dark matter candidates. The new approach of fixing the hidden gauge coupling by the relation (1.21) as a function of the kinetic mixing gave qualitatively different results for the cross sections. Our models were found to have interesting potential for testing in direct detection experiments, both for spin-independent and spin-dependent scattering. In the toy model and in the model with visible sector induced breaking, the Dirac fermion dark matter candidate can have spin-independent scattering cross sections which are able to explain the direct detection signals observed by DAMA, CoGeNT, CRESST and CDMS. The models themselves do, however, not provide the means to reduce the generic tension with the direct detection limits and would require non-standard assumptions for the dark matter halo. We showed that light hidden sector scenarios coming from models with radiatively induced breaking, which are most relevant for gravity mediation, can be viable, in contrast to what was claimed in earlier works. We found that these models can even be somewhat probed by direct detection experiments which are sensitive to spin-dependent scattering.

Very recent results following the observation of a signal by CDMS [39] might have implications for our updated analysis which have not been taken into account in this thesis. The XENON10 limit [331] applied in Sec. 4.4 excluded a large part of the parameter space in the toy model and in the models with visible sector induced breaking. However, in [336] it was found that the actual XENON10 limit is weaker by almost a factor of 10 than the one originally published in [331]. An erratum of [331] now also confirms the weaker limit. The new limit is therefore less constraining for the parameter space of our models than assumed in our analysis. In [336] it is further claimed that the signal observed by CDMS is no longer excluded, even with standard assumptions for the halo. A very recent update [337] of the analysis performed by CoGeNT in 2012 moved their signal region closer to the one of CDMS. The cross sections required to explain both signals might thus still be in agreement with current limits. Since these cross sections are similar to the ones considered in our analysis for DAMA and CoGeNT, both the toy model as well as the models with visible sector induced breaking could also yield the

cross sections preferred by the new observations. Including the weaker XENON10 limit as well as the signal regions in the analysis of the parameter space for both models is left for future work [332].

While we have focused on direct detection signatures in this thesis, there are further possible avenues to extend the work carried out in the context of these models. We plan to study the constraints on the dark matter annihilation from indirect detection experiments. These include gamma rays from dwarf spheroidal galaxies or from the galactic centre, radio waves produced in the halo from charged annihilation products, for example, by synchrotron radiation, and neutrinos from the Sun. Even though the dependence of our results on the visible sector parameters is small, changing the considered MSSM benchmark scenario could also be of interest.

Acknowledgements

This thesis would not have been possible without the help of several people who in one way or another contributed and assisted in the preparation and completion.

First of all, I owe my deepest gratitude to my supervisor Andreas Ringwald for his scientific and personal support as well as his encouragement and guidance. I am thankful to Torsten Bringmann and Günter Sigl for agreeing to referee my disputation and my dissertation, respectively.

I am especially grateful to Mark Goodsell, Oleg Lebedev, Carsten Niebuhr and Sául Ramos-Sánchez for their collaboration on different parts of this work and for all I have learned from them. It was a pleasure to work with them and to benefit from their enlightening insight on various topics. Many thanks to Mark for countless helpful discussions and comments, and also for his ongoing support and patience; to Oleg and Sául for stimulating and fruitful collaboration and for proofreading parts of this thesis; to Carsten for valuable discussions especially on experimental details of the analysis. I wish to thank Rouven Essig, Philip Schuster, and Natalia Toro for sharing their MadGraph code. I am very thankful to Aoife Bharucha for helpful discussions and suggestions on this thesis; to Andreas Goudelis for precious advice especially regarding dark matter; to Christian Hambrock for careful proofreading of this thesis and many valuable comments; to Valerie Domcke, Elina Fuchs, Sara Rydbeck and Václav Tlapák for proofreading parts of this thesis. I want to thank the people from the WISP and high-intensity community, especially Tobias Beranek, Fabio Bossi, Achim Denig, Rouven Essig, Jörg Jäckel, John Jaros, Axel Lindner, Harald Merkel, Javier Redondo, Chris Wallace and William Wester, for enriching discussions and an exciting research activity; in particular for setting up interesting workshops and for giving me the opportunity to participate.

My sincere thanks go to Michel Tytgat for the continuous support and advice; I am very glad to have worked with him for my Master's thesis. I am grateful to Thomas Hambye for his letter of recommendation. I wish to thank Pierre Fayet for stimulating discussions and look forward to future collaborations. Many thanks to the entire DESY theory group for an inspiring research environment and especially to my office mates for a nice working atmosphere, enjoyable coffee breaks and interesting discussions. In particular, I also want to thank Jan Möller for valuable conversations and advice.

Furthermore, I am thankful to my friends who stood by me through all the ups and downs. Especially thanks to Aoife, Babette, Christoph, Elina, Falk, Jan, Paola, Sara, Václav and Valerie for their support and encouragement and for all the fun we've had; thanks for making the last years in Hamburg a very special time. Thanks to Anna, Leonie, Johanna and Johannes for many years of continued friendship. Thanks to Isabelle and Christine for their advice and many pleasant moments. Merci à Thomas for enriching conversations and being a constant source of support and trust. A huge thanks to my flatmate Aoife for a great time, for standing my bad mood in stressful times and for being an amazing friend; I'll miss you in Paris. I am especially grateful to Christian who always believed in me, supported me in many ways during my thesis and enriched the last years with happiness and unforgettable memories; thank you for always having been there and for being someone I could count on. Last but not least, I want to thank my family, especially my parents Irene and Günther, my brother Florian, my grandparents Erika, Heiner, Auguste and Felix and my aunt Elisabeth, for their love and for being there when I needed them.

Appendix A

Kinetic Mixing

This appendix gives an overview of kinetic mixing. It is shown how the kinetic and mass terms are diagonalised in a Lagrangian which includes the hidden photon and the kinetic mixing. The resulting couplings of the physical gauge bosons to the matter fields are derived. Note that, since the kinetic mixing parameter χ is a small quantity we can often focus on the leading order effects while higher order corrections are negligible.

A.1 Mixing with the ordinary photon

We consider the most simple low energy effective Lagrangian

$$\mathcal{L} \supset -\frac{1}{4}\tilde{F}_{\mu\nu}\tilde{F}^{\mu\nu} - \frac{1}{4}\tilde{X}_{\mu\nu}\tilde{X}^{\mu\nu} + \frac{\chi}{2}\tilde{F}_{\mu\nu}\tilde{X}^{\mu\nu} + \frac{1}{2}\tilde{m}^2_{\gamma'}\tilde{X}_\mu\tilde{X}^\mu + \tilde{e}j^\mu_{\rm em}\tilde{A}_\mu \ , \tag{A.1}$$

where $\tilde{F}_{\mu\nu} = \partial_\mu\tilde{A}_\nu - \partial_\nu\tilde{A}_\mu$ is the field strength tensor of the ordinary U(1) gauge field $\tilde{A}_\mu$ and $\tilde{X}_{\mu\nu} = \partial_\mu\tilde{X}_\nu - \partial_\nu\tilde{X}_\mu$ is the field strength tensor of the hidden U(1) gauge field $\tilde{X}_\mu$. The electromagnetic current is $j^\mu_{\rm em} = Q\bar{\psi}\gamma^\mu\psi$. The Lagrangian contains a non-diagonal kinetic term with kinetic mixing parameter χ and all fields in this unrotated mixed basis are denoted with tilde. Those without tilde refer to the ones in the physical mass eigenbasis in which the kinetic terms and the mass terms are diagonal.

In order to diagonalise the field strength, the transformation

$$\tilde{X}_\mu = \frac{1}{\sqrt{1-\chi^2}}X_\mu \ , \tag{A.2}$$

$$\tilde{A}_\mu = A_\mu + \frac{\chi}{\sqrt{1-\chi^2}}X_\mu \ , \tag{A.3}$$

is applied to the Lagrangian. This results in

$$\begin{aligned}\mathcal{L} \supset & -\frac{1}{4}F_{\mu\nu}F^{\mu\nu} - \frac{1}{4}\frac{1}{1-\chi^2}(\chi^2+1-2\chi^2)X_{\mu\nu}X^{\mu\nu} + \frac{1}{2}\frac{\tilde{m}_{\gamma'}^2}{1-\chi^2}X_\mu X^\mu \\ & + \tilde{e}j^\mu_{\text{em}}A_\mu + \tilde{e}\frac{\chi}{\sqrt{1-\chi^2}}j^\mu_{\text{em}}X_\mu \\ & - \frac{1}{4}\frac{\chi}{\sqrt{1-\chi^2}}F_{\mu\nu}X^{\mu\nu} - \frac{1}{4}\frac{\chi}{\sqrt{1-\chi^2}}X_{\mu\nu}F^{\mu\nu} + \frac{1}{2}\frac{\chi}{\sqrt{1-\chi^2}}F_{\mu\nu}X^{\mu\nu}, \end{aligned} \tag{A.4}$$

in which the mixing terms in the last line cancel. The final Lagrangian

$$\mathcal{L} \supset -\frac{1}{4}F_{\mu\nu}F^{\mu\nu} - \frac{1}{4}X_{\mu\nu}X^{\mu\nu} + \frac{1}{2}\frac{\tilde{m}_{\gamma'}^2}{1-\chi^2}X_\mu X^\mu + \tilde{e}j^\mu_{\text{em}}A_\mu + \tilde{e}\frac{\chi}{\sqrt{1-\chi^2}}j^\mu_{\text{em}}X_\mu \tag{A.5}$$

shows that the term for the coupling of the electromagnetic current j^μ_{em} to the ordinary photon field A_μ is the standard one so that one can identify $\tilde{e} = e$. Expanding the Lagrangian to first order in χ gives

$$\mathcal{L} \supset -\frac{1}{4}F_{\mu\nu}F^{\mu\nu} - \frac{1}{4}X_{\mu\nu}X^{\mu\nu} + \frac{1}{2}m_{\gamma'}^2X_\mu X^\mu + ej^\mu_{\text{em}}A_\mu + e\chi j^\mu_{\text{em}}X_\mu\,. \tag{A.6}$$

It can be seen that the non-orthogonal rotation introduces a coupling between the visible sector current j^μ_{em} and the hidden gauge field X_μ. The visible sector particles acquire a non-zero minicharge under the hidden U(1). Thus, due to kinetic mixing the hidden photon couples to the ordinary electromagnetic current with a QED-like vertex $ieQ\chi\gamma^\mu$, when expanding the coupling to first order in χ.

A.2 Mixing with hypercharge

In analogy to (A.1), we consider the low energy effective Lagrangian for the mixing with the hypercharge gauge field, given by

$$\mathcal{L} \supset -\frac{1}{4}\tilde{B}_{\mu\nu}\tilde{B}^{\mu\nu} - \frac{1}{4}\tilde{X}_{\mu\nu}\tilde{X}^{\mu\nu} + \frac{\chi_Y}{2}\tilde{B}_{\mu\nu}\tilde{X}^{\mu\nu} + \frac{\tilde{m}_{\gamma'}^2}{2}\tilde{X}_\mu\tilde{X}^\mu + g_Yj^\mu_B\tilde{B}_\mu\,, \tag{A.7}$$

where now $\tilde{B}_{\mu\nu} = \partial_\mu\tilde{B}_\nu - \partial_\nu\tilde{B}_\mu$ is the field strength tensor of the $\text{U}(1)_Y$ hypercharge gauge field $\tilde{B}_\mu$ and $g_Y = e/c_W$ is the hypercharge gauge coupling[1] with c_W being the cosine of the Weinberg angle. Again $\tilde{X}_{\mu\nu}$ is the field strength tensor of the hidden U(1) gauge field $\tilde{X}_\mu$. The parameter χ_Y entering in the mixing term with the hypercharge is connected to χ in Eq. (A.1) by $\chi = \chi_Y c_W$. The visible sector current j^μ_B is discussed in Sec. A.3.

[1] To be precise, the couplings in the mixed basis here should again be labelled with a tilde as in (A.1). However, it is shown in Sec. A.1 that $\tilde{e} = e$ and since the other parameters are at most modified by higher orders of χ, we neglect this dependence in the following and write them directly without tilde.

In analogy to the previous section, the transformation

$$\tilde{X}_\mu = \frac{1}{\sqrt{1-\chi_Y^2}} X_\mu \,, \tag{A.8}$$

$$\tilde{B}_\mu = B_\mu + \frac{\chi_Y}{\sqrt{1-\chi_Y^2}} X_\mu \,, \tag{A.9}$$

diagonalises the kinetic terms in the Lagrangian and gives

$$\mathcal{L} \supset -\frac{1}{4} B_{\mu\nu} B^{\mu\nu} - \frac{1}{4} X_{\mu\nu} X^{\mu\nu} + \frac{1}{2} \frac{\tilde{m}_{\gamma'}^2}{1-\chi_Y^2} X_\mu X^\mu + g_Y j_B^\mu B_\mu + g_Y \frac{\chi_Y}{\sqrt{1-\chi_Y^2}} j_B^\mu X_\mu \,, \tag{A.10}$$

where again the visible sector particles get charged under the hidden U(1).

A.3 Currents

The currents used in this appendix are defined as

$$j_W^\mu = T_3 \bar{\psi} \gamma^\mu P_L \psi \,, \tag{A.11}$$

$$\begin{aligned} j_B^\mu &= Y_L \bar{\psi} \gamma^\mu P_L \psi + Y_R \bar{\psi} \gamma^\mu P_R \psi \\ &= Q \bar{\psi} \gamma^\mu \psi - T_3 \bar{\psi} \gamma^\mu P_L \psi \,, \end{aligned} \tag{A.12}$$

$$j_h = \bar{\psi}_h \gamma^\mu \psi_h \,, \tag{A.13}$$

where $Y_L = Q - T_3$, $Y_R = Q$ and

$$P_L = \frac{1}{2}(1-\gamma^5) \,, \qquad P_R = \frac{1}{2}(1+\gamma^5) \,, \qquad P_L + P_R = 1 \,, \tag{A.14}$$

$$\gamma^\mu = \begin{pmatrix} 0 & \sigma^\mu \\ \bar{\sigma}^\mu & 0 \end{pmatrix} \,, \qquad \gamma^5 = \begin{pmatrix} -1 & 0 \\ 0 & 1 \end{pmatrix} \,, \tag{A.15}$$

and ψ and ψ_h refer to Dirac spinors in the visible and hidden sector, respectively, with

$$\psi = \begin{pmatrix} \eta \\ \bar{\xi} \end{pmatrix} \,, \qquad \psi_L = P_L \psi \,, \quad \psi_R = P_R \psi \,. \tag{A.16}$$

The particle content in the visible sector is

$$\begin{pmatrix} u_L \\ d_L \end{pmatrix} \,, \quad \begin{pmatrix} \nu_L \\ e_L \end{pmatrix} \,, \quad u_R,\ d_R,\ e_R,\ (\nu_R) \,, \tag{A.17}$$

with assignments for the electric charge Q, the weak isospin T_3 and the hypercharge Y given by

$$\begin{array}{cccc|cccc} & Q & T_3 & Y & & Q & T_3 & Y \\ u_L & \frac{2}{3} & \frac{1}{2} & \frac{1}{6} & u_R & \frac{2}{3} & 0 & \frac{2}{3} \\ d_L & -\frac{1}{3} & -\frac{1}{2} & \frac{1}{6} & d_R & -\frac{1}{3} & 0 & -\frac{1}{3} \\ \nu_L & 0 & \frac{1}{2} & -\frac{1}{2} & \nu_R & 0 & 0 & 0 \\ e_L & -1 & -\frac{1}{2} & -\frac{1}{2} & e_R & -1 & 0 & -1 \end{array} \quad . \tag{A.18}$$

Then, for

$$j_A^\mu = j_W^\mu + j_B^\mu \ , \tag{A.19}$$

$$j_{Z^0}^\mu = \frac{1}{c_W s_W}(c_W^2 j_W^\mu - s_W^2 j_B^\mu) \ , \tag{A.20}$$

it follows with Eqs. (A.11) and (A.12) that

$$j_A^\mu = Q\bar{\psi}\gamma^\mu\psi \ , \tag{A.21}$$

$$\begin{aligned} j_{Z^0}^\mu &= \frac{1}{c_W s_W}\left(c_W^2 T_3 \bar{\psi}\gamma^\mu P_L\psi - s_W^2 Q\bar{\psi}\gamma^\mu\psi + s_W^2 T_3\bar{\psi}\gamma^\mu P_L\psi\right) \\ &= \frac{1}{c_W s_W}\left(T_3\bar{\psi}\gamma^\mu P_L\psi - s_W^2 Q\bar{\psi}\gamma^\mu\psi\right) \\ &= \frac{1}{c_W s_W}\bar{\psi}\gamma^\mu\left(T_3 P_L - s_W^2 Q\right)\psi \ . \end{aligned} \tag{A.22}$$

Thus, the currents can be also be written as

$$g_2 j_W^\mu = e(c_W j_{Z^0}^\mu + s_W j_A^\mu) \ , \tag{A.23}$$

$$g_Y j_B^\mu = e(c_W j_A^\mu - s_W j_{Z^0}^\mu) \ . \tag{A.24}$$

For direct detection experiments, it is most relevant to consider the currents in the vector and axial vector basis. While a hidden Dirac fermion may couple to both components, a $U(1)$ mixing primarily with the hypercharge will almost entirely only couple to the vector current. To see this, let us consider the hypercharge and weak currents slit into vector and axial vector contributions. The hypercharge current of Eq. (A.12) reads

$$j_B^\mu = \frac{1}{6}\bar{u}\gamma^\mu P_L u + \frac{1}{6}\bar{d}\gamma^\mu P_L d + \frac{2}{3}\bar{u}\gamma^\mu P_R u - \frac{1}{3}\bar{d}\gamma^\mu P_R d - \frac{1}{2}\bar{e}\gamma^\mu P_L e - \frac{1}{2}\bar{\nu}\gamma^\mu P_L\nu - \bar{e}\gamma^\mu P_R e \tag{A.25}$$

and can be written with P_L and P_R of Eq. (A.14) as

$$\begin{aligned} j_{B,\text{vec}}^\mu &= \frac{5}{12}\bar{u}\gamma^\mu u - \frac{1}{12}\bar{d}\gamma^\mu d - \frac{3}{4}\bar{e}\gamma^\mu e - \frac{1}{4}\bar{\nu}\gamma^\mu\nu \ , \\ j_{B,\text{axial}}^\mu &= \frac{1}{4}\bar{u}\gamma^\mu\gamma^5 u - \frac{1}{4}\bar{d}\gamma^\mu\gamma^5 d - \frac{1}{4}\bar{e}\gamma^\mu\gamma^5 e + \frac{1}{4}\bar{\nu}\gamma^\mu\gamma^5 \ . \end{aligned} \tag{A.26}$$

Accordingly, the weak current of Eq. (A.11) given by

$$j_W^\mu = \frac{1}{2}\bar{u}\gamma^\mu P_L u - \frac{1}{2}\bar{d}\gamma^\mu P_L d + \frac{1}{2}\bar{\nu}\gamma^\mu P_L \nu - \frac{1}{2}\bar{e}\gamma^\mu P_L e \tag{A.27}$$

splits into

$$\begin{aligned} j_{W,\text{vec}}^\mu &= \frac{1}{4}\bar{u}\gamma^\mu u - \frac{1}{4}\bar{d}\gamma^\mu d - \frac{1}{4}\bar{e}\gamma^\mu e + \frac{1}{4}\bar{\nu}\gamma^\mu \nu \,, \\ j_{W,\text{axial}}^\mu &= -\frac{1}{4}\bar{u}\gamma^\mu\gamma^5 u + \frac{1}{4}\bar{d}\gamma^\mu\gamma^5 d + \frac{1}{4}\bar{e}\gamma^\mu\gamma^5 e - \frac{1}{4}\bar{\nu}\gamma^\mu\gamma^5 \nu = -j_{B,\text{axial}}^\mu \,. \end{aligned} \tag{A.28}$$

A.4 Electroweak Lagrangian

Extending the Lagrangian (A.7) to include the electroweak couplings gives

$$\begin{aligned} \mathcal{L} \supset\ & -\frac{1}{4}\tilde{B}_{\mu\nu}\tilde{B}^{\mu\nu} - \frac{1}{4}\tilde{X}_{\mu\nu}\tilde{X}^{\mu\nu} + \frac{\chi_Y}{2}\tilde{B}_{\mu\nu}\tilde{X}^{\mu\nu} - \frac{1}{4}\tilde{W}_{\mu\nu}\tilde{W}^{\mu\nu} \\ & + \frac{1}{8}v^2(g_Y\tilde{B}_\mu - g_2\tilde{W}_\mu)^2 + \frac{1}{2}\tilde{m}_{\gamma'}^2\tilde{X}_\mu\tilde{X}^\mu \\ & + g_Y j_B^\mu \tilde{B}_\mu + g_2 j_W^\mu \tilde{W}_\mu + g_h j_h^\mu \tilde{X}_\mu \,, \end{aligned} \tag{A.29}$$

which describes the coupling of the currents j_B^μ, j_W^μ and j_h^μ to the respective unrotated gauge bosons $\tilde{B}_\mu$, $\tilde{W}_\mu$, and $\tilde{X}_\mu$ corresponding to hypercharge, weak and hidden gauge bosons, respectively. There, $\tilde{X}_{\mu\nu}$ is again the field strength tensor of the hidden U(1) gauge field $\tilde{X}_\mu$, $\tilde{B}_{\mu\nu}$ is the field strength tensor of the $\mathrm{U}(1)_Y$ hypercharge gauge field $\tilde{B}_\mu$, and $W_{\mu\nu}$ is the field strength tensor of the neutral $\mathrm{SU}(2)_L$ gauge field $W_\mu \equiv W_\mu^3$. The currents j_B^μ, j_W^μ and j_h^μ are discussed in Sec. A.3 and $g_2 = e/s_W$ is the weak coupling constant, where s_W is the sine of the Weinberg angle.

Applying again the transformation given by Eqs. (A.8) and (A.9) the Lagrangian reads

$$\begin{aligned} \mathcal{L} \supset\ & -\frac{1}{4}B_{\mu\nu}B^{\mu\nu} - \frac{1}{4}X_{\mu\nu}X^{\mu\nu} - \frac{1}{4}\tilde{W}_{\mu\nu}\tilde{W}^{\mu\nu} \\ & + \frac{1}{2}\frac{\tilde{m}_{\gamma'}^2}{1-\chi_Y^2}X_\mu X^\mu + \frac{1}{8}v^2\Big(g_Y B_\mu + g_Y\frac{\chi_Y}{\sqrt{1-\chi_Y^2}}X_\mu - g_2\tilde{W}_\mu\Big)^2 \\ & + g_Y j_Y^\mu B_\mu + g_2 j_W^\mu \tilde{W}_\mu + g_Y\frac{\chi_Y}{\sqrt{1-\chi_Y^2}}j_B^\mu X_\mu + g_h\frac{1}{\sqrt{1-\chi_Y^2}}j_h^\mu X_\mu \,, \end{aligned} \tag{A.30}$$

and has diagonal kinetic terms while the mass terms are not diagonal yet. It can be seen in the last term in the second line that the mass of the Z gets shifted due to the kinetic mixing as discussed also in the following.

We make further the definitions

$$\begin{aligned} \tilde{Z}_\mu &\equiv c_W \tilde{W}_\mu - s_W B_\mu \ , \\ A_\mu &\equiv s_W \tilde{W}_\mu + c_W B_\mu \ , \end{aligned} \tag{A.31}$$

where $\tilde{Z}_\mu$ is the usual Z-boson of the Standard Model, A_μ is the usual photon, s_W and c_W are sine and cosine of the weak mixing angle, respectively, and

$$\begin{aligned} e &= g_Y c_W \ = \ g_2 s_W \ , \\ g_Y^2 + g_2^2 &= \frac{e^2}{c_W^2 s_W^2} \ = \ \frac{g_Y^2}{s_W^2} \ = \ \frac{g_2^2}{c_W^2} \ , \\ \tilde{M}_Z^2 \ = \ \frac{v^2}{4}\,(g_y^2 + g_2^2) &= \frac{v^2}{4}\,\frac{e^2}{c_W^2 s_W^2} \ = \ \frac{v^2}{4}\,\frac{g_Y^2}{s_W^2} \ = \ \frac{v^2}{4}\,\frac{g_2^2}{c_W^2} \ , \\ \Longrightarrow g_Y s_W + g_2 c_W &= 2\,\frac{\tilde{M}_Z}{v}\,s_W^2 \ + \ 2\,\frac{\tilde{M}_Z}{v}\,c_W^2 \ = 2\,\frac{\tilde{M}_Z}{v} \ . \end{aligned} \tag{A.32}$$

Thus, applying the transformation

$$\begin{aligned} \tilde{W}_\mu &= c_W \tilde{Z}_\mu + s_W A_\mu \ , \\ B_\mu &= -\,s_W \tilde{Z}_\mu + c_W A_\mu \ , \end{aligned} \tag{A.33}$$

to the Lagrangian (A.30) and considering the mass term

$$\begin{aligned} \mathcal{L} \ \supset \ & \frac{1}{2}\frac{\tilde{m}_{\gamma'}^2}{1-\chi_Y^2} X_\mu X^\mu + \frac{v^2}{8}\left(g_Y B_\mu + \frac{g_Y \chi_Y}{\sqrt{1-\chi_Y^2}} X_\mu - g_2 \tilde{W}_\mu \right)^2 \\ \equiv \ & \frac{1}{2}(\tilde{Z}_\mu \ X_\mu)\mathbf{M}_{2\times 2}^2 \begin{pmatrix} \tilde{Z}_\mu \\ X_\mu \end{pmatrix} \ , \end{aligned} \tag{A.34}$$

this can be written using the relations in Eq. (A.32) as

$$\frac{1}{2}(\tilde{Z}_\mu \ X_\mu)\mathbf{M}_{2\times 2}^2 \begin{pmatrix} \tilde{Z}_\mu \\ X_\mu \end{pmatrix} \tag{A.35}$$

$$\begin{aligned} = \ & \frac{1}{2}\frac{\tilde{m}_{\gamma'}^2}{1-\chi_Y^2} X_\mu X^\mu + \frac{v^2}{8}\left((g_Y c_W - g_2 s_W) A_\mu - (g_Y s_W + g_2 c_W)\tilde{Z}_\mu + \frac{g_Y \chi_Y}{\sqrt{1-\chi_Y^2}} X_\mu \right)^2 \\ = \ & \frac{1}{2}\frac{\tilde{m}_{\gamma'}^2}{1-\chi_Y^2} X_\mu X^\mu + \frac{1}{2}\tilde{M}_Z^2 \left(\tilde{Z}_\mu - \frac{s_W \chi_Y}{\sqrt{1-\chi_Y^2}} X_\mu \right)^2 \ . \end{aligned} \tag{A.36}$$

The mass matrix $\mathbf{M}_{2\times 2}^2$ for $(\tilde{Z}_\mu,\ X_\mu)$ can then be written as

$$\mathbf{M}_{2\times 2}^2 \ = \ \tilde{M}_Z^2 \begin{pmatrix} 1 & -\tan\alpha \\ -\tan\alpha & \frac{x}{1-\chi^2} + \tan^2\alpha \end{pmatrix} \ , \tag{A.37}$$

where we defined

$$\tan\alpha = \frac{s_W\chi_Y}{\sqrt{1-\chi_Y^2}}\,, \quad \sin\alpha = \frac{s_W\chi_Y}{\sqrt{1-c_W^2\chi_Y^2}}\,, \quad \cos\alpha = \frac{\sqrt{1-\chi_Y^2}}{\sqrt{1-c_W^2\chi_Y^2}}\,, \tag{A.38}$$

$$x \equiv \frac{\tilde{m}_{\gamma'}^2}{\tilde{M}_Z^2}\,. \tag{A.39}$$

We find the eigenvalues for the matrix $\mathbf{M}_{2\times2}^2$ as

$$\begin{aligned} m_\pm^2 &= \frac{\tilde{M}_Z^2}{2(1-\chi_Y^2)}\left[1+x-\chi_Y^2+s_W^2\chi_Y^2 \pm \sqrt{(1+x-\chi_Y^2+s_W^2\chi_Y^2)^2-4x(1-\chi_Y^2)}\right] \\ &= \frac{\tilde{M}_Z^2}{2(1-\chi_Y^2)}\left[1+x-\chi_Y^2+s_W^2\chi_Y^2 \pm \sqrt{(1-x-\chi_Y^2+s_W^2\chi_Y^2)^2+4xs_W^2\chi_Y^2}\right] \\ &= \frac{\tilde{M}_Z^2}{2(1-\chi_Y^2)}\left[1+x-c_W^2\chi_Y^2 \pm \sqrt{(1+x-c_W^2\chi_Y^2)^2-4x(1-\chi_Y^2)}\right]\,, \end{aligned} \tag{A.40}$$

in which m_+ and m_- correspond to the Z mass M_Z and the hidden photon mass $m_{\gamma'}$, respectively. They are roughly given by

$$M_Z^2 \equiv m_+^2 = \tilde{M}_Z^2\left[1+\frac{s_W^2\chi_Y^2}{1-x}+...\right]\,, \tag{A.41}$$

$$m_{\gamma'}^2 \equiv m_-^2 = \tilde{m}_{\gamma'}^2\left[1+\frac{(1-s_W^2-x)\chi_Y^2}{1-x}+...\right]. \tag{A.42}$$

This shows that the kinetic mixing shifts the mass of the Z but the masses are only shifted at order χ_Y^2.

The transformation to diagonalise the mass term can in general be written as a unitary transformation described by the following ansatz as a function of an angle ϕ

$$\begin{pmatrix}\tilde{Z}_\mu\\ X_\mu\end{pmatrix} = \begin{pmatrix}c_\phi & s_\phi\\ -s_\phi & c_\phi\end{pmatrix}\begin{pmatrix}Z_\mu\\ \gamma'_\mu\end{pmatrix}\,, \tag{A.43}$$

so that the hidden photon γ' and the Z are thus defined as

$$\begin{aligned} Z_\mu &\equiv c_\phi\tilde{Z}_\mu - s_\phi X_\mu\,, \\ \gamma'_\mu &\equiv s_\phi\tilde{Z}_\mu + c_\phi X_\mu\,. \end{aligned} \tag{A.44}$$

We find that the mass matrix of Eq. (A.37) is diagonalised for

$$c_\phi = \cos\phi = \frac{\tilde{M}_Z^2 \tan\alpha}{\sqrt{\tilde{M}_Z^4 \tan^2\alpha + (\tilde{M}_Z^2 - m_+^2)^2}} = \frac{(\tilde{M}_Z^2 - m_-^2)}{\sqrt{\tilde{M}_Z^4 \tan^2\alpha + (\tilde{M}_Z^2 - m_-^2)^2}}$$
$$\simeq 1 - \frac{s_W^2 \chi_Y^2}{2(1-x)^2} + \dots , \tag{A.45}$$

$$s_\phi = \sin\phi = \frac{(m_+^2 - \tilde{M}_Z^2)}{\sqrt{\tilde{M}_Z^4 \tan^2\alpha + (\tilde{M}_Z^2 - m_+^2)^2}} = \frac{\tilde{M}_Z^2 \tan\alpha}{\sqrt{\tilde{M}_Z^4 \tan^2\alpha + (\tilde{M}_Z^2 - m_-^2)^2}}$$
$$\simeq \frac{s_W \chi_Y}{1-x} + \dots , \tag{A.46}$$

where $\tan\alpha$ from Eq. (A.38) has been used.

Applying the transformation (A.43) to the fields in the mass term of Eq. (A.36), the mass term can be expressed as

$$\begin{aligned}\mathcal{L} \supset\ & \frac{1}{2} Z_\mu Z^\mu \left[\frac{\tilde{m}_{\gamma'}^2}{1-\chi_Y^2} s_\phi^2 + \tilde{M}_Z^2 (c_\phi + s_\phi \frac{\chi_Y}{\sqrt{1-\chi_Y^2}} s_W)^2 \right] \\ & + \frac{1}{2} \gamma'_\mu \gamma'^\mu \left[\frac{\tilde{m}_{\gamma'}^2}{1-\chi_Y^2} c_\phi^2 + \tilde{M}_Z^2 (s_\phi - \frac{\chi_Y}{\sqrt{1-\chi_Y^2}} s_W c_\phi)^2 \right] \\ & + \gamma'_\mu Z^\mu \left[- \frac{\tilde{m}_{\gamma'}^2}{1-\chi_Y^2} s_\phi c_\phi + \tilde{M}_Z^2 (c_\phi + s_\phi \frac{\chi_Y}{\sqrt{1-\chi_Y^2}} s_W)(s_\phi - \frac{\chi_Y}{\sqrt{1-\chi_Y^2}} s_W c_\phi) \right] ,\end{aligned} \tag{A.47}$$

in which the term in parenthesis in the first line corresponds to the physical Z mass, the one in parenthesis in the second line to the physical hidden photon mass and the one in parenthesis in the last line has to vanish for the mass matrix to be diagonal, which gives a condition for the mixing angle ϕ as

$$- \frac{\tilde{m}_{\gamma'}^2}{1-\chi_Y^2} s_\phi c_\phi + \tilde{M}_Z^2 (c_\phi + s_\phi \frac{\chi_Y}{\sqrt{1-\chi_Y^2}} s_W)(s_\phi - \frac{\chi_Y}{\sqrt{1-\chi_Y^2}} s_W c_\phi) \stackrel{!}{=} 0. \tag{A.48}$$

Thus, the physical masses can be read off the first line for the Z as

$$M_Z^2 = m_+^2 = \tilde{M}_Z^2 (c_\phi + s_\phi s_W \frac{\chi_Y}{\sqrt{1-\chi_Y^2}})^2 + s_\phi^2 \frac{1}{1-\chi_Y^2} \tilde{m}_{\gamma'}^2$$
$$= \tilde{M}_Z^2 \left[1 - s_\phi^2 (1 + s_W^2 \frac{\chi_Y^2}{1-\chi_Y^2} + \frac{x}{1-\chi_Y^2}) + s_{2\phi} s_W \frac{\chi_Y}{\sqrt{1-\chi_Y^2}} \right] , \tag{A.49}$$

and off the second line for the hidden photon as

$$\begin{aligned} m_{\gamma'}^2 \;=\; m_-^2 \;&= \tilde{M}_Z^2(s_\phi - c_\phi s_W \frac{\chi_Y}{\sqrt{1-\chi_Y^2}})^2 + c_\phi^2 \frac{1}{1-\chi_Y^2}\tilde{m}_{\gamma'}^2 \\ &= \tilde{M}_Z^2\left[c_\phi^2 \frac{x}{1-\chi_Y^2} + s_W^2 \frac{\chi_Y^2}{1-\chi_Y^2} + s_\phi^2(1 - s_W^2 \frac{\chi_Y^2}{1-\chi_Y^2}) - s_{2\phi} s_W \frac{\chi_Y}{\sqrt{1-\chi_Y^2}}\right], \end{aligned} \tag{A.50}$$

which can be written as

$$\begin{pmatrix} M_Z^2 \\ m_{\gamma'}^2 \end{pmatrix} \;=\; \begin{pmatrix} m_+^2 \\ m_-^2 \end{pmatrix} \;=\; \begin{pmatrix} (c_\phi + s_\phi s_W \frac{\chi_Y}{\sqrt{1-\chi_Y^2}})^2 & s_\phi^2 \\ (s_\phi - c_\phi s_W \frac{\chi_Y}{\sqrt{1-\chi_Y^2}})^2 & c_\phi^2 \end{pmatrix} \begin{pmatrix} \tilde{M}_Z^2 \\ \frac{\tilde{m}_{\gamma'}^2}{1-\chi_Y^2} \end{pmatrix} . \tag{A.51}$$

Inverting the matrix then gives

$$\begin{pmatrix} \tilde{M}_Z^2 \\ \frac{\tilde{m}_{\gamma'}^2}{1-\chi_Y^2} \end{pmatrix} \;=\; \frac{1}{c_\phi^4 - s_\phi^4 + \frac{2c_\phi s_\phi s_W \chi_Y}{\sqrt{1-\chi_Y^2}}} \begin{pmatrix} c_\phi^2 & -s_\phi^2 \\ -(s_\phi - \frac{c_\phi s_W \chi_Y}{\sqrt{1-\chi_Y^2}})^2 & (c_\phi + \frac{s_\phi s_W \chi_Y}{\sqrt{1-\chi_Y^2}})^2 \end{pmatrix} \begin{pmatrix} M_Z^2 \\ m_{\gamma'}^2 \end{pmatrix}, \tag{A.52}$$

so that $\tilde{M}_Z$ and $\tilde{m}_{\gamma'}$ can be expressed in terms of the physical masses as

$$\tilde{M}_Z^2 \;= \frac{1}{c_\phi^4 - s_\phi^4 + \frac{2c_\phi s_\phi s_W \chi_Y}{\sqrt{1-\chi_Y^2}}} \left(c_\phi^2 M_Z^2 - s_\phi^2 m_{\gamma'}^2\right) , \tag{A.53}$$

$$\tilde{m}_{\gamma'}^2 \;= \frac{1-\chi_Y^2}{c_\phi^4 - s_\phi^4 + \frac{2c_\phi s_\phi s_W \chi_Y}{\sqrt{1-\chi_Y^2}}} \left(-(s_\phi - \frac{c_\phi s_W \chi_Y}{\sqrt{1-\chi_Y^2}})^2 M_Z^2 + (c_\phi + \frac{s_\phi s_W \chi_Y}{\sqrt{1-\chi_Y^2}})^2 m_{\gamma'}^2\right) . \tag{A.54}$$

Inserting this into the condition (A.48) which arises from the requirement that the off-diagonal mass term has to vanish and defining $S = (s_\phi - c_\phi s_W \chi_Y / \sqrt{1-\chi_Y^2})$ and $C = (c_\phi + s_\phi s_W \chi_Y / \sqrt{1-\chi_Y^2})$ gives

$$\begin{aligned} 0 \;&= -s_\phi c_\phi(-S^2 M_Z^2 + C^2 m_{\gamma'}^2) + (c_\phi^2 M_Z^2 - s_\phi^2 m_{\gamma'}^2) CS \\ 0 \;&= M_Z^2 c_\phi S(s_\phi S + c_\phi C) - m_{\gamma'}^2 s_\phi C(s_\phi S + c_\phi C) , \qquad \text{where } (s_\phi S + c_\phi C) = 1 \\ 0 \;&= M_Z^2 c_\phi s_\phi - M_Z^2 c_\phi^2 s_W \frac{\chi_Y}{\sqrt{1-\chi_Y^2}} - m_{\gamma'}^2 s_\phi c_\phi - m_{\gamma'}^2 s_\phi^2 s_W \frac{\chi_Y}{\sqrt{1-\chi_Y^2}} \\ 0 \;&= -s_\phi^2 s_W \frac{\chi_Y}{\sqrt{1-\chi_Y^2}} m_{\gamma'}^2 + c_\phi s_\phi (M_Z^2 - m_{\gamma'}^2) - c_\phi^2 s_W \frac{\chi_Y}{\sqrt{1-\chi_Y^2}} M_Z^2 \\ 0 \;&= -t_\phi^2 s_W \frac{\chi_Y}{\sqrt{1-\chi_Y^2}} m_{\gamma'}^2 + t_\phi (M_Z^2 - m_{\gamma'}^2) - s_W \frac{\chi_Y}{\sqrt{1-\chi_Y^2}} M_Z^2 , \end{aligned} \tag{A.55}$$

where $t_\phi = \tan\phi$.

This condition has the solutions

$$\begin{aligned}\tan\phi &= -\frac{\sqrt{1-\chi_Y^2}}{2s_W\chi_Y m_{\gamma'}^2}\left(-(M_Z^2-m_{\gamma'}^2)\pm\sqrt{(M_Z^2-m_{\gamma'}^2)^2-4s_W^2\frac{\chi_Y^2}{1-\chi_Y^2}M_Z^2m_{\gamma'}^2}\right)\\ &= -\frac{\sqrt{1-\chi_Y^2}}{2s_W\chi_Y\hat{x}}\left(-(1-\hat{x})\pm\sqrt{(1-\hat{x})^2-4s_W^2\frac{\chi_Y^2}{1-\chi_Y^2}\hat{x}}\right)\ , \end{aligned} \tag{A.56}$$

where we defined $\hat{x}\equiv\frac{m_{\gamma'}^2}{M_Z^2}$. For $x<1$, this can be estimated as

$$\begin{aligned}\tan\phi &\approx -\frac{\sqrt{1-\chi_Y^2}}{2s_W\chi_Y\hat{x}}(1-\hat{x})\left(-1+\sqrt{1-4s_W^2\frac{\chi_Y^2}{1-\chi_Y^2}\frac{\hat{x}}{(1-\hat{x})^2}}\right)\\ &\overset{x\ll1}{\approx} -\frac{\sqrt{1-\chi_Y^2}(1-\hat{x})}{2s_W\chi_Y\hat{x}}\left(-1+1-\frac{2s_W^2\chi_Y^2\hat{x}}{(1-\chi_Y^2)(1-\hat{x})^2}-\frac{1}{8}\left(\frac{4s_W^2\chi_Y^2\hat{x}}{(1-\chi_Y^2)(1-\hat{x})^2}\right)^2+...\right)\\ &\overset{x\ll1}{\approx}\frac{s_W\chi_Y}{\sqrt{1-\chi_Y^2}(1-\hat{x})}+\frac{s_W^3\chi_Y^3\hat{x}}{(1-\chi_Y^2)^{3/2}(1-\hat{x})^3}+...\ . \end{aligned} \tag{A.57}$$

As we are only interested in terms up to order χ_Y^2 at most, it follows that

$$\begin{aligned}\cos\phi &= \frac{1}{\sqrt{1+\tan^2\phi}} \approx 1-\frac{1}{2}\tan^2\phi+...\\ &\approx 1-\frac{1}{2}\frac{s_W^2\chi_Y^2}{(1-\chi_Y^2)(1-\hat{x})^2}+...\ , \end{aligned} \tag{A.58}$$

$$\begin{aligned}\sin\phi &= \cos\phi\tan\phi \approx \left(1-\frac{1}{2}\frac{s_W^2\chi_Y^2}{(1-\chi_Y^2)(1-\hat{x})^2}\right)\frac{s_W\chi_Y}{\sqrt{1-\chi_Y^2}(1-\hat{x})}\\ &\approx \frac{s_W\chi_Y}{\sqrt{1-\chi_Y^2}(1-\hat{x})}+\mathcal{O}(\chi_Y^3). \end{aligned} \tag{A.59}$$

In total, to diagonalise both the kinetic term and the mass terms the complete transformation

$$\begin{aligned}\tilde{W}_\mu &\equiv s_W A_\mu + c_W(c_\phi Z_\mu + s_\phi\gamma'_\mu)\ , \\ \tilde{B}_\mu &\equiv c_W A_\mu - s_W(c_\phi Z_\mu+s_\phi\gamma'_\mu)+\frac{\chi_Y}{\sqrt{1-\chi_Y^2}}(c_\phi\gamma'_\mu-s_\phi Z_\mu)\\ &= c_W A_\mu-(s_W c_\phi+\frac{\chi_Y}{\sqrt{1-\chi_Y^2}}s_\phi)Z_\mu+(\frac{\chi_Y}{\sqrt{1-\chi_Y^2}}c_\phi-s_W s_\phi)\gamma'_\mu\ , \\ \tilde{X}_\mu &\equiv \frac{1}{\sqrt{1-\chi_Y^2}}(-s_\phi Z_\mu+c_\phi\gamma'_\mu)\ , \end{aligned} \tag{A.60}$$

has to be applied to the Lagrangian (A.29).

The relevant terms of the Lagrangian then read

$$\begin{aligned}\mathcal{L} \supset & -\frac{1}{4}F_{\mu\nu}F^{\mu\nu} + \frac{1}{2}m_{\gamma'}^2\gamma'_\mu\gamma'^\mu + \frac{1}{2}M_Z^2 Z_\mu Z^\mu \\ & + eA_\mu \left[j_W^\mu + j_B^\mu\right] \\ & + Z_\mu \left[g_2 c_W c_\phi j_W^\mu - (s_W c_\phi + \frac{s_\phi \chi_Y}{\sqrt{1-\chi_Y^2}})g_Y j_B^\mu - \frac{s_\phi}{\sqrt{1-\chi_Y^2}} g_h j_h^\mu\right] \\ & + \gamma'_\mu \left[g_2 c_W s_\phi j_W^\mu + (\frac{c_\phi \chi_Y}{\sqrt{1-\chi_Y^2}} - s_W s_\phi)g_Y j_B^\mu + \frac{c_\phi}{\sqrt{1-\chi_Y^2}} g_h j_h^\mu\right].\end{aligned} \tag{A.61}$$

Using the approximations of c_ϕ and s_ϕ from Eqs. (A.45) and (A.46) to expand the couplings to first order, the interaction terms in the Lagrangian can be written as

$$\begin{aligned}\mathcal{L} \supset & \; eA_\mu \left[j_W^\mu + j_B^\mu\right] \\ & + Z_\mu \left[g_2 c_W j_W^\mu - g_Y s_W j_B^\mu - s_W \frac{\chi_Y}{1-x} g_h j_h^\mu\right] \\ & + \gamma'_\mu \left[g_2 c_W s_W \frac{\chi_Y}{1-x} j_W^\mu + g_Y \chi_Y (1 - \frac{s_W^2}{1-x}) j_B^\mu + g_h j_h^\mu\right] \\ \supset & \; eA_\mu \, j_A^\mu \\ & + Z_\mu \left[e j_{Z^0}^\mu - s_W \frac{\chi_Y}{1-x} g_h j_h^\mu\right] \\ & + \gamma'_\mu \left[e c_W \frac{\chi_Y}{1-x} j_A^\mu - \frac{e\chi_Y x}{c_W(1-x)} j_B^\mu + g_h j_h^\mu\right],\end{aligned} \tag{A.62}$$

where $g_Y = e/c_W$, $g_2 = e/s_W$ and the currents j_A^μ and $j_{Z^0}^\mu$ are defined by Eqs. (A.19) and (A.20) in Sec. A.3.

In the same way, the full interaction terms of the Lagrangian (A.61) can then be rewritten with Eqs. (A.23) and (A.24) in terms of j_A^μ and $j_{Z^0}^\mu$ instead of j_B^μ and j_W^μ as

$$\begin{aligned}\mathcal{L} \supset & \; eA_\mu \, j_A^\mu \\ & + Z_\mu \left[e j_{Z^0}^\mu (c_\phi + s_W s_\phi \frac{\chi_Y}{\sqrt{1-\chi_Y^2}}) - e c_W s_\phi \frac{\chi_Y}{\sqrt{1-\chi_Y^2}} j_A^\mu - \frac{s_\phi}{\sqrt{1-\chi_Y^2}} g_h j_h^\mu\right] \\ & + \gamma'_\mu \left[e j_{Z^0}^\mu (s_\phi - s_W c_\phi \frac{\chi_Y}{\sqrt{1-\chi_Y^2}}) + e s_W c_\phi \frac{\chi_Y}{\sqrt{1-\chi_Y^2}} j_A^\mu + \frac{c_\phi}{\sqrt{1-\chi_Y^2}} g_h j_h^\mu\right].\end{aligned} \tag{A.63}$$

Inserting further the expressions from (A.21) and (A.22) yields

$$
\begin{aligned}
\mathcal{L} \supset\ & eA_\mu j_A^\mu \\
& + Z_\mu \Bigg[- Q\frac{e}{c_W}\big(s_W c_\phi + s_\phi \frac{\chi_Y}{\sqrt{1-\chi_Y^2}}\big)\bar{\psi}\gamma^\mu\psi \\
& \qquad + T_3 \frac{e}{c_W s_W}\big(c_\phi + s_\phi s_W \frac{\chi_Y}{\sqrt{1-\chi_Y^2}}\big)\bar{\psi}\gamma^\mu P_L\psi - \frac{s_\phi}{\sqrt{1-\chi_Y^2}} g_h j_h^\mu \Bigg] \\
& + \gamma'_\mu \Bigg[- Q\frac{e}{c_W} s_W \big(s_\phi - c_\phi \frac{\chi_Y}{\sqrt{1-\chi_Y^2}}(s_W + c_W)\big)\bar{\psi}\gamma^\mu\psi \\
& \qquad + T_3 \frac{e}{c_W s_W}\big(s_\phi - s_W c_\phi \frac{\chi_Y}{\sqrt{1-\chi_Y^2}}\big)\bar{\psi}\gamma^\mu P_L\psi + \frac{c_\phi}{\sqrt{1-\chi_Y^2}} g_h j_h^\mu \Bigg] . \qquad \text{(A.64)}
\end{aligned}
$$

Appendix B

Number of Events from Hidden Photons in Electron Beam Dump Experiments

This appendix gives additional information and details on the hidden photon production in bremsstrahlung and the number of events expected in an electron beam dump experiment. The pseudophoton-flux is presented for the different experiments in Sec. B.1. Details on the integration of the cross section are given in Sec. B.2. The shape and numerical approximation of the electron energy distribution is discussed in Sec. B.3. The radiation length and unit radiation length are defined in Sec B.4. The so-called R-ratio and its use in the hidden photon decay width is explained in Sec. B.5. The peculiarities of the numerical calculation of the number of events are summarised in Sec. B.6. Finally, the determination of the 95% C.L. upper limits is given in Sec. B.7.

B.1 Weizsäcker–Williams pseudophoton-flux

As described in Sec. 3.1, the cross section for the production of hidden photons in bremsstrahlung can be computed in the Weizsäcker–Williams approximation according to Eq. (3.3) with a pseudophoton-flux given by Eq. (3.4). For the different experiments summarised in Sec. 3.2.1, the behaviour of the pseudophoton-flux as a function of the hidden photon mass is presented in Fig. B.1. The pseudophoton-flux varies between the experiments due to the different settings but shows in all cases for light hidden photons only a mild dependence on $m_{\gamma'}$. The right-hand plot indicates that for small masses the flux normalised to the atomic number Z of the target is similar for all experiments. The production cross section is thus expected do have the same dependence $\sigma_{\gamma'} \propto Z^2$.

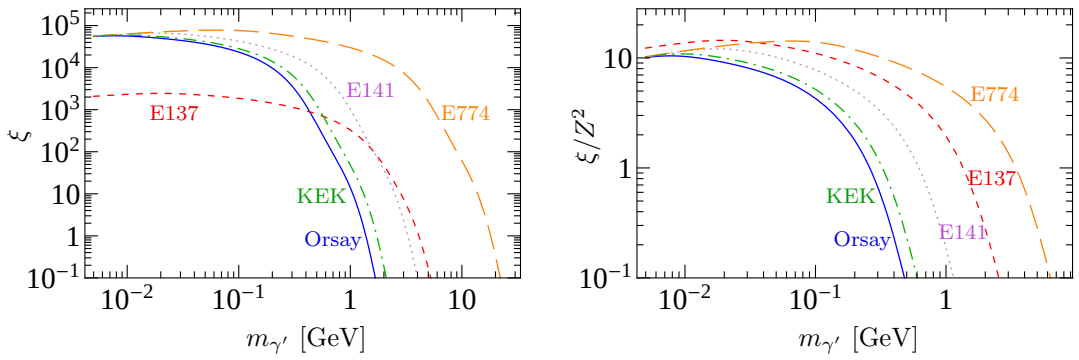

Figure B.1: Pseudophoton-flux ξ of the Weizsäcker–Williams approximation as a function of the hidden photon mass $m_{\gamma'}$.
Left: Pseudophoton-flux ξ for the different electron beam dump experiments KEK (dash-dotted green line), E141 (dotted purple line), E137 (dashed red line), Orsay (solid blue line) and E774 (long-dashed orange line), cf. Sec. 3.2.1.
Right: Normalised to the atomic number Z of the target, the pseudophoton-flux ξ is similar for all experiments and $\mathcal{O}(5-10)$ for the mass range of interest.

B.2 Hidden photon bremsstrahlung production cross section

To perform the integral of the production cross section over the emission angle $\theta_{\gamma'}$ we rewrite the function $U(x_e, E_e, m_{\gamma'}, \theta_{\gamma'})$ from Eq. (3.8) as

$$U(x_e, E_e, m_{\gamma'}, \theta_{\gamma'}) \;=\; E_e^2\, x_e \left(\theta_{\gamma'}^2 + \frac{m_{\gamma'}^2}{E_e^2}\frac{1-x_e}{x_e^2} + \frac{m_e^2}{E_e^2}\right) \;=\; E_e^2\, x_e\, (\theta_{\gamma'}^2 + \eta_e)\,, \tag{B.1}$$

with

$$\eta_e \;=\; \frac{m_{\gamma'}^2}{E_e^2}\frac{1-x_e}{x_e^2} + \frac{m_e^2}{E_e^2}\,. \tag{B.2}$$

Then the differential production cross Sec. (3.7) can be integrated as

$$\begin{aligned}\frac{d\sigma_{\gamma'}}{dx_e} \;=\; 8\alpha^3\chi^2\, \xi(E_e, m_{\gamma'}, Z, A)\, \sqrt{1-\frac{m_{\gamma'}^2}{E_e^2}} \Bigg[&\frac{1-x_e+\frac{x_e^2}{2}}{E_e^2 x_e} \int_{-1}^{1} \frac{d\cos\theta_{\gamma'}}{(\theta_{\gamma'}^2+\eta_e)^2} \\ &+ \frac{(1-x_e)^2 m_{\gamma'}^4}{(E_e^2 x_e)^3} \int_{-1}^{1} \frac{d\cos\theta_{\gamma'}}{(\theta_{\gamma'}^2+\eta_e)^4} - \frac{(1-x_e)x_e m_{\gamma'}^2}{(E_e^2 x_e)^2} \int_{-1}^{1} \frac{d\cos\theta_{\gamma'}}{(\theta_{\gamma'}^2+\eta_e)^3} \Bigg]\,,\end{aligned} \tag{B.3}$$

where the integration than is performed by changing to $\int_{-1}^{1} d\cos\theta_{\gamma'} = \int_0^{\pi} \sin\theta_{\gamma'}\, d\theta_{\gamma'} \to \int_0^{\theta_{\max}} \sin\theta_{\gamma'}\, d\theta_{\gamma'}$. The angle $\theta_{\gamma'}$ is not integrated up to π but only up to a small angle $\theta_{\max}$ determined by the angular acceptance of the different experiments.

Defining the three integrals over $\theta_{\gamma'}$ as $\tilde{U}_i$, with $i = 2, 3, 4$ labelling the power of the denominator, and computing them with Mathematica in the limit of small η_e yields

$$\tilde{U}_2 = \int_0^{\theta_{\max}} \frac{\sin\theta_{\gamma'} d\theta_{\gamma'}}{(\theta_{\gamma'}^2 + \eta_e)^2} \simeq \frac{1}{2\eta_e} - 1.8 + \frac{\log\eta_e}{12} + 7.3\eta_e + \frac{\eta_e \log\eta_e}{120} + \mathcal{O}(\eta_e^2) \ , \tag{B.4}$$

$$\tilde{U}_3 = \int_0^{\theta_{\max}} \frac{\sin\theta_{\gamma'} d\theta_{\gamma'}}{(\theta_{\gamma'}^2 + \eta_e)^3} \simeq \frac{1}{4\eta_e^2} - \frac{1}{24\eta_e} - 3.7 - \frac{\log\eta_e}{240} + 30\eta_e - 3.0\times10^{-4}\eta_e\log\eta_e + \\ + \mathcal{O}(\eta_e^2) \ , \tag{B.5}$$

$$\tilde{U}_4 = \int_0^{\theta_{\max}} \frac{\sin\theta_{\gamma'} d\theta_{\gamma'}}{(\theta_{\gamma'}^2 + \eta_e)^4} \simeq \frac{1}{6\eta_e^3} - \frac{1}{72\eta_e^2} + \frac{1}{720\eta_e} - 10 + 9.9\times10^{-5}\log\eta_e + 1.2\times10^2\eta_e + \\ + 5.5\times10^{-6}\eta_e\log\eta_e + \mathcal{O}(\eta_e^2) \ , \tag{B.6}$$

for $\theta_{\max} = 0.5$ rad.

Keeping only the leading terms in $\tilde{U}_i$ ($\eta_e \ll 1$, from Eq. (B.2) for $m_e \ll m_{\gamma'} \ll E_e$, $x_e \approx 1$) the differential cross section reads together with Eq. (B.2)

$$\frac{d\sigma_{\gamma'}}{dx_e} \simeq 8\alpha^3\chi^2\ \xi(E_e, m_{\gamma'}, Z, A)\ \sqrt{1 - \frac{m_{\gamma'}^2}{E_e^2}}\ \frac{1}{2}\ \frac{1}{m_{\gamma'}^2\frac{1-x_e}{x_e} + m_e^2 x_e} \\ \left[1 - x_e + \frac{x_e^2}{2} + \frac{1}{3}\frac{(1-x_e)^2 m_{\gamma'}^4}{(m_{\gamma'}^2\frac{1-x_e}{x_e} + m_e^2 x_e)^2} - \frac{1}{2}\frac{(1-x_e)x_e m_{\gamma'}^2}{m_{\gamma'}^2\frac{1-x_e}{x_e} + m_e^2 x_e}\right] . \tag{B.7}$$

Neglecting terms with higher orders of the electron mass this approximates to

$$\frac{d\sigma_{\gamma'}}{dx_e} \simeq 4\alpha^3\chi^2\ \xi(E_e, m_{\gamma'}, Z, A)\ \sqrt{1 - \frac{m_{\gamma'}^2}{E_e^2}}\ \frac{1 - x_e + \frac{1}{3}x_e^2}{m_{\gamma'}^2\frac{1-x_e}{x_e} + m_e^2 x_e} \tag{B.8}$$

$$\overset{m_e\to0}{\simeq} 4\alpha^3\chi^2\ \xi_{(m_{\gamma'}, E_e, Z, A)}\ \frac{x_e}{m_{\gamma'}^2}\ \sqrt{1 - \frac{m_{\gamma'}^2}{E_e^2}}\ \left(1 + \frac{x_e^2}{3(1-x_e)}\right), \tag{B.9}$$

which includes a factor 1/2 that erroneously omitted in the expression of [266].

The total hidden photon production cross section can then be estimated from integrating Eq. (B.9) as

$$\sigma = \frac{4}{3}\alpha^3\chi^2\ \xi(m_{\gamma'}, E_e, Z, A)\ \frac{1}{m_{\gamma'}^2}\log\left(\frac{1}{(1-x_e)_c}\right) \tag{B.10}$$

$$\propto \frac{4}{3}\alpha^3\ Z^2\ \frac{\chi^2}{m_{\gamma'}^2}, \tag{B.11}$$

where $(1 - x_e)_c = \max(m_e^2/m_{\gamma'}^2, m_{\gamma'}^2/E_e^2)$ according to [266].

B.3 Electron energy distribution $\mathbf{I_e(E_0, E_e, t)}$

The energy distribution I_e of the electrons after having passed through t radiation length of the target is given in Eq. (3.16). The shape of this distribution as a function of the electron energy E_e is shown in Fig. B.2 at various positions t in the target. The plot assumes an initial beam energy E_0 of 1.6 GeV which corresponds to the one used in the Orsay experiment. The black line corresponds to the very beginning of the target ($t = 0.01$) and peaks at large values of E_e close to the beam energy. With increasing depth in the target the distribution spreads out to lower energies (blue lines) until it eventually turns over (green lines) and peaks around zero for large values of t (red to magenta lines).

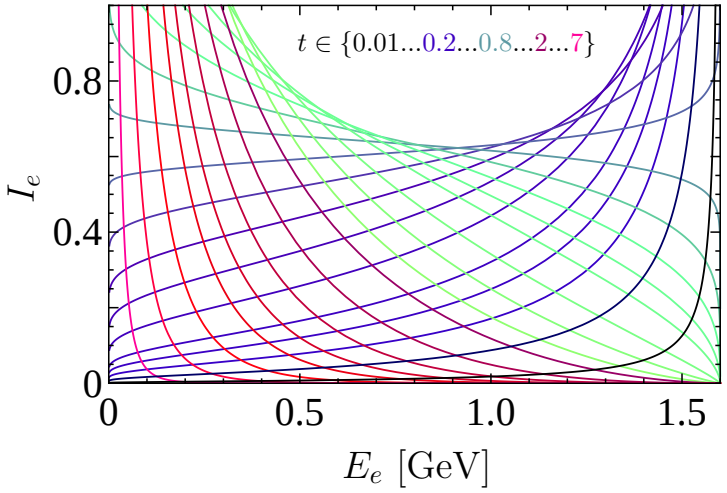

Figure B.2: Electron energy distribution I_e at different positions t in the target for a beam energy $E_0 = 1.6$ GeV.

B.4 Radiation length and unit radiation length

The radiation length r_0 of a target with density ρ_{sh} is determined by the unit radiation length X_0 in g/cm^2 as

$$r_0\ [\text{cm}] \;=\; \frac{X_0\ [\text{g/cm}^2]}{\rho_{\text{sh}}\ [\text{g/cm}^3]}\ . \tag{B.12}$$

The unit radiation length X_0 follows with the electron radius $r_e = \alpha/m_e$ from the definition in [4] as

$$X_0 \;=\; \frac{m_e^2 A}{4\alpha^3 N_0}\ \frac{1}{Z^2\ [L_{\text{rad}} - f(Z)]\ +\ Z\ L'_{\text{rad}}}\,, \tag{B.13}$$

in which Z and A are the atomic number and the mass number of the target material, respectively, $N_0 = 6.022 \times 10^{23}$ mole^{-1} is Avogadro's number and L_{rad} as well as L'_{rad}

are for elements with $Z > 4$ given by

$$L_{\rm rad} \;=\; \ln\left(184.15\; Z^{-1/3}\right) \qquad \text{and} \qquad L'_{\rm rad} \;=\; \ln\left(1194\; Z^{-2/3}\right). \tag{B.14}$$

The function $f(Z)$ is according to [4] an infinite sum which can be approximated with 4-digits accuracy for elements up to uranium by

$$f(Z) = \alpha^2 Z^2\Big[(1+\alpha^2 Z^2)^{-1} + 0.20206 - 0.0369\,\alpha^2 Z^2 + 0.0083\,\alpha^4 Z^4 - 0.002\,\alpha^6 Z^6\Big]. \tag{B.15}$$

With those definitions, the quantity $T_{\rm sh}$ in the upper limit of the integration over the target in units of the radiation length in Eq. (3.21) is then defined as

$$T \;\equiv\; \frac{L_{\rm sh}}{r_0} \;=\; \frac{L_{\rm sh}\;\rho_{\rm sh}}{X_0}\;. \tag{B.16}$$

It thus depends on the density $\rho_{\rm sh}$ and the unit radiation length X_0 of the target as well as the physical length $L_{\rm sh}$ of the target plus shield.

B.5 Remark on R-ratio

For large enough masses, the hidden photon can not only decay into leptons but also into hadrons. In this case, one has to properly take into account the occurrence of hadronic resonances. This is done by using the experimentally measured ratio of the electron-positron cross section into hadrons to the one into muons. This so-called R-ratio is defined as

$$R(\sqrt{s}) \;=\; \frac{\sigma(e^+e^- \longrightarrow \text{hadrons},\, \sqrt{s})}{\sigma(e^+e^- \longrightarrow \mu^+\mu^-,\, \sqrt{s})}. \tag{B.17}$$

The world data for R is given in Ref. [4].

As the photon and the hidden photon couple in the same way to charged particles (up to a factor χ), we take the ratio of the cross sections to be the roughly same for the photon and the hidden photon

$$\frac{\sigma(e^+e^- \longrightarrow \gamma \longrightarrow \text{hadrons})}{\sigma(e^+e^- \longrightarrow \gamma \longrightarrow \mu^+\mu^-)} \;\simeq\; \frac{\sigma(e^+e^- \longrightarrow \gamma' \longrightarrow \text{hadrons})}{\sigma(e^+e^- \longrightarrow \gamma' \longrightarrow \mu^+\mu^-)}. \tag{B.18}$$

For an on-shell hidden photon, we decompose the cross section using the narrow width approximation as

$$\begin{aligned}\left.\frac{\sigma(e^+e^- \longrightarrow \gamma' \longrightarrow \text{hadrons})}{\sigma(e^+e^- \longrightarrow \gamma' \longrightarrow \mu^+\mu^-)}\right|_{\sqrt{s}=m_{\gamma'}} &\simeq \left.\frac{\sigma(e^+e^- \longrightarrow \gamma')\;\text{BR}(\gamma' \longrightarrow \text{hadrons})}{\sigma(e^+e^- \longrightarrow \gamma')\;\text{BR}(\gamma' \longrightarrow \mu^+\mu^-)}\right|_{\sqrt{s}=m_{\gamma'}} \\ &= \left.\frac{\Gamma(\gamma' \longrightarrow \text{hadrons})}{\Gamma(\gamma' \longrightarrow \mu^+\mu^-)}\right|_{\sqrt{s}=m_{\gamma'}}.\end{aligned} \tag{B.19}$$

The decay width of the hidden photon into hadrons then follows as

$$\Gamma(\gamma' \longrightarrow \text{hadrons}) = \Gamma(\gamma' \longrightarrow \mu^+\mu^-) \left.\frac{\sigma(e^+e^- \longrightarrow \text{hadrons})}{\sigma(e^+e^- \longrightarrow \mu^+\mu^-)}\right|_{\sqrt{s}=m_{\gamma'}} \tag{B.20}$$

$$= \Gamma(\gamma' \longrightarrow \mu^+\mu^-)\, R(m_{\gamma'})\,, \tag{B.21}$$

which has been used in Eq. (3.11).

B.6 Number of expected events $N_{\gamma'}$

The total number of events predicted in an electron beam dump experiment is given according to Eq. (3.24) by

$$N_{\gamma'} = N_e \frac{N_0 X_0}{A}\, 8\alpha^3\chi^2\, \text{BR}_{\text{detect}} \int_{m_{\gamma'}}^{E_0-m_e} dE_{\gamma'} \int_{E_{\gamma'}+m_e}^{E_0} dE_e \int_0^{T_{\text{sh}}} dt_{\text{sh}} \tag{B.22}$$
$$\left\{ \frac{1}{E_0} \frac{\left[\ln\frac{E_0}{E_e}\right]^{bt_{\text{sh}}-1}}{\Gamma(bt_{\text{sh}})}\, \xi_{(m_{\gamma'},E_e,Z,A)} \left(e^{-L_{\text{sh}}/l_{\gamma'}} - e^{-L_{\text{tot}}/l_{\gamma'}}\right) \frac{1}{E_e^2\, E_{\gamma'}} \sqrt{1-\frac{m_{\gamma'}^2}{E_e^2}} \right.$$
$$\left. \left[\left(\frac{E_e - E_{\gamma'}}{E_e} + \frac{E_{\gamma'}^2}{2E_e^2}\right)\tilde{U}_{2(E_e)} + \left(\frac{E_e - E_{\gamma'}}{E_e^2 E_{\gamma'}}\right)^2 m_{\gamma'}^4 \tilde{U}_{4(E_e)} - \frac{E_e - E_{\gamma'}}{E_e^3} m_{\gamma'}^2 \tilde{U}_{3(E_e)} \right] \right\},$$

where the electron energy distribution I_e from Eq. (3.16), the differential production cross section $d\sigma/dx_e$ from Eq. (B.3) and the integrals $\tilde{U}_i$ from Eqs. (B.4) to (B.6) have been used, the effective photon flux $\xi_{(m_{\gamma'},E_e,Z,A)}$ and the decay length $l_{\gamma'}$ are defined in Eqs. (3.4) and (3.13), respectively, and $\text{BR}_{\text{detect}}$ refers to the branching ratio for the decay of the hidden photon into those particles the detector is sensitive too (usually electrons and positrons so that $\text{BR}_{\text{detect}} = 1$ for $m_{\gamma'} < 2m_\mu$ in the absence of other lighter particles in the hidden sector).

Integration borders

It is equivalent to perform the integration with the following choices of the integration borders

$$\int_{m_{\gamma'}}^{E_0-m_e} \left(\int_{E_{\gamma'}+m_e}^{E_0} f(E_e, E_{\gamma'})\, dE_e \right) dE_{\gamma'} \equiv \int_{m_{\gamma'}+m_e}^{E_0} \left(\int_{m_{\gamma'}}^{E_e-m_e} f(E_e, E_{\gamma'})\, dE_{\gamma'} \right) dE_e\,.$$

Numerical integration

The integration of Eq. (B.22) can not be carried out analytically. We therefore perform numerical computations for each of the experiments discussed in Sec. 3.2.1, using the specific parameters for E_0, $L_{\rm sh}$, $L_{\rm dec}$, Z and A given in Tab. 3.1, and scanning over the entire parameter space $\{m_{\gamma'}, \chi\}$. These numerical integrations, however, diverge since for small t the function $I_e(E_0, E_e, t)$ of Eq. (3.16) sharply peaks at $E_e \simeq E_0$ (cf. also black and blue lines in Fig. B.2). Therefore, we define a cut ϵ at which we split the integral over $t_{\rm sh}$ in two parts: for very small $t_{\rm sh} \leq \epsilon$ we approximate the function $I_e(E_0, E_e, t_{\rm sh})$ by the delta-function according to Eq. (3.18); for larger $t_{\rm sh} \geq \epsilon$ we keep the exact expression of Eq. (3.16). In this way, in the region $t_{\rm sh} \leq \epsilon$, the integration both over t and E_e can be carried out analytically and the one for $t_{\rm sh} \geq \epsilon$ can be done numerically. An example for this separation for the integral solely of I_e over E_e is illustrated in Fig. B.3, in a specific scenario with $E_0 = 1.6$ GeV and $E_{\gamma'} = 0.8$ GeV. Considering only $t > 0$, the integration of I_e Eq. (3.16) over E_e can be carried out analytically and is plotted as a function of t in Fig. B.3 as dashed blue line. The numerical integration shown as solid orange line does not yield good results at small t, where the result is well represented by the analytic integration over the delta-function, shown as solid green line.

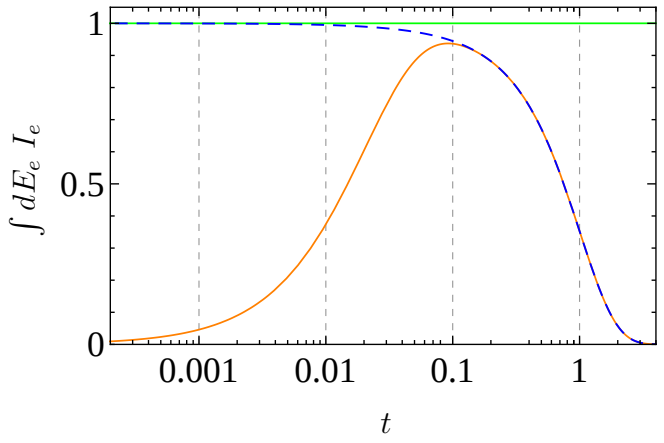

Figure B.3: Comparison of the analytic integration for $\int dE_e\ I_e$ with the numerical one. This represents the average energy of the electrons in the beam normalised to E_0 at position t in the target (in units of the radiation length). The results from the integration are shown for $E_0 = 1.6$ GeV and $E_{\gamma'} = 0.8$ GeV where the different lines correspond to:

dashed blue line: analytic integration of $\displaystyle\int_{E_{\gamma'}}^{E_0} dE_e\ \frac{1}{E_0}\ \frac{\left[\ln\left(\frac{E_0}{E_e}\right)\right]^{\frac{4}{3}t-1}}{\Gamma(\frac{4}{3}t)}$,

solid green line: analytic integration of $\displaystyle\int_{E_{\gamma'}}^{E_0} dE_e\ \delta(E_e - E_0)$,

solid orange line: numerical integration of $\displaystyle\int_{E_{\gamma'}}^{E_0} dE_e\ \frac{1}{E_0}\ \frac{\left[\ln\left(\frac{E_0}{E_e}\right)\right]^{\frac{4}{3}t-1}}{\Gamma(\frac{4}{3}t)}$.

Thus, combining the result $N_{\leq\epsilon}$ of the partly analytical integration for $t_{\rm sh} \leq \epsilon$ with the result $N_{\geq\epsilon}$ for the numerical integration at $t_{\rm sh} \geq \epsilon$, the total number of events predicted in an electron beam dump experiment follows from Eq. (B.22) as

$$N_{\gamma'} \;=\; N_e \,\frac{N_0 X_0}{A}\; 8\alpha^3\chi^2 \;(\; N_{\leq\epsilon} + N_{\geq\epsilon}\;)\;{\rm BR}_{\rm detect}\,, \tag{B.23}$$

with

$$\begin{aligned} N_{\leq\epsilon} = \int_{m_{\gamma'}}^{E_0-m_e} dE_{\gamma'} \int_{E_{\gamma'}+m_e}^{E_0} dE_e \int_0^{\epsilon} dt_{\rm sh} \;\Bigg\{ & \delta(E_e-E_0) \\ & \frac{1}{E_e^2\;E_{\gamma'}}\,\xi_{(m_{\gamma'},E_e,Z,A)}\,\left(e^{-L_{\rm sh}/l_{\gamma'}} - e^{-L_{\rm tot}/l_{\gamma'}}\right)\,\sqrt{1-\frac{m_{\gamma'}^2}{E_e^2}} \\ & \left[\left(\frac{E_e-E_{\gamma'}}{E_e}+\frac{E_{\gamma'}^2}{2E_e^2}\right)\tilde{U}_{2(E_e)} + \left(\frac{E_e-E_{\gamma'}}{E_e^2 E_{\gamma'}}\right)^2 m_{\gamma'}^4\tilde{U}_{4(E_e)} - \frac{E_e-E_{\gamma'}}{E_e^3}m_{\gamma'}^2\tilde{U}_{3(E_e)}\right]\Bigg\} \end{aligned} \tag{B.24}$$

and

$$\begin{aligned} N_{\geq\epsilon} = \int_{m_{\gamma'}}^{E_0-m_e} dE_{\gamma'} \int_{E_{\gamma'}+m_e}^{E_0} dE_e \int_{\epsilon}^{T_{\rm sh}} dt_{\rm sh} \;\Bigg\{ & \frac{1}{E_0}\,\frac{\left[\ln\frac{E_0}{E_e}\right]^{bt_{\rm sh}-1}}{\Gamma(bt_{\rm sh})} \\ & \frac{1}{E_e^2\;E_{\gamma'}}\,\xi_{(m_{\gamma'},E_e,Z,A)}\,\left(e^{-L_{\rm sh}/l_{\gamma'}} - e^{-L_{\rm tot}/l_{\gamma'}}\right)\,\sqrt{1-\frac{m_{\gamma'}^2}{E_e^2}} \\ & \left[\left(\frac{E_e-E_{\gamma'}}{E_e}+\frac{E_{\gamma'}^2}{2E_e^2}\right)\tilde{U}_{2(E_e)} + \left(\frac{E_e-E_{\gamma'}}{E_e^2 E_{\gamma'}}\right)^2 m_{\gamma'}^4\tilde{U}_{4(E_e)} - \frac{E_e-E_{\gamma'}}{E_e^3}m_{\gamma'}^2\tilde{U}_{3(E_e)}\right]\Bigg\}. \end{aligned} \tag{B.25}$$

In $N_{\leq\epsilon}$, the integral over $t_{\rm sh}$ can be carried out analytically as

$$\begin{aligned} N_{\leq\epsilon} = \int_{m_{\gamma'}}^{E_0-m_e} dE_{\gamma'} \int_{E_{\gamma'}+m_e}^{E_0} dE_e \;\Bigg\{ & \epsilon\;\delta(E_e-E_0) \\ & \frac{1}{E_e^2\;E_{\gamma'}}\,\xi_{(m_{\gamma'},E_e,Z,A)}\,\left(e^{-L_{\rm sh}/l_{\gamma'}} - e^{-L_{\rm tot}/l_{\gamma'}}\right)\,\sqrt{1-\frac{m_{\gamma'}^2}{E_e^2}} \\ & \left[\left(\frac{E_e-E_{\gamma'}}{E_e}+\frac{E_{\gamma'}^2}{2E_e^2}\right)\tilde{U}_{2(E_e)} + \left(\frac{E_e-E_{\gamma'}}{E_e^2 E_{\gamma'}}\right)^2 m_{\gamma'}^4\tilde{U}_{4(E_e)} - \frac{E_e-E_{\gamma'}}{E_e^3}m_{\gamma'}^2\tilde{U}_{3(E_e)}\right]\Bigg\}, \end{aligned}$$

and the integral over E_e with the δ-function as

$$N_{\leq\epsilon} = \int_{m_{\gamma'}}^{E_0 - m_e} dE_{\gamma'} \left\{ \epsilon \, \frac{1}{E_0^2 \, E_{\gamma'}} \, \xi_{(m_{\gamma'}, E_0, Z, A)} \, \left(e^{-L_{\rm sh}/l_{\gamma'}} - e^{-L_{\rm tot}/l_{\gamma'}} \right) \sqrt{1 - \frac{m_{\gamma'}^2}{E_0^2}} \right.$$
$$\left. \left[\left(\frac{E_0 - E_{\gamma'}}{E_0} + \frac{E_{\gamma'}^2}{2E_0^2} \right) \tilde{U}_{2(E_0)} + \left(\frac{E_0 - E_{\gamma'}}{E_0^2 E_{\gamma'}} \right)^2 m_{\gamma'}^4 \tilde{U}_{4(E_0)} - \frac{E_0 - E_{\gamma'}}{E_e^3} m_{\gamma'}^2 \tilde{U}_{3(E_0)} \right] \right\} .$$

Together with Eqs. (B.13) and (B.15), the total number of events can then be written as

$$N_{\gamma'} \;=\; 2 \, N_e \, m_e^2 \, \chi^2 \, \frac{1}{Z^2 \, [L_{\rm rad} - f(Z)] + Z L'_{\rm rad}} \, (\, N_{\leq\epsilon} + N_{\geq\epsilon} \,) \, {\rm BR}_{\rm detect} \, . \qquad \text{(B.26)}$$

Experimental exclusion contours

In the computation of the exclusion contours shown in Fig. 3.8, the parameter ϵ is set to 0.07. For the functions $\tilde{U}_i$ of Eqs. (B.4) to (B.6), arising from the hidden photon production cross section, the two leading terms of the approximations are included. The total number $N_{\gamma'}$ of events is then obtained by scanning over the parameter space in $m_{\gamma'}$ and χ and numerically integrating Eq. (B.26) at each point $\{m_{\gamma'}, \chi\}$ for the parameters E_0, $L_{\rm sh}$, $L_{\rm dec}$, Z and A of a particular experiment as given in Tab. 3.1. A certain experimental limit is then obtained by comparing this theoretical prediction for $N_{\gamma'}$ with the 95% C.L. upper limit $N_{95\%{\rm up}}$ on the number of events observed by the experiment. The resulting limit, however, assumes an ideal experiment that can observe all of the decay-leptons. Therefore, the actual experimental acceptance still has to be taken into account in order to derive the final exclusion contour. In this way, the final exclusion contour of an experiment becomes slightly weaker then the ideal exclusion contour.

For each experiment, the different acceptances are obtained as described in Sec. 3.2.2 by comparing the results from Monte Carlo simulations with the specific set-up of the respective experiments. These simulations are performed at several points $\{m_{\gamma'}, \chi\}$ in the parameter space such that the region where the aforementioned prediction of the ideal exclusion limit is entirely covered. At each point $\{m_{\gamma'}, \chi\}$, the acceptance is then computed from the simulations. The final exclusion contours shown in Fig. 3.8, are then derived by interpolating these acceptances as a function of $m_{\gamma'}$ and χ and multiplying them with the ideal limit obtained from Eq. (B.26) for a certain 95% C.L. upper limit $N_{95\%{\rm up}}$ of the number of observed events.

B.7 Number of observed events and 95% C.L. upper limit

The number $N_{\rm obs}$ of events that where observed in an experiment are given in Tab. 3.1. From this number, the 95% C.L. upper limit on the number $N_{95\%\rm up}$ of events used in the exclusion contour is deduced for a Poisson and a Gaussian signal as described in the following.

Poisson signal

For very few or zero observed events, the 95% C.L. intervals for a Poisson signal are presented in Tab. VI of Ref. [338]. There, the 95% C.L. upper limit corresponding to zero observed event is given as

$$N_{95\%\rm up} \;=\; 3\,, \tag{B.27}$$

for $N_{\rm obs} = 0$.

Gaussian signal

In the case of a Gaussian distribution with mean μ and error σ, we derive the number corresponding to the 95% C.L. upper limit using a modified distribution in order to exclude the non-physical part which arises when the distribution gets negative. This negative part of the distribution has to be ignored and the positive part has to be normalised again to 1.

We then define $f(x)$ as the integral over the normal distribution from $-\infty$ to x by

$$f(x) \;=\; \int_{-\infty}^{x} \frac{1}{\sqrt{2\pi}\sigma}\; e^{-\frac{(x-\mu)^2}{2\sigma^2}}\,, \tag{B.28}$$

with mean μ and error σ.

If the negative part of the distribution was not excluded, the 95% C.L. upper limit would be obtained by solving

$$f(N_{95\%\rm C.L.}) \;=\; 0.95 \tag{B.29}$$

for $N_{95\%\rm C.L.}$.

In our case, however, we need to define a new function $f_{>0}(x)$ by removing the negative part (which is given by $f(0)$) of the original distribution

$$f_{>0}(x) \;=\; \frac{1}{\|f_{>0}(x)\|}\,\Big(f(x) - f(0)\Big)\,\theta(x)\,, \tag{B.30}$$

and normalising the new function back to 1 according to

$$\begin{aligned} f_{>0}(\infty) &\stackrel{!}{=} 1 = \frac{1}{\|f_{>0}(x)\|}\Big(f(\infty) - f(0)\Big)\,, \\ \|f_{>0}(x)\| &= f(\infty) - f(0)\,, \end{aligned}$$

so that the desired function is given by

$$f_{>0}(x) = \frac{1}{f(\infty) - f(0)}\Big(f(x) - f(0)\Big)\,\theta(x)\,. \tag{B.31}$$

Therefore, the 95% C.L. upper limit $N_{95\%\text{C.L.}}$ on the number of events for a Gaussian distribution with mean μ and error σ is found by solving

$$f_{>0}(N_{95\%\text{C.L.}}) = 0.95 \tag{B.32}$$

for $N_{95\%\text{C.L.}}$.

Appendix C

Dirac Fermion Dark Matter Annihilation

C.1 Dark matter t-channel annihilation cross section

The dark matter annihilation into two real hidden photons, which in the text we refer to as t-channel annihilation involves the two diagrams shown in Fig. C.1. Summing over both contributions, the matrix element reads

$$\begin{aligned} i\mathcal{M} &= \bar{v}(k)(-ig_h\gamma^\nu)\epsilon^*_\nu(k')\frac{i(\not{p}-\not{p}'+m_\psi)}{(p-p')^2-m_\psi^2}\epsilon^*_\mu(p')(-ig_h\gamma^\mu)u(p) \\ &\quad + \bar{v}(k)(-ig_h\gamma^\mu)\epsilon^*_\mu(p')\frac{i(\not{p}-\not{k}'+m_\psi)}{(p-k')^2-m_\psi^2}\epsilon^*_\nu(k')(-ig_h\gamma^\nu)u(p) \qquad \text{(C.1)} \\ &= -ig_h^2\epsilon^*_\nu(k')\epsilon^*_\mu(p')\bar{v}(k)\left(\frac{\gamma^\nu(\not{p}-\not{p}'+m_\psi)\gamma^\mu}{(p-p')^2-m_\psi^2}+\frac{\gamma^\mu(\not{p}-\not{k}'+m_\psi)\gamma^\nu}{(p-k')^2-m_\psi^2}\right)u(p). \qquad \text{(C.2)} \end{aligned}$$

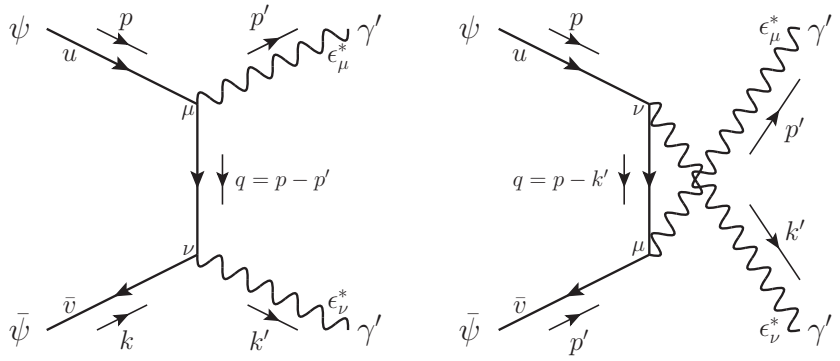

Figure C.1: Feynman diagrams for the dark matter annihilation in the t- and u-channel into two real hidden photons γ'.

Both denominators can be simplified using $p^2 = m_\psi^2$ and $p'^2 = k'^2 = m_{\gamma'}^2$ to $m_{\gamma'}^2 - 2p\cdot p'$ and $m_{\gamma'}^2 - 2p\cdot k'$, respectively. Then, the squared matrix element summed over the photon polarization and averaged over the dark matter spin follows as

$$\begin{aligned}\frac{1}{4}\sum_{\text{spin}}|\mathcal{M}|^2 \;=\; & \frac{1}{4}g_h^4\left(-g_{\nu\nu'}+\frac{k'_\nu k'_{\nu'}}{m_{\gamma'}^2}\right)\left(-g_{\mu\mu'}+\frac{p'_\mu p'_{\mu'}}{m_{\gamma'}^2}\right)\\ & \text{Tr}\left[(\not{k}-m_\psi)\left(\frac{\gamma^\nu(\not{p}-\not{p}'+m_\psi)\gamma^\mu}{m_{\gamma'}^2-2p\cdot p'}+\frac{\gamma^\mu(\not{p}-\not{k}'+m_\psi)\gamma^\nu}{m_{\gamma'}^2-2p\cdot k'}\right)\right.\\ & \left.(\not{p}+m_\psi)\left(\frac{\gamma^{\mu'}(\not{p}-\not{p}'+m_\psi)\gamma^{\nu'}}{m_{\gamma'}^2-2p\cdot p'}+\frac{\gamma^{\nu'}(\not{p}-\not{k}'+m_\psi)\gamma^{\mu'}}{m_{\gamma'}^2-2p\cdot k'}\right)\right]. \qquad \text{(C.3)}\end{aligned}$$

Inserting the kinematic in the centre of mass system and evaluating the trace this becomes

$$\begin{aligned}\frac{1}{4}\sum_{\text{spin}}|\mathcal{M}|^2 \;=\; & \frac{16g_h^4}{((-2m_\psi^2+m_{\gamma'}^2-2|\vec{p}|^2)^2-4c_\theta^2|\vec{p}|^2|\vec{p}'|^2)^2} \qquad \text{(C.4)}\\ & \Big[-4c_\theta^4|\vec{p}|^4|\vec{p}'|^4-c_\theta^2|\vec{p}|^2|\vec{p}'|^2(8m_\psi^4+8m_\psi^2(m_{\gamma'}^2+|\vec{p}|^2)+m_{\gamma'}^4+8m_{\gamma'}^2|\vec{p}|^2)\\ & +(-2m_\psi^2+m_{\gamma'}^2-2|\vec{p}|^2)^2(m_\psi^4-m_\psi^2(m_{\gamma'}^2-4|\vec{p}|^2)+|\vec{p}|^2(m_{\gamma'}^2+|\vec{p}|^2))\Big],\end{aligned}$$

where c_θ stands for $\cos\theta$ with θ being the hidden photon angle in the centre of mass frame between p and p'. In terms of the Mandelstam variables this is

$$\begin{aligned}\frac{1}{4}\sum_{\text{spin}}|\mathcal{M}|^2 \;=\; & \frac{2g_h^4}{(m_\psi^2-t)^2(s+t-m_\psi^2-2m_{\gamma'}^2)^2}\Big[-2m_\psi^8-4m_{\gamma'}^8 \qquad \text{(C.5)}\\ & +8m_\psi^6(t-m_{\gamma'}^2)+4m_{\gamma'}^6(s+3t)-m_{\gamma'}^4(s^2+6st+14t^2)+2m_{\gamma'}^2t(s+2t)^2\\ & -t(s+t)(s^2+2st+2t^2)-m_\psi^4(30m_{\gamma'}^4+3s^2+4st+12t^2-8m_{\gamma'}^2(2s+3t))\\ & +m_\psi^2\big(s^3-28m_{\gamma'}^6+2ts^2+8st^2+8t^3+m_{\gamma'}^4(22s+28t)-2m_{\gamma'}^2(3s^2+4st+12t^2)\big)\Big].\end{aligned}$$

The cross section is then obtained from [4]

$$\frac{d\sigma}{dt} \;=\; \frac{1}{64\pi s(\frac{s}{4}-m_\psi^2)}|\mathcal{M}|^2, \qquad \text{(C.6)}$$

by integration with the limiting values $t_0(\theta=0)$ and $t_1(\theta=\pi)$ as $t_0(t_1) = -(|\vec{p}| \mp |\vec{p}'|)^2$ and multiplying by $1/2$ to account for the double counting because of identical particles in the final state. The annihilation cross section times velocity in the limit of small velocities is then roughly given by

$$\sigma_{\text{ann}}v \;\simeq\; \frac{\pi\alpha_h^2}{m_\psi^2}\sqrt{1-\frac{m_{\gamma'}^2}{m_\psi^2}}\,. \qquad \text{(C.7)}$$

C.2 Dark matter s-channel annihilation cross section

For the s-channel annihilation of the dark matter particle through a virtual hidden photon into Standard Model particles shown in Fig. C.2, the matrix element is given by

$$i\mathcal{M} = \bar{v}(k)(-ig_h\gamma^\mu)u(p)\ \frac{-ig_{\mu\nu}}{(p+k)^2 - m_{\gamma'}^2}\ \bar{u}(p')(-i\chi e\gamma^\nu)v(k') \tag{C.8}$$

$$= \frac{ig_h\chi e}{(p+k)^2 - m_{\gamma'}^2}\ \bar{v}(k)\gamma^\mu u(p)\ \bar{u}(p')\gamma_\mu v(k')\ . \tag{C.9}$$

Summing over the spins in the final state and averaging over those of the dark matter, the squared matrix element is

$$\frac{1}{4}\sum_{\text{spin}}|\mathcal{M}|^2 = \frac{1}{4}\frac{g_h^2\chi^2e^2}{(p+k)^2 - m_{\gamma'}^2} \tag{C.10}$$

$$\text{Tr}\Big[(\not{k} - m_\psi)\gamma^\mu(\not{p} + m_\psi)\gamma^{\mu'}\Big]\text{Tr}\Big[(\not{p}' + m_f)\gamma_\mu(\not{k}' - m_f)\gamma_{\mu'}\Big]$$

$$= \frac{8e^2g_h^2\chi^2}{(p+k)^2 - m_{\gamma'}^2}\left(k\cdot p'\ k'\cdot p + k\cdot k'\ p\cdot p' + m_f^2\ k\cdot p + m_\psi^2\left(k'\cdot p' + 2m_f^2\right)\right)$$

$$= \frac{4e^2g_h^2\chi^2}{m_{\gamma'}^2 - s^2}\left(ts - 2t\left(m_\psi^2 + m_f^2\right) + \left(m_\psi^2 + m_f^2\right)^2 + t^2 + \frac{1}{2}s^2\right)\ , \tag{C.11}$$

where in the last line the Mandelstam variables are used. In the centre of mass frame, the cross section is then obtained by integrating Eq. (C.6) with $t_0(t_1) = -(|\vec{p}| \mp |\vec{p}'|)^2$ and taking the limit for small velocity as

$$\sigma_{\text{ann}}v \simeq \frac{\chi^2e^2g_h^2}{2\pi}\frac{m_\psi^2}{(4m_\psi^2 - m_{\gamma'}^2)^2}\sqrt{1 - \frac{m_f^2}{m_\psi^2}}\left(1 + \frac{m_f^2}{2m_\psi^2}\right)\ . \tag{C.12}$$

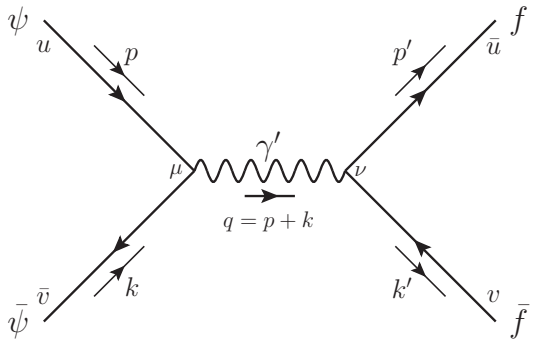

Figure C.2: Feynman diagram for the dark matter annihilation in the s-channel via a virtual hidden photons γ' into fermions.

Bibliography

[1] G. Jungman, M. Kamionkowski and K. Griest, "Supersymmetric dark matter." *Phys.Rept.* **267** (1996) 195–373 [hep-ph/9506380].

[2] L. Bergstrom, "Nonbaryonic dark matter: Observational evidence and detection methods." *Rept.Prog.Phys.* **63** (2000) 793 [hep-ph/0002126].

[3] G. Bertone, D. Hooper and J. Silk, "Particle dark matter: Evidence, candidates and constraints." *Phys.Rept.* **405** (2005) 279–390 [hep-ph/0404175].

[4] **Particle Data Group** Collaboration, J. Beringer *et al.*, "Review of Particle Physics (RPP)." *Phys.Rev.* **D86** (2012) 010001.

[5] M. Taoso, G. Bertone and A. Masiero, "Dark Matter Candidates: A Ten-Point Test." *JCAP* **0803** (2008) 022 [0711.4996].

[6] L. Bergstrom, "Dark Matter Candidates." *New J.Phys.* **11** (2009) 105006 [0903.4849].

[7] J. L. Feng, "Dark Matter Candidates from Particle Physics and Methods of Detection." *Ann.Rev.Astron.Astrophys.* **48** (2010) 495–545 [1003.0904].

[8] M. W. Goodman and E. Witten, "Detectability of Certain Dark Matter Candidates." *Phys.Rev.* **D31** (1985) 3059.

[9] C. Munoz, "Dark matter detection in the light of recent experimental results." *Int.J.Mod.Phys.* **A19** (2004) 3093–3170 [hep-ph/0309346].

[10] D. G. Cerdeno and A. M. Green, "Direct detection of WIMPs." *G. Bertone (ed.): Particle Dark Matter: Observations, Models and Searches, Cambridge University Press* **17** (2010) 347–369 [1002.1912].

[11] L. Baudis, "Direct dark matter detection: the next decade." *Phys.Dark Univ.* **1** (2012) 94–108 [1211.7222].

[12] L. Bergstrom, T. Bringmann and J. Edsjo, "Complementarity of direct dark matter detection and indirect detection through gamma-rays." *Phys. Rev.* **D83** (2011) 045024 [1011.4514].

[13] J. Lavalle and P. Salati, "Dark Matter Indirect Signatures." *Comptes Rendus Physique* **13** (2012) 740–782 [1205.1004].

[14] D. Chung, L. Everett, G. Kane, S. King, J. D. Lykken *et al.*, "The Soft supersymmetry breaking Lagrangian: Theory and applications." *Phys.Rept.* **407** (2005) 1–203 [hep-ph/0312378].

[15] P. Meade, N. Seiberg and D. Shih, "General Gauge Mediation." *Prog.Theor.Phys.Suppl.* **177** (2009) 143–158 [0801.3278].

[16] P. Fayet, "Spontaneously Broken Supersymmetric Theories of Weak, Electromagnetic and Strong Interactions." *Phys.Lett.* **B69** (1977) 489.

[17] P. Fayet, "Relations Between the Masses of the Superpartners of Leptons and Quarks, the Goldstino Couplings and the Neutral Currents." *Phys.Lett.* **B84** (1979) 416.

[18] P. Fayet, "Extra U(1)'s And New Forces." *Nucl.Phys.* **B347** (1990) 743–768.

[19] K. R. Dienes, C. F. Kolda and J. March-Russell, "Kinetic mixing and the supersymmetric gauge hierarchy." *Nucl.Phys.* **B492** (1997) 104–118 [hep-ph/9610479].

[20] M. Goodsell, J. Jaeckel, J. Redondo and A. Ringwald, "Naturally Light Hidden Photons in LARGE Volume String Compactifications." *JHEP* **11** (2009) 027 [0909.0515].

[21] M. Cicoli, M. Goodsell, J. Jaeckel and A. Ringwald, "Testing String Vacua in the Lab: From a Hidden CMB to Dark Forces in Flux Compactifications." *JHEP* **1107** (2011) 114 [1103.3705].

[22] L. Okun, "Limits Of Electrodynamics: Paraphotons?." *Sov.Phys.JETP* **56** (1982) 502.

[23] P. Galison and A. Manohar, "Two Z's or not two Z's?." *Phys.Lett.* **B136** (1984) 279.

[24] B. Holdom, "Two U(1)'s and Epsilon Charge Shifts." *Phys. Lett.* **B166** (1986) 196.

[25] R. Foot and X.-G. He, "Comment on Z Z-prime mixing in extended gauge theories." *Phys.Lett.* **B267** (1991) 509–512.

[26] M. Pospelov, "Secluded U(1) below the weak scale." *Phys. Rev. D* **80** (2009), no. 9 095002 [0811.1030].

[27] A. Sommerfeld, "Über die Beugung und Bremsung der Elektronen." *Annalen der Physik* **403** (1931), no. 3 257–330.

[28] **PAMELA** Collaboration, O. Adriani *et al.*, "An anomalous positron abundance in cosmic rays with energies 1.5-100 GeV." *Nature* **458** (2009) 607–609 [0810.4995].

[29] **The Fermi LAT** Collaboration, A. A. Abdo *et al.*, "Measurement of the Cosmic Ray $e^+ + e^-$ spectrum from 20 GeV to 1 TeV with the Fermi Large Area Telescope." *Phys.Rev.Lett.* **102** (2009) 181101 [0905.0025].

[30] **Fermi LAT** Collaboration, M. Ackermann *et al.*, "Measurement of separate cosmic-ray electron and positron spectra with the Fermi Large Area Telescope." *Phys.Rev.Lett.* **108** (2012) 011103 [1109.0521].

[31] **AMS** Collaboration, M. Aguilar *et al.*, "First Result from the Alpha Magnetic Spectrometer on the International Space Station: Precision Measurement of the Positron Fraction in Primary Cosmic Rays of $0.5 - 350$ GeV." *Phys.Rev.Lett.* **110** (2013), no. 14 141102.

[32] R. Bernabei, P. Belli, F. Montecchia, W. Di Nicolantonio, A. Incicchitti *et al.*, "Searching for WIMPs by the annual modulation signature." *Phys.Lett.* **B424** (1998) 195–201.

[33] **DAMA** Collaboration, R. Bernabei *et al.*, "First results from DAMA/LIBRA and the combined results with DAMA/NaI." *Eur. Phys. J.* **C56** (2008) 333–355 [0804.2741].

[34] **DAMA/LIBRA** Collaboration, R. Bernabei *et al.*, "New results from DAMA/LIBRA." *Eur.Phys.J.* **C67** (2010) 39–49 [1002.1028].

[35] **CoGeNT** Collaboration, C. Aalseth *et al.*, "Results from a Search for Light-Mass Dark Matter with a P-type Point Contact Germanium Detector." *Phys.Rev.Lett.* **106** (2011) 131301 [1002.4703].

[36] **CoGeNT** Collaboration, C. Aalseth, P. Barbeau, J. Colaresi, J. Collar, J. Diaz Leon *et al.*, "Search for an Annual Modulation in a P-type Point Contact Germanium Dark Matter Detector." *Phys.Rev.Lett.* **107** (2011) 141301 [1106.0650].

[37] G. Angloher, M. Bauer, I. Bavykina, A. Bento, C. Bucci *et al.*, "Results from 730 kg days of the CRESST-II Dark Matter Search." *Eur.Phys.J.* **C72** (2012) 1971 [1109.0702].

[38] L. Stodolsky, G. Angloher, M. Bauer, I. Bavykina, A. Bento *et al.*, "The CRESST II Dark Matter Search." *J.Phys.Conf.Ser.* **384** (2012) 012013 [1203.6835].

[39] **CDMS** Collaboration, R. Agnese *et al.*, "Dark Matter Search Results Using the Silicon Detectors of CDMS II." 1304.4279.

[40] J. D. Bjorken, S. Ecklund, W. R. Nelson, A. Abashian, C. Church, B. Lu, L. W. Mo, T. A. Nunamaker and P. Rassmann, "Search for Neutral Metastable Penetrating Particles Produced in the SLAC Beam Dump." *Phys.Rev.* **D38** (1988) 3375.

[41] S. Andreas, O. Lebedev, S. Ramos-Sanchez and A. Ringwald, "Constraints on a very light CP-odd Higgs of the NMSSM and other axion-like particles." *JHEP* **08** (2010) 003 [1005.3978].

[42] S. Andreas, C. Niebuhr and A. Ringwald, "New Limits on Hidden Photons from Past Electron Beam Dumps." *Phys.Rev.* **D86** (2012) 095019 [1209.6083].

[43] S. Andreas, M. D. Goodsell and A. Ringwald, "Dark matter and Dark Forces from a supersymmetric hidden sector." *Phys. Rev. D* **87** (2013) 025007 [1109.2869].

[44] D. Clowe, M. Bradac, A. H. Gonzalez, M. Markevitch, S. W. Randall *et al.*, "A direct empirical proof of the existence of dark matter." *Astrophys.J.* **648** (2006) L109–L113 [astro-ph/0608407].

[45] **Planck** Collaboration, P. Ade *et al.*, "Planck 2013 results. XVI. Cosmological parameters." 1303.5076.

[46] J. Silk, "Cosmic black body radiation and galaxy formation." *Astrophys.J.* **151** (1968) 459–471.

[47] A. A. Klypin, A. V. Kravtsov, O. Valenzuela and F. Prada, "Where are the missing Galactic satellites?." *Astrophys.J.* **522** (1999) 82–92 [astro-ph/9901240].

[48] A. V. Kravtsov, "Dark matter substructure and dwarf galactic satellites." *Adv.Astron.* **2010** (2010) 281913 [0906.3295].

[49] S.-H. Oh, W. de Blok, E. Brinks, F. Walter and J. Kennicutt, Robert C., "Dark and luminous matter in THINGS dwarf galaxies." 1011.0899.

[50] M. Boylan-Kolchin, J. S. Bullock and M. Kaplinghat, "Too big to fail? The puzzling darkness of massive Milky Way subhaloes." *Mon.Not.Roy.Astron.Soc.* **415** (2011) L40 [1103.0007].

[51] L. G. van den Aarssen, T. Bringmann and C. Pfrommer, "Is dark matter with long-range interactions a solution to all small-scale problems of ΛCDM cosmology?." *Phys.Rev.Lett.* **109** (2012) 231301 [1205.5809].

[52] S. Tulin, H.-B. Yu and K. M. Zurek, "Beyond Collisionless Dark Matter: Particle Physics Dynamics for Dark Matter Halo Structure." *Phys. Rev.* **D87** (2013) 115007 [1302.3898].

[53] J. Fan, A. Katz, L. Randall and M. Reece, "Double-Disk Dark Matter." 1303.1521.

[54] K. A. Olive, G. Steigman and T. P. Walker, "Primordial nucleosynthesis: Theory and observations." *Phys.Rept.* **333** (2000) 389–407 [astro-ph/9905320].

[55] G. G. Raffelt, "Particle Physics from Stars." *Ann. Rev. Nucl. Part. Sci.* **49** (1999) 163–216 [hep-ph/9903472].

[56] E. W. Kolb and M. S. Turner, *The Early Universe.* Addison-Wesley, 1988.

[57] G. Belanger, F. Boudjema, A. Pukhov and A. Semenov, "MicrOMEGAs: A Program for calculating the relic density in the MSSM." *Comput.Phys.Commun.* **149** (2002) 103–120 [hep-ph/0112278].

[58] G. Belanger, F. Boudjema, A. Pukhov and A. Semenov, "MicrOMEGAs 2.0: A Program to calculate the relic density of dark matter in a generic model." *Comput.Phys.Commun.* **176** (2007) 367–382 [hep-ph/0607059].

[59] G. Belanger, F. Boudjema, A. Pukhov and A. Semenov, "micrOMEGAs 2.0.7: A program to calculate the relic density of dark matter in a generic model." *Comput.Phys.Commun.* **177** (2007) 894–895.

[60] G. Belanger, F. Boudjema, A. Pukhov and A. Semenov, "Dark matter direct detection rate in a generic model with micrOMEGAs 2.2." *Comput.Phys.Commun.* **180** (2009) 747–767 [0803.2360].

[61] G. Belanger, F. Boudjema, A. Pukhov and A. Semenov, "micrOMEGAs: A Tool for dark matter studies." *Nuovo Cim.* **C033N2** (2010) 111–116 [1005.4133].

[62] J. F. Navarro, C. S. Frenk and S. D. White, "A Universal density profile from hierarchical clustering." *Astrophys.J.* **490** (1997) 493–508 [astro-ph/9611107].

[63] B. Moore, S. Ghigna, F. Governato, G. Lake, T. R. Quinn *et al.*, "Dark matter substructure within galactic halos." *Astrophys.J.* **524** (1999) L19–L22 [astro-ph/9907411].

[64] J. Einasto and U. Haud, "Galactic models with massive corona." *Astronomy and Astrophysics* **223** (1989) 89.

[65] A. M. Green, "Astrophysical uncertainties on direct detection experiments." *Mod.Phys.Lett.* **A27** (2012) 1230004 [1112.0524].

[66] J. Diemand, M. Kuhlen, P. Madau, M. Zemp, B. Moore *et al.*, "Clumps and streams in the local dark matter distribution." *Nature* **454** (2008) 735–738 [0805.1244].

[67] V. Springel, J. Wang, M. Vogelsberger, A. Ludlow, A. Jenkins *et al.*, "The Aquarius Project: the subhalos of galactic halos." *Mon.Not.Roy.Astron.Soc.* **391** (2008) 1685–1711 [0809.0898].

[68] M. Boylan-Kolchin, V. Springel, S. D. White, A. Jenkins and G. Lemson, "Resolving Cosmic Structure Formation with the Millennium-II Simulation." *Mon.Not.Roy.Astron.Soc.* **398** (2009) 1150 [0903.3041].

[69] J. Read, G. Lake, O. Agertz and V. P. Debattista, "Thin, thick and dark discs in ΛCDM." *Monthly Notices of the Royal Astronomical Society* **389** (2008), no. 3 1041–1057 [0803.2714].

[70] T. Bruch, J. Read, L. Baudis and G. Lake, "Detecting the Milky Way's Dark Disk." *Astrophys.J.* **696** (2009) 920–923 [0804.2896].

[71] J. Read, L. Mayer, A. Brooks, F. Governato and G. Lake, "A dark matter disc in three cosmological simulations of Milky Way mass galaxies." *Monthly Notices of the Royal Astronomical Society* **397** (2009), no. 1 44–51 [0902.0009].

[72] F. Prada, A. Klypin, J. Flix Molina, M. Martinez and E. Simonneau, "Dark Matter Annihilation in the Milky Way Galaxy: Effects of Baryonic Compression." *Phys.Rev.Lett.* **93** (2004) 241301 [astro-ph/0401512].

[73] R. Catena and P. Ullio, "A novel determination of the local dark matter density." *JCAP* **1008** (2010) 004 [0907.0018].

[74] P. Salucci, F. Nesti, G. Gentile and C. Martins, "The dark matter density at the Sun's location." *Astron.Astrophys.* **523** (2010) A83 [1003.3101].

[75] Y. Sofue, "A Grand Rotation Curve and Dark Matter Halo in the Milky Way Galaxy." 1110.4431.

[76] F. Iocco, M. Pato, G. Bertone and P. Jetzer, "Dark Matter distribution in the Milky Way: microlensing and dynamical constraints." *JCAP* **1111** (2011) 029 [1107.5810].

[77] C. McCabe, "The Astrophysical Uncertainties Of Dark Matter Direct Detection Experiments." *Phys.Rev.* **D82** (2010) 023530 [1005.0579].

[78] P. J. Fox, J. Kopp, M. Lisanti and N. Weiner, "A CoGeNT Modulation Analysis." *Phys.Rev.* **D85** (2012) 036008 [1107.0717].

[79] M. T. Frandsen, F. Kahlhoefer, C. McCabe, S. Sarkar and K. Schmidt-Hoberg, "Resolving astrophysical uncertainties in dark matter direct detection." *JCAP* **1201** (2012) 024 [1111.0292].

[80] P. Gondolo and G. B. Gelmini, "Halo independent comparison of direct dark matter detection data." *JCAP* **1212** (2012) 015 [1202.6359].

[81] C. Arina, J. Hamann and Y. Y. Y. Wong, "A Bayesian view of the current status of dark matter direct searches." *JCAP* **1109** (2011) 022 [1105.5121].

[82] A. Goudelis, *Detection of WIMP-like dark matter in some extensions of the Standard Model*. PhD thesis, Université Paris - Sud, 2011. 1106.3778.

[83] A. Drukier, K. Freese and D. Spergel, "Detecting Cold Dark Matter Candidates." *Phys.Rev.* **D33** (1986) 3495–3508.

[84] K. Freese, J. A. Frieman and A. Gould, "Signal Modulation in Cold Dark Matter Detection." *Phys.Rev.* **D37** (1988) 3388.

[85] C. J. Copi, J. Heo and L. M. Krauss, "Directional sensitivity, WIMP detection, and the galactic halo." *Phys.Lett.* **B461** (1999) 43–48 [hep-ph/9904499].

[86] **XENON100** Collaboration, E. Aprile *et al.*, "Dark Matter Results from 100 Live Days of XENON100 Data." *Phys.Rev.Lett.* **107** (2011) 131302 [1104.2549].

[87] **XENON100** Collaboration, E. Aprile *et al.*, "Dark Matter Results from 225 Live Days of XENON100 Data." *Phys.Rev.Lett.* **109** (2012) 181301 [1207.5988].

[88] **CDMS-II** Collaboration, Z. Ahmed *et al.*, "Dark Matter Search Results from the CDMS II Experiment." *Science* **327** (2010) 1619–1621 [0912.3592].

[89] **CDMS-II** Collaboration, Z. Ahmed *et al.*, "Results from a Low-Energy Analysis of the CDMS II Germanium Data." *Phys.Rev.Lett.* **106** (2011) 131302 [1011.2482].

[90] J. I. Collar, "A Realistic Assessment of the Sensitivity of XENON10 and XENON100 to Light-Mass WIMPs." 1106.0653.

[91] J. I. Collar, "A comparison between the low-energy spectra from CoGeNT and CDMS." 1103.3481.

[92] G. Bertone, "Dark Matter: The Connection with Gamma-Ray Astrophysics." *Astrophys.Space Sci.* **309** (2007) 505–515 [astro-ph/0608706].

[93] I. Cholis, L. Goodenough, D. Hooper, M. Simet and N. Weiner, "High Energy Positrons From Annihilating Dark Matter." *Phys.Rev.* **D80** (2009) 123511 [0809.1683].

[94] M. Cirelli, M. Kadastik, M. Raidal and A. Strumia, "Model-independent implications of the $e^{\pm}$, anti-proton cosmic ray spectra on properties of Dark Matter." *Nucl.Phys.* **B813** (2009) 1–21 [0809.2409].

[95] O. Adriani, G. Barbarino, G. Bazilevskaya, R. Bellotti, M. Boezio *et al.*, "A new measurement of the antiproton-to-proton flux ratio up to 100 GeV in the cosmic radiation." *Phys.Rev.Lett.* **102** (2009) 051101 [0810.4994].

[96] P. Meade, M. Papucci, A. Strumia and T. Volansky, "Dark Matter Interpretations of the Electron/Positron Excesses after FERMI." *Nucl. Phys.* **B831** (2010) 178–203 [0905.0480].

[97] P. Jean, J. Knoedlseder, V. Lonjou, M. Allain, J.-P. Roques *et al.*, "Early SPI / INTEGRAL measurements of 511 keV line emission from the 4th quadrant of the Galaxy." *Astron.Astrophys.* **407** (2003) L55 [astro-ph/0309484].

[98] J. Knodlseder, V. Lonjou, P. Jean, M. Allain, P. Mandrou *et al.*, "Early SPI / INTEGRAL contraints on the morphology of the 511 keV line emission in the 4th galactic quadrant." *Astron.Astrophys.* **411** (2003) L457–L460 [astro-ph/0309442].

[99] C. Boehm, D. Hooper, J. Silk, M. Casse and J. Paul, "MeV dark matter: Has it been detected?." *Phys.Rev.Lett.* **92** (2004) 101301 [astro-ph/0309686].

[100] P. Fayet, "U-boson production in e^+e^- annihilations, ψ and Υ decays, and Light Dark Matter." *Phys.Rev.* **D75** (2007) 115017 [hep-ph/0702176].

[101] J.-H. Huh, J. E. Kim, J.-C. Park and S. C. Park, "Galactic 511 keV line from MeV milli-charged dark matter." *Phys.Rev.* **D77** (2008) 123503 [0711.3528].

[102] M. Pospelov, A. Ritz and M. B. Voloshin, "Secluded WIMP Dark Matter." *Phys. Lett.* **B662** (2008) 53–61 [0711.4866].

[103] **Planck** Collaboration. http://www.nasa.gov/mission_pages/planck/news/planck20120213.html.

[104] D. P. Finkbeiner, "WMAP microwave emission interpreted as dark matter annihilation in the inner galaxy." astro-ph/0409027.

[105] D. Hooper, D. P. Finkbeiner and G. Dobler, "Possible evidence for dark matter annihilations from the excess microwave emission around the center of the Galaxy seen by the Wilkinson Microwave Anisotropy Probe." *Phys.Rev.* **D76** (2007) 083012 [0705.3655].

[106] D. Hooper and T. Linden, "Gamma Rays From The Galactic Center and the WMAP Haze." *Phys.Rev.* **D83** (2011) 083517 [1011.4520].

[107] L. Goodenough and D. Hooper, "Possible Evidence For Dark Matter Annihilation In The Inner Milky Way From The Fermi Gamma Ray Space Telescope." 0910.2998.

[108] D. Hooper and L. Goodenough, "Dark Matter Annihilation in The Galactic Center As Seen by the Fermi Gamma Ray Space Telescope." *Phys.Lett.* **B697** (2011) 412–428 [1010.2752].

[109] D. Hooper and T. Linden, "On The Origin Of The Gamma Rays From The Galactic Center." *Phys.Rev.* **D84** (2011) 123005 [1110.0006].

[110] T. Linden, D. Hooper and F. Yusef-Zadeh, "Dark Matter and Synchrotron Emission from Galactic Center Radio Filaments." *Astrophys.J.* **741** (2011) 95 [1106.5493].

[111] D. Hooper, N. Weiner and W. Xue, "Dark Forces and Light Dark Matter." *Phys.Rev.* **D86** (2012) 056009 [1206.2929].

[112] T. Bringmann, X. Huang, A. Ibarra, S. Vogl and C. Weniger, "Fermi LAT Search for Internal Bremsstrahlung Signatures from Dark Matter Annihilation." *JCAP* **1207** (2012) 054 [1203.1312].

[113] C. Weniger, "A Tentative Gamma-Ray Line from Dark Matter Annihilation at the Fermi Large Area Telescope." *JCAP* **1208** (2012) 007 [1204.2797].

[114] **ATLAS** Collaboration, G. Aad *et al.*, "Search for dark matter candidates and large extra dimensions in events with a jet and missing transverse momentum with the ATLAS detector." *JHEP* **1304** (2013) 075 [1210.4491].

[115] **CMS** Collaboration, S. Chatrchyan *et al.*, "Search for dark matter and large extra dimensions in monojet events in pp collisions at $\sqrt{s} = 7$ TeV." *JHEP* **1209** (2012) 094 [1206.5663].

[116] **ATLAS** Collaboration, G. Aad *et al.*, "Search for dark matter candidates and large extra dimensions in events with a photon and missing transverse momentum in pp collision data at $\sqrt{s} = 7$ TeV with the ATLAS detector." *Phys.Rev.Lett.* **110** (2013) 011802 [1209.4625].

[117] **CMS** Collaboration, S. Chatrchyan *et al.*, "Search for Dark Matter and Large Extra Dimensions in pp Collisions Yielding a Photon and Missing Transverse Energy." *Phys.Rev.Lett.* **108** (2012) 261803 [1204.0821].

[118] E. A. Baltz, M. Battaglia, M. E. Peskin and T. Wizansky, "Determination of dark matter properties at high-energy colliders." *Phys.Rev.* **D74** (2006) 103521 [hep-ph/0602187].

[119] N. Bernal, A. Goudelis, Y. Mambrini and C. Munoz, "Determining the WIMP mass using the complementarity between direct and indirect searches and the ILC." *JCAP* **0901** (2009) 046 [0804.1976].

[120] C. Arina, G. Bertone and H. Silverwood, "Complementarity of direct and indirect Dark Matter detection experiments." 1304.5119.

[121] D. Hooper, "The Empirical Case For 10 GeV Dark Matter." *Phys.Dark Univ.* **1** (2012) 1–23 [1201.1303].

[122] J. Jaeckel and A. Ringwald, "The Low-Energy Frontier of Particle Physics." *Ann. Rev. Nucl. Part. Sci.* **60** (2010) 405–437 [1002.0329].

[123] J. Jaeckel, "A force beyond the Standard Model - Status of the quest for hidden photons." *Frascati Phys.Ser.* **56** (2013) 172–192 [1303.1821].

[124] P. Langacker, "The Physics of Heavy Z' Gauge Bosons." *Rev.Mod.Phys.* **81** (2009) 1199–1228 [0801.1345].

[125] P. Langacker, "Grand Unified Theories and Proton Decay." *Phys.Rept.* **72** (1981) 185.

[126] A. Lukas and K. S. Stelle, "Heterotic anomaly cancellation in five dimensions." *JHEP* **01** (2000) 010 [hep-th/9911156].

[127] R. Blumenhagen, G. Honecker and T. Weigand, "Loop-corrected compactifications of the heterotic string with line bundles." *JHEP* **06** (2005) 020 [hep-th/0504232].

[128] M. Goodsell and A. Ringwald, "Light hidden-sector U(1)s in string compactifications." *Fortsch.Phys.* **58** (2010) 716–720 [1002.1840].

[129] M. Goodsell, S. Ramos-Sanchez and A. Ringwald, "Kinetic Mixing of U(1)s in Heterotic Orbifolds." *JHEP* **1201** (2012) 021 [1110.6901].

[130] S. A. Abel and B. W. Schofield, "Brane-antibrane kinetic mixing, millicharged particles and SUSY breaking." *Nucl. Phys.* **B685** (2004) 150–170 [hep-th/0311051].

[131] D. Lust and S. Stieberger, "Gauge threshold corrections in intersecting brane world models." *Fortsch. Phys.* **55** (2007) 427–465 [hep-th/0302221].

[132] S. A. Abel, J. Jaeckel, V. V. Khoze and A. Ringwald, "Illuminating the hidden sector of string theory by shining light through a magnetic field." *Phys. Lett.* **B666** (2008) 66–70 [hep-ph/0608248].

[133] S. A. Abel, M. D. Goodsell, J. Jaeckel, V. V. Khoze and A. Ringwald, "Kinetic Mixing of the Photon with Hidden U(1)s in String Phenomenology." *JHEP* **07** (2008) 124 [0803.1449].

[134] K. Benakli and M. D. Goodsell, "Dirac Gauginos and Kinetic Mixing." *Nucl. Phys.* **B830** (2010) 315–329 [0909.0017].

[135] F. Gmeiner and G. Honecker, "Complete Gauge Threshold Corrections for Intersecting Fractional D6-Branes: The Z6 and Z6' Standard Models." *Nucl.Phys.* **B829** (2010) 225–297 [0910.0843].

[136] M. Goodsell, "Light Hidden U(1)s from String Theory." 0912.4206.

[137] M. Williams, C. Burgess, A. Maharana and F. Quevedo, "New Constraints (and Motivations) for Abelian Gauge Bosons in the MeV-TeV Mass Range." *JHEP* **1108** (2011) 106 [1103.4556].

[138] C. Boehm and P. Fayet, "Scalar dark matter candidates." *Nucl. Phys.* **B683** (2004) 219–263 [hep-ph/0305261].

[139] P. Fayet, "Light spin 1/2 or spin 0 dark matter particles." *Phys.Rev.* **D70** (2004) 023514 [hep-ph/0403226].

[140] D. Feldman, B. Kors and P. Nath, "Extra-weakly Interacting Dark Matter." *Phys.Rev.* **D75** (2007) 023503 [hep-ph/0610133].

[141] N. Arkani-Hamed, D. P. Finkbeiner, T. R. Slatyer and N. Weiner, "A Theory of Dark Matter." *Phys. Rev.* **D79** (2009) 015014 [0810.0713].

[142] M. Pospelov and A. Ritz, "Astrophysical Signatures of Secluded Dark Matter." *Phys. Lett.* **B671** (2009) 391–397 [0810.1502].

[143] E. J. Chun and J.-C. Park, "Dark matter and sub-GeV hidden U(1) in GMSB models." *JCAP* **0902** (2009) 026 [0812.0308].

[144] C. Cheung, J. T. Ruderman, L.-T. Wang and I. Yavin, "Kinetic Mixing as the Origin of Light Dark Scales." *Phys. Rev.* **D80** (2009) 035008 [0902.3246].

[145] A. Katz and R. Sundrum, "Breaking the Dark Force." *JHEP* **0906** (2009) 003 [0902.3271].

[146] D. E. Morrissey, D. Poland and K. M. Zurek, "Abelian Hidden Sectors at a GeV." *JHEP* **07** (2009) 050 [0904.2567].

[147] H. An, S.-L. Chen, R. N. Mohapatra, S. Nussinov and Y. Zhang, "Energy Dependence of Direct Detection Cross Section for Asymmetric Mirror Dark Matter." *Phys. Rev. D* **82** (2010), no. 2 023533 [1004.3296].

[148] R. Essig, J. Kaplan, P. Schuster and N. Toro, "On the Origin of Light Dark Matter Species." 1004.0691.

[149] T. Cohen, D. J. Phalen, A. Pierce and K. M. Zurek, "Asymmetric Dark Matter from a GeV Hidden Sector." *Phys.Rev.* **D82** (2010) 056001 [1005.1655].

[150] Y. Mambrini, "The kinetic dark-mixing in the light of CoGENT and XENON100." *JCAP* **1009** (2010) 022 [1006.3318].

[151] Z. Kang, T. Li, T. Liu, C. Tong and J. M. Yang, "Light Dark Matter from the $U(1)_X$ Sector in the NMSSM with Gauge Mediation." *JCAP* **1101** (2011) 028 [1008.5243].

[152] E. J. Chun, J.-C. Park and S. Scopel, "Dark matter and a new gauge boson through kinetic mixing." *JHEP* **02** (2011) 100 [1011.3300].

[153] Y. Mambrini, "Specific Dark Matter signatures from hidden U(1)." *PoS* **QFTHEP2010** (2010) 027 [1012.0447].

[154] Y. Mambrini, "The ZZ' kinetic mixing in the light of the recent direct and indirect dark matter searches." *JCAP* **1107** (2011) 009 [1104.4799].

[155] N. Fornengo, P. Panci and M. Regis, "Long-Range Forces in Direct Dark Matter Searches." *Phys.Rev.* **D84** (2011) 115002 [1108.4661].

[156] M. Pospelov, A. Ritz and M. B. Voloshin, "Bosonic super-WIMPs as keV-scale dark matter." *Phys.Rev.* **D78** (2008) 115012 [0807.3279].

[157] J. Redondo and M. Postma, "Massive hidden photons as lukewarm dark matter." *JCAP* **0902** (2009) 005 [0811.0326].

[158] P. Arias, D. Cadamuro, M. Goodsell, J. Jaeckel, J. Redondo *et al.*, "WISPy Cold Dark Matter." *JCAP* **1206** (2012) 013 [1201.5902].

[159] J. Jaeckel, J. Redondo and A. Ringwald, "Signatures of a hidden cosmic microwave background." *Phys. Rev. Lett.* **101** (2008) 131801 [0804.4157].

[160] **WMAP** Collaboration, E. Komatsu *et al.*, "Seven-Year Wilkinson Microwave Anisotropy Probe (WMAP) Observations: Cosmological Interpretation." *Astrophys. J. Suppl.* **192** (2011) 18 [1001.4538].

[161] J. Dunkley, R. Hlozek, J. Sievers, V. Acquaviva, P. Ade *et al.*, "The Atacama Cosmology Telescope: Cosmological Parameters from the 2008 Power Spectra." *Astrophys.J.* **739** (2011) 52 [1009.0866].

[162] C. P. Burgess, J. P. Conlon, L.-Y. Hung, C. H. Kom, A. Maharana and F. Quevedo, "Continuous Global Symmetries and Hyperweak Interactions in String Compactifications." *JHEP* **0807** (2008) 073 [0805.4037].

[163] D. Feldman, Z. Liu and P. Nath, "The Stueckelberg Z' extension with kinetic mixing and milli-charged dark matter from the hidden sector." *Phys. Rev.* **D75** (2007) 115001 [hep-ph/0702123].

[164] **Muon g-2** Collaboration, G. Bennett *et al.*, "Final Report of the Muon E821 Anomalous Magnetic Moment Measurement at BNL." *Phys.Rev.* **D73** (2006) 072003 [hep-ex/0602035].

[165] B. L. Roberts, "Status of the Fermilab Muon $(g-2)$ Experiment." *Chin.Phys.* **C34** (2010) 741–744 [1001.2898].

[166] M. Davier, A. Hoecker, B. Malaescu and Z. Zhang, "Reevaluation of the Hadronic Contributions to the Muon g-2 and to alpha(MZ)." *Eur.Phys.J.* **C71** (2011) 1515 [1010.4180].

[167] K. Hagiwara, R. Liao, A. D. Martin, D. Nomura and T. Teubner, "$(g-2)_\mu$ and $\alpha(M_Z^2)$ re-evaluated using new precise data." *J.Phys.* **G38** (2011) 085003 [1105.3149].

[168] M. Endo, K. Hamaguchi, S. Iwamoto and T. Yoshinaga, "Muon g-2 vs LHC in Supersymmetric Models." 1303.4256.

[169] R. Foot, "Mirror dark matter and the new DAMA/LIBRA results: A Simple explanation for a beautiful experiment." *Phys.Rev.* **D78** (2008) 043529 [0804.4518].

[170] L. Ackerman, M. R. Buckley, S. M. Carroll and M. Kamionkowski, "Dark Matter and Dark Radiation." *Phys. Rev.* **D79** (2009) 023519 [0810.5126].

[171] J. L. Feng, M. Kaplinghat, H. Tu and H.-B. Yu, "Hidden Charged Dark Matter." *JCAP* **0907** (2009) 004 [0905.3039].

[172] X. Chu, T. Hambye and M. H. Tytgat, "The Four Basic Ways of Creating Dark Matter Through a Portal." *JCAP* **1205** (2012) 034 [1112.0493].

[173] J. Lavalle, Q. Yuan, D. Maurin and X. Bi, "Full Calculation of Clumpiness Boost factors for Antimatter Cosmic Rays in the light of ΛCDM N-body simulation results. Abandoning hope in clumpiness enhancement?." *Astron.Astrophys.* **479** (2008) 427–452 [0709.3634].

[174] M. Cirelli and A. Strumia, "Minimal Dark Matter predictions and the PAMELA positron excess." *PoS* **IDM2008** (2008) 089 [0808.3867].

[175] I. Cholis, D. P. Finkbeiner, L. Goodenough and N. Weiner, "The PAMELA Positron Excess from Annihilations into a Light Boson." *JCAP* **0912** (2009) 007 [0810.5344].

[176] Y. Nomura and J. Thaler, "Dark Matter through the Axion Portal." *Phys. Rev.* **D79** (2009) 075008 [0810.5397].

[177] M. Cirelli, A. Strumia and M. Tamburini, "Cosmology and Astrophysics of Minimal Dark Matter." *Nucl.Phys.* **B787** (2007) 152–175 [0706.4071].

[178] Y. Cui, D. E. Morrissey, D. Poland and L. Randall, "Candidates for Inelastic Dark Matter." *JHEP* **0905** (2009) 076 [0901.0557].

[179] R. Essig, R. Harnik, J. Kaplan and N. Toro, "Discovering New Light States at Neutrino Experiments." *Phys.Rev.* **D82** (2010) 113008 [1008.0636].

[180] M. T. Frandsen, F. Kahlhoefer, S. Sarkar and K. Schmidt-Hoberg, "Direct detection of dark matter in models with a light Z'." *JHEP* **1109** (2011) 128 [1107.2118].

[181] J. M. Cline and A. R. Frey, "Minimal hidden sector models for CoGeNT/DAMA events." *Phys.Rev.* **D84** (2011) 075003 [1108.1391].

[182] A. Semenov, "LanHEP: A Package for automatic generation of Feynman rules in gauge models." hep-ph/9608488.

[183] A. Semenov, "LanHEP: A package for automatic generation of Feynman rules from the Lagrangian." *Comput.Phys.Commun.* **115** (1998) 124–139.

[184] A. Semenov, "LanHEP: A Package for automatic generation of Feynman rules in field theory. Version 2.0." hep-ph/0208011.

[185] A. Semenov, "LanHEP: A Package for the automatic generation of Feynman rules in field theory. Version 3.0." *Comput.Phys.Commun.* **180** (2009) 431–454 [0805.0555].

[186] A. Semenov, "LanHEP - a package for automatic generation of Feynman rules from the Lagrangian. Updated version 3.1." 1005.1909.

[187] D. Hooper and T. M. P. Tait, "Neutralinos in an extension of the minimal supersymmetric standard model as the source of the PAMELA positron excess." *Phys. Rev.* **D80** (2009) 055028 [0906.0362].

[188] J. J. Heckman and C. Vafa, "An Exceptional Sector for F-theory GUTs." *Phys.Rev.* **D83** (2011) 026006 [1006.5459].

[189] M. Bullimore, J. P. Conlon and L. T. Witkowski, "Kinetic mixing of U(1)s for local string models." *JHEP* **11** (2010) 142 [1009.2380].

[190] J. J. Heckman and S.-J. Rey, "Baryon and Dark Matter Genesis from Strongly Coupled Strings." *JHEP* **1106** (2011) 120 [1102.5346].

[191] B. Allanach, "SOFTSUSY: a program for calculating supersymmetric spectra." *Comput.Phys.Commun.* **143** (2002) 305–331 [hep-ph/0104145].

[192] J. E. Kim and H. P. Nilles, "The μ Problem and the Strong CP Problem." *Phys. Lett.* **B138** (1984) 150.

[193] S. P. Martin, "A Supersymmetry primer." hep-ph/9709356.

[194] U. Ellwanger, C. Hugonie and A. M. Teixeira, "The Next-to-Minimal Supersymmetric Standard Model." *Phys. Rept.* **496** (2010) 1–77 [0910.1785].

[195] R. Dermisek and J. F. Gunion, "Escaping the large fine tuning and little hierarchy problems in the next to minimal supersymmetric model and h $\to$ a a decays." *Phys. Rev. Lett.* **95** (2005) 041801 [hep-ph/0502105].

[196] R. Dermisek and J. F. Gunion, "The NMSSM close to the R-symmetry limit and naturalness in h $\to$ aa decays for $m_a < 2m_b$." *Phys. Rev. D* **75** (2007) 075019 [hep-ph/0611142].

[197] **ATLAS** Collaboration, G. Aad *et al.*, "Observation of a new particle in the search for the Standard Model Higgs boson with the ATLAS detector at the LHC." *Phys.Lett.* **B716** (2012) 1–29 [1207.7214].

[198] **CMS** Collaboration, S. Chatrchyan *et al.*, "Observation of a new boson at a mass of 125 GeV with the CMS experiment at the LHC." *Phys.Lett.* **B716** (2012) 30–61 [1207.7235].

[199] **ALEPH** Collaboration, S. Schael *et al.*, "Search for neutral Higgs bosons decaying into four taus at LEP2." *JHEP* **05** (2010) 049 [1003.0705].

[200] **BABAR** Collaboration, B. Aubert *et al.*, "Search for a low-mass Higgs boson in Y(3S) $\to \gamma A^0$, $A^0 \to \tau^+\tau^-$ at BABAR." *Phys. Rev. Lett.* **103** (2009) 181801 [0906.2219].

[201] **BABAR** Collaboration, B. Aubert *et al.*, "Search for Dimuon Decays of a Light Scalar Boson in Radiative Transitions $\Upsilon \to \gamma A^0$." *Phys. Rev. Lett.* **103** (2009) 081803 [0905.4539].

[202] R. Dermisek and J. F. Gunion, "New constraints on a light CP-odd Higgs boson and related NMSSM Ideal Higgs Scenarios." *Phys. Rev.* **D81** (2010) 075003 [1002.1971].

[203] A. Rashed, M. Duraisamy and A. Datta, "Probing light pseudoscalar, axial vector states through $\eta_b \to \tau^+\tau^-$." *Phys. Rev.* **D82** (2010) 054031 [1004.5419].

[204] O. Lebedev and S. Ramos-Sanchez, "The NMSSM and String Theory." *Phys. Lett.* **B684** (2010) 48–51 [0912.0477].

[205] Y. Bai, M. Carena and J. Lykken, "The PAMELA excess from neutralino annihilation in the NMSSM." *Phys. Rev.* **D80** (2009) 055004 [0905.2964].

[206] B. A. Dobrescu and K. T. Matchev, "Light axion within the next-to-minimal supersymmetric standard model." *JHEP* **09** (2000) 031 [hep-ph/0008192].

[207] D. J. Miller, 2, R. Nevzorov and P. M. Zerwas, "The Higgs sector of the next-to-minimal supersymmetric standard model." *Nucl. Phys.* **B681** (2004) 3–30 [hep-ph/0304049].

[208] L. J. Hall and T. Watari, "Electroweak supersymmetry with an approximate U(1) Peccei-Quinn symmetry." *Phys. Rev. D* **70** (2004), no. 11 115001 [hep-ph/0405109].

[209] P. C. Schuster and N. Toro, "Persistent fine-tuning in supersymmetry and the NMSSM." hep-ph/0512189.

[210] R. Barbieri, L. J. Hall, A. Y. Papaioannou, D. Pappadopulo and V. S. Rychkov, "An alternative NMSSM phenomenology with manifest perturbative unification." *JHEP* **03** (2008) 005 [0712.2903].

[211] M. Dine, W. Fischler and M. Srednicki, "A Simple Solution to the Strong CP Problem with a Harmless Axion." *Phys. Lett.* **B104** (1981) 199.

[212] A. Zhitnitsky, "On Possible Suppression of the Axion Hadron Interactions. (In Russian)." *Sov.J.Nucl.Phys.* **31** (1980) 260.

[213] G. Hiller, "b-physics signals of the lightest CP-odd Higgs in the NMSSM at large $\tan\beta$." *Phys. Rev.* **D70** (2004) 034018 [hep-ph/0404220].

[214] D. L. Anderson, C. D. Carone and M. Sher, "Probing the light pseudoscalar window." *Phys. Rev. D* **67** (2003) 115013 [hep-ph/0303215].

[215] F. Larios, G. Tavares-Velasco and C. P. Yuan, "A very light CP-odd scalar in the two-Higgs-doublet model." *Phys. Rev. D* **64** (2001), no. 5 055004 [hep-ph/0103292].

[216] B. A. Dobrescu, "Minimal composite Higgs model with light bosons." *Phys. Rev. D* **63** (2000) 015004 [hep-ph/9908391].

[217] J. F. Gunion, G. Gamberini and S. F. Novaes, "Can the Higgs bosons of the minimal supersymmetric model be detected at a hadron collider via two-photon decays?." *Phys. Rev.* **D38** (1988) 3481.

[218] A. Ali, P. Ball, L. T. Handoko and G. Hiller, "A Comparative study of the decays $B \to (K, K^*) l^+ l^-$ in standard model and supersymmetric theories." *Phys. Rev. D* **61** (2000) 074024 [hep-ph/9910221].

[219] W. J. Marciano and Z. Parsa, "Rare kaon decays with "missing energy"." *Phys. Rev. D* **53** (1996), no. 1 R1–R5.

[220] L. J. Hall and M. B. Wise, "Flavor changing Higgs boson couplings." *Nucl. Phys.* **B187** (1981) 397.

[221] J. M. Frere, J. A. M. Vermaseren and M. B. Gavela, "The elusive axion." *Phys. Lett.* **B103** (1981) 129–133.

[222] M. Freytsis, Z. Ligeti and J. Thaler, "Constraining the Axion Portal with $B \to K l^+ l^-$." *Phys. Rev. D* **81** (2010), no. 3 034001 [0911.5355].

[223] B. Batell, M. Pospelov and A. Ritz, "Multi-lepton Signatures of a Hidden Sector in Rare B Decays." *Phys.Rev.* **D83** (2011) 054005 [0911.4938].

[224] **CLEO** Collaboration, R. Ammar *et al.*, "Search for the familon via $B^\pm \to \pi^\pm X^0$, $B^\pm \to K^\pm X^0$, and $B^0 \to K^0_S X^0$ decays." *Phys. Rev. Lett.* **87** (2001) 271801 [hep-ex/0106038].

[225] **BABAR** Collaboration, B. Aubert *et al.*, "A Search for the decay $B^- \to K^- \nu\bar{\nu}$." hep-ex/0304020.

[226] **E787** Collaboration, S. S. Adler *et al.*, "Further search for the decay $K^+ \to \pi^+ \nu\bar{\nu}$ in the momentum region P $<$ 195 MeV/c." *Phys. Rev. D* **70** (2004) 037102 [hep-ex/0403034].

[227] **E787** Collaboration, S. S. Adler *et al.*, "Search for the decay $K^+ \to \pi^+ \nu\bar{\nu}$ in the momentum region $P_\pi < 195$ MeV/c." *Phys. Lett.* **B537** (2002), no. 3-4 211–216 [hep-ex/0201037].

[228] **BNL-E949** Collaboration, A. V. Artamonov *et al.*, "Study of the decay $K^+ \to \pi^+ \nu\bar{\nu}$ in the momentum region $140 < 199$ MeV/c." *Phys. Rev. D* **79** (May, 2009) 092004 [0903.0030].

[229] **Belle** Collaboration, A. Ishikawa *et al.*, "Observation of the electroweak penguin decay $B \to K^* l^+ l^-$." *Phys. Rev. Lett.* **91** (2003) 261601 [hep-ex/0308044].

[230] E. Goudzovski, "Measurement of the FCNC decays $K^\pm \to \pi^\pm l^+ l^-$ by the NA48/2 experiment at CERN." *PoS* **KAON09** (2009) 009 [0908.3860].

[231] **BaBar** Collaboration, B. Aubert *et al.*, "Measurements of the rare decays $B \to K l^+ l^-$ and $B \to K^* l^+ l^-$." hep-ex/0507005.

[232] T. Yamazaki *et al.*, "Search for a Neutral Boson in a Two-Body Decay of $K^+ \to \pi^+ X^0$." *Phys. Rev. Lett.* **52** (1984) 1089–1091.

[233] **SINDRUM** Collaboration, R. Eichler *et al.*, "Limits for short-lived neutral particles emitted in μ^+ or π^+ decay." *Phys. Lett.* **B175** (1986) 101.

[234] W. A. Bardeen, R. D. Peccei and T. Yanagida, "Constraints on variant axion models." *Nucl. Phys.* **B279** (1987) 401.

[235] **CLEO** Collaboration, R. Balest *et al.*, "$\Upsilon(1S) \to \gamma$ + noninteracting particles." *Phys. Rev. D* **51** (1995) 2053–2060.

[236] **BABAR** Collaboration, S. J. Sekula, "Recent Searches for Exotic Physics at the BaBar/PEP-II B- factory." 0810.0315.

[237] **BaBar** Collaboration, B. Aubert *et al.*, "Search for Invisible Decays of a Light Scalar in Radiative Transitions $\Upsilon(3S) \to \gamma A^0$." 0808.0017.

[238] F. Wilczek, "Problem of Strong p and t Invariance in the Presence of Instantons." *Phys. Rev. Lett.* **40** (1978) 279–282.

[239] H. E. Haber, A. S. Schwarz and A. E. Snyder, "Hunting The Higgs In B Decays." *Nucl. Phys.* **B294** (1987) 301.

[240] Q. Chang and Y.-D. Yang, "Rare decay $\pi^0 \to e^+ e^-$ as a sensitive probe of light CP-odd Higgs in NMSSM." *Phys. Lett.* **B676** (2009) 88 [0808.2933].

[241] **KTeV** Collaboration, E. Abouzaid *et al.*, "Measurement of the rare decay $\pi^0 \to e^+ e^-$." *Phys. Rev. D* **75** (2007), no. 1 012004 [hep-ex/0610072].

[242] A. E. Dorokhov and M. A. Ivanov, "Rare decay $\pi^0 \to e^+ e^-$: theory confronts KTeV data." *Phys. Rev. D* **75** (2007), no. 11 114007 [0704.3498].

[243] A. E. Dorokhov, M. A. Ivanov and S. G. Kovalenko, "Complete structure dependent analysis of the decay $P \to l^+ l^-$." *Phys. Lett.* **B677** (2009) 145–149 [0903.4249].

[244] M. E. Peskin and D. V. Schroeder, *Introduction to Quantum Field Theory.* Westview Press, 1995.

[245] T. Teubner, K. Hagiwara, R. Liao, A. D. Martin and D. Nomura, "Update of $g-2$ of the muon and $\Delta\alpha$." *Chin.Phys.* **C34** (2010) 728–734 [1001.5401].

[246] F. Domingo and U. Ellwanger, "Constraints from the Muon $g-2$ on the Parameter Space of the NMSSM." *JHEP* **2008** (2008) 079 [0806.0733].

[247] **CLEO** Collaboration, J. Insler *et al.*, "Search for the Decay $J/\psi \to \gamma+$ invisible." *Phys. Rev.* **D81** (2010) 091101 [1003.0417].

[248] C. Bird, P. Jackson, R. V. Kowalewski and M. Pospelov, "Search for dark matter in $b \to s$ transitions with missing energy." *Phys. Rev. Lett.* **93** (2004), no. 20 201803 [hep-ph/0401195].

[249] S. Raychaudhuri and A. Raychaudhuri, "Singlet Higgs boson signals at electron positron colliders." *Phys. Rev. D* **44** (1991), no. 9 2663–2668.

[250] G. Rupak and E. H. Simmons, "Limits on pseudoscalar bosons from rare Z decays at LEP." *Phys. Lett.* **B362** (1995) 155–163 [hep-ph/9507438].

[251] M. Altmann *et al.*, "Search for the electron positron decay of axions and axion - like particles at a nuclear power reactor at Bugey." *Z. Phys.* **C68** (1995) 221–227.

[252] H. M. Chang *et al.*, "Search for axions from the Kuo-Sheng nuclear power reactor with a high-purity germanium detector." *Phys. Rev. D* **75** (2007), no. 5 052004 [hep-ex/0609001].

[253] C. N. Brown *et al.*, "New Limit on Axion Production in 800-GeV Hadronic Showers." *Phys. Rev. Lett.* **57** (1986), no. 17 2101–2104.

[254] E. Riordan, M. Krasny, K. Lang, P. De Barbaro, A. Bodek *et al.*, "A Search For Short Lived Axions In An Electron Beam Dump Experiment." *Phys.Rev.Lett.* **59** (1987) 755–758.

[255] A. Bross, M. Crisler, S. H. Pordes, J. Volk, S. Errede and J. Wrbanek, "A Search for Shortlived Particles Produced in an Electron Beam Dump." *Phys.Rev.Lett.* **67** (1991) 2942–2945.

[256] **CHARM** Collaboration, F. Bergsma *et al.*, "Search for axion-like particle production in 400 GeV proton-copper interactions." *Phys. Lett.* **B157** (1985) 458.

[257] M. Davier and H. Nguyen Ngoc, "An unambiguous search for a light Higgs boson." *Phys. Lett.* **B229** (1989) 150.

[258] R. Dermisek and J. F. Gunion, "Direct production of a light CP-odd Higgs boson at the Tevatron and LHC." *Phys. Rev. D* **81** (2010), no. 5 055001 [0911.2460].

[259] M. M. Almarashi and S. Moretti, "Muon Signals of Very Light CP-odd Higgs states of the NMSSM at the LHC." *Phys.Rev.* **D83** (2011) 035023 [1101.1137].

[260] M. M. Almarashi and S. Moretti, "Scope of Higgs production in association with a bottom quark pair in probing the Higgs sector of the NMSSM at the LHC." 1205.1683.

[261] A. Belyaev, J. Pivarski, A. Safonov, S. Senkin and A. Tatarinov, "LHC discovery potential of the lightest NMSSM Higgs in the $h_1 \to a_1 a_1 \to 4$ muons channel." *Phys. Rev. D* **81** (2010), no. 7 075021 [1002.1956].

[262] **CMS** Collaboration, S. Chatrchyan *et al.*, "Search for a non-standard-model Higgs boson decaying to a pair of new light bosons in four-muon final states." 1210.7619.

[263] D. G. Cerdeno, P. Ghosh and C. B. Park, "Probing the two light Higgs scenario in the NMSSM with a low-mass pseudoscalar." *JHEP* **1306** (2013) 031 [1301.1325].

[264] J. Schweppe, A. Gruppe, K. Bethge, H. Bokemeyer, T. Cowan *et al.*, "Observation of a peak structure in positron spectra from U + Cm collisions." *Phys.Rev.Lett.* **51** (1983) 2261–2264.

[265] A. Konaka, K. Imai, H. Kobayashi, A. Masaike, K. Miyake, T. Nakamura, N. Nagamine, N. Sasao, A. Enomoto, Y. Fukushima, E. Kikutani, H. Koiso, H. Matsumoto, K. Nakahara, S. Ohsawa, T. Taniguchi, I. Sato and J. Urakawa, "Search for Neutral Particles in Electron-Beam-Dump Experiment." *Phys. Rev. Lett.* **57** (1986), no. 6 659–662.

[266] J. D. Bjorken, R. Essig, P. Schuster and N. Toro, "New Fixed-Target Experiments to Search for Dark Gauge Forces." *Phys. Rev.* **D80** (2009) 075018 [0906.0580].

[267] Y. S. Tsai, "Axion bremsstrahlung by an electron beam." *Phys. Rev. D* **34** (1986), no. 5 1326–1331.

[268] K. J. Kim and Y.-S. Tsai, "Improved Weizsäcker-Williams Method and Its Application to Lepton and W-Boson Pair Production." *Phys. Rev. D* **8** (1973), no. 9 3109–3125.

[269] Y.-S. Tsai, "Pair Production and Bremsstrahlung of Charged Leptons." *Rev. Mod. Phys.* **46** (1974), no. 4 815–851.

[270] M. Davier, J. Jeanjean and H. Nguyen Ngoc, "Search For Axions In Electron Bremsstrahlung." *Phys.Lett.* **B180** (1986) 295.

[271] C. Bouchiat and P. Fayet, "Constraints on the parity-violating couplings of a new gauge boson." *Phys.Lett.* **B608** (2005) 87–94 [hep-ph/0410260].

[272] P. Fayet, "Effects Of The Spin 1 Partner Of The Goldstino (gravitino) On Neutral Current Phenomenology." *Phys.Lett.* **B95** (1980) 285.

[273] P. Fayet, "Parity Violation Effects Induced By A New Gauge Boson." *Phys.Lett.* **B96** (1980) 83.

[274] P. Fayet, "A la recherche d'un nouveau boson de spin un." *Nucl. Phys.* **B187** (1981) 184–204.

[275] P. Fayet, "Constraints on Light Dark Matter and U bosons, from ψ, Υ, K^+, π^0, η and η' decays." *Phys.Rev.* **D74** (2006) 054034 [hep-ph/0607318].

[276] P. Fayet, "U(1)$_A$ Symmetry in two-doublet models, U bosons or light pseudoscalars, and ψ and Υ decays." *Phys.Lett.* **B675** (2009) 267–271 [0812.3980].

[277] J. Alwall, M. Herquet, F. Maltoni, O. Mattelaer and T. Stelzer, "MadGraph 5 : Going Beyond." *JHEP* **1106** (2011) 128 [1106.0522].

[278] R. Essig, P. Schuster and N. Toro. MadGraph Monte Carlo for Hidden Photons in Fixed Target Experiments, unpublished, private correspondence.

[279] J. Blumlein and J. Brunner, "New Exclusion Limits for Dark Gauge Forces from Beam-Dump Data." *Phys. Lett.* **B701** (2011) 155–159 [1104.2747].

[280] S. Gninenko, "Stringent limits on the $\pi^0 \to \gamma X$, $X \to e^+e^-$ decay from neutrino experiments and constraints on new light gauge bosons." *Phys.Rev.* **D85** (2012) 055027 [1112.5438].

[281] S. Gninenko, "Constraints on sub-GeV hidden sector gauge bosons from a search for heavy neutrino decays." *Phys.Lett.* **B713** (2012) 244–248 [1204.3583].

[282] H. Davoudiasl, H.-S. Lee and W. J. Marciano, "Dark Side of Higgs Diphoton Decays and Muon $g-2$." *Phys.Rev.* **D86** (2012) 095009 [1208.2973].

[283] M. Endo, K. Hamaguchi and G. Mishima, "Constraints on Hidden Photon Models from Electron $g-2$ and Hydrogen Spectroscopy." *Phys.Rev.* **D86** (2012) 095029 [1209.2558].

[284] T. Beranek and M. Vanderhaeghen, "Constraints on the Dark Photon Parameter Space from Leptonic Rare Kaon Decays." *Phys.Rev.* **D87** (2013) 015024 [1209.4561].

[285] **A1** Collaboration, H. Merkel *et al.*, "Search for Light Gauge Bosons of the Dark Sector at the Mainz Microtron." *Phys.Rev.Lett.* **106** (2011) 251802 [1101.4091].

[286] R. Essig, P. Schuster, N. Toro and B. Wojtsekhowski, "An Electron Fixed Target Experiment to Search for a New Vector Boson A′ Decaying to e^+e^-." *JHEP* **02** (2011) 009 [1001.2557].

[287] **APEX** Collaboration, S. Abrahamyan *et al.*, "Search for a New Gauge Boson in Electron-Nucleus Fixed-Target Scattering by the APEX Experiment." *Phys.Rev.Lett.* **107** (2011) 191804 [1108.2750].

[288] **APEX** Collaboration. http://hallaweb.jlab.org/experiment/APEX/.

[289] F. Archilli, D. Babusci, D. Badoni, I. Balwierz, G. Bencivenni *et al.*, "Search for a vector gauge boson in ϕ meson decays with the KLOE detector." *Phys.Lett.* **B706** (2012) 251–255 [1110.0411].

[290] **KLOE-2** Collaboration, D. Babusci *et al.*, "Limit on the production of a light vector gauge boson in ϕ meson decays with the KLOE detector." *Phys.Lett.* **B720** (2013) 111–115 [1210.3927].

[291] **BABAR** Collaboration, B. Aubert *et al.*, "Search for Dimuon Decays of a Light Scalar in Radiative Transitions $\Upsilon(3S) \to \gamma A^0$." 0902.2176.

[292] M. Reece and L.-T. Wang, "Searching for the light dark gauge boson in GeV-scale experiments." *JHEP* **07** (2009) 051 [0904.1743].

[293] A. Hook, E. Izaguirre and J. G. Wacker, "Model Independent Bounds on Kinetic Mixing." *Adv.High Energy Phys.* **2011** (2011) 859762 [1006.0973].

[294] B. Echenard, "Search for Low-Mass Dark Matter at BABAR." *Mod.Phys.Lett.* **A27** (2012) 1230016 [1205.3505].

[295] S. Gninenko, "Constraints on dark photons from π^0 decays." *Phys. Rev.* **D87** (2013) 035030 [1301.7555].

[296] J. Jaeckel, M. Jankowiak and M. Spannowsky, "LHC probes the hidden sector." 1212.3620.

[297] **ATLAS** Collaboration, N. Tal Hod and Y. Silver, "Search for high-mass dilepton resonances with 5 fb^{-1} of pp collisions at $\sqrt{s} = 7$ TeV.". ATL-PHYS-SLIDE-2012-309.

[298] **ALTAS** Collaboration, ALTAS, "Search for high-mass dilepton resonances with 5 fb^{-1} of pp collisions at $\sqrt{s} = 7$ TeV with the ATLAS experiment.". ATLAS-CONF-2012-007.

[299] **CMS** Collaboration, S. Chatrchyan *et al.*, "Search for narrow resonances in dilepton mass spectra in pp collisions at $\sqrt{s} = 7$ TeV." *Phys.Lett.* **B714** (2012) 158–179 [1206.1849].

[300] B. Batell, M. Pospelov and A. Ritz, "Probing a Secluded U(1) at B-factories." *Phys. Rev. D* **79** (2009), no. 11 115008 [0903.0363].

[301] R. Essig, P. Schuster and N. Toro, "Probing Dark Forces and Light Hidden Sectors at Low-Energy e^+e^- Colliders." *Phys. Rev.* **D80** (2009) 015003 [0903.3941].

[302] M. Freytsis, G. Ovanesyan and J. Thaler, "Dark Force Detection in Low Energy e-p Collisions." *JHEP* **01** (2010) 111 [0909.2862].

[303] B. Batell, M. Pospelov and A. Ritz, "Exploring Portals to a Hidden Sector Through Fixed Targets." *Phys. Rev. D* **80** (2009), no. 9 095024 [0906.5614].

[304] J. Hewett, H. Weerts, R. Brock, J. Butler, B. Casey *et al.*, "Fundamental Physics at the Intensity Frontier." 1205.2671.

[305] B. Wojtsekhowski, "Searching for a U-boson with a positron beam." *AIP Conf.Proc.* **1160** (2009) 149–154 [0906.5265].

[306] **DarkLight** Collaboration. http://dmtpc.mit.edu/DarkLight/.

[307] **The Heavy Photon Search (HPS)** Collaboration. https://confluence.slac.stanford.edu/display/hpsg/.

[308] **CDMS** Collaboration, D. S. Akerib *et al.*, "Limits on spin-independent WIMP nucleon interactions from the two-tower run of the Cryogenic Dark Matter Search." *Phys. Rev. Lett.* **96** (2006) 011302 [astro-ph/0509259].

[309] F. Giuliani, "Are direct search experiments sensitive to all spin-independent WIMP candidates?." *Phys.Rev.Lett.* **95** (2005) 101301 [hep-ph/0504157].

[310] J. L. Feng, J. Kumar, D. Marfatia and D. Sanford, "Isospin-Violating Dark Matter." *Phys. Lett.* **B703** (2011) 124–127 [1102.4331].

[311] M. T. Frandsen, F. Kahlhoefer, J. March-Russell, C. McCabe, M. McCullough and K. Schmidt-Hoberg, "On the DAMA and CoGeNT Modulations." *Phys.Rev.* **D84** (2011) 041301 [1105.3734].

[312] C. McCabe, "DAMA and CoGeNT without astrophysical uncertainties." *Phys.Rev.* **D84** (2011) 043525 [1107.0741].

[313] X. Gao, Z. Kang and T. Li, "Origins of the Isospin Violation of Dark Matter Interactions." *JCAP* **1301** (2013) 021 [1107.3529].

[314] H.-B. Jin, S. Miao and Y.-F. Zhou, "Implications of the latest XENON100 and cosmic ray antiproton data for isospin violating dark matter." *Phys.Rev.* **D87** (2013) 016012 [1207.4408].

[315] P. Ullio, M. Kamionkowski and P. Vogel, "Spin dependent WIMPs in DAMA?." *JHEP* **0107** (2001) 044 [hep-ph/0010036].

[316] R. Kappl and M. W. Winkler, "New Limits on Dark Matter from Super-Kamiokande." *Nucl.Phys.* **B850** (2011) 505–521 [1104.0679].

[317] **PICASSO** Collaboration, S. Archambault, F. Aubin, M. Auger, E. Behnke, B. Beltran *et al.*, "Dark Matter Spin-Dependent Limits for WIMP Interactions on F-19 by PICASSO." *Phys.Lett.* **B682** (2009) 185–192 [0907.0307].

[318] **COUPP** Collaboration, E. Behnke *et al.*, "Improved Limits on Spin-Dependent WIMP-Proton Interactions from a Two Liter CF_3I Bubble Chamber." *Phys.Rev.Lett.* **106** (2011) 021303 [1008.3518].

[319] **SIMPLE** Collaboration, M. Felizardo *et al.*, "Final Analysis and Results of the Phase II SIMPLE Dark Matter Search." *Phys. Rev. Lett.* **108** (2011) 201302 [1106.3014].

[320] J. I. Collar, "Comments on 'Final Analysis and Results of the Phase II SIMPLE Dark Matter Search'." 1106.3559.

[321] **SIMPLE** Collaboration, SIMPLE, "Reply to arxiv:1106.3559 by J.I. Collar." 1107.1515.

[322] **COUPP** Collaboration, E. Behnke *et al.*, "Improved Spin-Dependent WIMP Limits from a Bubble Chamber." *Science* **319** (2008) 933–936 [0804.2886].

[323] **KIMS** Collaboration, H. Lee *et al.*, "Limits on WIMP-nucleon cross section with CsI(Tl) crystal detectors." *Phys.Rev.Lett.* **99** (2007) 091301 [0704.0423].

[324] **Super-Kamiokande** Collaboration, S. Desai *et al.*, "Search for dark matter WIMPs using upward through-going muons in Super-Kamiokande." *Phys. Rev.* **D70** (2004) 083523 [hep-ex/0404025].

[325] **XENON10** Collaboration, J. Angle, E. Aprile, F. Arneodo, L. Baudis, A. Bernstein *et al.*, "Limits on spin-dependent WIMP-nucleon cross-sections from the XENON10 experiment." *Phys.Rev.Lett.* **101** (2008) 091301 [0805.2939].

[326] D. Y. Akimov, H. Araujo, E. Barnes, V. Belov, A. Bewick *et al.*, "WIMP-nucleon cross-section results from the second science run of ZEPLIN-III." *Phys.Lett.* **B709** (2012) 14–20 [1110.4769].

[327] **CDMS** Collaboration, Z. Ahmed *et al.*, "Search for Weakly Interacting Massive Particles with the First Five-Tower Data from the Cryogenic Dark Matter Search at the Soudan Underground Laboratory." *Phys.Rev.Lett.* **102** (2009) 011301 [0802.3530].

[328] B. Allanach, M. Battaglia, G. Blair, M. S. Carena, A. De Roeck *et al.*, "The Snowmass points and slopes: Benchmarks for SUSY searches." *Eur.Phys.J.* **C25** (2002) 113–123 [hep-ph/0202233].

[329] **DAMIC** Collaboration, J. Barreto *et al.*, "Direct Search for Low Mass Dark Matter Particles with CCDs." *Phys.Lett.* **B711** (2012) 264–269 [1105.5191].

[330] R. Essig, J. Mardon and T. Volansky, "Direct Detection of Sub-GeV Dark Matter." *Phys.Rev.* **D85** (2012) 076007 [1108.5383].

[331] **XENON10** Collaboration, J. Angle *et al.*, "A search for light dark matter in XENON10 data." *Phys.Rev.Lett.* **107** (2011) 051301 [1104.3088].

[332] S. Andreas, M. D. Goodsell and A. Ringwald, "Hidden Photons in connection to Dark Matter." *to appear in AIP Conf.Proc. for the "Workshop to Explore Physics Opportunities with Intense, Polarized Electron Beams up to 300 MeV" held at MIT, Cambridge, Massachusetts in March 2013* (2013) [1306.1168].

[333] **PICASSO** Collaboration, S. Archambault *et al.*, "Constraints on Low-Mass WIMP Interactions on ^{19}F from PICASSO." *Phys.Lett.* **B711** (2012) 153–161 [1202.1240].

[334] **COUPP** Collaboration, E. Behnke *et al.*, "First Dark Matter Search Results from a 4-kg CF_3I Bubble Chamber Operated in a Deep Underground Site." *Phys.Rev.* **D86** (2012) 052001 [1204.3094].

[335] **XENON100** Collaboration, E. Aprile *et al.*, "Limits on spin-dependent WIMP-nucleon cross sections from 225 live days of XENON100 data." 1301.6620.

[336] M. T. Frandsen, F. Kahlhoefer, C. McCabe, S. Sarkar and K. Schmidt-Hoberg, "The unbearable lightness of being: CDMS versus XENON." 1304.6066.

[337] **CoGeNT** Collaboration, C. Aalseth *et al.*, "CoGeNT: A Search for Low-Mass Dark Matter using p-type Point Contact Germanium Detectors." 1208.5737.

[338] G. J. Feldman and R. D. Cousins, "Unified approach to the classical statistical analysis of small signals." *Phys.Rev.* **D57** (1998) 3873–3889 [physics/9711021].